Measurement of pH using Chemical Exchange Saturation Transfer Magnetic Resonance Imaging

Kevin James Ray

Department of Oncology
The Oxford Institute for Radiation Oncology
Lincoln College



A thesis submitted in partial fulfilment of the requirements for the degree of Doctor of Philosophy

Trinity Term 2017

To my late father,
Frank Arthur Ray.

Acknowledgments

"Few misfortunes can befall a boy which bring worse consequences than to have a really affectionate mother."

— W. Somerset Maugham, A Writer's Notebook, 1896

A lot can change in 100 years.

I am indebted to my own affectionate mother, whose actions and efforts have effected consequences that I am fortunate to have experienced. Her encouragement and support have been ever-present through over 20 years of education. The focus of the latter half of that time was shaped predominantly by the infectious enthusiasm my late father had for all things aviation. If not for him, and my sister Ginette's advice 11 years ago – "well you could teach yourself History" – my education in physics would have stopped at age 16.

As such, Messrs. Darren, Hibbard and Amadeo of Aylesford School, Warwick, deserve much praise for vindicating the decision to continue, as well as Adrian Wilson at the University of Warwick for convincing me that particle physics has applications outside of the Swiss-French border region. Thanks also to Joanna Collingwood, Michael Chappell and Gavin Morley for letting me join their research groups as an undergraduate at the University of Warwick, and Mary Finnegan for her guidance and tolerance of my fortnight-long obsession with Olympic Handball. Rory, Vicky, Jack, Paul, and the rest of Flats 37 & 39, thank you for always having something that wasn't physics to talk about; Ben, Sally, Kamal, Ashwin and Adam, thank you for making talking about physics (when I *really* had to) so bearable.

Travelling down the M40, I should like to thank innumerable members of the Middle and Senior Common Rooms of Lincoln College for making Oxford immediately feel like home. It has been my absolute pleasure to spend four years of my life in your company. Special mention should go to Simon and Laura, who have enriched my time here no end. I will cherish the memories of Lincoln College and Deep Hall...though perhaps I can recall more of the former than the latter.

I have also been fortunate enough to be part of a supportive Department. Sarah Norman, thank you for your enthusiasm and reassurance when I first arrived. Katy Higgins, thank you for all you do behind the scenes to make everything run like clockwork. You will be missed. A huge thanks to Caroline, Mari-lenna, Katie and Andy for keeping the RRI in one piece, which is no small feat, and to Mio and Anne-Marie for making admin enjoyable. Thanks to Sean, Paul, and the rest of the Imaging Core group for all that you do. Thanks also to the Medical Research Council, the Institute of Physics and Engineering in Medicine, Guarantors of Brain, Lincoln College, and Cancer Imaging Centre Oxford for funding which has contributed immensely to my continued survival. I am also grateful to Peter Jezzard and Geoff Higgins for examining me at various points through the DPhil process, and especially Bart Cornellisen who suffered through both Transfer and Confirmation of Status.

I have been lucky enough to work with some brilliant collaborators. Andrew Baldwin and Gogulan Karunanithy, thank you for reminding me that my DPhil is firmly entrenched in the physical sciences, regardless of what the University Divisions might say. George Harston and James Kennedy, thank you for forcing me to consider the clinical relevance of my work. James Coates, thank you for coming back and forth across the car park through some long days of imaging. Valerio Pereno and Luca Bau, thank you for your efforts in numerous experiments. Robert Brand and Paula Croal, thank you for being fellow CEST-nerds. Brian Burns and Dan Bulte, thank you for two years of sage advice and words of wisdom. Oh, and for Stockholm.

I have been luckier still to call the Sibsonites my colleagues and friends, and I will miss each and every one. Sarah, thank you for being as reliant on caffeine as I am, and always having a spare £1. Manon, who *isn't* addicted to coffee but still enjoys the walk, thank you for providing

entertainment and encouragement through the long days of sitting in the bunker. Nili, thank you for also being a coffee buddy, and your contagious smile. Jess, I will never fully understand your desire to wake up early just to shout, but I do understand your affection for Belgian Buns. Perhaps the two are linked. Kleo, thank you for telling me to take it easy. I don't want to know how much of a pain I would be if you hadn't. Christina, thank you for your generosity, it truly knows no bounds. Vinton, thank you for introducing swords to the office. I consider myself fortunate to be escaping with my eyesight (mostly) intact. Axel, I promise to never visit the Kassam Stadium without you. One day we'll go as Oxford United fans. *Je suis la gare!*

John, Stav and Emma, thank you for providing such good examples to emulate. Sébastien, the office isn't quite the same without you, and I hope Nottingham realise how lucky they are. Claire, thank you for abiding my incessant questions about grant codes and POs. Sasha, thank you for tolerating the most mundane problems with `VnmrJ`, and for blowing up the gradient amplifier for me so I didn't have to do it alone. Vas, thank you for being a fellow metastatic colony as we spread Sibsons throughout the RRI. Maria, thank you for being as enthusiastic as I am about heading to the pub on a Friday afternoon. I've lost count of the rounds that need squaring. Mario, I will miss your cheerful morning greetings. Vanessa, thank you for sharing the burden of the Aperio when I finally succumbed to its charm. Helen, it's been a pleasure getting to know you since you joined the group.

Manuel, thank you for having time for anyone, and doing it with your inherent kindness. You have taught me more than you might realise. Seville is lucky to have you and your family move there, and Oxford is a worse place for your absence. Jack, thank you for everything you've taught me about MR. Once and for all – *you are the better physicist*. And finally James, who has had the considerable task of dealing with my ineptitude at anything involving a pipette or fur. Thank you for your patience, guidance and unwavering support. And for suggesting consecutive 18 h days in the bunker as though it's the most obvious thing in the world. For one last time: thank you, James.

Penultimately, I would like to express the utmost gratitude to my supervisors, Prof. Michael Chappell and Prof. Nicola Sibson. Michael - thank you for your useful advice, encouragement, and the countless reference letters (some even addressed to yourself). I look forward to continuing to work with you, and maintaining the unique accolade of being supervised by both Michael Chappells currently working in British university engineering departments. Niki - thank you for letting be a Sibsonite, allowing me to pursue such interesting research, and indulging my occasional physics-nerd moments. Our meetings on Thursday mornings have been a true pleasure. Thank you both for always asking the right questions and making me a better scientist.

Finally, Elise – thank you for being a bastion of support, especially over the last four months. You are an unending source of love, belief and laughter, and I count myself incredibly lucky that you've chosen to spend the last few years of your life with me. I look forward to many, many more. *Ik zie u graag*.

Abstract

Measurement of pH using Chemical Exchange Saturation Transfer Magnetic Resonance Imaging

A thesis submitted in partial fulfillment for the requirements of the degree of Doctor of Philosophy

Trinity Term 2017

Kevin James Ray, Lincoln College

Altered metabolic phenotypes, with consequential alterations in tissue pH, are commonplace in a number of pathologies. The metabolic reprogramming common in cancer leads to acidification of the tumour microenvironment and alkalosis of the intracellular space, whereas the cessation of blood flow in ischaemic stroke results in systemic acidification of the affected tissue. Thus far, however, measurement of pH is under-utilised as a physiological parameter of interest in the clinic, despite its potential ability to measure treatment response or stratify patients to optimal therapeutic strategies. This lack of interest in pH is likely a result of a lack of non-invasive, clinically translatable measurement methods.

One modality that may be able to be used for non-invasive pH measurements *in vivo* is Chemical Exchange Saturation Transfer (CEST) Magnetic Resonance Imaging (MRI). CEST MRI measures changes in signal from water protons owing to their association with other biomolecules and metabolites, particularly via exchange of protons in amide and amine functional groups. The rate at which chemical exchange of these protons occurs affects the measured CEST MRI signal, and is sensitive to the environmental pH. Hence, through careful calibration, CEST MRI may be used to measure pH *in vivo*.

The development of CEST MRI to enable measurement of pH *in vivo* is the focus of this thesis. Firsly, novel, realistic phantom models of the *in vivo* intracellular environment of brain metastases and naïve mouse brain were developed to determine that the CESTR* metric with compensation for water T_1 and T_2 relaxation effects overcomes many challenges facing interpretation of CEST MRI data. An extension to this metric – isoCESTR* – was developed, and shown to potentially permit measurement of pH using simulated data.

Subsequently, three separate animal models of human disease were used to examine the ability of isoCESTR* to measure pH. Through combination of *in vivo* CEST MRI data and *ex vivo* protein concentration measurements, tissue pH was estimated using CEST MRI data from rats with brain metastasis and ischaemic stroke. Additionally, the pH change induced by alleviation of tumour hypoxia was measured in mice with subcutaneous tumours.

Finally, a novel pulse sequence combining stimulated echo diffusion and CEST methods was developed and validated as a means of separating intra- and extracellular CEST effects. This pulse sequence was used to estimate the proportion of CEST signal originating from the intracellular space for the first time.

CEST MRI is an imaging technique with great potential to permit pH measurement *in vivo* in clinical as well as research settings. It is hoped that the work presented here goes some way to improving the understanding of CEST effects from endogenous sources, and exploiting these effects for measurement of tissue pH.

Research Outcomes

Peer-reviewed Journal Articles

- **K.J. Ray**, J.R. Larkin, Y.K. Tee, A.A. Khrapitchev, G. Karunanithy, M. Barber, A.J. Baldwin, M.A. Chappell and N.R. Sibson, "Determination of an optimally sensitive and specific chemical exchange saturation transfer MRI quantification metric in relevant biological phantoms", *NMR in Biomedicine*, vol. 29, no. 11, pp. 1624 – 1633, 2016.

- **K.J. Ray**, N.R. Sibson and A.E. Kiltie, "Treatment of Breast and Prostate Cancer by Hypofractionated Radiotherapy: Potential Risks and Benefits", *Clinical Oncology*, vol. 27, no. 7, pp. 420 – 426, 2015.

Peer-reviewed Conference Proceedings

MusicCity CEST Workshop (2017), Nashville, USA

- P.L. Croal, **K.J. Ray** and M.A. Chappell, "How many frequencies? Reducing acquisition time for clinical application of model-based analysis of CEST data"

ISMRM 25 (2017), Honolulu, USA

- **K.J. Ray**, J.R. Larkin, M.A. Chappell and N.R. Sibson, "isoAPTR* - a novel method to measure tumour pH_i using CEST MRI"

- **K.J. Ray**, J.R. Larkin, B.A. Sutherland, G. Harston, A.J. Baldwin, A.M. Buchan, P. Jezzard, J. Kennedy, M.A. Chappell and N.R. Sibson, "Investigation into the origin of the APT MRI signal in ischemic stroke"

- **K.J. Ray**, J. Coates, R. Puliyadi, T. Ashton, P. Kinchesh, S. Smart, M.A. Chappel, G.S. Higgins and N.R. Sibson, "Modification of tumour hypoxia with Atovaquone measured by CEST MRI"

- P.L. Croal, **K.J. Ray**, Y. Msayib, J.R. Larkin, B.A. Sutherland, G. Harston, A.J. Baldwin, A.M. Buchan, P. Jezzard, J. Kennedy, N.R. Sibson and M.A. Chappell, "Model-Based Analysis of Partial Z-Spectra for Rapid Quantification of Amide Proton Transfer MRI"

- Y.K. Tee, B. Abidin, A.A. Khrapitchev, B.A. Sutherland, J.R. Larkin, **K.J. Ray**, G. Harston, A.M. Buchan, J. Kennedy, N.R. Sibson and M.A. Chappell, "CEST and NOE Signals in Ischemic Stroke at 9.4 T Evaluated Using a Lorentzian Multi-Pool Analysis: A Drop, an Increase or No Change?"

- M.A. Simard, J.R. Larkin, A.A. Khrapitchev, **K.J. Ray**, M.A. Chappell and N.R. Sibson, "Application of Multiphase Pseudo-Continuous ASL for Quantitative Blood Flow Measurement in Rat Brain Metastasis"

- J. Buck, J.R. Larkin, A.A. Khrapichev, M. Simard, **K.J. Ray**, M.A. Chappell and N.R. Sibson, "Multiphase Pseudo-Continuous ASL to Image Cerebral Blood Flow in Mice at 9.4 T"

- J. Miller, J.R. Larkin, K. Fisher, V. Ball, **K.J. Ray**, S. Serres, D.J. Tyler, A.Z. Lau and N.R. Sibson, "Transport Across the Blood-Brain-Barrier May Be Limiting for Hyperpolarized [1-^{13}C]pyruvate Neuro-Oncology Studies"

ISMRM 24 (2016), Singapore

- **K.J. Ray**, G. Karunanithy, J.R. Larkin, A.A. Khrapitchev, A.J. Baldwin, M.A. Chappell and N.R. Sibson, "Separation of intracellular and extracellular Z-spectra by DiffusionCEST"
- J.R. Larkin, M.A. Simard, A.A. Khrapitchev, **K.J. Ray**, J.A. Meakin, P. Kinchesh, S. Smart, P. Jezzard, M.A. Chappell and N.R. Sibson, "Multiphase pCASL for imaging blood flow in rodent brains"

CRUK Cancer Imaging Centre National Meeting (2016), Manchester

- **K.J. Ray**, M. Simard, J.R. Larkin, A.A. Khrapitchev, M.A. Chappell and N.R. Sibson, "Exploring endogenous CEST MRI as a means of for pH imaging of brain metastases"

British Chapter ISMRM (2015), London

- **K.J. Ray**, J.R. Larkin, Y.K. Tee, A.A. Khrapitchev, M.A. Chappell and N.R. Sibson, "Sensitivity of CEST MRI for pH measurement in brain metastases"

ISMRM 23 (2015), Toronto

- **K.J. Ray**, J.R. Larkin, Y.K. Tee, A.A. Khrapitchev, M.A. Chappell and N.R. Sibson, "Sensitivity of CEST MRI for pH measurement in brain metastases"

Contents

Acknowledgments i

Abstract iii

Research Outcomes v

Table of Contents vii

List of Figures xiii

List of Tables xvii

1 Motivation and methods for pH measurement 1

1.1 Regulation of pH . . . 2

1.2 Cancer . . . 3

1.2.1 Metabolism in Cancer . . . 3

1.2.2 Tumour microenvironment . . . 5

1.2.2.1 pH in Cancer . . . 5

1.2.2.2 Hypoxia in Cancer . . . 6

1.2.3 Treatment of Cancer . . . 7

1.3 Ischaemic Stroke . . . 8

1.3.1 Pathophysiology of Ischaemic Stroke . . . 9

1.3.2 Stroke treatment . . . 10

1.3.3 pH in Stroke . . . 11

1.4 Summary of Motivations for pH measurement . . . 12

1.5 Methods of pH measurement . . . 12

1.5.1 ^{1}H NMR . . . 12

1.5.2 ^{31}P NMR . . . 13

1.5.3 Hyperpolarised ^{13}C NMR/MRI . . . 13

1.5.4 Relaxometry . . . 13

1.5.5 Electron Paramagnetic Resonance . . . 14

1.5.6 Positron Emission Tomography . . . 14

1.5.7 Optical imaging . . . 14

1.5.8 pH electrode . . . 15

1.5.9 Summary of pH measurement methods . . . 15

2 Theory and Applications of Nuclear Magnetic Resonance 17

2.1 Nuclear Magnetic Resonance & Magnetic Resonance Imaging . . . 18

2.1.1 From Spin to Magnetisation . . . 18
2.1.2 Radiofrequency Pulses . . . 20
2.1.3 Relaxation . . . 21
2.1.4 Gradients and Signal Detection . . . 22
2.1.5 Magnetisation Transfer . . . 23
2.1.5.1 Dipolar coupling . . . 23
2.1.5.2 Nuclear Overhauser Effects . . . 24
2.1.5.3 Relayed NOE & NOE-relayed exchange . . . 27
2.2 Chemical Exchange Saturation Transfer NMR/MRI . . . 28
2.2.1 Chemical Exchange in NMR/MRI . . . 28
2.2.2 CEST MRI . . . 30
2.2.2.1 Exogenous CEST MRI . . . 34
2.2.3 The Bloch-McConnell Equations . . . 34
2.2.4 CEST MRI Acquisition Methods . . . 35
2.2.5 CEST MRI Analysis Methods . . . 37
2.2.5.1 Source of the CEST Effect . . . 37
2.2.5.2 Measuring the CEST Effect . . . 38
2.2.6 Applications . . . 41
2.2.7 Limitations . . . 43
2.2.7.1 Accurate quantification of effect size . . . 43
2.2.7.2 Signal source *in vivo* . . . 43
2.2.7.3 Physical location of signal source *in vivo* . . . 44
2.3 Diffusion NMR/MRI . . . 44
2.3.1 The Bloch-Torrey Equations . . . 47
2.3.2 Limitations . . . 47
2.4 Thesis aims . . . 48

3 Determination of an optimally specific and sensitive quantification metric for CEST MRI 49

3.1 Introduction . . . 50
3.2 Methods . . . 50
3.2.1 Phantom Preparation . . . 50
3.2.2 Validation of phantom models . . . 51
3.2.3 NMR & MRI experiments . . . 52
3.2.4 MRI Data Analysis . . . 53
3.2.5 Determination of optimal metric & measurement of pH . . . 54
3.3 Results . . . 56

3.3.1 Phantom Validation . . . 56
3.3.2 Measurement of CEST effect . . . 57
3.3.3 Determination of optimal metric . . . 59
3.3.4 Measurement of phantom pH . . . 62
3.4 Discussion . . . 64
3.5 Conclusion . . . 66

4 Further development of CESTR* 67
4.1 Introduction . . . 68
4.2 Methods . . . 69
4.2.1 Simulations . . . 69
4.2.2 Performance of model based analysis & dependency of CESTR* on labile pool parameters . . . 70
4.2.3 Effect of noise on model based analysis . . . 70
4.2.4 *In vivo* dataset . . . 72
4.2.5 Model based analysis of CEST data . . . 72
4.2.6 isoCESTR* method . . . 73
4.3 Results . . . 74
4.3.1 Performance of model based analysis . . . 74
4.3.2 CESTR* is a degenerate metric . . . 80
4.3.3 Effect of noise on model based analysis . . . 84
4.3.4 CESTR* measurements from *in vivo* data . . . 87
4.3.5 Feasibility of isoCESTR* method . . . 88
4.4 Discussion . . . 90
4.5 Conclusion . . . 92

5 Elucidation of *in vivo* CEST MRI signals 95
5.1 Introduction . . . 96
5.2 Methods . . . 97
5.2.1 Brain metastasis animal model . . . 97
5.2.2 Ischaemic stroke animal model . . . 97
5.2.3 Hypopharyngeal squamous cell carcinoma animal model . . . 99
5.2.4 MRI experiments . . . 99
5.2.4.1 Brain metastasis experiment . . . 100
5.2.4.2 Ischaemic stroke experiment . . . 101
5.2.4.3 Atovaquone treatment experiment . . . 101
5.2.5 MRI data analysis . . . 102
5.2.6 Region of interest definitions . . . 104

5.2.6.1 Brain metastasis experiment . . . 104
5.2.6.2 Ischaemic stroke experiment . . . 105
5.2.6.3 Atovaquone treatment experiment . . . 105
5.2.7 Subcellular fractionation & protein concentration measurements . . . 106
5.2.8 Histology . . . 107
5.2.8.1 Brain metastasis experiment . . . 109
5.2.8.2 Ischaemic stroke experiment . . . 109
5.2.8.3 Atovaquone treatment experiment . . . 109
5.2.9 pH estimation using isoCESTR* . . . 110
5.3 Results . . . 110
5.3.1 Brain metastasis experiment . . . 110
5.3.1.1 CEST MRI Results . . . 110
5.3.1.2 CESTR* with and without voxelwise T_1 and T_2 correction . . . 111
5.3.1.3 Protein concentration measurements . . . 111
5.3.1.4 Estimation of tumour pH by isoCESTR* . . . 114
5.3.2 Ischaemic stroke experiment . . . 117
5.3.2.1 CEST MRI Results . . . 117
5.3.2.2 Protein concentration measurements . . . 118
5.3.2.3 Estimation of pH in infarct core . . . 119
5.3.3 Atovaquone treatment experiment . . . 121
5.3.3.1 CEST MRI Results . . . 121
5.3.3.2 Protein concentration measurements . . . 122
5.3.3.3 Estimation of pH change in atovaquone treated animals . . . 126
5.4 Discussion . . . 126
5.4.1 Histological measurement of protein concentration . . . 127
5.4.2 Brain metastasis experiment . . . 128
5.4.3 Ischaemic stroke experiment . . . 131
5.4.4 Atovaquone treatment experiment . . . 132
5.4.5 Accuracy of amide proton concentration estimates by isoCESTR* . . . 133
5.5 Conclusion . . . 135

6 Separation of intra- and extracellular CEST effects 137
6.1 Introduction . . . 138
6.2 Methods . . . 139
6.2.1 Simulations . . . 139
6.2.2 DiffusionCEST Pulse Sequence . . . 141
6.2.3 Sample Preparation . . . 142

6.2.3.1 Giant Unilamellar Vesicles (GUVs) . . . 143
6.2.3.2 Cells . . . 144
6.2.3.3 Post-mortem animals . . . 144
6.2.4 NMR Experiments . . . 145
6.2.5 Data Analysis . . . 145
6.3 Results . . . 147
6.3.1 Simulations . . . 147
6.3.2 GUVs . . . 149
6.3.3 Cells . . . 150
6.3.4 Post-mortem animals . . . 153
6.4 Discussion . . . 155
6.5 Conclusion . . . 158

7 Conclusions, Criticisms, and Future Work 159
7.1 Conclusions . . . 160
7.2 Criticisms & Future Work . . . 160
7.2.1 Effect of protein conformation on CEST signal . . . 160
7.2.2 Validation of pH estimates made using isoCESTR* . . . 161
7.2.3 Application of diffusionCEST with imaging readout . . . 162
7.2.4 Modification of tumour pH using glucose . . . 162
7.2.5 Subregional analysis of tumours . . . 163
7.2.6 Minimal data required for accurate model fitting results . . . 164
7.3 Closing Remarks . . . 164

Bibliography 167

A Detection of doxorubicin using CEST MRI 189
A.1 Introduction . . . 189
A.2 Methods . . . 190
A.3 Results . . . 191
A.4 Discussion . . . 193

B Treatment of Breast and Prostate Cancer 195
B.1 Abstract . . . 196
B.2 Introduction . . . 196
B.3 Radiotherapy Treatment, Normal Tissue Effects and the Linear Quadratic Model . 196
B.4 Hypofractionated Radiotherapy . . . 198
B.5 Hypofractionated Radiotherapy in Breast and Prostate Cancer . . . 198
B.6 Benefits of Hypofractionation in Prostate and Breast Cancer . . . 199

B.7 Risks Associated with Hypofractionation in Breast and Prostate Cancer 202
B.8 Discussion 204
B.9 Future Directions 205
B.10 Acknowledgements 205
B.11 Statement of Search Strategies Used and Sources of Information 205
B.12 References 205

List of Figures

1.1 Increase in scientific research in cancer over recent years. . . . 4
1.2 Estimated cerebral blood flow (CBF) thresholds for induction of metabolic disturbances in tissue. . . . 9

2.1 Summary of the nuclear Overhauser effect (NOE) arising from dipolar coupling and cross-relaxation. . . . 25
2.2 Variation of T_1 and T_2 relaxation times with correlation time τ_c. . . . 26
2.3 Magnetisation transfer pathways encountered *in vivo*. . . . 27
2.4 Demonstration of how chemical exchange can affect recorded NMR signals. . . . 29
2.5 A typical CEST MRI pulse sequence (A) and the resultant CEST or Z-spectrum (B). . . . 31
2.6 Multi-pool nature of the *in vivo* Z-spectrum demonstrated by simulations using the Bloch-McConnell equations. . . . 33
2.7 Graphical representation of the CESTR* calculation procedure. . . . 41

3.1 Demonstration of the Bayesian Bloch-McConnell fitting algorithm BayCEST fitting well to the measured Z-spectra . . . 54
3.2 R^2 as a function of pH of 4T1-GFP phantom . . . 55
3.3 NMR spectra of novel phantom model . . . 58
3.4 4T1-GFP metabolites affect measured Z-spectra . . . 59
3.5 Linear regression relationships of CEST metrics with phantom properties . . . 60
3.6 T_1 and T_2 variation in phantoms . . . 61
3.7 Demonstration of the source of negative APT*/MTR_{Rex} values . . . 61
3.8 Correlation of experimentally measured CEST effects to theoretical values . . . 63
3.9 Measurements of pH made *in vitro* using CESTR* with measured T_1/T_2 priors . . . 64

4.1 Schematic of realistic six pool model used to evaluate dependency of CESTR* on labile pool parameters and evaluate the performance of the BayCEST model based analysis method. . . . 69
4.2 Demonstration of the generalised isoCESTR* method. . . . 73
4.3 Comparison of fitted and true parameter values for amide proton concentration (A) and exchange rate (B) for all 121 Z-spectra simulated. . . . 75
4.4 CESTR*, amide concentration, and amide exchange rates estimated from the BayCEST algorithm applied to *in vivo* data. . . . 78
4.5 CESTR*, amide concentration, and amide exchange rates estimated from the same *in vivo* data analysed in Fig. 4.4 analysed with the new BayCEST algorithm with amide proton concentration information included. . . . 79

4.6 Comparison of fitted and true parameter values for amide proton concentration and exchange rate for all 121 Z-spectra simulated analysed using a BayCEST algorithm with informative prior information for the amide proton concentration. 80
4.7 Comparison of fitted and true parameter values for amide proton concentration and exchange rate for 35 Z-spectra in a biologically plausible parameter range, analysed using the new BayCEST algorithm with informative prior information for the amide proton concentration. 81
4.8 Comparison of fitted and true parameter values for amide proton concentration and exchange rate for 35 Z-spectra in a biologically plausible parameter range, analysed using the original BayCEST algorithm. 82
4.9 Variation of CESTR* as a function of amide proton concentration and exchange rate. . 82
4.10 CESTR* is a degenerate metric. 83
4.11 Comparison between CESTR* measured using the original or new BayCEST algorithm and the true CESTR* determined from the known ground truth simulation parameters. 84
4.12 Example of typical simulated Z-spectra, with random noise added, for five different random noise levels ε. 85
4.13 Effect of noise on CESTR* and amide pool parameter estimates when using the new BayCEST algorithm. 85
4.14 Effect of noise on CESTR* and amide pool parameter estimates when using the original BayCEST algorithm. 86
4.15 RD increases with ε. 87
4.16 Example model fitted Z-spectra and raw data for two example voxels. 88
4.17 Spatial distribution of voxels fitted with $RD > 7\%$ *in vivo*. 88
4.18 Application of isoCESTR* to simulated data. 89

5.1 Location of collected biopsies in MCAO model 98
5.2 Respiration gated CEST MRI pulse sequence implemented for the atovaquone experiment. 102
5.3 Example of defined ROIs in animals following ischaemic stroke. 105
5.4 Coomassie standard curve to show conversion between transformed blue RGB intensity to protein concentration. 109
5.5 CESTR* map, T_1-weighted image, RD map, and $RD > 7\%$ binary map of a representative rat from the brain metastasis experiment. 112
5.6 rCESTR* values from tumour rim and necrotic tumour core regions in all animals in the brain metastasis experiment. 113
5.7 Comparison of rCESTR* in tumour rim and core with regional or voxelwise T_1 and T_2 priors. 113

5.8 Cytoplasmic, non-cytoplasmic and total protein concentrations measured by BCA assay of biopsied tissue from the contralateral healthy brain and tumour of animals with brain metastasis. 114
5.9 Example of Coomassie stained sections through a tumour from a representative rat. . 115
5.10 Comparison of adjacent tissue sections stained for Coomassie, pimonidazole and CD31.116
5.11 Demonstration of the isoCESTR* method to measure the pH of ENU tumours. 116
5.12 Multiparametric imaging of a representative rat in the ischaemic stroke experiment. . 117
5.13 rCESTR* values in infarct core, infarct growth and oligemia regions at 1 h and 2 h post-MCAO. 118
5.14 Cytoplasmic, non-cytoplasmic and total protein concentrations measured by BCA assay in each tissue region biopsied from animals with ischaemic stroke. 119
5.15 Example of Coomassie stained sections through a stroke lesion from a representative rat. 120
5.16 Verification that the infarct core lesion identified on Coomassie by lower protein concentration is the infarct core by staining an adjacent tissue section with NeuN. . . . 121
5.17 Demonstration of the isoCESTR* method to measure the pH of infarct core region of ischaemic stroke. 122
5.18 Representative CESTR* maps from mice in the atovaquone treated and control (DMSO treated) groups. 122
5.19 Cumulate frequency distributions for CESTR* values within the atovaquone treated and control groups of mice. 123
5.20 Cytoplasmic, non-cytoplasmic and total protein concentrations measured by BCA assay of tumour tissue recovered from mice treated with atovaquone or DMSO. 124
5.21 Examples of Coomassie stained sections from tumours in atovaquone treated and control mice. 124
5.22 Comparison of Coomassie and EF5 staining. 125
5.23 Demonstration of the isoCESTR* method to measure the change in tumour pH due to atovaquone treatment. 126
5.24 Comparison of protein concentrations measured by Coomassie and BCA assay methods for the tissue samples that are able to be directly compared across all three experiments in this chapter. 128

6.1 Schematic of realistic model used for simulations in Chapter 6. 140
6.2 DiffusionCEST pulse sequence 143
6.3 Example Z-spectra for the simulations of normal (black) and tumour (red) tissue, along with the model fitted Z-spectra from BayCEST and the fitting residual. 147

6.4 Variation of CESTR* as a function of transcytolemmal exchange in deterministic simulation of normal and tumour tissue. 149
6.5 Separated intra- and extracellular Z-spectra and MTR_{asym} curves for GUVs. 150
6.6 Variable Δ dataset acquired from a sample of GUVs in the 14 T NMR spectrometer. . . 151
6.7 Microscope image of GUVs and frequency distribution of GUV diameters. 151
6.8 Separated intra- and extracellular Z-spectra and MTR_{asym} curves from 4T1-GFP cells suspended in PBS. 152
6.9 Separated intra- and extracellular Z-spectra and MTR_{asym} curves from homogenously suspended 4T1-GFP cells in matrigel. 152
6.10 Variable Δ dataset acquired from a sample of 4T1-GFP cells suspended in matrigel in the 14 T NMR spectrometer. 153
6.11 Separated intra- and extracellular Z-spectra and MTR_{asym} curves from rat brain tissue in an NMR tube. 154
6.12 Separated intra- and extracellular Z-spectra and MTR_{asym} curves from intact post-mortem mouse brain. 155

A.1 Chemical structure of doxorubicin, with labile hydroxyl and amine protons highlighted. 189
A.2 Z-spectrum from a sample of 34 mM doxorubicin, showing effects at 3 ppm, 1.2 ppm, and 0.8 ppm associated with labile hydroxyl and amine groups (see Fig. A.1). 191
A.3 Variation of CEST effect as saturation power (left) and duration (right) are varied. The optimal saturation parameters for Doxorubicin were determined as 9.5 µT for 7.5 s. . . 192
A.4 Omega Plot for a sample of 34 mM doxorubicin estimates the exchange rate for the protons associated with the CEST effect at 3 ppm as 389 Hz. 192
A.5 Concentration dependence of CEST effect measured from samples of doxorubicin alone (left) and doxorubicin in a physiological phantom (right). 192
A.6 Z-spectra and MTR_{asym} curves from subcutaneous tumour pre- and post-injection of doxorubicin. 193

B.1 Sigmoid-shaped curves for tumour control and normal tissue complication/damage probability. 197

List of Tables

2.1 Parameters for each pool used to simulate the Z-spectrum displayed in Fig. 2.6. 33

3.1 Model parameter prior values used for Bayesian fitting of Bloch-McConnell equations to measured Z-spectra. 55
3.2 p values for the results of t–tests comparing the linear regression gradient values for CEST effect measurements from 4T1-GFP and naïve brain phantom. 59

4.1 Simulation parameters used in the Monte Carlo simulation of Z-spectra to realistically reflect the physiological noise affecting *in vivo* data. 71
4.2 Parameters for simulation of healthy brain tissue. The exchange constants k_{ba} and k_{fa} (i.e. amides and amines) were determined from the defined pH. 74
4.3 Parameters for simulation of tumour tissue. The exchange constants k_{ba} and k_{fa} (i.e. amides and amines) were determined from the defined pH. 74

5.1 Best fit values for the one-site binding equation in Eq. 5.6. 108
5.2 Table of amino acid residues within the human proteome and their relative abundance. 134

6.1 Simulation parameters used to reflect Z-spectra acquired from normal brain. 141
6.2 Simulation parameters used to reflect Z-spectra acquired from tumour tissue. 141
6.3 CESTR* and rCESTR* values for each deterministic simulation to determine the extent to which each parameter contributes to the measured CESTR* difference between simulated normal and tumour tissue. 148
6.4 Biexponential and complex model diffusion results for GUVs. 150
6.5 Comparison of diffusion characteristics of cells suspended in PBS acquired using diffusionCEST and a similar sample used in a previous study. 151
6.6 Diffusion properties of cells suspended in matrigel samples. 153
6.7 Comparison of diffusion characteristics of the rat brain tissue acquired using diffusionCEST and a similar sample used in a previous study. 154
6.8 Comparison of diffusion characteristics of intact post-mortem mouse brain tissue acquired using diffusionCEST and a similar sample used in a previous study. 155

B.1 α/β ratios estimated from START-A trial. 200
B.2 Summary of the breast cancer hypofractionation trials mentioned in this review. . . . 201
B.3 Summary of the prostate cancer hypofractionation trials mentioned in this review . . 202

Chapter 1

Motivation and methods for pH measurement

Contents

1.1 Regulation of pH . . . 2
1.2 Cancer . . . 3
1.2.1 Metabolism in Cancer . . . 3
1.2.2 Tumour microenvironment . . . 5
1.2.3 Treatment of Cancer . . . 7
1.3 Ischaemic Stroke . . . 8
1.3.1 Pathophysiology of Ischaemic Stroke . . . 9
1.3.2 Stroke treatment . . . 10
1.3.3 pH in Stroke . . . 11
1.4 Summary of Motivations for pH measurement . . . 12
1.5 Methods of pH measurement . . . 12
1.5.1 ^{1}H NMR . . . 12
1.5.2 ^{31}P NMR . . . 13
1.5.3 Hyperpolarised ^{13}C NMR/MRI . . . 13
1.5.4 Relaxometry . . . 13
1.5.5 Electron Paramagnetic Resonance . . . 14
1.5.6 Positron Emission Tomography . . . 14
1.5.7 Optical imaging . . . 14
1.5.8 pH electrode . . . 15
1.5.9 Summary of pH measurement methods . . . 15

The aim of this introductory chapter is to discuss the importance of pH and its regulation in biological tissues. The mechanisms by which alterations of pH in cancer and ischaemic stroke occur are introduced, as well as the functional importance of measuring pH to assess treatment response or inform treatment decisions. Since the two pathologies studied in this thesis are cancer and ischaemic stroke, these are the only diseases discussed in detail.

1.1 Regulation of pH

Hydrogen potential (pH) is defined specifically as $pH = -\log_{10} \alpha_{H^+}$, where α_{H^+} is the activity (or effective concentration) of hydrogen ions [1]. The measurement of pH is commonplace in a number of industries[1], and its importance in biology, chemistry and medicine has been well-established for many years. pH is measured on a traceable continuous logarithic scale [2], with terminological definitions given to solutions with pH > 7 (basic), pH < 7 (acidic) and pH = 7 (neutral). Extremely acidic or basic environments within biomedical contexts are confined to specific locations, such as lysosomes [3] or the stomach [4], and pH in the body typically falls within the physiological range of 6 < pH < 8.

The regulation of pH in biological systems is crucial to their function [5]. The complex array of chemical reactions that are necessary for cells, tissues, organs and organisms to survive are in-part dependent on the environmental pH. A simple example is that enzymatic activity varies with pH, and the optimal pH for enzyme activity varies immensely depending on the enzyme and its function. Pepsin, the most prominent digestive enzyme in vertebrates that breaks down large protein structures, operates optimally at pH 2.0 [6]. In contrast, the activity of carbonic anhydrase, which catalyses the interconversion of carbon dioxide and bicarbonate, is highest for pH > 9 [7]. The differences in optimal pH level for each enzyme's activity is a contributing factor to the marked variation of pH within the body and even within a cell, where pH within certain organelles can be much lower than the surrounding cytoplasmic pH [3]. Nevertheless, even with this high level of variation of pH within the body, the pH of each specific space is very highly regulated to within tight tolerances. The intracellular cytosolic fluid, for instance, is typically in the range pH 7.0 – 7.2 [5], and the pH of the extracellular space (pH_e) and of blood is 7.35 – 7.45 [8].

This acid-base homeostasis is maintained via different mechanisms depending on the microenvironment in question. In the blood, for instance, the bicarbonate buffering system (Eq. 1.1) acts in conjunction with the respiration system and kidneys to maintain blood pH. In other cells, as well as the bicarbonate buffering system, the intracellular pH (pH_i) is well regulated by a complex system of sensory molecules, which in turn speed up or slow down various acid-base

[1] Particularly in brewing — pH as a concept was invented by Søren Sørensen while working for Carlsberg.

transporter mechanisms [9]. These acid-base transporter mechanisms can be broadly categorised as either acid extruders (which act to increase pH_i) or acid loaders (which act to decrease pH_i).

$$CO_2 + H_2O \overset{CA}{\rightleftarrows} H_2CO_3 \rightleftarrows HCO_3^- + H^+ \tag{1.1}$$

Acid extruders use energy to either pump H^+ ions out of the cell, or transport weak bases such as HCO_3^- into the cell. Specific examples of acid extruders include the Na^+/H^+ exchanger (NHE) and the HCO_3^- transporter mechanisms. Acid loaders, conversely, mediate the passive exit of weak bases from the cell. The primary acid loads within cells are passive diffusion of H^+ ions into the cell and HCO_3^- out of the cell along concentration gradients, and production of H^+ ions as a by-product of metabolism.

As might be expected for a complex network subject to regulation at numerous different points, dysregulation of pH is implicated in a number of diseases. Since this thesis primarily deals with cancer and ischaemic stroke, a brief introduction to these pathologies follows.

1.2 Cancer

Cancer, broadly defined, is a group of diseases that can affect many different cell types, which ultimately are characterised by rapid and uncontrolled cell growth. The most recent statistics from Cancer Research UK at the time of writing show that in 2014 a total of 356,860 new cases were identified and 163,444 deaths caused by cancer [10], and estimates of the cost of cancer diagnosis, treatment, other services and associated loss of productivity are around £18.3 billion per year in the UK [11]. As a consequence of the growing burden on healthcare providers, and the growing incidence of all types of cancer, clinical and basic scientific research on the diseases has increased dramatically (Fig. 1.1).

Two seminal works on cancer by Hanahan and Weinberg succinctly review the state of numerous avenues of cancer research, identifying what are known as the Hallmarks of Cancer [12, 13]. These hallmarks are common to most variants of cancer, and describe the underlying principles of the transformation of a normal, healthy cell into a malignant, cancerous one. The most relevant hallmark to the work described in this thesis is the deregulation of cellular energetics, introduced as an 'Emerging Hallmark' in the second Hanahan and Weinberg review [13] and outlined briefly in the following section.

1.2.1 Metabolism in Cancer

Biological and chemical processes in both normal and malignant cells require energy to function. The chemical reactions required to provide this energy are collectively known as metabolism, and

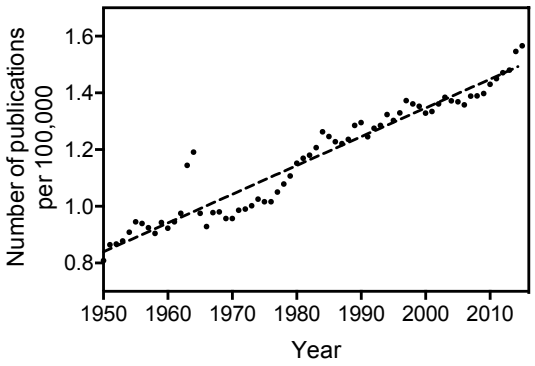

Figure 1.1: Scientific research in cancer has increased dramatically in output over the previous century. Data were retrieved from a search of the PubMed database for publications with the phrase "cancer" in the title between 01-01-1940 and 25-07-2017, normalised to the total number of publications in the same period of time. The dashed line represents the linear fit to the data.

are comparatively well-understood. Typically cells metabolise glucose via glycolysis followed by oxidative phosphorylation. Briefly, glucose is converted to pyruvate through a series of ten chemical reactions in the cytoplasm of the cell, and subsequently the pyruvate undergoes oxidative phosphorylation within the mitochondria. The prerequisites for the full set of chemical reactions are an adequate supply of molecular oxygen and glucose; the reward is the production of around 30 adenosine triphosphate (ATP) molecules per glucose molecule. ATP is used to transport chemical energy within cells, and fuels the cellular processes necessary for life.

If molecular oxygen is not available in sufficient supply to meet demand, cells will tend to metabolise glucose via anaerobic glycolysis. In this case, glucose is converted to pyruvate as above, which then undergoes fermentation to produce lactic acid, producing only two ATP molecules per glucose molecule. A peculiarity of malignant cell metabolism, first noted by Otto Warburg in 1931 [14], is the preferential metabolism via glycolytic and fermentation pathways, even with adequate oxygen supply. This so-called aerobic glycolysis pathway is energetically much less efficient than glycolysis followed by oxidative phosphorylation of pyruvate, but is favoured in malignant cells of various types, leading to the identification of 'Reprogramming of Energy Metabolism' as an 'Emerging Hallmark of Cancer' [13].

The switch in malignant cells to aerobic glycolytic metabolism is not without consequence. Firstly, tumours must compensate for the marked reduction in ATP production by upregulating the transport of glucose into the cytoplasm. Such increased consumption of glucose has been utilised to image tumour metabolism by positron emission tomography (PET) with a radiolabeled glucose analogue (^{18}F-fluorodeoxyglucose, FDG) [15]. Secondly, the downstream waste product of pyruvate fermentation is lactic acid, which cells must extrude from the cytoplasm in order to survive and proliferate. The consequential effect of increased lactate concentration in the

extracellular space is an acidosis of pH_e, which is returned to in Section 1.2.2. Finally, the increased glycolytic rate allows for the diversion of intermediate molecules into various pathways associated with synthesis of macromolecules and organelles as pre-cursors of cell division [16, 17]. Indeed, observations of high glycolytic rates in embryonic tissues has lead to the hypothesis that a higher glycolytic rate is preferential for rapidly dividing cells, which provides the rationale for the metabolic switch in the first place [18].

The mechanism by which higher glycolytic rates are induced is associated with a number of activated oncogenes and mutant tumour suppressor genes. For instance, mutations of the *ras* oncogene which upregulates the Ras family of proteins[2] leads to an upregulation of the transcription factors hypoxia-inducible factor 1α and 2α (HIF-1α and HIF-2α) [20]. Separately, HIF-1α and HIF-2α are both upregulated in response to an hypoxic microenvironment (described in more detail in Section 1.2.2) [21]. Downstream effects of upregulated HIF1α are numerous, but the most relevant to this discussion are the upregulation of GLUT1 and GLUT3 glucose transporters (to increase glucose transport into the cell), PDK1 (pyruvate dehydrogenase kinase 1, which phosphorylates pyruvate dehydrogenase and prevents pyruvate from entering the mitochondria), and BNIP3 that triggers mitochondrial autophagy [21].

1.2.2 Tumour microenvironment

Malignant cells, much as normal cells, do not reside in isolation. Rather, they form tumours comprising of a collection of cancer cells, immune cells, blood vessels, signalling molecules and the extracellular matrix [22]. These various components constitute the tumour microenvironment. The functional hallmarks of cancer cells introduced in the previous sections not only serve to alter specific cellular functions such as proliferation, growth or metabolic phenotype, but also have consequences on the overall tumour microenvironment. The most important factors for this discussion are an increase in hypoxia (compared to normal cells) and alterations in intra- and extracellular pH.

1.2.2.1 pH in Cancer

Tumours, compared to normal tissues, exhibit an extracellular acidosis and an intracellular alkalosis. Whereas pH regulation in normal tissues keeps pH_i in a range between 7.0 - 7.2 and pH_e around 7.4, in tumours pH_i is elevated to around 7.3 and pH_e decreased to 6.4 - 6.8 [22–25]. The level of extracellular acidosis is dependent on the tumour type. The change in pH_i and pH_e, and the reversal of the pH_i/pH_e gradient, is a result of a number of separate cellular processes. Firstly, the glycolytic metabolic pathway increases the intracellular acid load from the increase in

[2]The Ras proteins are predominantly selected for in tumours because of their benefits in conferring increased cell growth, differentiation and survival. Mutations in HRas, KRas and NRas (the three *ras* genes in humans) are present in 20% of all human cancers [19].

lactate production. To deal with this increased acid load, several acid extrusion mechanisms such as the Na^+/H^+ exchanger (NHE), HCO_3^- transporter, carbonic anhydrase IX, vacuolar-ATPase, and the H^+/K^+ ATPase are upregulated. The extracellular space is consequently acidified.

However, the altered pH of the intra- and extracellular spaces in tumours is not only a consequence of their altered metabolic phenotype, but also a result of specific genetic mutations. For instance, carbonic anhydrase IX, which is a catalyst for the bicarbonate buffering reaction, is highly upregulated in a number of tumour types [26]. In addition, cells with a mutation of the *ras* oncogene (which also alters the metabolic phenotype of the cells) have been shown to maintain pH_i at a more alkaline level than cells without the mutation, regardless of the pH of the extracellular environment [20].

An alkaline pH_i acts to increase cell proliferation and evade apoptotic pathways [27, 28]. An acidic pH_e has been linked with increased invasiveness and metastatic potential of tumours [13, 22]. Some tumours have even been shown to exhibit two populations of cells metabolising in different but complimentary ways — one population metabolises via glycolysis and exhibits the well-known Warburg effect, whereas another population takes extracellular lactate as the metabolic fuel and converts it to ATP via the citric acid cycle [29, 30].

In summary, tumour cells self-select for genetic mutations that will result in an alkaline pH_i and acidic pH_e, which are important indicators of the functional capability for a tumour to grow, metastasise, and evade treatment. Measuring tumour pH (whether pH_i or pH_e) in a non-invasive manner would provide additional information on tumour function, grade, and likelihood to respond to therapy (see Section 1.2.3).

1.2.2.2 Hypoxia in Cancer

Within a solid tumour, an additional important factor in the tumour microenvironment is the availability of oxygen. In general, tumours exhibit large areas of hypoxia (inadequate oxygen supply) as a result of a poor vascular environment within the tumour [22]. In order for tumours to grow past a certain size, they require a dedicated blood supply. This requirement leads to the well-known hallmark of tumour angiogenesis [13, 31] or *de novo* vessel growth. However, the blood vessels that grow within a tumour are chaotic, dilated and an irregular shape compared to those in normal tissue. Consequently, the oxygen delivery to the tumour is non-uniform, resulting in hypoxic areas of the tumour with very minimal or no oxygen supply.

Hypoxia has been linked with poor clinical outcomes in patients, with an increased likelihood for metastasis, poor response to radio- and chemotherapies, and the altered regulation of a number of transcription factors and genes [32]. The production of the HIF-1 transcription

factor is increased in hypoxic cells, with consequential alterations on the production of various enzymes involved in the glycolytic pathway (hexokinase 2, phosphoglucose isomerase, lactate dehydrogenase, and many others), ensuring that the cell survives without an adequate oxygen supply. These hypoxia-induced alterations in gene expression are further exacerbated by the tumour self-selection of genetic mutations to ensure survival, and are naturally closely linked to areas of tumours with the most servere acidosis of pH_e and alkalosis of pH_i.

1.2.3 Treatment of Cancer

Treatment options for cancer are numerous and various. The most popular curative therapy remains surgical intervention and resection of the tumour, but other therapeutic options include chemotherapy and radiotherapy. Chemotherapy generally speaking aims to kill cancer cells by introducing a cytotoxic agent into the cell, which is usually achieved by non-specifically injecting a dose of the drug into a patient's circulatory system. As a consequence of the non-specific nature of the therapy, normal tissue toxicity is relatively high and side-effects are common. Chemotherapy is also generally limited by the abnormal tumour vasculature, which can mean that delivery of the drug to the entire tumour site is not possible. For brain tumours this problem is exacerbated further by the presence of the protective blood-brain barrier, which stops pathogens in the blood stream entering the brain parenchyma [33]. Only in areas of high tumour burden, where tumour angiogenesis and bulk growth effects have disrupted the blood-brain barrier, are chemotherapeutic agents able to enter the tumour.

Delivery of chemotherapeutic agents is also limited by other tumour microenvironmental factors, including pH and hypoxia. Novel treatment options which alter the tumour microenvironment, or target the tumour based on its microenvironment, are in growing popularity. For instance, using a chemotherapeutic agent that is weakly acidic has been shown to be more effective than weakly basic drugs because the acidic extracellular environment leads to 'ion trapping' of the weakly basic drug in the extracellular space, limiting its cytotoxic effect [34]. Alternatively, drugs can be used to alter the tumour microenvironment, such as bevacuzimab which inhibits angiogenic signalling pathways, thereby balancing pro- and antiangiogenic signalling, inducing normalisation of the tumour vasculature, and decreasing tumour hypoxia [35]. Another method to alter tumour hypoxia is by decreasing the oxygen consumption rate of tumour cells, as has been recently shown with the anti-malarial drug atovaquone [36].

An alternative treatment option is radiotherapy, where high energy photon beams are directed at the tumour site [37]. These photons knock orbital electrons from atoms, and these electrons go on to break DNA strands (so-called 'direct effect' of radiation). Alternatively, the perturbed electrons interact with nearby water molecules to produce a free radical hydroxyl group, which

then goes on to cause DNA damage (the 'indirect effect' of radiation) [38]. Other forms of radiotherapy that utilise alternative forms of radiation, such as α-emitting radioisotopes or beams of ionised particles (e.g. H^+, C^+), also exist, but the majority of radiotherapy treatments are performed using photon beams [39, 40]. The aim of all forms of radiotherapy is to induce as many DNA double strand breaks as possible, which induces cell death. Radiotherapy treatments are generally more targeted in nature than chemotherapy and utilise anatomical imaging (either by computed tomography (CT) or MRI) to localise the photon beam to the desired area of tissue.

However, the efficacy of radiotherapy is not uniform throughout a tumour owing to microenvironmental heterogeneity within a tumour volume. For instance, in areas where oxygen is in abundance, molecular oxygen reacts with broken DNA strands to form stable organic peroxides which are more difficult for the cell to repair. In hypoxic areas, where oxygen is in limited supply, this reaction occurs less frequently, a greater proportion of DNA double strand breaks are repaired, and more cells survive the radiation treatment, thus leading to radioresistance in hypoxic regions [38]. Several *in vitro* studies of cell survival following radiation treatment for cells cultured in acidic or normal pH environments suggest that low extracellular pH also confers radioresistance to the cells, even when in a well-oxygenated environment [25, 41–43].

Treatment response in the clinic is usually determined by non-invasive imaging (generally CT or MRI) of the extent of the tumour volume. A tumour that does not show obvious signs of shrinkage on standard anatomical imaging is defined as non-responsive, and the patient's treatment plan altered. However, for certain treatments that are designed in the first instance to alter the tumour microenvironment (usually delivered with concurrent radiotherapy to kill cancer cells), tumour volume may not be an effective method to measure treatment response. A more accurate determination of treatment response for these therapies would be to measure tumour pH or hypoxia, which provides information about the state of tumour metabolism and functional capability.

1.3 Ischaemic Stroke

Stroke is a cerebrovascular condition characterised by a loss of brain function due to a sudden disruption in blood supply to the brain [44]. This disruption can be caused by a blocked vessel, in which case the stroke is termed ischaemic, or by internal bleeding, which is categorised as haemorrhagic. The most recently available statistics from the Stroke Association at the time of writing show that stroke incidence fell by 19% between 1990 and 2010 in the UK. Nevertheless, over 150,000 people suffer a stroke each year, and it is the fourth largest cause of death in the UK. The economic cost of stroke is estimated at around £9 billion a year (approximately half of the economic cost of cancer), but research funding of stroke is estimated at just £56 million per

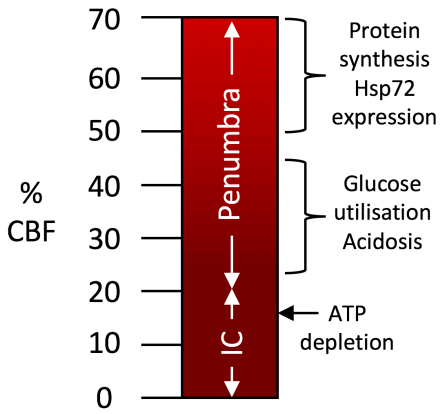

Figure 1.2: Estimated cerebral blood flow (CBF) thresholds for induction of metabolic disturbances in tissue. Hsp72 = Heat shock protein 72. IC = Infarct Core. ATP = Adenosine triphosphate. Adapted from [44].

year (compared to £544 million per year on cancer) [45]. The work in this thesis is predominantly focussed on ischaemic stroke, which comprises approximately 85% of the disease burden each year, and so the introduction that follows will discuss only ischaemic stroke.

Under normal physiological conditions, the energy demand of the brain is met entirely by glucose and oxygen carried by the inflowing blood [46]. Upon ischaemia, the blood flow decreases dramatically and the energy demand is not adequately supplied. The primary consequence is cerebral hypoxia, which causes rapid damage to the brain cells known as cerebral infarction. The timescale of damage is incredibly quick; a lack of blood flow for as little as 10 s can cause unconsciousness, and irreversible brain damage occurs after a few minutes [46]. Ischaemic strokes can be further subcategorised based on the location of the clot in the brain, whether the clot originated in the brain (thrombotic) or elsewhere in the body (embolic), and the type of blood vessel that is blocked; large-vessel thrombosis if the clot is in the carotid or middle-cerebral artery, or small-vessel thrombosis if the clot involves one or more of the brain's smaller arteries. Figure 1.2 highlights the estimated cerebral blood flow thresholds to induce a number of metabolic disturbances to tissue, which are explored in more detail in the following sections.

1.3.1 Pathophysiology of Ischaemic Stroke

A number of pathophysiological processes mediate ischaemic injury within the cerebral parenchyma over various timescales. The incorrectly named 'ischaemic cascade'[3] describes the biochemical reactions that occur in the immediate aftermath through to days and weeks after ischaemic injury [46]. In a similar manner to the response of hypoxic cancer cells to a lack of oxygen, hypoxic neurons in the healthy brain respond to the decreased molecular oxygen avail-

[3]Incorrectly named because a cascade is a series of events in which one event triggers the next in a linear fashion, whereas events in the ischaemic cascade can be initiated by many previous reactions, and are often circular in nature.

ability by switching to glycolytic and fermentation metabolic pathways, resulting in increased lactic acid within the cell. This first step of the ischaemic cascade is one of the most interesting in terms of pH imaging, since the increased lactic acid load leads to rapid acidification of the intracellular space (see Section 1.3.3). Additionally, the metabolic shift alters the osmolality of the cell, which causes a shift of water from the extracellular to the intracellular space and consequential cytotoxic oedema.

The decreased ATP production from switching to a less energy efficient metabolic pathway results in ATP-reliant ion transport pumps failing, allowing ions and water to inhabit the intracellular space in higher concentrations than usual [47]. This response to failing cellular energetics is known as cytotoxic oedema. Of particular interest is inflowing Ca^{2+}, which is excitatory and causes the production of reactive oxygen species, free radicals, and calcium-dependent enzymes such as phospholipases. These phospholipases break down the cell membrane, leading to a greater influx of Ca^{2+} and harmful species, and ultimately necrosis. In addition, mitochondria are broken down and apoptotic factors released into the cytoplasm of the cell, inducing the apoptosis cascade. The microenvironment very quickly becomes toxic, with abundant necrotic and apoptotic cells, toxic species such as free radicals and reactive oxygen species, and low intra- and extracellular pH. This tissue is often referred to as the infarct core, and represents tissue for which the damage is rapid and very often irreversible [48]. Over longer timescales, an inflammatory response is mounted by the immune system and phagocytic cells flock to damaged, but still viable tissue to remove the debris of necrotic cells.

Crucially, the blood flow within ischaemic regions of the brain is very rarely entirely cut off. Indeed, various threshold values of blood flow have been postulated to instigate different aspects of ischaemic injury, and the blood flow in the brain following ischaemic injury is often heterogenous [44]. Typically the ischaemic insult is focal in nature (i.e. restricted to a certain brain region), with a characteristic pattern of an area of infarct core tissue that is severely damaged, surrounded by damaged but viable penumbral tissue with a less reduced blood flow known as the ischaemic penumbra. Without treatment, the tissue that has impaired blood flow will likely go on to become infarcted.

1.3.2 Stroke treatment

Current therapeutic strategies for ischaemic stroke focus primarily on the recanalisation of the occluded vessel to restore blood flow to the brain [49]. Intravenous thrombolysis and mechanical thrombectomy both act to remove the blockage within the affected blood vessel, though via different mechanisms, with the hypothesis that restoring blood flow to the brain parenchyma will reduce the extent of the tissue damage. However, recanalisation of the vessel does not always

lead to reperfusion of the brain tissue. Further blockages in the blood vessel may exist, or the artery may reocclude, both of which contribute to the so-called 'no-reflow' phenomenon [50]. In addition, reperfusion does not necessarily result in tissue survival. Reperfusion of already infarcted tissue will be of no clinical benefit, and non-reversible neuronal injury via apoptosis may already be under way by the time blood flow is restored. Paradoxically, successful reperfusion can often result in further injury to the reperfused tissue [51]. This so-called reperfusion injury is not very well understood, but hypothesised mechanisms include excitotoxic pathways of cell death following glutamate release after restoration of blood flow. Additionally, complications following recanalisation of occluded vessels include intracranial haemorrhage, with an incident rate of *ca.* 10% [52]. Thus, a reliable method to identify patients that will benefit from recanalisation therapy is required.

The most common method used to distinguish potentially salvagable tissue thus far is based on two separate MRI acquisitions [53]. Diffusion-weighted MRI (DW-MRI) is sensitive to the diffusion of water molecules in tissue, and the lesion on DW-MRI is thought to reflect infarcted tissue with a high intracellular water content (and, therefore, greater restriction on water diffusion). Perfusion-weighted MRI (PW-MRI) shows areas of tissue that have reduced blood flow, and the lesion on PW-MRI is usually greater than that on diffusion-weighted MRI [54]. The mismatch between the diffusion and perfusion lesions, therefore, is thought to represent the ischaemic penumbral tissue. A number of recent studies that tested selection of patients based on non-invasive imaging of the ischaemic penumbra returned negative results, suggesting that current imaging strategies to define the ischaemic penumbra are not ideal [55]. Hence, what is really required is identification of the true salvagable tissue extent; that is, tissue that is currently only metabolically challenged through a lack of blood flow, and has not already become infarcted or begun non-reversible neuronal injury.

1.3.3 pH in Stroke

Identifying the tissue that is only metabolically challenged and has not already died or begun the process of dying is closely related to the pH of the tissue. The first stage of the ischaemic cascade is switching to glycolytic metabolism, with a consequential increase in acid load in the intracellular space. In addition, pH alterations are induced predominantly in areas of tissue that are severely ischaemic and associated with irreversible infarction. The distinction between stroke lesions defined on diffusion, perfusion and pH-weighted CEST MRI has been studied extensively in preclinical models of ischaemic stroke [56, 57]. A recent study [48] of patients with acute ischaemic stroke has shown that a decreased signal in pH-weighted CEST MRI (indicative of a reduction in intracellular pH) is closely related to final tissue outcome. That study found that infarct core tissue has a lower pH-weighted signal than penumbral tissue. However, within

the classically defined ischaemic penumbra, tissue that became infarcted regardless of therapeutic intervention was more acidic than tissue that did not infarct, despite being hypoperfused. With the current diffusion-perfusion mismatch methodology, there is no way of separating the ischaemic penumbra into these two tissue types with vastly different outcomes, which has led to challenges as to the suitability of the diffusion-perfusion mismatch for imaging the ischaemic penumbra [58]. In summary, pH imaging in ischaemic stroke may act as a more accurate method to predict final tissue fate in the very acute stages of the disease and, hence, provide a more sensitive method to delineate salvagable tissue.

1.4 Summary of Motivations for pH measurement

In this chapter, pH has been introduced as a fundamental biological quantity of interest in cells and tissues, and the motivation for making pH measurements provided in two pathologies. Thus far, pH has been largely under exploited as a physiological quantity to be measured in oncology or stroke. Developing accurate and reliable pH measurement technology with wide clinical applicability would allow interrogation of the metabolic state of tissue, and potentially inform treatment decisions in stroke, or allow determination of treatment response at an earlier stage than is currently possible in oncology. The development of such a tool has been an active area of research for many decades, and the following section highlights various efforts that have been made to this end.

1.5 Methods of pH measurement

1.5.1 ^{1}H NMR

Extracellular pH has been measured by taking advantage of the pH-sensitivity of the H2 resonance of $(\pm)$ 2-imidazole-1-yl-3-ethoxycarbonyl propionic acid (IEPA) [59]. This non-toxic exogenous compound has been shown to stay restricted to the extracellular environment, and phantom studies of IEPA titrated to different pH environments shows that its chemical shift δ_{obs} is pH-dependent according to a form of the Henderson-Hasselbalch equation (Eq. 1.2, [60]), with pKa = 6.49, $\delta_{\text{acid}} = 8.92$ and $\delta_{\text{base}} = 7.77$. IEPA has been used in preclinical studies, primarily to investigate the extracellular acidity of tumours, and chemical shift imaging sequences used to provide low resolution imaging readouts.

$$\text{pH} = \text{pKa} + \log\left[\frac{(\delta_{\text{obs}} - \delta_{\text{acid}})}{(\delta_{\text{base}} - \delta_{\text{obs}})}\right] \tag{1.2}$$

1.5.2 ^{31}P NMR

The most common method of measuring pH using $^{31}\mathrm{P}$ NMR utilises the endogenous phosphorous signal associated with phosphocreatine (PCr) and inorganic phosphate (Pi) [61, 62]. The chemical shift difference between PCr and Pi, δ_{obs}, is pH dependent according to a form of the Henderson-Hasselbalch equation (Eq. 1.2) where for Pi in human skeletal muscle pKa = 6.73, $\delta_{\mathrm{acid}} = 3.275$ and $\delta_{\mathrm{base}} = 5.685$. Since the intracellular Pi concentration is higher than extracellular, it is generally thought that pH measurements using PCr and Pi peaks reflect $\mathrm{pH_i}$. The pH-sensitive $^{31}\mathrm{P}$ peak of the exogenous agent 3-aminopropylphosphate (3-APP) has been used to measure $\mathrm{pH_e}$ [24]. However, $^{31}\mathrm{P}$ NMR based methods are generally limited by the poor spatial and temporal resolution of spectroscopy, and the need for specialist hardware to perform $^{31}\mathrm{P}$ NMR.

1.5.3 Hyperpolarised ^{13}C NMR/MRI

Hyperpolarised $^{13}\mathrm{C}$ NMR/MRI has emerged as a potential technique for pH imaging *in vivo*. Briefly, bicarbonate labelled with $^{13}\mathrm{C}$ is hyperpolarised through a process known as Dynamic Nuclear Polarisation (DNP), which increases the sensitivity of $^{13}\mathrm{C}$ NMR/MRI by several orders of magnitude. Since bicarbonate is a component of the buffering system of cells to maintain cellular pH, the interconversion rate of bicarbonate and carbon dioxide provides information about the extracellular pH of the environment. One study [63] has shown that by acquiring $^{13}\mathrm{C}$ NMR/MRI data from tumour xenografts shortly after injection of hyperpolarised bicarbonate to measure the concentrations of bicarbonate and carbon dioxide, pH values from the tumour can be obtained that agree well with those measured using $^{31}\mathrm{P}$ NMR. A similar approach has been used to measure the intracellular pH of rodent hearts [64]. However, limitations exist relating to the need for specialist hardware and the ability of the exogenous agent to reach the tissue of interest.

1.5.4 Relaxometry

Molecules can be manufactured that have an ability to alter the T_1 relaxation time of the water in a pH-sensitive manner [65]. Generally these consist of Gd^{3+} chelated to a pH-sensitive ligand, which can modulate the accessibility of the Gd^{3+} ion to water in a pH dependent way. Gd-DOTA-4Amp is such a molecule which has been used to measure $\mathrm{pH_e}$ [66], though since the measured MRI signal is sensitive to both the concentration of Gd and the T_1-weighting effect of the Gd (which is in turn dependent on pH), knowledge of the concentration of the agent in imaging voxels is required to generate images of pH. To alleviate this problem a pH-insensitive molecule with similar chemical structure is generally used, with the assumption that the biodistribution of the two molecules is identical. Whilst Gd^{3+} chelates are used extensively in the clinic for

anatomical imaging, particularly to measure the extent of blood-brain barrier breakdown in primary and secondary brain tumours, their continued use over a period of time in individual patients has been linked to toxic Gd^{3+} deposition in the brain [67].

1.5.5 Electron Paramagnetic Resonance

Electron Paramagnetic Resonance (EPR) is the electronic equivalent of NMR. Molecules with unpaired electrons exhibit an EPR signal, which offers a unique opportunity to study systems with very little background signal[4]. The hyperfine coupling constant of some EPR-active molecules varies in a pH dependent way, which allows quantification of pH when the molecule is introduced to an *in vivo* environment [68]. Unfortunately, the resonant frequencies involved in EPR studies are generally in the microwave frequency range (*c.f.* NMR resonant frequencies in the radiowave frequency range), which limits the clinical translatability of the technique.

1.5.6 Positron Emission Tomography

Positron Emission Tomography (PET) is an imaging modality that relies on imaging photons emitted from a positron-electron collision event. Radioactive nuclei such as $^{11}\mathrm{C}$ or $^{64}\mathrm{Cu}$ are conjugated to a functionalised peptide, which targets certain molecular events, and injected into the body. When the β^+-particles (also known as positrons, or a positively-charged electron) emitted from the radioactive nuclei collide with a nearby electron, two photons with a characteristic energy (511 keV) are released in opposite directions. These photons can be detected, and tomographic image processing techniques used to reconstruct a three-dimensional image of the distribution of the radiotracer within the body.

One recent example of pH measurement using PET was achieved using $^{64}\mathrm{Cu}$ conjugated to a pH low insertion peptide (pHLIP) [69]. These peptides insert themselves across the cell membrane when the extracellular pH is acidic, and so act as a targetting agent to accumulate where $\mathrm{pH_e}$ is sufficiently acidic. The uptake of the $^{64}\mathrm{Cu}$-pHLIP conjugate has been shown to correlate with $\mathrm{pH_e}$ as measured using $^{31}\mathrm{P}$ NMR of 3-APP. Whilst these techniques have potential for clinical translation given the wide accessibility of PET scanners in clinical environments, PET is ultiamtely limited by poor spatial and temporal resolution, as well as the dependence on contrast agent distribution via perfusion.

1.5.7 Optical imaging

Optical imaging using fluorecence represents an attractive option for pH imaging since it is fairly low cost with unparalleled spatial resolution. A fluorescent molecule can be engineered

[4]Since most stable molecules have their electrons paired, and therefore have no net spin.

to couple with a peptide, antibody or other biomolecule which selectively targets certain tissue types (tumour, stroke, etc.) [70]. Concentration-independent measurements can be obtained, for example, by observing the ratio of fluorescence intensities at different emission wavelengths. Optical imaging is able to detect nanomolar concentrations of such fluorescent agents, and has good temporal resolution. However, this method is limited to surface-accessible tissues only *in vivo* or tissue sections *ex vivo* since the fluorescence intensity is strongly attenuated by tissue.

1.5.8 pH electrode

Whilst the principle of using an electrode to measure pH is fairly straightforward, such methods are typically invasive and so only suited to preclinical studies, or topical or surface-accessible tissues in humans. In addition, even though microelectrodes have been used for measurements of pH, the electrodes are typically several orders of magnitude larger than the cells that comprise the tissue [71]. There is, therefore, a strong likelihood of damage to the cellular environment when using microelectrodes to measure pH, as well as uncertainty regarding the exact environment being probed. Finally, electrode measurements are unable to provide spatial information of pH.

1.5.9 Summary of pH measurement methods

A number of different approaches have been developed to measure pH. In particular, magnetic resonance based methods offer the greatest potential to measure pH non-invasively *in vivo*. The majority of these methods are spectroscopy based, with any imaging readouts a result of a chemical shift imaging acquisition. As a consequence, these spectroscopic methods can be useful to provide validation of other, novel methodologies, but they are unlikely to make the translation from research tool to routine clinical practice. This translation is important if pH measurement is to be used to measure treatment response or stratify patients. Non-magnetic resonance based methods such as PET can be used *in vivo*, but with limited spatial and temporal resolution. A number of methods highlighted here involve injection of an exogenous compound to measure pH, limiting their translatability to particular patient groups.

Chemical Exchange Saturation Transfer (CEST) MRI is an imaging technique that may able to be used to non-invasively measure pH *in vivo*, and the development of CEST MRI to enable its routine use for this application is the focus of the work in this thesis. A full introduction of CEST MRI is presented in Section 2.2, after the following introduction to some fundamental concepts of NMR and MRI.

Chapter 2

Theory and Applications of Nuclear Magnetic Resonance

Contents

2.1 Nuclear Magnetic Resonance & Magnetic Resonance Imaging 18
2.1.1 From Spin to Magnetisation 18
2.1.2 Radiofrequency Pulses 20
2.1.3 Relaxation 21
2.1.4 Gradients and Signal Detection 22
2.1.5 Magnetisation Transfer 23
2.2 Chemical Exchange Saturation Transfer NMR/MRI 28
2.2.1 Chemical Exchange in NMR/MRI 28
2.2.2 CEST MRI 30
2.2.3 The Bloch-McConnell Equations 34
2.2.4 CEST MRI Acquisition Methods 35
2.2.5 CEST MRI Analysis Methods 37
2.2.6 Applications 41
2.2.7 Limitations 43
2.3 Diffusion NMR/MRI 44
2.3.1 The Bloch-Torrey Equations 47
2.3.2 Limitations 47
2.4 Thesis aims 48

The previous chapter introduced the unmet need for pH measurement in clinical settings and summarised current attempts to enable such measurements. In this chapter, a brief introduction to the phenomenon of nuclear magnetic resonance (NMR) and its application in biomedical imaging is given in Section 2.1. This introduction is necessary as a precursor to full discussions of chemical exchange saturation transfer (CEST) magnetic resonance imaging (MRI) in Section 2.2, which is the predominant MRI method employed and studied in this thesis in order to measure pH non-invasively, and of diffusion MRI in Section 2.3.

2.1 Nuclear Magnetic Resonance & Magnetic Resonance Imaging

Numerous textbooks [72–76] have covered the full theory of NMR and MRI to varying extents, and repeating that exercise here is unnecessary. As such, the description of the physical principles of NMR and MRI that follows is somewhat limited in its scope. Areas where a more in depth discussion than is presented here are highlighted in footnotes.

2.1.1 From Spin to Magnetisation

The quantum mechanical property of spin, S, is inherent to all fundamental particles, and represents the quantisation of angular momentum. In a similar sense to other quantised properties such as electrical charge, spin is quantised as $S = \hbar\{-s, -(s-1), ..., s-1, s\}$ where s is either an integer or half-integer value and $\hbar$ is the reduced Planck constant. All protons, neutrons and electrons are known as spin-$1/2$ particles, where $s = 1/2$ and so $S = 1/2$ (spin "up") or $S = -1/2$ (spin "down")[1]. The vast majority of NMR and MRI studies are conducted on spin-$1/2$ nuceli (^{1}H, ^{13}C, ^{19}F, and ^{31}P), so the following discussion will be restricted to these systems[2]. These two spin states are associated with energy levels that the particles can occupy. When a spin-$1/2$ particle is placed within a strong magnetic field, such as those present in NMR spectrometers or MRI scanners, a phenomenon known as Zeeman splitting causes the particle to occupy one of the two possible energy states.

A spin-$1/2$ particle occupying spin up or down energy states in a magnetic field can be equivalently thought of as a classical[3] magnetic dipole aligning itself parallel or anti-parallel to the external magnetic field. The magnetic dipole has an associated magnetic moment, $\boldsymbol{\mu} = \gamma S$,

[1] The factor of $\hbar$ 'disappearing' here is owing to the use of natural units, common in particle physics and cosmology, which sets $\hbar = c = k_B = 1$ (c is the speed of light, and k_B is the Boltzmann constant). In addition, protons and neutrons are not fundamental particles, themselves comprised of quarks. All quarks are spin-$1/2$ particles, which given the composition of protons and neutrons of uud and udd, respectively, would imply protons and neutrons are spin-$3/2$ particles if only quarks carry the spin of the proton and neutron. An experiment to study the spin composition of the proton was carried out by the European Muon Collaboration in 1987 [77], with the unexpected result that almost none of the proton spin was being carried by quarks. The ensuing "proton spin crisis" is, at the time of writing, still unsolved.

[2] The spin of a nucleus is not merely the sum of the spins of its constituent particles. Various selection rules govern the calculation of nuclear spin, which in the interests of brevity are not discussed in detail here. A full description is given in [73].

[3] Classical in the sense of classical electromagnetism.

where the quantity γ is the gyromagnetic ratio, a proportionality constant that is unique to each nucleus. The energy of a particular level associated with the dipole being aligned parallel or anti-parallel to the external magnetic field $\boldsymbol{B_0}$ is defined as $E = -\boldsymbol{\mu} \cdot \boldsymbol{B_0} = -\gamma S \hbar B_0$, where $S = \pm 1/2$. Transitions between the two energy levels can be driven by incoming photons with an energy equal to the difference between the two energy levels. Conservation of energy, therefore, gives $\hbar\omega = \Delta E = \gamma \hbar B_0$, which simplified gives the condition for magnetic resonance; otherwise known as the Larmor equation (Eq. 2.1). The Larmor equation introduces the concept of a 'magnetic resonance frequency' for $S \neq 0$ nuceli and particles, since γ is a property unique to each nuclei.

$$\omega = \gamma B_0 \tag{2.1}$$

Typical NMR or MRI experiments involve macroscopic samples with many nuclei. For a population of N nuclei with $S = \pm 1/2$ at thermal equilibrium in a magnetic field B_0 at temperature T, the ratio of the number of nuclei in upper and lower energy states (or equivalently spin up or spin down states) can be described by the Boltzmann distribution (Eq. 2.2), where k_B is the Boltzmann constant. It is also useful to define the polarisation, P, which is the excess number of nuclei in the upper energy state (Eq. 2.3). For ^{1}H nuclei (with $\gamma = 26.75 \times 10^7\,\mathrm{T^{-1}\,s^{-1}}$) in a high-$B_0$ system (e.g. 9.4 T) at 37 °C, $\frac{\mathrm{N_{upper}}}{\mathrm{N_{lower}}} = 0.999938463$ and $P = 3 \times 10^{-5}$. These simple calculations serve to demonstrate the domination of thermal interactions in samples studied by NMR, and also illustrate the relative insensitivity of NMR/MRI methods since only 30 nuclei per million are able to contribute signal.

$$\frac{\mathrm{N_{upper}}}{\mathrm{N_{lower}}} = e^{-\frac{\Delta E}{k_B T}} = e^{-\frac{\hbar\omega}{k_B T}} = e^{-\frac{\hbar\gamma B_0}{k_B T}} \tag{2.2}$$

$$P = \frac{\mathrm{N_\uparrow} - \mathrm{N_\downarrow}}{\mathrm{N_\uparrow} + \mathrm{N_\downarrow}} = \tanh \frac{\gamma \hbar B_0}{2 k_B T} \tag{2.3}$$

The utility of NMR and MRI, therefore, arises from the fact that there are abundant $S \neq 0$ nuclei in a macroscopic sample. By considering such an ensemble of spin-1/2 nuclei, for which each has a magnetic moment $\boldsymbol{\mu} = \pm 1/2 \hbar\gamma$, it is useful to define the bulk magnetisation vector from the ensemble as $\mathbf{M} = 1/2 N \hbar\gamma(\mathrm{N_\downarrow} - \mathrm{N_\uparrow})$ where $N = \mathrm{N_\uparrow} + \mathrm{N_\downarrow}$. In terms of classical electrodynamics, $\mathbf{M}$ is subject to a torque $\mathbf{M} \times \mathbf{B}$, which is equal to the rate of change of angular momentum, $\mathbf{J}$. Since $\mathbf{J} = \frac{\mathbf{M}}{\gamma}$ (the classical equivalent of $\boldsymbol{\mu} = \gamma S$), it is possible to write the generalised Bloch equations (Eq. 2.4) [78].

$$\frac{\mathrm{d}\mathbf{M}}{\mathrm{d}t} = \gamma(\mathbf{M} \times \mathbf{B}) \tag{2.4}$$

The solution to Eq. 2.4 in a Cartesian coordinate system with unit vectors **ijk** and a magnetic field $\mathbf{B} = B_0\mathbf{k}$ is given by Eq. 2.5, which demonstrates clearly that the Larmor frequency, $\omega = \gamma B_0$, is the frequency of precession of the bulk magnetisation **M** about the magnetic field $\mathbf{B} = B_0\mathbf{k}$.

$$\begin{aligned} M_x(t) &= M_x(0)\cos(\gamma B_0 t) + M_y(0)\sin(\gamma B_0 t) \\ M_y(t) &= -M_x(0)\sin(\gamma B_0 t) + M_y(0)\cos(\gamma B_0 t) \\ M_z(t) &= M_z(0). \end{aligned} \tag{2.5}$$

Thus far, only homogenous samples have been considered, where a single population of nuclei contribute to a bulk magnetisation **M**. In addition, a further simplifying assumption that has been made is that nuclear spins do not interact with one another. In reality, however, specimens investigated using NMR and MRI are usually comprised of a plethora of disparate NMR-active nuclei, with microscopic interactions between nuclei serving to alter the strength of the magnetic field experienced for any given nucleus. Hence rather than the usual idealised scenario of a single resonant frequency ω within a sample, a number of resonant frequencies are present within biological specimens, arising from distinct populations of nuclei. This complicating factor is returned to in Section 2.1.5.

2.1.2 Radiofrequency Pulses

With the fundamental principles and framework of NMR and MRI outlined in Section 2.1.1, it is now possible to gain some insight as to how magnetic resonance can be used to probe the microscopic properties of a sample. The first instance to consider is irradiation of a sample with photons that satisfy the Larmor resonance condition. The most common method of performing NMR or MRI studies is to provide a short burst of radiofrequency (RF) for a time τ. The RF pulse is often referred to by its magnetic field component, B_1. Assuming with no loss of generality that the main magnetic field $\mathbf{B} = B_0\mathbf{k}$ points in the z-direction, and B_1 is applied as an oscillating field in the xy plane (i.e. $\mathbf{B_1} = B_1\cos(\omega t)\mathbf{i} - B_1\sin(\omega t)\mathbf{j}$), then the resulting precession of **M** is around an effective field $\mathbf{B_{eff}}$ with two different precession frequencies — ω around B_0 and $\omega_1 = \gamma B_1$ around B_1. This precession around the effective field $\mathbf{B_{eff}}$ allows the definition of the flip angle of a pulse as $\theta = \gamma B_1 \tau$. For instance, for an initial condition of $\mathbf{M} = M_0\mathbf{k}$, a 90° pulse serves to flip the magnetisation vector into the xy (or transverse) plane.

RF pulses can be used to great effect by the imaginative physicist to measure properties of the system being investigated. Particular terms of nomenclature are important when discussing RF pulses and pulse sequences. For instance, excitation pulses are typically 90° pulses designed to tip the magnetisation into the xy plane for detection. Inversion pulses are so-named because they flip the magnetisation by 180°, inverting its direction. Saturation pulses are typically applied as a train of RF pulses (or one long RF pulse) with the effect of reducing the net magnetisation to zero. The importance of these different pulse types will become clear in the following sections.

2.1.3 Relaxation

Bulk magnetisation perturbed by an external RF pulse (or equivalently B_1 field) will always tend to relax back to its thermal equilibrium condition. This relaxation occurs over a number of characteristic timescales, and is mediated by interactions of the spins within the system interacting with one another (spin-spin interactions) and their environment (spin-lattice interactions). Felix Bloch proposed in 1946 [78] that spin-lattice interactions relax **M** to its thermal equilibrium value exponentially with a characteristic time T_1, whereas spin-spin interactions reduce the transverse components of **M** exponentially, with a characteristic time T_2. Alterations of the Bloch equations in Eq. 2.4 can be written (Eq. 2.6), which describe the propagation of magnetisation in a medium within a magnetic field accounting for relaxation.

$$\begin{aligned}
\frac{\mathrm{d}M_x}{\mathrm{d}t} &= \gamma(\mathbf{M}\times\mathbf{B})_x - \frac{M_x}{T_2} \\
\frac{\mathrm{d}M_y}{\mathrm{d}t} &= \gamma(\mathbf{M}\times\mathbf{B})_y - \frac{M_y}{T_2} \\
\frac{\mathrm{d}M_z}{\mathrm{d}t} &= \gamma(\mathbf{M}\times\mathbf{B})_z + \frac{M_0 - M_z}{T_1}
\end{aligned} \tag{2.6}$$

The variation of T_1 and T_2 times of ^{1}H nuclei in water in biological tissues is the primary mechanism by which contrast is generated in MRI scans. T_1 relaxation processes are in general always longer than T_2. Further, T_2 is not the only mechanism by which transverse magnetisation can relax back to thermal equilibrium. Local magnetic field inhomogeneities due to complex interactions between the main magnetic field B_0 and the geometry of the sample being studied tend to alter the magnetic field experienced by spins in a particular environment. These inhomogeneities serve to reduce the observed time constant of the exponential decay of transverse signal to a characteristic time T_2^*. It is customary to define a separate relaxation time constant for these static field inhomogeneities, T_2', related by

$$\frac{1}{T_2^*} = \frac{1}{T_2} + \frac{1}{T_2'}. \tag{2.7}$$

2.1.4 Gradients and Signal Detection

The discussion so far has focussed on samples located within a homogenous, static magnetic field $\mathbf{B} = B_0\mathbf{k}$. However, the presence of a physical object within a magnetic field will cause local inhomogeneities, which must be mitigated to be able to use magnetic resonance to probe the sample in question. The homogeneity of the B_0 field is restored as far as possible through a process called 'shimming', which involves applying local magnetic fields of varying spatial extent using resistive elctromagnets (known as shim coils), effectively adding and subtracting B-field as necessary to ensure that the main B_0 field is homogenous. NMR spectrometers and MRI scanners both utilise shim coils.

Further resistive electromagnets can be utilised to impose further gradients on the main magnetic field, however. These electromagnets, called gradient coils, are usually able to generate field gradients in all three directions in MRI scanners, but in just one in NMR spectrometers (typically along the same direction of the main magnetic field). These gradient coils can be used, in an opposite sense to the shim coils, to impose known spatial variation in the magnetic field across a sample. The effect of spatial variation of the B_0 field (arbitrarily in the z direction) is spatial variation of the Larmor frequency ω. Hence, upon simultaneous irradiation with an RF pulse, only a portion of the nuceli within the subject will be affected. This use of gradient coils is known as frequency encoding for slice selection. Similarly, frequency encoding can be employed within an imaging slice by applying a second gradient in an orthogonal direction to impose further spatial variation of the Larmor frequencies of protons within a slice. Frequency encoding alone permits the localisation of proton signals within two-dimensions, but in order to localise fully in three-dimensions an additional gradient applied orthogonally to both slice select and frequency encoding gradients must be used. When turned on, this gradient imposes a spatial variation in the relative phase of the precession of protons. By recording the signals after imposing this gradient (a so-called phase encoding gradient), and varying the magnitude of this gradient iteratively, it is possible to fully localise signals within three-dimensions and calculate images from these signals. A further example of the use of gradient coils to encode useful information in MRI signals is discussed in detail in Section 2.3.

A detailed discussion of the detection of NMR and MRI signals is beyond the scope of this thesis, but it is necessary to at least briefly mention that NMR and MRI signals are detected as voltages induced in an RF coil. The voltage induced is proportional to the magnitude and rate of precession of the magnetisation only in the transverse plane[4]. Often in pulse sequences, immediately prior to acquisition of the signal, a short gradient pulse will be played whose net effect is to reduce the transverse magnetisation component to zero — such gradients are known

[4]Hence the terminology used to refer to 90° pulses as excitation pulses.

as spoiling or crusher gradients. The induced voltage takes the form of a damped oscillation at the Larmor frequency, and is known as the Free Induction Decay (FID). Fourier transforms of the recorded FID signals generate the spectral or imaging information expected from NMR or MRI systems, respectively.

It should be noted that whilst NMR spectrometers and MRI scanners are governed by the same fundamental physics, NMR spectrometers are typically used to acquire a spectrum of the distribution of resonant frequencies within a sample, whereas MRI scanners are focussed on imaging ^{1}H nuclei. Since in humans and animal subjects the vast majority of ^{1}H nuclei are found in water, the images obtained from MRI scanners generally reflect the spatial distribution of water within the subject. Through imaginative use of gradient and RF pulse sequences, the water magnetisation can be manipulated to generate images with various weightings, for instance maximising imaging contrast based on differences in T_1, T_2 or T_2^* relaxation times. One other important distinction to make is that MRI is sensitive only to ^{1}H nuclei with a long ($\mathcal{O}(10\,\mathrm{ms})$) T_2 relaxation time. Therefore, only ^{1}H nuclei in water are able to be directly detected and used to generate images. However, ^{1}H nuclei in other biomolecules present within the body can interact with ^{1}H nuclei in water and influence the MRI signal acquired. This phenomena is explored in more detail in Section 2.1.5.

2.1.5 Magnetisation Transfer

The complications of inhomogeneities in samples studied by NMR and MRI was briefly alluded to at the end of Section 2.1.1. One example of these inhomogeneities leading to interesting phenomena, which can be exploited to gather valuable information about the sample, was discussed in Section 2.1.3. A second important example is known as Magnetisation Transfer, and is discussed here. Magnetisation Transfer (MT), unsurprisingly, refers to the transfer of magnetisation from one population of nuclei to another [79–81].

There are many different pathways by which MT can occur, and a detailed discussion of all of them is unnecessary within the confines of this thesis[5]. However, particular pathways that are of interest include dipolar coupling (which gives rise to nuclear Overhauser effects, NOE), chemical exchange saturation transfer (CEST, discussed in detail in Section 2.2), and relayed-NOE.

2.1.5.1 Dipolar coupling

Dipolar coupling is the phenomena of two particles with magnetic dipole moments $\boldsymbol{\mu_1} = \gamma_1 I_1$ and $\boldsymbol{\mu_2} = \gamma_2 I_2$ separated by a distance $\mathbf{r_{12}}$ interacting with one another to transfer the spin of one particle on to the other. Briefly, each dipole induces its own small magnetic field, and a

[5] See [73, 82, 83] for more information

dipole in close physical proximity to another will be affected by the magnetic field arising from the other. These locally experienced fields alter the effective magnetic field experienced by one particle in a manner that is dependent on the spin orientation of the other. The strength of the dipolar coupling between two spins is determined by the dipolar coupling constants, b_{12} and d_{12} in Eq. 2.8, where $\mu_0 = 4\pi \times 10^7\,\mathrm{H\,m^{-1}}$ is the magnetic permeability of free space and θ_{12} is the angle between the axis connecting the two dipoles and the external magnetic field direction.

$$\begin{aligned} \mathrm{b}_{12} &= -\frac{\mu_0}{4\pi}\frac{\gamma_1\gamma_2\hbar}{r_{12}^3} \\ \mathrm{d}_{12} &= \mathrm{b}_{12}\frac{1}{2}(3\cos^2\theta_{12} - 1) \end{aligned} \tag{2.8}$$

Since the dipolar coupling constant b_{12} is inversely proportional to the cube of the distance between two spins, dipolar coupling is only prevalent when the distances between spins is very small $\mathcal{O}(10^{-10}\,\mathrm{m})$. In addition, dipolar coupling is not observed if the sample being studied is in a liquid state, as in this case the chaotic motion of molecules averages all possible orientations of the dipoles to the magnetic field[6]. Dipolar coupling is the pathway that gives rise to the magnetisation transfer between protons on immobile macromolecules and nearby water molecules, the so-called MT effect in MRI.

2.1.5.2 Nuclear Overhauser Effects

The nuclear Overhauser effect (NOE) is the observed change in the signal recorded from one population of nuclei when the spin population of a physically-close nuclear spin population is saturated [84]. The effect arises because of the dipolar coupling between the two nuclear spin populations. The NOE effect is summarised briefly in Fig. 2.1. Consider a sample of a hypothetical molecule in some solvent with two spin-1/2 nuclear populations comprising a total of N nuclei in close proximity. Dipolar coupling between the populations means there are four possible energy states for the system to occupy (↑↑, ↑↓, ↓↑, or ↓↓). The spin populations at equilibrium are $N/4$ nuclei in the ↑↓ and ↓↑ states, $N/4 + \Delta$ in the ↑↑ (low-energy) state, and $N/4 - \Delta$ in the ↓↓ (high-energy) state, where Δ represents the excess nuclei in the low energy state. Probabilities for the various relaxation pathways between each state can be assigned (labelled ω_0, ω_1 and ω_2 in Fig. 2.1). The NOE experiment involves pushing the system out of equilibrium by saturating the spins of one population (i.e. eliminating the population difference) and observing the signal recorded from the other population. Depending on which of the relaxation processes ω_0, ω_1 and ω_2 dominates, different signals will be recorded. ω_0 and ω_2 pathways are known as cross-relaxation pathways, and give rise to negative and positive NOE, respectively.

[6] In molecules with more than one proton, dipolar coupling is the dominant T_1 relaxation pathway.

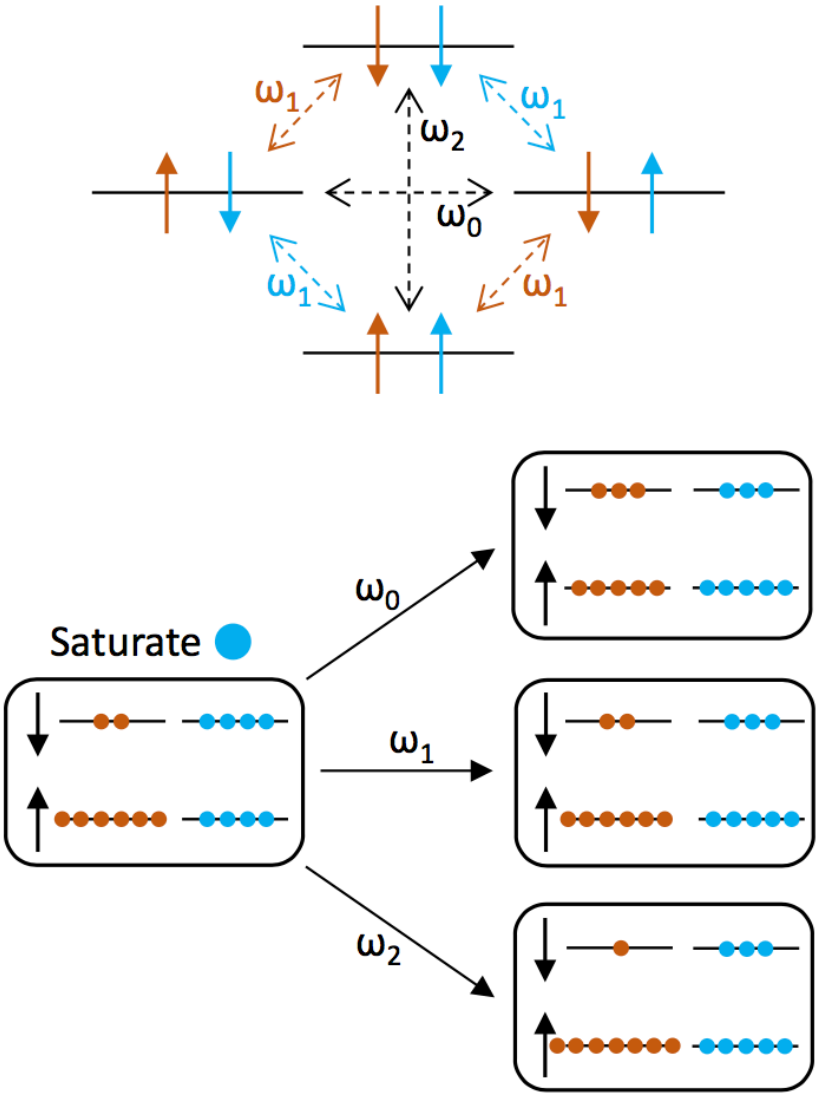

Figure 2.1: Summary of the nuclear Overhauser effect (NOE) arising from dipolar coupling and cross-relaxation. Following saturation of the blue proton population (thereby creating no population difference), the system can relax via ω_0, ω_1 or ω_2 pathways. ω_0 and ω_2 are called cross-relaxation pathways because relaxation of the blue proton population towards thermal equilibrium causes population differences in the orange proton pool relative to the initial state. The ω_0 and ω_2 pathways give rise to negative and positive NOE, respectively.

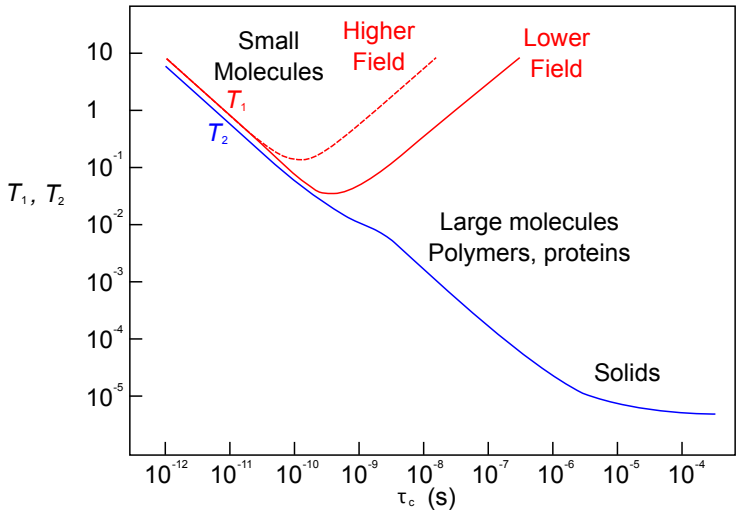

Figure 2.2: Variation of T_1 and T_2 relaxation times with correlation time τ_c.

The factor that determines the relative contributions of the ω_0, ω_1 and ω_2 relaxation processes is molecular motion, which can be fully described by a parameter known as the correlation time, τ_c, defined as the time taken for a molecule to rotate through one radian[7]. τ_c is in turn dependent on environmental factors, such as the viscosity of the solvent, and instrinsic factors, such as the shape and molecular weight of the molecule. In general, τ_c can be used to categorise the size and motion of molecules into 'small mobile' (e.g. metabolites, $\tau_c \sim \mathcal{O}(10^{-11}\,\mathrm{s})$), 'large mobile' (e.g. proteins, polymers, $\tau_c \sim \mathcal{O}(10^{-9}\,\mathrm{s})$), and 'large immobile/semi-solid' (e.g. membrane-associated macromolecules, $\tau_c \sim \mathcal{O}(10^{-7}\,\mathrm{s})$). Correspondingly, since τ_c determines which relaxation processes are prevalent, it also influences the T_1 and T_2 relaxation times for these molecules (Fig. 2.2).

Such NOE effects occur between any two protons in sufficiently close proximity, leading to the categorisation of inter- and intramolecular NOE effects, depending on whether the dipolar coupling arises between protons on different molecules or within the same molecule. NOE effects can, and have, been used to great extent in the study of macromolecular structures by NMR spectroscopy[8]. In addition, NOE effects have been utilised as a contrast mechanism in MRI. The contrast known as NOE in MRI is typically assigned to intermolecular dipolar coupling between protons on large mobile proteins and water, whereas MT MRI contrast is produced by dipolar coupling between immobile macromolecules and water. Section 2.1.5.3 and Fig. 2.3 summarise the dominant magnetisation transfer pathways encountered *in vivo*.

[7] The inverse of the correlation time is sometimes known as the molecular tumbling rate

[8] A plethora of NOE spectroscopy methods have been developed, which are summarised in [85].

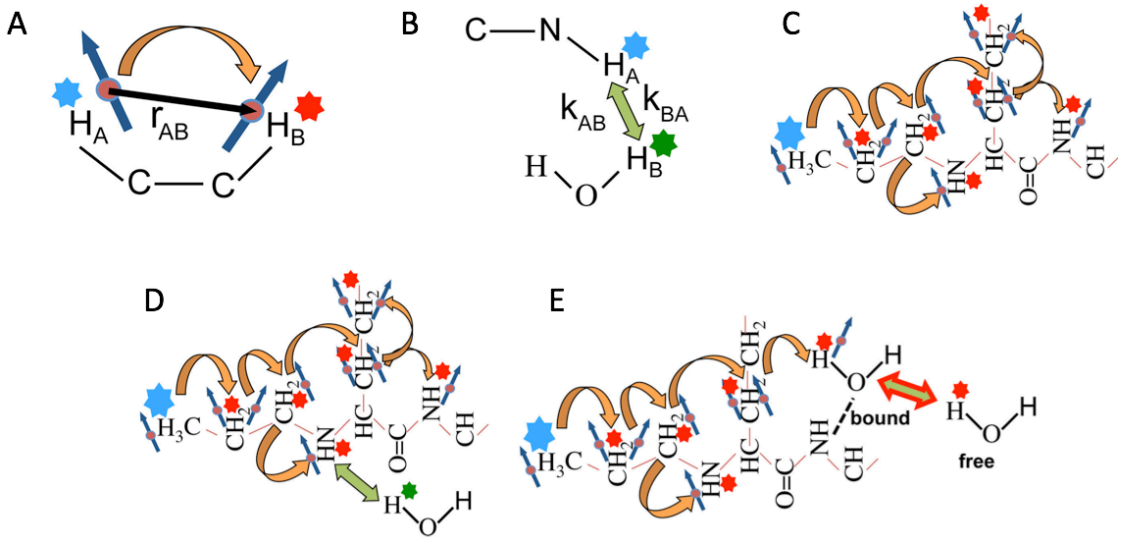

Figure 2.3: Magnetisation transfer pathways encountered *in vivo*. The blue star signifies protons labelled using RF saturation, orange arrow represents magnetisation transfer by cross-relaxation via dipolar coupling, green arrow magnetisation transfer by chemical exchange, red star protons involved in dipolar coupling pathways, and green star protons involved in chemical exchange pathways. A and B illustrate dipolar coupling and chemical exchange pathways, respectively. C shows relayed NOE, where magnetisation transfer occurs via numerous intramolecular NOE interactions. D demonstrates NOE-relayed exchange, where intramolecular relayed NOE transfers the magnetisation to a labile proton, which then transfers to free water via chemical exchange. E illustrates a similar process where relayed NOE followed by intermolecular NOE transfers magnetisation to a bound water molecule, and subsequent chemical exchange or intermolecular NOE allows imaging of the magnetisation transfer by affecting the free water pool. Adapted from [**VanZijl2017a**] with permission.

2.1.5.3 Relayed NOE & NOE-relayed exchange

Further magnetisation transfer pathways exist that combine the effects of dipolar coupling and chemical exchange (which is described in Section 2.2). Figure 2.3 briefly outlines the predominant magnetisation transfer pathways encountered *in vivo* where Fig. 2.3A and Fig. 2.3B illustrate dipolar coupling and chemical exchange, respectively. Figure 2.3C shows relayed dipolar transfer or relayed NOE, where intramolecular NOEs transfer magnetisation through a molecule. Figure 2.3D demonstrates an interesting phenomena where magnetisation is transferred to water via both relayed NOE and chemical exchange. This pathway is known as NOE-relayed exchange, and is a contributing factor to the effects commonly labelled as NOE in the upfield portion of Z-spectra (discussed in Section 2.2.2). Finally, Fig. 2.3E illustrates the predominant pathway by which the MT effect is mediated, namely initial intramolecular NOE-relayed transfer followed by intermolecular NOE to a bound water proton population, and subsequent intermolecular NOE or chemical exchange with the free water proton pool.

2.2 Chemical Exchange Saturation Transfer NMR/MRI

Chemical Exchange Saturation Transfer (CEST) is the other predominant mechanism of magnetisation transfer that is encountered when investigating chemical, biological or biomedical specimens with NMR or MRI. CEST MRI is the MRI method most used in this thesis, and an extensive introduction to its origins, applications and limitations follows.

2.2.1 Chemical Exchange in NMR/MRI

Protons within a given molecule will exhibit different resonant frequencies when placed inside a magnetic field. These differing resonant frequencies are a result of the local magnetic environment encountered by the nuclei, which in turn is related to their position within the molecule and their affinity to other nuclei via chemical bonds. Chemical exchange refers to the reversible exchange of nuclei from one location to another, whether those locations are within the same molecule or in two separate molecules. Such nuclei are said to be labile. The effect that chemical exchange has on the measured NMR signals from molecules is significant, and is illustrated for a simple case in Fig. 2.4.

As the temperature of the sample (and hence chemical exchange rate, k_{ex}) changes, the recorded NMR spectrum also changes. At low temperatures (slow exchange rate, $k_{ex} \ll \Delta\omega$), the spectrum reflects the two distinct environments as two sharp peaks at two resonant frequencies separated by $\Delta\omega$. As k_{ex} increases with temperature, to an intermediate value ($k_{ex} \sim \Delta\omega$), the peaks broaden until no signal is evident. As k_{ex} further increases to a fast value ($k_{ex} \gg \Delta\omega$), a peak located at the population-weighted average resonant frequency is observed, broadened slightly compared to the lineshapes measured with slow exchange. The timescales over which the exchange reaction takes place are defined as fast, intermediate and slow on the NMR timescale, since $\Delta\omega$ is dependent on the magnetic field strength.

Commonly the chemical exchange of molecular protons with solvent-associated protons is studied, with various factors determining the value of k_{ex}. As demonstrated already, temperature is a key contributor to the exchange kinetics, since as temperature increases, more energy is available to the system for exchange to occur. The relationship between k_{ex} and temperature, T, is given by the Arrhenius relation, $k_{ex} \sim e^{E_a/k_B T}$, where E_a is the activation energy for the exchange reaction [86]. The solvent accessibility of a nucleus (i.e. how physically available it is to chemical exchange with other nuclei) also affects k_{ex}, which has been used to elucidate protein structure and conformation. The concentration or abundance of labile protons also affects k_{ex}, in a similar way to solvent accessibility. Finally, and most relevant for this thesis, in some cases of proton chemical exchange the reaction is base- or acid-catalysed, meaning that the pH of the environment affects the exchange kinetics of the reaction.

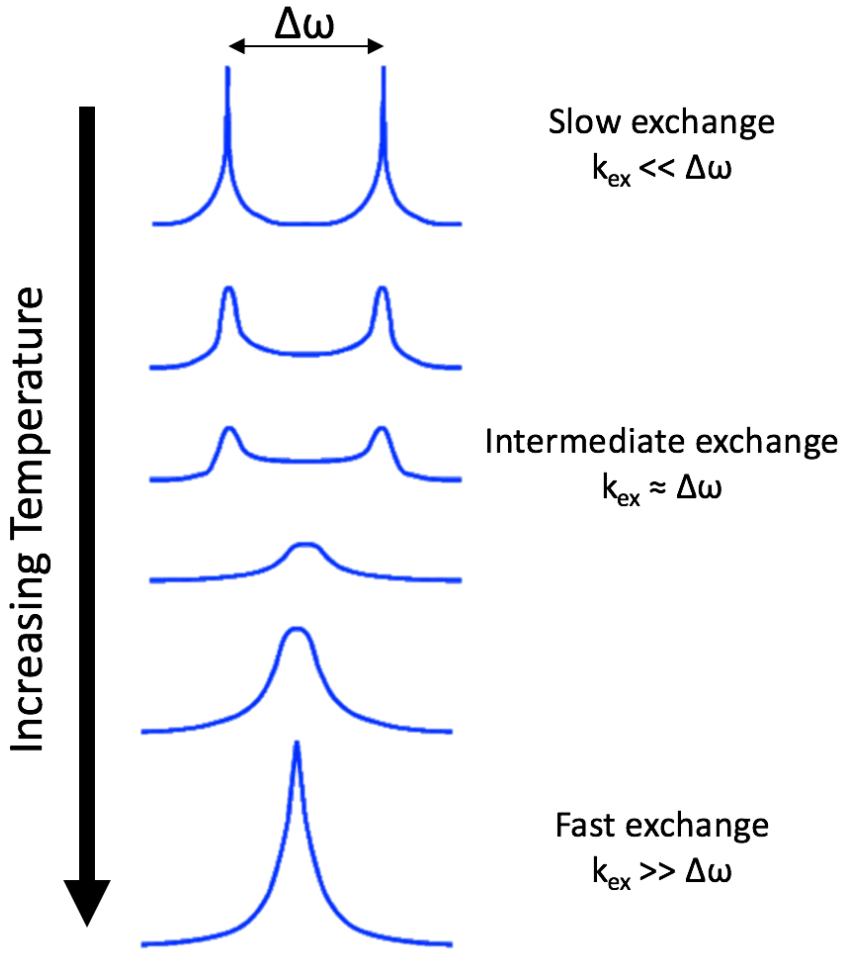

Figure 2.4: Demonstration of how chemical exchange can affect recorded NMR signals. At low temperature, exchange between two states giving rise to NMR spectral peaks separated by a frequency $\Delta\omega$ is slow, and both peaks are readily resolvable. As temperature increases and more energy is available to the system, the two states coalesce, eventually resulting in a single peak at the population averaged frequency $\omega_{\text{av}} = p_A\omega_A + p_B\omega_B$. In this example, $p_A = p_B = 0.5$, and so $\omega_{\text{av}} = {}^{\Delta\omega}/_{2}$.

The situation changes somewhat when considering the effect of chemical exchange on MRI data. In a typical MRI scan, as mentioned in Section 2.1.4, rather than acquire a spectrum of resonant frequencies of the various chemical species present within a biological subject, an image predominantly reflective of the distribution and concentration of water molecules is acquired. Chemical exchange is still present and ongoing within the person or animal being imaged, and the MRI data are sensitive to its presence[9]. However, the effects of chemical exchange are hard to directly observe, because an MRI image merely observes one population of nuclei (the ^{1}H nuclei in H_2O).

2.2.2 CEST MRI

CEST MRI [87] is born from the idea of sensitising the H_2O signal detected in MRI acquisitions to the effects of chemical exchange more directly, and relies on the principle that (i) protons in other chemical environments have a different resonant frequency than that of the protons associated with water, and (ii) the two proton populations are in constant chemical exchange with one another. By saturating the signal from the protons not associated with water, through irradiation of the sample with RF at the resonant frequency of those protons, the chemical exchange of protons will transfer that signal saturation to the water proton population. Given a sufficiently long saturation period, a sufficiently strong saturation RF pulse power, and chemical exchange kinetics that do not prevent the build up of saturated protons in the water proton population, a decrease in water proton signal will be measured compared to the signal without the saturation present. This decrease in signal can be utilised to introduce contrast into MRI scans. The magnitude of the decrease in signal is proportional to, amongst other things, the chemical exchange rate k_{ex} between the two proton populations. It may already be clear how CEST MRI can, therefore, be used to measure pH. This point is returned to explicitly in Section 2.2.5.1.

The protons involved in chemical exchange with water in biological systems are numerous and varied. The most prevalent are protons associated with amide (-NH), amine (-NH_2), and hydroxyl (-OH) functional groups [88]. *In vivo*, amide protons tend to be found on the backbone and sidechains of polypeptides and proteins, amine protons are found in the sidechains of polypeptides and in free amino acids, and hydroxyl groups are present in a number of metabolites [89, 90]. Usually, resonant frequencies of the functional groups are quoted as relative to the water frequency, which is defined as 0 ppm[10]. The assignment of these functional groups to specific resonant frequencies is a matter of debate within the CEST literature[11], but typically amide groups are characterised as having a resonant frequency of approximately 3.5 ppm, amine protons of

[9] Predominantly as alterations in the T_1 relaxation time.

[10] This is a confusing factor in the CEST MRI literature, where water at approximately 4.7 ppm is redefined as 0 ppm, compared to the standardised way of reporting resonance frequencies in NMR which is relative to Trimethylsilylpropanoic acid (TSP) defined as 0 ppm.

[11] This point is returned to later in this section.

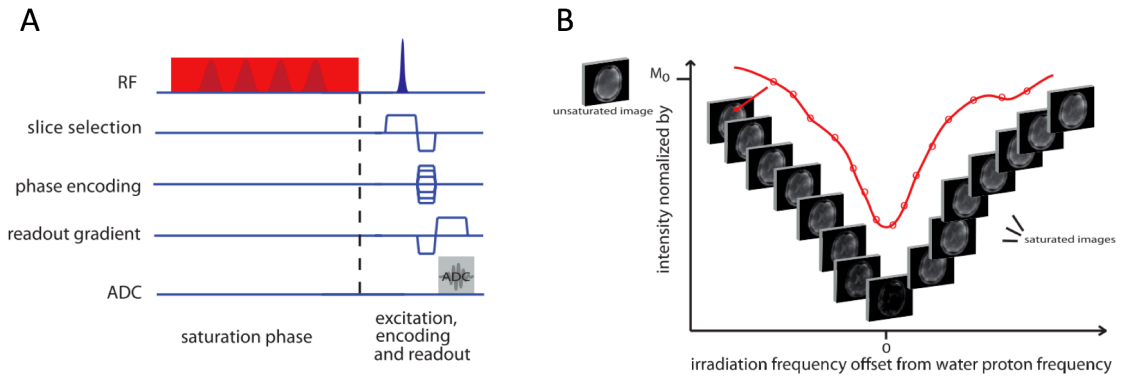

Figure 2.5: A typical CEST MRI pulse sequence (A) is split into saturation and readout phases. The pulse sequence is repeated many times for different RF irradiation frequencies Ω, and the water signal after each saturation phase recorded to plot a CEST or Z-spectrum (B). Adapted from [91] with permission.

2.0 ppm, and hydroxyl protons of 0.8 ppm. The functional group most investigated in this thesis is the amide group. Amide Proton Transfer (APT) is the most studied variant of CEST in the literature to date, predominantly because its exchange dynamics satisfy the requirements to observe a CEST signal (see below).

A typical CEST MRI experiment is performed, as briefly described above, by irradiating a sample with RF at a frequency Ω followed by acquiring the signal from water protons (S), which have a resonant frequency Ω_w. Ω is rastered through a range of values, and S measured after each saturation period. A plot of S against Ω is known as a Z- or CEST spectrum (Fig. 2.5), where typically S is normalised by the signal acquired without any RF saturation, S_0. The Z-spectrum is so named because during the saturation period the water magnetisation direction is unperturbed and remains pointing along the z-axis, and so the images acquired are of the magnitude of the z component of the water magnetisation following saturation at frequency Ω[12]. Characteristic decreases in signal intensity are observed in the Z-spectrum at frequencies that correspond to the resonant frequencies of exchanging proton populations, and are termed as CEST signals or CEST effects[13]. The symmetric effect of direct saturation of water is the most dominant effect in the Z-spectrum, and accounts for the reduction of measured signal to zero when saturating on the water resonance.

In order to observe a CEST signal, the exchange dynamics must be such that the exchange of labile protons transfers saturated protons to the water population without returning to the labile population prior to signal acquisition. This requirement is met for proton exchange that is slow on the NMR timescale ($k_{ex} \ll \Delta\omega$) with low concentration ($\sim$ mM) *in vivo*. CEST MRI,

[12]Equivalent notation where M replaces S and ω replaces Ω is also common, and may be used interchangeably throughout this thesis.

[13]Confusingly, despite CEST effects being observed as decreases in signal intensity, they are also often referred to as CEST peaks.

therefore, increases the sensitivity of MRI by several orders of magnitude since we image the $\sim$ M concentration water signal, but with a B_0 dependency on the ability to resolve certain CEST effects (since $\Delta\omega$ depends on B_0). In addition, a CEST signal is observed only from molecules with a sufficiently quick tumbling rate (or equivalently, a sufficiently short correlation time). This restriction limits the range of biomolecules that generate CEST effects to those that are not bound to cellular membranes.

The size of the CEST effect is determined by several factors. Intrinsic factors include the rate of exchange between the labile and water protons, the concentration of the labile protons, and the solvent accessibility of labile protons. Contaminants to the CEST signal include the water T_1 and T_2 times, which serve to decrease the observed CEST signal, without changing the exchange dynamics of the system, by forcing the water magnetisation back to its equilibrium state throughout the saturation period.

It is important to note a complication of performing CEST MRI *in vivo* where there are multiple populations of exchanging labile protons within a single imaging voxel. Each 'pool' of protons contributes to the measured Z-spectrum (Fig. 2.6), which ultimately is a compartment-averaged measurement of the water magnetisation in each voxel. *In vivo*, contributions to the Z-spectrum from amide, amine, and hydroxyl protons from chemical exchange are commonly accounted for. However, the Z-spectrum also has contributions from non-chemically exchanging proton populations, such as CH_3 protons that interact with water protons via NOE pathways, or protons in macromolecules associated with cellular membranes that provide the widely-known MT effect. So-called relayed-NOE saturation transfer pathways also contribute to the Z-spectrum, where intramolecular NOEs transfer magnetisation to a labile proton that goes on to chemically exchange.

In addition, the peak for each pool has an associated non-zero linewidth, related to the effective T_2 relaxation time of the protons within that pool, meaning that two pools with similar but non-equal resonant frequencies may not be resolved if the peaks are sufficiently broad. Another factor which broadens the linewidth of CEST peaks is the fact that the resonance frequency of a particular proton population is not necessarily well-defined to a single resonance frequency since the protons comprising the population may not be in magnetically equivalent environments. This peak broadening means that the water signal measured following saturation at a particular frequency may be encoded with CEST effects from multiple distinct proton pools. This effect is most evident for the macromolecular protons giving rise to the MT effect, since their T_2 time is $\mathcal{O}(10^{-6}\,\mathrm{s})$, broadening their lineshape across >$20\,\mathrm{ppm}$. In addition, one particular complication in the MT pool is whether the lineshape is symmetric about the water peak, with some studies suggesting it is asymmetric [92, 93]. Measuring the size of a CEST effect from one proton

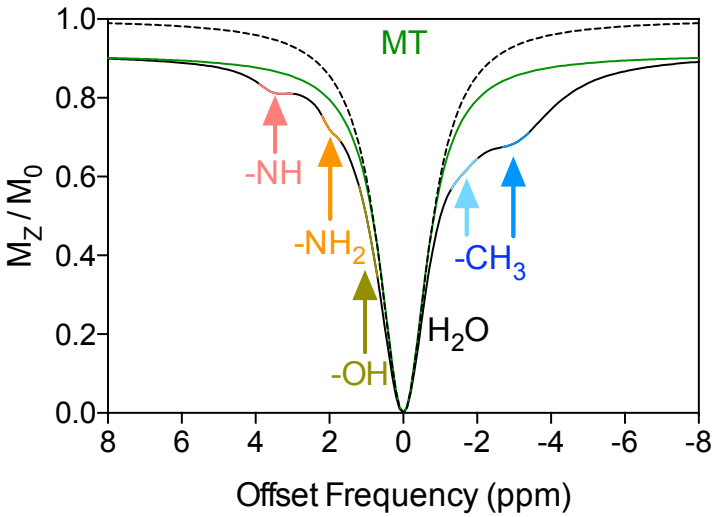

Figure 2.6: Multi-pool nature of the *in vivo* Z-spectrum demonstrated using simulations using the Bloch-McConnell equations. The dashed line is the effect of direct saturation of water, and represents what would be measured in the absence of magnetisation transfer via dipolar coupling and chemical exchange. The simulation performed assumes $B_0 = 9.4\,\mathrm{T}$ and $B_1 = 1.25\,\mu\mathrm{T}$, both with perfect homogeneity, and a saturation period of 10 s. Note how the hydroxyl CEST effect is hard to distinguish from the direct water saturation because the exchange is in the fast regime. Simulation parameters are shown in Table 2.1.

	H_2O	**-NH**	**-NH_2**	**-OH**	**-CH_3**	**-CH_3**	**MT**
Offset Frequency (ppm)	0	3.5	2.0	1.0	-1.6	-3.0	0
k_{iw} (Hz)	-	29	420	5000	50	50	13
M_0^i (mM)	112000	200	35	800	800	800	11200
T_1 (s)	1.6	1	1	1	1	1	1
T_2 (ms)	42	2	10	10	1	0.5	7.5×10^{-3}

Table 2.1: Parameters for each pool used to simulate the Z-spectrum displayed in Fig. 2.6.

population in isolation from all others is a non-trivial exercise, an active area of research in the CEST literature, and is discussed in more detail in Section 2.2.5.2.

Further experimental complications arise when performing CEST MRI studies in that the Z-spectrum is a field-dependent measurement. The value of B_0 determines the NMR timescale, and so also the ability to be able to distinguish CEST effects arising from certain proton populations. In general, a larger B_0 is advantageous in CEST MRI, because the greater chemical shift separation between proton populations at higher field will lead to maximal detection of CEST signals. In addition, the homogeneity of B_0 across the sample being imaged is crucial to ensuring subsequent CEST MRI maps are accurate. Voxelwise correction for small B_0 variations is a common post-processing step in CEST MRI experiments. Finally, the B_1 saturation field strength is an important

experimental factor to consider since its effect will differ depending on whether exchanging protons are in slow, intermediate, or fast exchange regimes. For slowly exchanging protons (e.g. -NH protons with $k_{ex} \sim 30\,\text{Hz}$), lower B_1 powers (e.g. $< 1\,\mu\text{T}$) provide adequate saturation to observe a CEST effect, with the added benefit of a minimal direct saturation effect on the water.

Having outlined the concept of chemical exchange, its effect on the NMR/MRI signal, and introduced the underlying principles of CEST MRI, the remainder of this chapter constitutes a brief discussion of various CEST MRI acquisition and analysis methods that can be used to determine certain biophysical parameters of the system being studied, as well as certain limitations of the CEST MRI methodology.

2.2.2.1 Exogenous CEST MRI

The description of CEST MRI thus far has only considered CEST effects arising from endogenous biomolecules found within humans and animals. These endogenous effects are the most studied in the literature, and form the focus of this thesis. In general, however, CEST effects arise from any molecule with labile protons, which has resulted in a wide range of molecules being synthesised or re-purposed as exogenous CEST MRI contrast agents. For instance, molecules containing paramagnetic lanthanide ions complexed with ligands (e.g. EuDOTA-(glycine ethyl ester)$_4$ [94]) induce a shift in the resonance frequency of water bound to the compound compared to free water. The exchange of protons between bound and free states is slow on the NMR timescale, and so able to be detected by CEST MRI. Such contrast agents are referred to as paraCEST agents owing to their paramagnetic properties.

Similarly, diaCEST contrast agents exhibiting diamagnetic properties have also been utilised in CEST MRI, most notably as the repurposing of iodinated contrast agents commonly used in computed tomography (CT) imaging (e.g. iopamidol [95]). Paramagnetic complexes encased within liposomal capsules (lipoCEST agents) have also been developed and functionalised to accumulate at certain biological targets [96]. Finally, contrast agents utilising the sensitivity enhancements of both CEST and hyperpolarisation (hyperCEST) have been developed, predominantly based around ^{129}Xe MRI [97].

2.2.3 The Bloch-McConnell Equations

It is useful at this point to introduce the Bloch equations modified for chemical exchange, also known as the Bloch-McConnell equations (Eq. 2.9) [98]. The Bloch-McConnell equations describe the propagation of magnetisation in the x, y and z directions for two populations of protons, labelled a and b in Eq. 2.9. The two populations have resonant frequencies Ω_a and Ω_b, Ω is the frequency of the saturating RF with field strength $\omega_1 = \gamma B_1$, and $\Delta_i = \Omega_i - \Omega$ for $i = a, b$. k_{ba}

and k_{ab} are the forward and back exchange rates of protons from population a to b, $T_{1,2i}$ are the longitudinal or transverse relaxation times and $k_{1,2i} = \frac{1}{T_{1,2i}+k_i}$ for $i = a, b$.

$$\begin{aligned}
\frac{\mathrm{d}M_{ax}}{\mathrm{d}t} &= -\Delta_a M_{ay} - k_{2a} M_{ax} + k_{ba} M_{bx} \\
\frac{\mathrm{d}M_{ay}}{\mathrm{d}t} &= \Delta_a M_{ax} - k_{2a} M_{ay} + k_{ba} M_{by} - \omega_1 M_{az} \\
\frac{\mathrm{d}M_{az}}{\mathrm{d}t} &= \frac{M_{a0}}{T_{1a}} - k_{1a} M_{az} + k_{ba} M_{bz} + \omega_1 M_{ay} \\
\frac{\mathrm{d}M_{bx}}{\mathrm{d}t} &= -\Delta_b M_{by} - k_{2b} M_{bx} + k_{ab} M_{ax} \\
\frac{\mathrm{d}M_{by}}{\mathrm{d}t} &= \Delta_b M_{bx} - k_{2b} M_{by} + k_{ab} M_{ay} - \omega_1 M_{bz} \\
\frac{\mathrm{d}M_{bz}}{\mathrm{d}t} &= \frac{M_{b0}}{T_{1b}} - k_{1b} M_{bz} + k_{ab} M_{az} + \omega_1 M_{by}
\end{aligned} \tag{2.9}$$

The Bloch-McConnell equations can be generalised to any number of exchanging populations and written in matrix form $\frac{\mathrm{d}\mathbf{M}}{\mathrm{d}t} = \mathbf{AM} + \mathrm{B}$ where

$$\mathbf{A} = \begin{pmatrix} \mathbf{D}_a & \mathbf{O}_{ab} & \mathbf{O}_{ac} & \cdots \\ \mathbf{O}_{ba} & \mathbf{D}_b & \mathbf{O}_{bc} & \cdots \\ \mathbf{O}_{ca} & \mathbf{O}_{cb} & \mathbf{D}_c & \cdots \\ \vdots & \vdots & \vdots & \ddots \end{pmatrix}, \mathbf{D}_i = \begin{pmatrix} -k_{2i} & -(\Omega - \Omega_i) & 0 \\ (\Omega - \Omega_i) & -k_{2i} & -\omega_1 \\ 0 & \omega_1 & -k_{1i} \end{pmatrix}, \mathbf{O}_{ij} = k_{ij} \begin{pmatrix} 1 & 0 & 0 \\ 0 & 1 & 0 \\ 0 & 0 & 1 \end{pmatrix}$$

and $\mathbf{B} = \begin{pmatrix} \mathbf{B}_a & \mathbf{B}_b & \cdots \end{pmatrix}^\intercal$ with $\mathbf{B}_i = \begin{pmatrix} 0 & 0 & \frac{M_{0i}}{T_{1i}} \end{pmatrix}^\intercal$, which is solved by

$$\mathbf{M} = \mathrm{expm}(\mathbf{A}t)(\mathbf{M}_0 + \mathbf{A}^{-1}\mathbf{B}) - \mathbf{A}^{-1}\mathbf{B}$$

where $\boldsymbol{M}_0 = \begin{pmatrix} \boldsymbol{M_0^a} & \boldsymbol{M_0^b} & \cdots \end{pmatrix}^\intercal$, $\boldsymbol{M_0^i} = \begin{pmatrix} 0 & 0 & M_0^i \end{pmatrix}^\intercal$, and t is the saturation duration.

2.2.4 CEST MRI Acquisition Methods

A number of CEST MRI acquisition methods have been published in the literature, each with their own benefits and limitations. The simplest sequences implemented are continuous wave (CW) CEST sequences, so named because the RF saturation before acquisition comprises a single, long duration RF pulse. Following acquisition, a relaxation period must be allowed for the system to return to equilibrium before the next frequency can be saturated. These are the easiest sequences to model using the Bloch-McConnell equations (see Section 2.2.3). A short gradient is usually played after saturation and before readout to eliminate any residual transverse magnetisation from the saturation period.

CW-CEST sequences are difficult to implement on clinical MRI systems owing to hardware limitations and specific absorption rate considerations. Instead, a train of RF pulses is typically used to encode CEST signals, each followed by a short gradient to spoil transverse magnetisation. Pulsed CEST sequences are more difficult to model accurately using the Bloch-McConnell equations since the signal evolution during the periods where no saturating RF pulse is being played must be specifically accounted for, significantly increasing the computational cost of such modelling exercises. Approxmiations of the equivalent average continuous power (AP = $\sqrt{\frac{1}{t}\int_0^t B_1^2 dt}$) and average continuous field (AF = $\frac{1}{t}\int_0^t B_1 dt$) were derived for a general pulsed CEST sequence to alleviate such issues, and the average power shown to be a suitable approximation for a pulsed CEST sequence [99, 100].

Typically CEST sequences are implemented such that the saturation period is followed by a fast imaging readout. These methods are slow to acquire a full Z-spectrum, since long saturation and relaxation periods must be allowed for each frequency sampled. An alternative method is to interleave the saturation and imaging readout modules to reduce the acquisition time. Such sequences typically re-order the acquisition of k-space lines such that the centre of k-space is acquired last, thus ensuring that as much saturation has been imposed on the system at the time that the most imaging information is obtained[14].

One thing common to all CEST MRI pulse sequences, however, is that the imaging readout is completed in a very short period of time so as to minimise the amount of magnetisation relaxation that occurs during the imaging readout. Typical implementations of CEST MRI sequences use an echo planar imaging (EPI, [101]) or tubo spin echo (TSE, [102]) readout. Other variants include fast imaging with free precession (FISP, [103]), spectroscopy with linear algeraic modelling (SLAM, [104]), compressed sensing (CS, [105]), or simple gradient echo (GE, [106]) sequences.

One further distinction between CEST acquisition methods is the imaging volume studied. Typically in clinical settings, a single slice acquisition is performed. This is the simplest to implement, though provides limited spatial coverage. Multi-slice sequences can be used, though care must be taken to ensure that relaxation does not occur during the multi-slice acquisition that would artificially decrease the CEST MRI signal [107]. Three-dimensional sequences have been implemented by interleaving CEST saturation pulses with acquisitions of k-space lines through 3D k-space [108]. In addition, simultaneous multi-slice (SMS) methods utilising parallel transmit RF coils[15] have also been used to greatly accelerate the acquisition of CEST MRI data [110].

[14]The concept of k-space and specific details of various k-space trajectories are not discussed within this thesis, but more information can be found in [74].

[15]Essentially using two independent RF coils to transmit RF power and receive MRI signals; a full description of parallel transmit hardware can be found in [109].

Whatever the differences in imaging readout, the fundamental principle of CEST MRI data remains the same, namely to encode a CEST signal on to the water magnetisation using RF saturation, followed by rapid imaging of the water magnetisation to measure that signal. The quantification of the size of that signal, and the determination of the parameters that contribute to it, are discussed in the following section.

2.2.5 CEST MRI Analysis Methods

Analysis of CEST MRI data is predominantly concerned with quantifying the size of the CEST effect without contamination from factors not associated with the exchanging proton population. As such, before highlighting a number of methods used to quantify CEST MRI data, it is important to outline the theoretical derivation of the true size of the CEST effect.

2.2.5.1 Source of the CEST Effect

It has been shown [111] that the pure CEST signal size is given by the proton transfer rate (PTR):

$$\text{PTR} = \chi \cdot \alpha \cdot k_{ex} \cdot T_{1a} \cdot (1 - e^{-t_{\text{sat}}/T_{1a}}) \tag{2.10}$$

where χ is the ratio of solute proton and water proton concentrations, T_{1a} is the longitudinal relaxation time of water, k_{ex} is the exchange rate of solute protons to water, t_{sat} is the duration of the CEST saturation period, and $\alpha = \frac{(\gamma B_1)^2}{(\gamma B_1)^2 + k_{ex}^2}$ is the saturation efficiency of the solute protons. α describes the expected ability for a given B_1 saturation power to saturate protons exchanging at an exchange rate k_{ba}; faster exchanging protons can only be saturated with a stronger B_1 power, but for slower exchanging protons (e.g. amide protons with $k_{ex} \simeq 30\,\text{Hz}$ *in vivo*), $\alpha \simeq 0.99$ for $B_1 = 1\,\mu\text{T}$.

It is important to understand the factors that influence the intrinsic elements of the exchanging system, k_{ex} and χ. Various contributions to determining k_{ex} were outlined in Section 2.2.1, but here it is prudent to focus on the influence that environmental pH has on the exchange rate. Focussing once more on amide proton transfer *in vivo*, the most studied variant of CEST MRI, the exchange rate has been shown to follow a base-catalysed relationship $k_{ex} = k_{\text{base}} \times 10^{\text{pH}-\text{pKw}}$ with the base-catalysed exchange rate $k_{\text{base}} = 5.57 \times 10^9$ and pKw = 15.4 for amide protons at 37 °C, resulting in a final relationship between pH and exchange rate of $k_{ex} = 5.57 \times 10^{\text{pH}-6.4}$ [89]. Thus, in principle, a two-step calibration process can transform images of the CEST effect from amide protons *in vivo* into maps of amide proton exchange rate, which can in turn be converted into pH maps. The pH-dependency of amide proton exchange rate is the primary mechanism by which pH measurement using CEST MRI has been investigated, though pH-sensitivity of amine exchange rate has also been explored [112].

The χ factor is determined by both the abundance of solute and water protons. Water proton concentration *in vivo* is typically assumed as 112 M, leaving only the solute concentration to vary to alter χ. Again referring to amide protons, which are typically found on the backbone of proteins and polypeptides, the abundance of amide protons is assumed to be correlated with the abundance of cytoplasmic proteins. Only cytoplasmic proteins are usually considered since CEST effects are only measured from molecules with a sufficiently quick tumbling rate, which would require a liquid-like environment as found in the cytoplasm of cells. Pathologies where protein synthesis is altered, such as in tumours, have been shown to exhibit elevated CEST effects from amide protons, which has been suggested to reflect the relative increase in protein levels in these diseases.

However, the solute proton concentration used to calculate χ is really an *effective* concentration, where only solvent-accessible protons are included in the calculation. Hence, alterations of protein conformation, without a change in protein abundance, would also modify χ. Finally, variations in water content within tissue is a complicating factor in the determination of χ, particularly in pathological tissue where water content has been shown to vary. It is possible to make independent measurements of water content using MRI based methods, but equally these require care to ensure all possible contaminant variations are accounted for [113].

The elucidation of the source of the CEST effect is a non-trivial exercise, particularly when comparing changes in CEST effects in diseased tissues. Various independent measurements can be used to eliminate certain factors, such as the water content component of χ or T_{1a}, but ultimately we are limited by the fact that one measurement may arise from alterations in many factors. Nevertheless, CEST MRI holds great promise as a method of parametric mapping of biophysical parameters such as protein concentration or pH. To achieve this goal, an accurate measurement of the true CEST effect, together with improved understanding of the contributing factors, is required.

2.2.5.2 Measuring the CEST Effect

A number of quantification metrics of CEST MRI data have been developed to provide an estimate of the PTR, some of which are defined in Eq. 2.11 — Eq. 2.17. The first and simplest quantification metric is the Magnetisation Transfer Ratio (MTR), defined in Eq. 2.11, where $S(\Omega)$ is the water signal measured following saturation at RF frequency Ω and S_0 is the water signal measured without saturation [114]. In simple model solutions, where only two proton populations exist (e.g. water and labile protons), this serves as a good approximation. However, in the complex environment encountered *in vivo*, with multiple proton populations, MTR tends to overestimate the true CEST effect size.

A way to mitigate the effects of the multiple proton populations *in vivo* is to use the $\text{MTR}_{\text{asym}}(\Omega)$ metric, defined in Eq. 2.12 [89]. By using the signal on the opposite side of the spectrum to calculate an MTR, symmetric effects on the Z-spectrum are cancelled out. Symmetric effects often encountered *in vivo* include the direct saturation of water and the broad magnetisation transfer effect from immobile macromolecules. Removing these effects from the quantification of the effect size results in an estimate that is, in theory, more accurate. However other saturation effects arise *in vivo* that are non-symmetric, which affect the suitability of MTR_{asym} as a quantification method. For instance, for amide protons with a resonant frequency of 3.5 ppm, the $\text{MTR}_{\text{asym}}(3.5\,\text{ppm})$ value involves the signal $S(-3.5\,\text{ppm})$, which is strongly affected by NOE-mediated magnetisation transfer processes.

One metric designed to quantify CEST effects from individual proton populations without interference from others is APT*, calculated by Eq. 2.13, where $\delta\Omega$ is sufficiently small that only frequencies around the resonant frequency of the pool of interest contribute to the measured APT* value [115]. Whilst contributions from other proton populations is minimal with this metric, a high level of spectral selectivity is required such that a well-defined 'dip' is observed in the Z-spectrum. Data of sufficient quality are generally only obtained with very high magnetic field strength ($> 7\,\text{T}$), and so the applicability of APT* to clinical MRI systems is limited. In addition, water T_1 relaxation time (T_{1w}) changes are not explicitly accounted for in the APT* metric. An ideal quantification metric for CEST MRI would be sensitive only to changes in the k_{ba} and χ portions of PTR.

One such metric that does explicitly correct for T_{1w} variations is AREX, defined in Eq. 2.16, which also utilises MTR_{Rex} defined in Eq. 2.14 [116–118]. The mathematical derivation of these metrics, using a theoretical description of the Z-spectrum in CEST MRI based on its equivalence to a different type of MRI known as spin locking, demonstrates that the AREX metric is proportional only to the k_{ba} and χ portions of PTR. Application of the AREX metric, however, is similarly restricted to high field strengths as APT* is, and instabilities in the metric appear as $\Omega \to 0$ because $S(\Omega) \to 0$.

$$\text{MTR}(\Omega) = 1 - \frac{S(\Omega)}{S_0} \tag{2.11}$$

$$\text{MTR}_{\text{asym}}(\Omega) = \frac{S(-\Omega) - S(\Omega)}{S_0} \tag{2.12}$$

$$\text{APT}^*(\Omega) = S_{\text{ref}}(\Omega) - S(\Omega) \tag{2.13}$$

$$\text{MTR}_{\text{Rex}}(\Omega) = \frac{1}{S(\Omega)} - \frac{1}{S_{\text{ref}}(\Omega)} \tag{2.14}$$

$$S_{\text{ref}}(\Omega) = \frac{S(\Omega - \delta\Omega) + S(\Omega + \delta\Omega)}{2} \tag{2.15}$$

$$\text{AREX}(\Omega) = \frac{\text{MTR}_{\text{Rex}}(\Omega)}{T_{1w}} \tag{2.16}$$

$$\text{CESTR}^*(\Omega) = \frac{S_{\text{1-pool}}(\Omega) - S_{\text{2-pool}}(\Omega)}{S_0} \tag{2.17}$$

To overcome the need for high field strengths, an alternative approach to quantifying CEST effects is to use model fitting approaches. These methods fit either the Bloch-McConnell equations or a simplified version of them to a measured Z-spectrum, with the idea being that contaminant factors can be removed during the fitting process, thereby providing a more accurate and suitable quantification of the CEST effect. The simplest of these methods is fitting a sum of Lorentzian lineshapes to a Z-spectrum, which essentially acts as a simplified version of the Bloch-McConnell equations. Semi-quantitative features of the Lorentzian lineshapes, such as the linewidth and amplitude, have been used to quantify the CEST effect [119]. Alternatively, Lorentzian Difference Analysis (LDA) has been used to calculate the effect of individual components of the Z-spectrum in isolation [120].

An alternative approach termed EMR (extrapolated semi-solid magnetisation transfer reference, [121]) fits the portion of an acquired Z-spectrum with $\Omega > 21\,\text{ppm}$ and $\Omega < -21\,\text{ppm}$ with a super-Lorentzian lineshape to eliminate contributions to CEST signals from immobile macromolecules. The raw data are then subtracted by the fitted lineshape, with the resulting CEST effects (known as APT$^{\#}$ for the amide protons with $\Omega = 3.5\,\text{ppm}$, for example) thought to be a more specific representation of the true CEST effect size.

Finally, methods employing full fitting of the Bloch-McConnell equations to acquired data have also been implemented. Whether fitting the raw dataset to the Bloch-McConnell equations [122], or using simulated Z-spectra generated using the Bloch-McConnell equations to match to the raw dataset using a look-up table [123], these methods arguably account for the full array of variables when quantifying CEST effects.

An approach called BayCEST uses Bayesian inference to fit the Bloch-McConnell equations to a full Z-spectrum. The exchange rate and relaxation times for each population of protons in the Z-spectrum are defined by Bayesian prior distributions to prevent the model returning unphysical fitted parameter values [124, 125]. The output of BayCEST is a model-fitted Z-spectrum with associated fitted values of the exchange rate and relative concentration of the protons in each pool, and T_1 and T_2 relaxation times for all proton pools. The fitted exchange rate and concentration for a particular proton population of interest are then used to simulate idealised systems of water alone, as well as water with labile protons, using the Bloch-McConnell equations, thereby eliminating contributions from other proton pools. The size of the CEST effect is then quantified by the CESTR* metric, defined in Eq. 2.17, where $S_{\text{1-pool}}$ and $S_{\text{2-pool}}$ are the signals from the idealised simulations with water and water with labile protons, respectively (see Fig. 2.7).

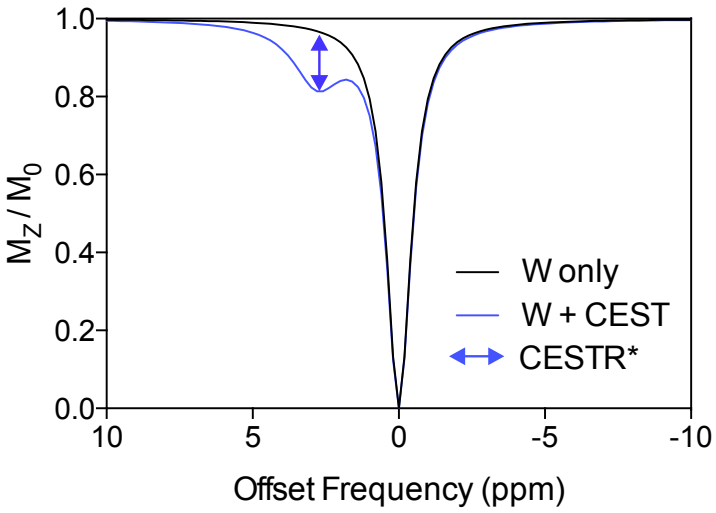

Figure 2.7: Graphical representation of the CESTR* calculation procedure. The W and W + CEST Z-spectra are simulated using the Bloch-McConnell equations. The exchange rate and concentration parameters used in the simulation of W + CEST are those fitted from the Bayesian Bloch-McConnell fitting, and the T_1 and T_2 times of each pool are kept constant. CESTR* is calculated as the difference in Z-spectrum signal at the frequency of interest between the 1-pool and 2-pool simulations.

CESTR* (also known as APTR* when referring specifically to amide protons) has been shown to be a more robust and relibable quantification method than competing metrics in a clinical cohort of acute ischaemic stroke patients [126]. As with all model-fitting methods, however, the technique is fundamentally limited by an increased acquisition time (since an entire Z-spectrum must be sampled rather than just individual points on it), long computational time to perform the model-fitting, strong dependence on the quality of the data being fitted, and potential degeneracies within the model which may result in erroneous results.

2.2.6 Applications

The applications of CEST MRI have grown immensely since its first use in 2000 [87, 114], and summaries of the CEST MRI literature have been completed numerous times in that period [88, 127–131]. This section highlights a few particular applications that are relevant to the topics of this thesis, predominantly focussing on the CEST effect arising from amide protons *in vivo*.

CEST MRI of the amide protons was first applied to measure the pH of ischaemic stroke lesions in rats [89]. By quantifying the CEST effect using the MTR_{asym} metric, with assumptions that MTR_{asym} = Amide PTR and that the amide proton concentration was unchanged at early stages of stroke, pH maps were derived from the MTR_{asym} measurements. Subsequent studies using a variety of other analysis metrics have utilised the pH sensitivity of CEST MRI of amide protons in ischaemic stroke in rats [56, 132, 133] and humans [126] to derive pH maps, all generally

assuming that the amide proton concentration is unchanged. Some studies have also used the pH-weighted nature of the signal (rather than calculating absolute pH maps) to delineate areas of tissue that are at risk of infarct [48, 57, 134], potentially enabling earlier and more-accurate identification of patients who would benefit from treatment than is currently available using diffusion- and perfusion-weighted MRI (see Chapter 1).

Measurement of pH is the primary area of parametric mapping research in the CEST MRI field. Other applications of CEST MRI have generally been restricted to simply measuring a CEST effect in pathological and healthy tissue, and attempting to discriminate between tissue types using the CEST measurement. Again focussing on the amide proton CEST effect, its application in brain tumour imaging has shown that CEST MRI highlights areas of tissue not commonly visualised as tumour on conventional T_1-weighted anatomical imaging [101, 135]. This finding suggests CEST MRI may be a more sensitive marker for delineating tumour boundaries within the brain than current clinically standardised methods [136, 137]. In addition, CEST MRI has been shown to discriminate between recurrent tumour tissue and radiation necrosis in preclinical [138] and clinical [139] cohorts, as well as between pseudo- and true progression [140], something that with current standard anatomical imaging is not routinely possible. Importantly, each of these studies observe and measure a difference in CEST signal between healthy and tumour tissue, but then merely speculate as to the biophysical origin of the altered signals; very little independent validation or further elucidation of proposed mechanisms of CEST signal changes are performed.

Aside from observing the endogenous CEST effects, some studies have utilised CEST-active exogenous contrast agents for specific applications. Iopromide, an FDA-approved contrast agent for CT imaging, exhibits CEST effects from two separate locations on the molecule. It has been shown that the ratio of the two CEST effects correlates with pH, and has been used in preclinical and clinical studies to measure the extracellular pH of tumours [141, 142]. Though limited by the need for sufficient concentration of the contrast agent to be present within an imaging voxel to make pH measurements, which is not guaranteed to be the case in poorly-perfused tumour microenvironments, such studies represent the closest attempt at measuring tumour pH using CEST MRI.

Other exogenous agents studied in preclinical and clinical settings include glucose, which can be imaged with CEST MRI owing to chemical exchange of the hydroxyl groups in the molecule. CEST MRI of glucose (also termed glucoCEST) has been used to image tumours [143], which preferentially metabolise through glycolytic pathways. The uptake of fluorodeoxyglucose ([^{18}F]FDG) imaged by positron emission tomography (PET) has been shown to colocalise well with the glucoCEST signal, suggesting that glucoCEST may be able to replace [^{18}F]FDG-PET imaging [144]. Dynamic Glucose Enhanced (DGE) imaging has also emerged from glucoCEST,

which follows the concentration of glucose over time using repeated CEST MRI acquisitions, in a similar way to how Dynamic Contrast Enhanced (DCE) MRI tracks the concentration of a Gadolinium-based contrast agent in repeated T_1-weighted scans. A comparison of DGE and DCE methods in preclinical and clinical environments has demonstrated that DGE may be a suitable alternative to DCE for patients in vulnerable populations, such as those with renal impairment or children [145].

Finally, a lesser-studied aspect of CEST MRI is its sensitivity to protein conformation [146, 147]. CEST MRI studies of the NOE-relayed exchange signal have shown its sensitivity to protein conformation in well-controlled *in vitro* samples, and its potential to image protein misfolding in a preclinical model of prion disease [148].

2.2.7 Limitations

Whilst CEST MRI has been used to great benefit for a number of different applications, there remain a number of key challenges in the interpretation of CEST MRI studies, which currently limit its widespread clinical applicability. The following three limitations have been identified for the purpose of focussing the work of this thesis.

2.2.7.1 Accurate quantification of effect size

Section 2.2.5 listed a number of different methods to quantify the size of CEST effects. In order for CEST MRI to have utility in clinical settings, it is important that a reliable, reproducible, and robust method for quantification of the true CEST effect size is implemented across a number of indepedent centres. In reality, however, the current state of the CEST MRI field is such that each research centre uses its own metric, which often is predicated on the specific research question being studied and/or the acquisition strategy being used. An ideal CEST MRI quantification metric is sensitive only to changes in the labile proton population (that is, the exchange rate and concentration of those protons), while being insensitive to alterations in T_1 and T_2 relaxation of water.

2.2.7.2 Signal source *in vivo*

Another challenge preventing the widespread application of CEST MRI to the clinic is a relative lack of understanding with regard to the source of the CEST effect *in vivo*. For instance, whilst general agreement in the field has been established that amide protons on the backbone of proteins and peptides have a resonant frequency of $\Omega = 3.5\,\mathrm{ppm}$, a number of studies claim to measure NOE-mediated magnetisation transfer at similar frequencies. In addition, alterations in the measured CEST signal (regardless of which quantification method is chosen) can manifest from a number of different changes to the exchanging proton pool. For instance, a given decrease

in CEST signal may be a result of a decrease in exchange rate, concentration, proton availability, or concurrent alterations of each factor. In order to convert CEST MRI signals into images of relevant biophysical parameters (for example, pH or protein concentration), certain assumptions of the source of the signal changes are made for the specific pathology being investigated. Improving the ability of CEST MRI to discriminate between changes in pH and protein concentration specifically is a necessary step before clinical translation of CEST MRI to measure pH can occur.

2.2.7.3 Physical location of signal source *in vivo*

Another aspect where specificity of the CEST MRI signal is lacking relates to the physical location of the molecules that contribute to the signal. The physical location of a molecule giving rise to a CEST signal is of course closely related to the type of molecule it is, but for any given molecule (e.g. quickly tumbling large proteins with amide groups resident in the backbone and sidechains) they are in general likely to reside within and outside cellular boundaries. These two environments are distinct in their biophysical properties, chemical environment, and biological purpose, particularly in pathological tissue, and reporting on either in isolation is likely to be of some benefit clinically. Reporting on a compartment-averaged signal, as is the case now, could be simplifying the complex environment encountered *in vivo* and potentially concealing additional important information. For example, as is discussed in Chapter 1, the intra- and extracellular pH of cells in tumours are markedly different. A certain proportion of amide proton CEST signal is likely to arise from the extracellular environment, but the extent to which the CEST MRI signal is composed of intra- and extracellular effects has not yet been determined.

2.3 Diffusion NMR/MRI

Whilst the primary focus of this thesis is on CEST MRI, elements of the work presented hereafter (particularly in Chapter 6) rely on an understanding of the principles of diffusion-weighted MRI. This section introduces the concept of measuring diffusion using magnetic resonance and how the NMR/MRI signal is sensitive to the diffusion of molecules, outlines a number of methodologies by which measuring diffusion-weighted MRI data is possible, discusses a number of popular applications of diffusion MRI, and finally highlights some key limitations of the field today.

Particles suspended within fluids move in a random, irregular way owing to the random, irregular collisions between those particles [149]. The diffusion of particles can be characterised by a diffusion coefficient, D, which describes the ability of a particle to move through an area of space in a given time. It has been shown that the mean square displacement of a particle $\overline{x^2}$ undergoing Brownian diffusion for a time t in n-dimentions is given by $\overline{x^2} = 2nDt$. From an MRI perspective, the focus of study is on the diffusion properties of water molecules within anatomical structures, so the discussion that follows is restricted only to the diffusion of water.

NMR and MRI signals can be sensitised to the diffusion of water within samples by using a pair of pulsed magnetic field gradients [150]. Briefly, the magnetisation at thermal equilibrium $\mathbf{M} = M_0\mathrm{k}$ within a sample is tipped into the transverse plane by a 90° RF pulse. A gradient in the magnetic field of magnitude G is then applied to the sample for a time δ, imposing a spatial variation of the precession frequency ω of individual nuclei within the sample. A 180° inversion pulse flips the magnetisation, a second gradient applied with equal magnitude, duration, and direction as the first, and the NMR/MRI signal acquired. The effect of the second gradient is to 'rephase' any nuclei that have not moved during the time gap between the gradient pulses Δ, and 'dephase' any nuclei that have diffused away from their original position. The resultant detected magnetisation S is, therefore, decreased (relative to the signal measured without diffusion S_0) by a factor that is proportional to the diffusion characteristics of the sample, as well as the timing and magnitude properties of the applied gradients. Such a signal is described by the Stejskal-Tanner equation [150]:

$$S = S_0 e^{-\gamma^2 G^2 \delta^2 (\Delta - \delta/3) D} \tag{2.18}$$

where γ is the gyromagnetic ratio. The vast majority of MRI studies of diffusion use a spin-echo pulse sequence [150]. Of importance to this thesis, though not implemented as wideley, is the stimulated echo diffusion pulse sequence, which is very similar in principle to the spin echo sequence but with the single 180° pulse being separated into two 90° pulses by a mixing time, TM [151, 152]. This modification has the added benefit of allowing substantially longer diffusion times Δ between the two gradient pulses since during TM the relaxation of the magnetisation is governed by T_1 rather than T_2, but there is an intrinsic decrease in signal by a factor of two.

When applied clinically in MRI, it is useful to define the concept of a diffusion b-value, which encapsulates the full extent of the diffusion-encoding capabilities of all the imposed gradients during an MRI sequence, even those not designed to encode diffusion information on to the signal [153]. Generally, the spatial-encoding gradients are of insufficient strength to have a substantial effect, leading to the definition of $b = \gamma^2 G^2 \delta^2 (\Delta - \delta/3)$ and the measured signal being $S = S_0 e^{-b \cdot ADC}$. ADC is the Apparent Diffusion Coefficient, and is different from the *true* diffusion coefficient D because diffusion of water in tissues is not unhindered.

The separation of D and ADC, as well as the fact that diffusion in tissue is not free, are important concepts to the application of diffusion MRI. Most commonly, diffusion-weighted MRI (DW-MRI) scans are performed with diffusion gradients applied equally in all three directions such that $b \neq 0$. Alternatively, a number of separate DW-MRI acquisitions may be performed with different b values and fit to an exponential signal model to derive spatial maps of the ADC. Additionally,

multiple acquisitions with diffusion gradients applied in different directions for each acqusition can be used to examine the anisotropy of diffusion within tissues [154].

Applications of DW-MRI in clinical settings have aided the management of acute stroke patients [53]. DW-MRI allows non-invasive visualisation of the extent of tissue damage after a stroke. The altered DW-MRI signal in regions of infarcted tissue is thought to reflect the larger intracellular water fraction in these areas, which occurs after initiation of the ischaemic cascade. In addition, further clinical applications of DW-MRI and ADC mapping have appeared in oncology settings, where the DW-MRI signal has been correlated with the cellularity of tumours and used to separate patients based on their tumour grade [155–157].

Of particular importance to this thesis is the ability of diffusion-encoding to separate intra- and extracellular signals in tissues. Intracellular water is restricted in its motion by the cell membrane, which reduces the apparent diffusion coefficient of water within cells. Extracellular water, on the other hand, is comparatively free, with only a small element of hindered motion arising from the compactness of cells. Diffusion-weighted NMR studies on cells have demonstrated that it is in principle possible to separate the intra- and extracellular signals based on the different ADC values in the two spaces owing to this restriction [158].

The extent to which DW-MRI can be used to separate signals from different compartments, however, is debated within the literature. For instance, typically a multi-exponential dependency of signal on diffusion b-value is interpreted as representing multi-compartmentalisation of the system being examined. This analysis framework was used to determine the physical location of N-acetyl aspartate in the rat brain to be within cell bodies and the intra-axonal space [159]. A similar biexponential signal model was used to determine the intracellular water volume fraction of perfused cancer cells *in vitro* [160]. Application of the same model to diffusion MRI of the rat brain *in vivo* has returned two distinct water populations [161]. However, the interpretation of these populations as being the intra- and extracellular compartments is complicated by the fact that the slowly diffusing component (that would usually be assigned to the intracellular space) has a smaller volume fraction than the fast diffusing component. This interpretation lies contrary to known water volume fraction measurements in the brain, where the intracellular compartment usually contains *ca.* 80% of the total water [162, 163]. Indeed, a number of other studies have demonstrated that both components of a biexponential signal decay arise from the intracellular space *in vitro* [164], or that compartmentalisation is not necessary to observe a multi-exponential signal behaviour [165]. On the other hand, other studies which use more complex biophysical models to analyse DW-MRI data incorporating the restriction of cellular membranes and the effect of water exchange across the membrane have measured accurate intra- and extracellular water fraction volumes [166]. Additionally, studies where the extracellular water signal has been

supressed using selective T_1 relaxation contrast agents have also determined accurate intracellular water volume fraction, as well as showing that the monoexponential analysis derived ADC is predominantly reporting on the intracellular environment [167]. As such, careful experimental validation of any signal interpretation must be carried out before firm conclusions can be made regarding the ability of DW-MRI to separate signals from different compartments.

2.3.1 The Bloch-Torrey Equations

Similar to the way in which the Bloch equations describe the dynamics of magnetisation in the presence of relaxation, and the Bloch-McConnell equations describe the dynamics of magnetisation in the presence of relaxation and chemical exchange, Henry Torrey derived the Bloch-Torrey equations to describe the dynamics of magnetisation in the presence of diffusion [168]. The Bloch-Torrey equations are shown below for completeness, where ∇ is the three-dimensional partial derivative operator $\nabla = \frac{\partial}{\partial x}\mathbf{i} + \frac{\partial}{\partial y}\mathbf{j} + \frac{\partial}{\partial z}\mathbf{k}$.

$$\frac{\mathrm{d}\mathbf{M}}{\mathrm{d}t} = \gamma(\mathbf{M} \times \mathbf{B}) - \frac{M_x\mathbf{i} + M_y\mathbf{j}}{T_2} - \frac{(M_z - M_0)\mathbf{k}}{T_1} + \nabla \cdot D\nabla\mathbf{M} \tag{2.19}$$

2.3.2 Limitations

The primary challenge in DW-MRI lies in the analysis of the acquired diffusion-weighted signals. Typical clinical implementations are fairly simple, assuming that diffusion causes signal attenuation described by a single exponential function. Evidence exists of bi- or tri-exponential signal decay, however, especially in more complex tissue environments encountered *in vivo* [159–161, 166, 169–174]. In these models, each exponent is characterised by a population fraction and diffusion coefficient. Attempts have been made to assign these bi- or tri-exponential signal models to tissue compartments, such as the extracellular or intravascular spaces, with varying degrees of success based on validation using histology [175, 176]. However, fundamentally these mathematical descriptions of the diffusion signal lack the specificity required to assign signals to certain tissue compartments.

To overcome this limitation, biophysical models of tissue have been used to simulate or derive the expected diffusion signal from a given tissue geometry. One such example is the Vascular, Extracellular and Restricted Diffusion for Cytometry in Tumours (VERDICT) framework, which fits a rich diffusion-weighted dataset to a signal model derived from assuming certain physical properties of the expected tissue components [177]. By treating blood vessels as cylinders which allow anisotropic water diffusion along one primary axis, intracellular spaces as spheres that allow isotropic diffusion within a restricted space, and extracellular spaces as hindered isotropic diffusion, parameters such as the water fraction in each space, the intracellular radius, and

the diffusion coefficient in each space can be estimated. Whilst the benefit of this form of analysis method is that maps of important biophysical parameters such as cellular radius can be constructed, there are a large number of correlated parameters that must be fit. One way to alleviate such issues is to fix or constrain parameters within the model to certain values, with the downside being that these values must be assumed or calculated *a priori*. Nevertheless, VERDICT MRI has been used with success to investigate several tumour types *in vivo*, as well as their response to therapy, with validation completed by histology [178].

2.4 Thesis aims

In Chapter 1 the biological motivation for making pH measurements *in vivo* was provided in two pathologies and the technical aspects of a number of different pH measurement methods were outlined. In this chapter, following a brief overview of the fundamental physics of NMR and MRI, CEST MRI was identified as a potential modality with the ability to be translated into clinical practice to non-invasively measure pH. What follows in this thesis is a body of work with the ultimate goal of developing the capability of CEST MRI to measure pH *in vivo*. Three specific areas of investigation were identified to focus on and the specific aims of this thesis, therefore, are:

1. To develop a quantification metric for CEST MRI data that is specific only to alterations in the exchanging proton pool, with no contamination from relaxation time changes;
2. To identify the proportion of CEST MRI signals that are associated with pH, or other biophysical parameters of interest such as protein concentration; and
3. To investigate the possibility of separating the CEST signal into intra- and extracellular components in order to specifically quantify pH_i or pH_e.

Chapter 3

Determination of an optimally specific and sensitive quantification metric for CEST MRI

Contents

3.1 Introduction . . . 50
3.2 Methods . . . 50
3.2.1 Phantom Preparation . . . 50
3.2.2 Validation of phantom models . . . 51
3.2.3 NMR & MRI experiments . . . 52
3.2.4 MRI Data Analysis . . . 53
3.2.5 Determination of optimal metric & measurement of pH . . . 54
3.3 Results . . . 56
3.3.1 Phantom Validation . . . 56
3.3.2 Measurement of CEST effect . . . 57
3.3.3 Determination of optimal metric . . . 59
3.3.4 Measurement of phantom pH . . . 62
3.4 Discussion . . . 64
3.5 Conclusion . . . 66

Parts of this chapter have been published previously as K.J. Ray, J.R. Larkin, Y.K. Tee, A.A. Khrapitchev, G. Karunanithy, M. Barber, A.J. Baldwin, M.A. Chappell and N.R. Sibson, "Determination of an optimally sensitive and specific chemical exchange saturation transfer MRI quantification metric in relevant biological phantoms", *NMR in Biomedicine*, vol. 29, no. 11, pp. 1624 — 1633, 2016. doi: 10.1002/nbm.3614.

Reproduction of this publication is permitted under the terms of the Creative Commons Attribution License (CC-BY).

3.1 Introduction

CEST MRI holds great promise as a means for non-invasive pH measurement. For clinical translation of this promise to manifest, for example to measure pH in oncology settings, a reliable and reproducible quantification of the CEST effect size *in vivo* is necessary. As discussed in Section 2.2.5.2, current metrics to quantify the size of the CEST effect are usually associated with particular acquisition methods and implemented in single-centre research studies to study specific questions. The CEST effect is sensitive to a number of variables (see Eq. 2.10). An ideal metric for quantification of the CEST effect would be sensitive only to the labile proton exchange rate (i.e. pH) and labile proton concentration, whilst being insensitive to water T_1 and T_2 relaxation effects, which are typically altered in pathological tissue.

To develop and validate such a metric, previous studies have used simple phantoms with a single exchanging pool of protons [125, 179]. These phantoms allow useful insights into the CEST MRI signal source, but do not adequately represent the complex *in vivo* intracellular biomolecular environment. Methods such as qCEST [179] and the Omega plot [180] have been used in such phantoms to successfully quantify labile proton exchange rate and concentration independently. However, these methods require many Z-spectra to be acquired with varying saturation parameters, which is impractical in a clinical environment. The AREX metric has also been proposed to correct for contamination of CEST effects by T_1 relaxation of water [117, 118, 122, 181] but this method has not been validated in physiologically relevant phantoms.

In this chapter the aims, therefore, were (i) to develop novel phantom models from cellular extracts that are representative of the *in vivo* intracellular environment of both normal brain, and brain metastases, (ii) to use these phantoms to determine the sensitivity of the CEST MRI signal as measured by a number of different analysis metrics, to changes in pH, labile proton concentration, T_1 and T_2, (iii) to identify an optimally specific analysis metric for quantification of CEST MRI data, and (iv) to evaluate the ability of the optimal metric to quantify pH differences in these phantoms.

3.2 Methods

3.2.1 Phantom Preparation

Phantoms were prepared to represent the intracellular environment of naïve mouse brain and *in vitro* cultured 4T1-GFP mouse metastatic breast carcinoma cells. The 4T1-GFP cell line is commonly used as a mouse model of metastatic breast cancer, including studies of metastatic spread to the brain [182]. It is an appropriate tumour model here as previous measurements of human breast cancers have displayed intracellular alkalosis [183]. For the mouse brain phantoms, female

BALB/c mice aged 6 – 8 weeks ($n = 6$) were terminally anaesthetized with sodium pentobarbital and transcardially perfused with 20 ml heparinised saline. Subsequently, the brains were removed, frozen in liquid nitrogen and stored at –80 °C until further use. For the 4T1-GFP cell phantoms, cells were cultured in Dulbecco's Modified Eagle Medium and passaged every second day to grow a sufficient quantity of cells.

Perchloric acid extracts of either naïve brain or 4T1-GFP cells were prepared. Briefly, either naïve mouse brains ($n = 6$) or a pellet of 4T1-GFP cells (8 g) were homogenized and coated with 0.1 M HCl in methanol in a dry ice bath. Subsequently, the mixture was warmed to wet ice bath temperature, 0.02 M HCl and 3 M perchloric acid added to the homogenizer and the precipitated protein sedimented by centrifugation ($4800 \times g$, 20 min, 4 °C). The supernatant was neutralized to pH $\sim$ 7 with KOH and the precipitated potassium perchlorate sedimented by centrifugation ($4800 \times g$, 20 min, 4 °C). The supernatant was lyophilised. All volumes of solutions added were scaled to the weight of starting material to match metabolite concentration to their *in vivo* or *in vitro* intracellular values.

The lyophilised samples were divided into 26 equal fractions and added to bovine serum albumin (BSA) to produce phantoms representative of the intracellular environment of either naïve brain or 4T1-GFP tumour cells. The pH (6.0 – 7.6 , $n = 6$), BSA content (4 – 16 % *w/v*, $n = 7$), T_1 time (0.3 – 1.7 s, $n = 7$) and T_2 time (29 – 140 ms, $n = 6$) of each phantom was serially varied for a total of 52 phantoms ($n = 26$ for each cell type). T_1 and T_2 relaxation times were varied by addition of gadolinium-DTPA (Omniscan, GE Healthcare) and iron nanoparticles (25 – 30 nm diameter), respectively. Where pH and BSA content were not varied, the phantoms were pH 7.4 with a BSA concentration of 8 % *w/v*. BSA has been used in previous studies as a protein representative of the *in vivo* protein pool, and 8 % *w/v* is a reasonable assumption of the protein content of the rodent brain [184, 185]. The BSA was not cross-linked to avoid macromolecular magnetization transfer effects being introduced, and the phantom pH was titrated after addition of BSA.

3.2.2 Validation of phantom models

The validity of the perchloric acid extract supplemented with BSA model as a reasonable representation of the intracellular environment of brain/tumour cells *in vivo* was confirmed using high-resolution NMR spectroscopy. One dimensional ^{1}H spectra with WATERGATE solvent suppression were acquired (see Section 3.2.3) from samples of PCA-extracted naïve mouse brain, *in vitro* cultured 4T1-GFP cells, and subcutaneous 4T1-GFP tumours. The subcutaneous tumours were grown by injecting 5×10^5 4T1-GFP cells in 100 µl PBS subcutaneously into female BALB/c mice aged 6 – 8 weeks ($n = 6$). Tumours were allowed to grow until 10 mm geometric mean

diameter, at which point the mice were terminally anaesthetized with sodium pentobarbital and transcardially perfused with 20 ml heparinised saline. The tumours were then isolated from the surrounding skin and fat, frozen in liquid nitrogen and stored at –80 °C until further use.

Additional spectra were obtained from the lysate of *in vitro* cultured 4T1-GFP cells and the respective phantom model (PCA-extracted *in vitro* cultured 4T1-GFP cells supplemented with 8 % *w/v* BSA). For the PCA-extracts, the lyophilized samples were dissolved in pH 7.4 potassium phosphate buffer (1 M) to provide suitable buffering capability over the range required for this study. The cell lysate sample was produced by suspending 4T1-GFP cells in NP-40 lysis buffer (2.74 ml 1 M NaCl, 2 ml 200 mM pH 7 Tris HCl, 80 µl 0.5 M EDTA, 200 µl NP-40, 4.98 ml dH_2O) and sedimenting the precipitated cellular membranes by centrifugation ($21,000 \times g$, 20 min, 4 °C). All samples were prepared to a final volume of 600 µl with 5 % D_2O.

In addition, samples of 8 % *w/v* BSA in potassium phosphate buffer (1 M, pH 7.4) were supplemented with varying concentration of PCA extracted *in vitro* cultured 4T1-GFP cells ($1\times$, $1.5\times$, and $2\times$ intracellular metabolite concentration) to confirm that the presence of metabolites from the PCA extracted cells in the sample influences the measured CEST spectrum.

3.2.3 NMR & MRI experiments

For validation of the phantom models, proton NMR spectra were acquired using a vertical bore 600 MHz (14.1 T) spectrometer (Agilent Technologies, Santa Clara, CA, USA), with the sample temperature controlled at 25 °C, using a WATERGATE sequence with a relaxation delay of 2 s, an acquisition time of 2 s, and 128 transients per free induction decay recorded[1]. The carrier was centred on water (4.7 ppm) with a sweep width of 9551 Hz. Spectra were processed using NMRPipe [186].

All MRI experiments were performed using a horizontal bore 400 MHz (9.4 T) spectrometer (Agilent Technologies, Santa Clara, CA, USA) with a volume transmit/receive coil (i.d. 40 mm, RAPID Biomedical, Rimpar, Germany). The phantoms were scanned at ambient room temperature. Shimming was performed prior to each experiment to minimize the B_0 field inhomogeneity. CEST images were acquired from 26 phantoms simultaneously using a saturation scheme of 300 Gaussian pulses of 26 ms duration and $180°$ flip angle each (50 % duty cycle, equivalent continuous wave saturation power 0.8 µT) at 85 saturation frequencies spaced equally between $\pm 10\,\mathrm{ppm}$, followed by an 8-shot spin-echo EPI readout. Additional images were acquired following saturation at $\pm 100\,\mathrm{ppm}$ for normalization; field of view $38\,\mathrm{mm} \times 38\,\mathrm{mm}$, matrix size 32×32, slice thickness 2 mm, echo time (TE) 8.22 ms and repetition time (TR) 7.85 ms. Total scan time for each set of phantoms was 3 h 6 min.

[1] NMR experiments were performed by Gogulan Karunanithy.

In addition to CEST imaging, the T_1 and T_2 relaxation times of each phantom were measured using inversion recovery (TR = 10 s, TE = 8.22 ms, inversion time (TI) varied in 9 steps from 13.14 ms to 8 s, signals fitted to $M_Z = M_0\left(1 - 2e^{-\frac{\mathrm{TI}}{T_1}}\right)$ and spin echo (TR = 10 s, TE varied in 10 steps from 30 ms to 160 ms, signals fitted to $M_Z = M_0 e^{-\frac{\mathrm{TE}}{T_2}}$) experiments, respectively. In both cases 8-shot spin-echo EPI readout was used to acquire images.

3.2.4 MRI Data Analysis

All MRI data were processed in MATLAB (MathWorks Inc., Natick, MA, USA). The relaxation maps of the water pool were obtained by least square fitting of the measured intensity against the inversion time (T_1 map) and echo time (T_2 map). Six metrics were used to analyse the Z-spectra: conventional asymmetry analysis ($\mathrm{MTR}_{\mathrm{asym}}$ [89]), multiple-offset analysis (APT* [115]), inverse Z-spectrum multiple-offset analysis ($\mathrm{MTR}_{\mathrm{Rex}}$ [117]), apparent relaxation due to exchange (AREX [117]), and two variants of a Bayesian model-based analysis (CESTR* [125]), as defined in equations Eq. 2.12 – Eq. 2.17, respectively. CEST effects were measured for all metrics at $\Omega = 2.8\,\mathrm{ppm}$ with $\delta\Omega = 1.4\,\mathrm{ppm}$ for APT* and $\mathrm{MTR}_{\mathrm{Rex}}$. B_0 inhomogeneity was corrected prior to $\mathrm{MTR}_{\mathrm{asym}}$, APT*, and $\mathrm{MTR}_{\mathrm{Rex}}$ analysis by shifting the minimum point of the Z-spectrum to 0 ppm on a voxel-wise basis; CESTR* corrects for B_0 inhomogeneity during the analysis. All analyses were performed on a voxel-wise basis, and the data presented for each phantom are the mean $\pm$ standard deviation for a fixed-area region of interest (ROI) over each phantom.

Prior to calculating the CESTR* metric, the raw Z-spectra were analysed using BayCEST (FMRIB Software Library, www.fmrib.ox.ac.uk/fsl/baycest). Three pools were fitted using BayCEST: the water pool at 0 ppm (W), the labile amine proton pool at 2.8 ppm (CEST), and an exchange pool centred at –3.5 ppm. The output of BayCEST is a model-fitted Z-spectrum with associated fitted values of the exchange rate and relative concentration of the protons in each pool, and T_1 and T_2 relaxation times for all proton pools (Fig. 3.1). BayCEST was run for each phantom with default values for the mean of the prior distributions for water T_1 (1.8 s) and T_2 (100 ms). Subsequently, the water T_1 and T_2 times measured from each phantom in the T_1 and T_2 maps were included as the means of the associated prior distributions in the model fitting (Table 3.1). In both cases the T_1 and T_2 values remained as parameters within the fitting procedure to be estimated from the data. Goodness of fit for the model-fitted Z-spectrum to each dataset was verified and quantified by calculation of R^2 (Fig. 3.2).

Table 3.1 lists the parameters included in the model fitted to the measured data. The values are the initial estimates used in the fitting algorithm, expressed as the mean $\pm$ standard deviation of a normal distribution. The algorithm assumed a continuous wave saturation pulse of power 0.8 µT and duration 7.8 s, equivalent to the pulsed saturation scheme implemented, to decrease

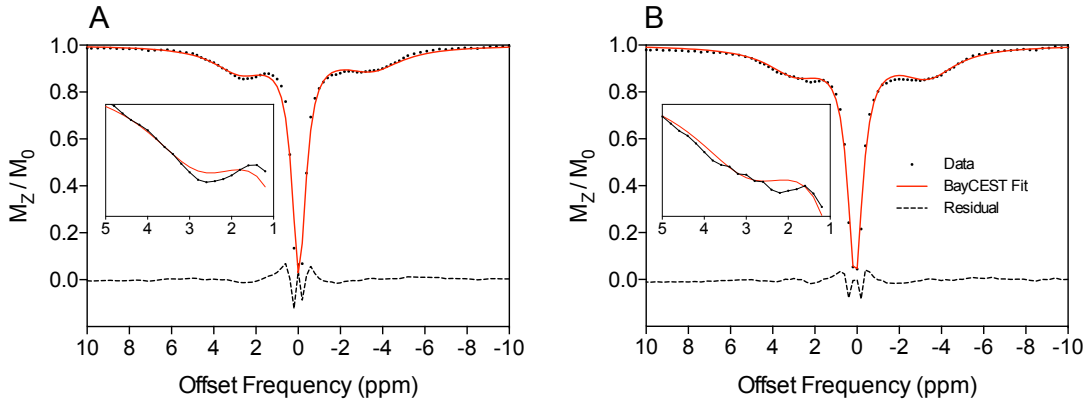

Figure 3.1: Demonstration of the Bayesian Bloch-McConnell fitting algorithm BayCEST. The measured data are from an 8 % *w/v* BSA supplemented with 4T1-GFP PCA extract phantom at pH 6.0 (A) and pH 7.6 (B). The red line shows the result of the Bloch-McConnell equation fitting with three pools. The residual between the measured data and fitted Z-spectrum is also shown (black dash), demonstrating a good fit for both phantoms, with the largest residuals appearing around the water frequency. Insets in each panel show a zoomed version of the data and Bayesian Bloch-McConnell fit for offset frequencies 1 – 5 ppm. It is apparent that two peaks appear at higher pH in the raw data, although, in this study, a 3 pool model fits the low and high pH phantoms equally well (pH = 6.0 data are fitted with R^2 = 0.9849, pH = 7.6 data fitted with R^2 = 0.9892). Visually, however, it appears that the fits could be improved by moving to a 4 pool model at high pH. A 3 pool model was fitted because otherwise over-fitting the measured Z-spectra is a concern, and the results of this phantom study would have limited applicability to the *in vivo* environment.

computation time.

CESTR* was calculated from the 2.8 ppm pool by simulating 1-pool (W only) and 2-pool (W + CEST) systems using only the fitted estimates of exchange rate and relative concentration, and measuring the difference in signal at 2.8 ppm (see Fig. 2.7). This analysis produced two values for CESTR* - one calculated with default priors for water T_1 (1.8 s) and T_2 (100 ms), and a second with phantom specific measured T_1 and T_2 prior means, hereafter called CESTR* with measured T_1/T_2 priors. The fitted exchange rate was not used directly, as correlation exists between the fitted exchange rate and concentration [125].

3.2.5 Determination of optimal metric & measurement of pH

The relationship between the calculated CEST effect using each metric and the serially varied parameters was determined by linear regression, and its absolute value (in $|\,\%\, M_0\,|$ / parameter unit change) compared between phantom models using a t-test corrected for multiple comparisons using the Holm-Sidak method [187]. Statistical significance was defined as $p < 0.05$, which post-correction gave an effective significance level of $p < 0.003$. These comparisons were used to determine whether pooling the data from both phantom models was appropriate.

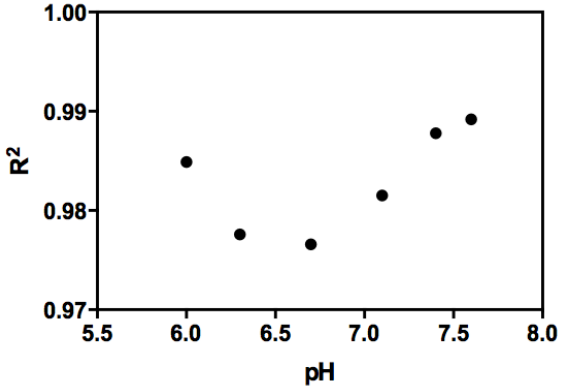

Figure 3.2: Goodness-of-fit (R^2) for a 3-pool Bayesian Bloch-McConnell fitting algorithm as shown in Fig. 3.1 varies as the pH of the phantom changes. R^2 is consistently high (> 0.976) for the full range of pH values.

	Water Pool	**CEST Pool**	**NOE Pool**
Offset Frequency (ppm)	0	2.8 ± 0.3	-3.5 ± 0.3
k_{iw} (Hz)	-	500 ± 10	50 ± 10
$\log(k_{iw})^*$	-	2.7 ± 1.0	1.7 ± 1.0
M_0^i	0 ± 10^6	-	-
rM_0^i (M_0^i/M_0^w)	-	0.0 ± 0.1	0.0 ± 0.1
T_1 (s)$^\#$	1.80 ± 0.36 or From T_1 map	1.80 ± 0.36	1.80 ± 0.36
T_2 (ms)$^\#$	100 ± 20 or From T_2 map	0.25 ± 0.05	0.25 ± 0.05

Table 3.1: Model parameter prior values used for Bayesian fitting of Bloch-McConnell equations to measured Z-spectra. Values are expressed as the mean $\pm$ standard deviation of a normal distribution. * indicates that the log value of the exchange rate was fitted during the model fitting, so the prior and standard deviation were defined as the log value. # indicates that the mean and standard deviation defined for the T_1 time or T_2 time was varied to either be identical for all phantoms or varied each time to be the values measured by the T_1 and T_2 maps.

Subsequently, a further multi-parameter linear regression model was used to determine the optimal analysis metric in terms of specificity. Data from both phantom models (tumour and naïve brain) were combined and fitted to a model of the form of Eq. 3.1, which describes the response of an ideal CEST quantification metric (i.e. only dependent on pH and [BSA]).

$$\text{CEST Effect} = \alpha \cdot \text{pH} + \beta \cdot [\text{BSA}] + \epsilon \tag{3.1}$$

The coefficients α,β,ϵ of Eq. 3.1 are constants (units $[\alpha] = \%M_0/\text{pH}$, $[\beta] = \%M_0/[\text{BSA}]$, $[\epsilon] = \%M_0$) that describe the level of sensitivity of the experimentally measured data to the varied parameters in the phantoms. Using these fitted coefficient values and the known pH and [BSA] for each phantom, theoretical CEST effects were calculated and correlated to the experimentally measured CEST effects for each metric. The R^2 values for these correlations were used as indications of the specificity of the metric to changes in only pH and [BSA]. The optimal metric was defined as that with the highest R^2 value for the correlation between calculated and experimentally measured CEST effect, which represents a metric with minimal contamination by T_1 and T_2 time.

For the optimal metric, differences in experimentally measured CEST effects were calculated between each pair of phantoms ($\Delta\text{CEST} = \text{CEST}_1 - \text{CEST}_2$). These differences were tested for statistical significance, defined as a difference larger than the standard deviations on each CEST effect measurement added in quadrature $\Delta\text{CEST} > \sigma_{\Delta\text{CEST}} = \sqrt{\sigma^2_{\text{CEST1}} + \sigma^2_{\text{CEST2}}}$.

For statistically significant differences in CEST effect, pH differences as measured by pH-probe ('Experimental ΔpH') and back calculated from the linear regression coefficients from Eq. 3.1 ('Calculated ΔpH') were correlated to verify the suitability of the metric for measuring pH differences.

3.3 Results

3.3.1 Phantom Validation

The metabolite peaks in spectra obtained from PCA extracted *in vitro* cultured 4T1-GFP cells and the same cells grown *in vivo* as a subcutaneous tumour were very similar in magnitude (Fig. 3.3A). Thus, *in vitro* cultured 4T1-GFP cells are metabolically similar to an *in vivo* tumour. However, clear differences were seen in the distribution and magnitude of metabolite peaks from PCA extracted naïve mouse brain and *in vivo* tumour, revealing their distinctly different metabolite compositions (Fig. 3.3B). Upon comparing the spectra from the lysate of *in vitro* cultured 4T1-GFP cells and the representative phantom model (Fig. 3.3C), the marked similarities in the magnitude of the broad

protein lineshapes indicate that the phantom (extract) model is a reasonable approximation of the intracellular environment of 4T1-GFP cells.

Clear differences between the Z-spectra from phantoms of BSA only and those containing 4T1-GFP cell PCA extracts were evident in the region $-1--5$ ppm, and indicates additional NOE-mediated saturation of the water signal owing to the presence of the intracellular metabolites (Fig. 3.4). The CEST effect centered at 2.8 ppm is also altered with increasing concentration of PCA extracted tissue.

3.3.2 Measurement of CEST effect

The relationships between the measured CEST effect at 2.8 ppm and the pH, BSA concentration, T_1 time and T_2 time were determined using multiple analysis metrics for phantoms containing BSA supplemented with extracts from either 4T1-GFP cells or naïve mouse brain (Fig. 3.5). The T_2 time was considered constant for increasing concentrations of gadolinium-DTPA, and the T_1 time constant for increasing concentration of iron nanoparticles, as these varied minimally compared to the objective relaxation time (Fig. 3.6).

Decreases in MTR_{asym}, APT* and MTR_{Rex} were observed with increasing pH, which is expected for the fast-exchanging amine protons at this frequency [188] (Fig. 3.5A.i, B.i, C.i). Conversely, however, since CESTR* estimates the exchange rate and concentration directly from the Z-spectrum, an increase in CESTR* (calculated with default T_1/T_2 priors) was seen as pH increases (Fig. 3.5D.i). The AREX metric also showed a significant decrease as pH increased (Fig. 3.5E.i), and the increase in CESTR* became significant when measured T_1/T_2 priors were included (Fig. 3.5F.i).

Significant increases in all metrics apart from MTR_{asym} were evident with increasing protein concentration (Fig. 3.5B.ii – F.ii). In contrast, MTR_{asym} decreased as protein concentration increased (Fig. 3.5A.ii). APT*, MTR_{Rex} and CESTR* (default T_1/T_2 priors) were found to be sensitive to changes in both proton relaxation times in both phantom models (Fig. 3.5B.iii – iv, C.iii – iv, D.iii – iv), whilst MTR_{asym} was sensitive only to changes in T_1 in the 4T1-GFP phantom model (Fig. 3.5A.iii – iv). Some measurements of MTR_{Rex} and APT* were negative because in these instances the relaxation time change resulted in no discernible CEST peak at 2.8 ppm (Fig. 3.7). Since a negative CEST effect measurement is unphysical, these measurements were set to zero. As expected, AREX was insensitive to T_1 relaxation time variations in both phantom models, but sensitive to T_2 time changes (Fig. 3.5E.iii – iv). CESTR* (measured T_1/T_2 priors) was the only metric insensitive to both relaxation times in both models (Fig. 3.5F.iii – iv).

Significance levels for the comparisons of linear regression gradients between the two phantom

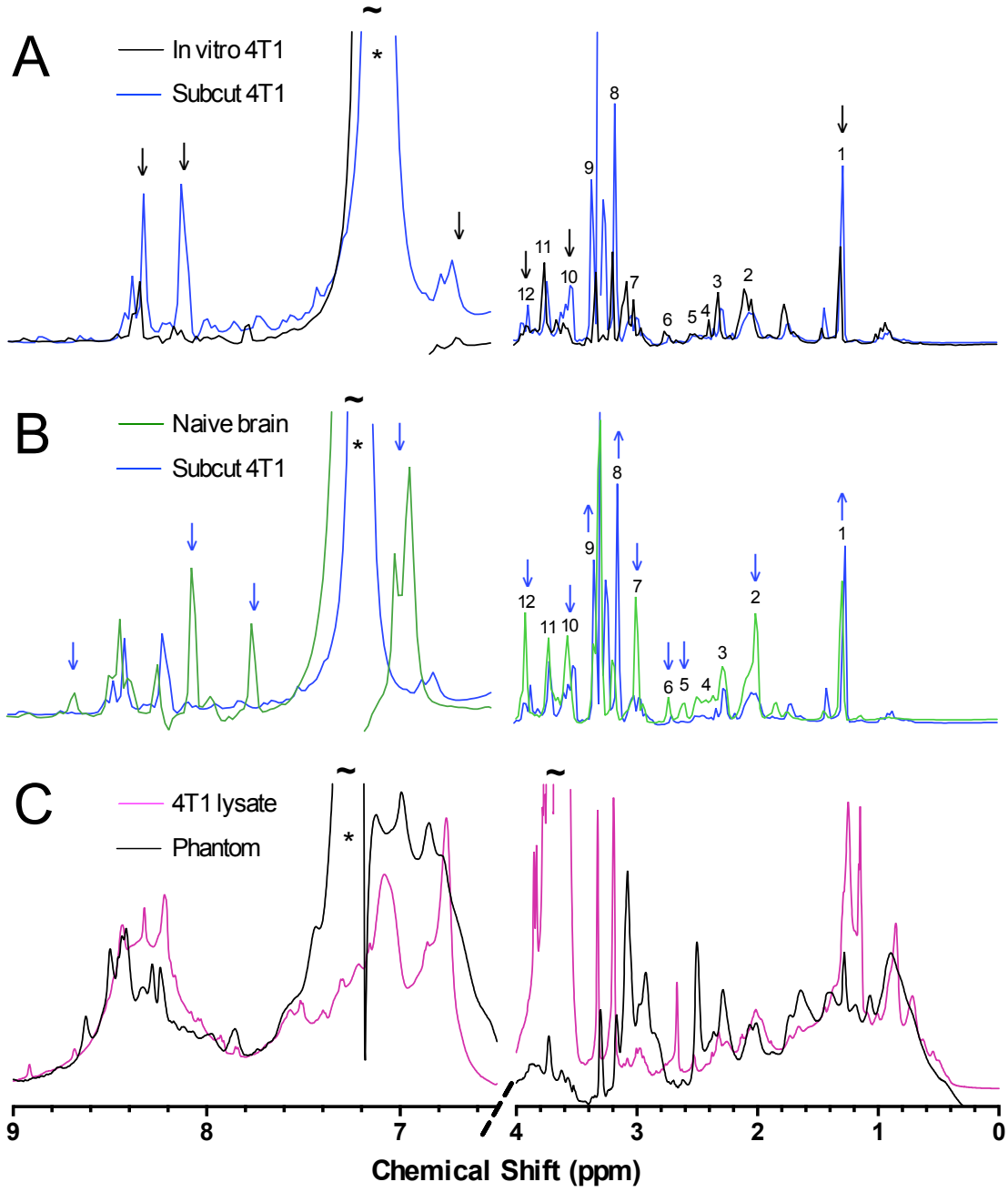

Figure 3.3: One-dimensional ^{1}H NMR spectra, showing (A) the metabolic similarity of 4T1-GFP cells grown *in vivo* as a subcutaneous tumour (blue) or *in vitro* (black) in culture flasks, (B) the metabolic distinctness of 4T1-GFP mouse mammary carcinoma cells (blue) from naïve mouse brain (green), and (C) the similarity of the broad line shape component of the spectrum from cell lysate of 4T1-GFP cells (pink) to the PCA extract of the same cell line supplemented with 8 % *w/v* BSA (black). Coloured arrows signify relative differences between spectra, and * signifies signal from a contaminant from the PCA extraction procedure. ˜ signifies points where the peaks exceed the axes limits. Numbers are metabolite identification: 1: Lac, 2: NAA, 3: Glu, 4: Gln, 5: NAA, 6: Asp, 7: Cr/PCr, 8: PC/GPC, 9: Tau, 10: Myo-ins, 11: Asc/Gln/Glu/GSH, 12: Cr/PCr.

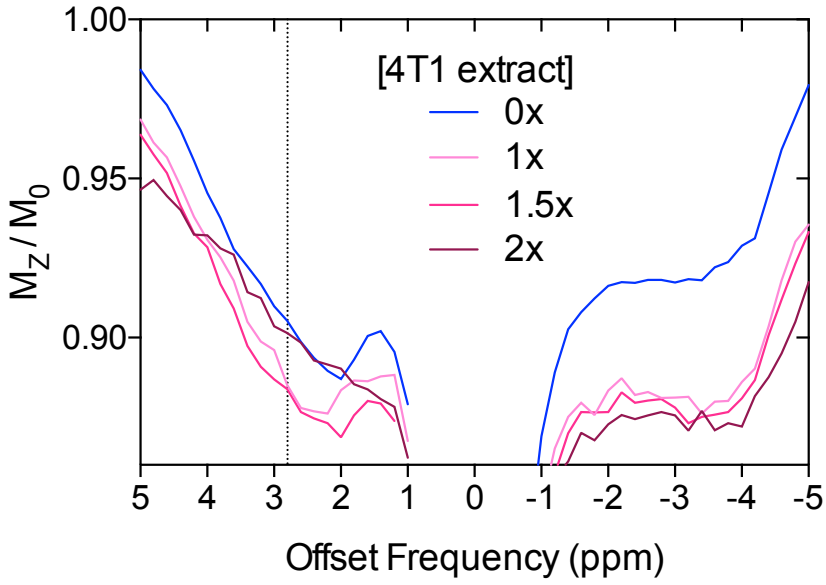

Figure 3.4: Z-spectra of 8 % *w/v* BSA phantoms at pH 7.2 supplemented with PCA extract from 4T1-GFP cells, replicating metabolite concentrations of $1\times$, $1.5\times$, and $2\times$ intracellular levels. The 4T1-GFP intracellular metabolites clearly alter the measured Z-spectrum from the BSA-only Z-spectrum ($0\times$). The CEST effect at 2.8 ppm broadens with increasing metabolite content, consistent with an increasing average chemical exchange rate.

	MTR_{asym}	MTR_{Rex}	APT*	CESTR* (Default T_1/T_2 priors)	AREX	CESTR* (Measured T_1/T_2 priors)
pH	0.001 *	0.001 *	0.002 *	0.02	0.02	0.45
[BSA]	0.04	0.01	0.02	0.10	0.003	0.04
T_1 Time	0.05	0.10	0.06	0.001 *	0.54	0.03
T_2 Time	0.49	0.36	0.36	0.99	0.09	0.16

Table 3.2: p values for the results of t–tests comparing the linear regression gradient values for CEST effect measurements from 4T1-GFP and naïve brain phantom. $p < 0.05$ was defined as statistically significant, with correction for multiple t–tests using the Holm-Sidak method. p values marked * are statistically significant differences.

models are shown in Table 3.2. Significant differences were found between phantom models for MTR_{asym}, APT* and MTR_{Rex} as pH was varied, and for CESTR* with default T_1/T_2 priors as T_1 time was varied (Fig. 3.5A.i, B.i, C.i, D.iii, p-values in Table 3.2).

3.3.3 Determination of optimal metric

MTR_{asym}, APT*, MTR_{Rex} and CESTR* with default T_1/T_2 priors all showed a significant sensitivity to serial variation in T_1 and T_2 time, indicating the contaminant effect the water relaxation times have on these metrics when quantifying CEST effects. Of the two methods that incorporate compensation for relaxation times (AREX and CESTR* with measured T_1/T_2 priors), the CESTR*

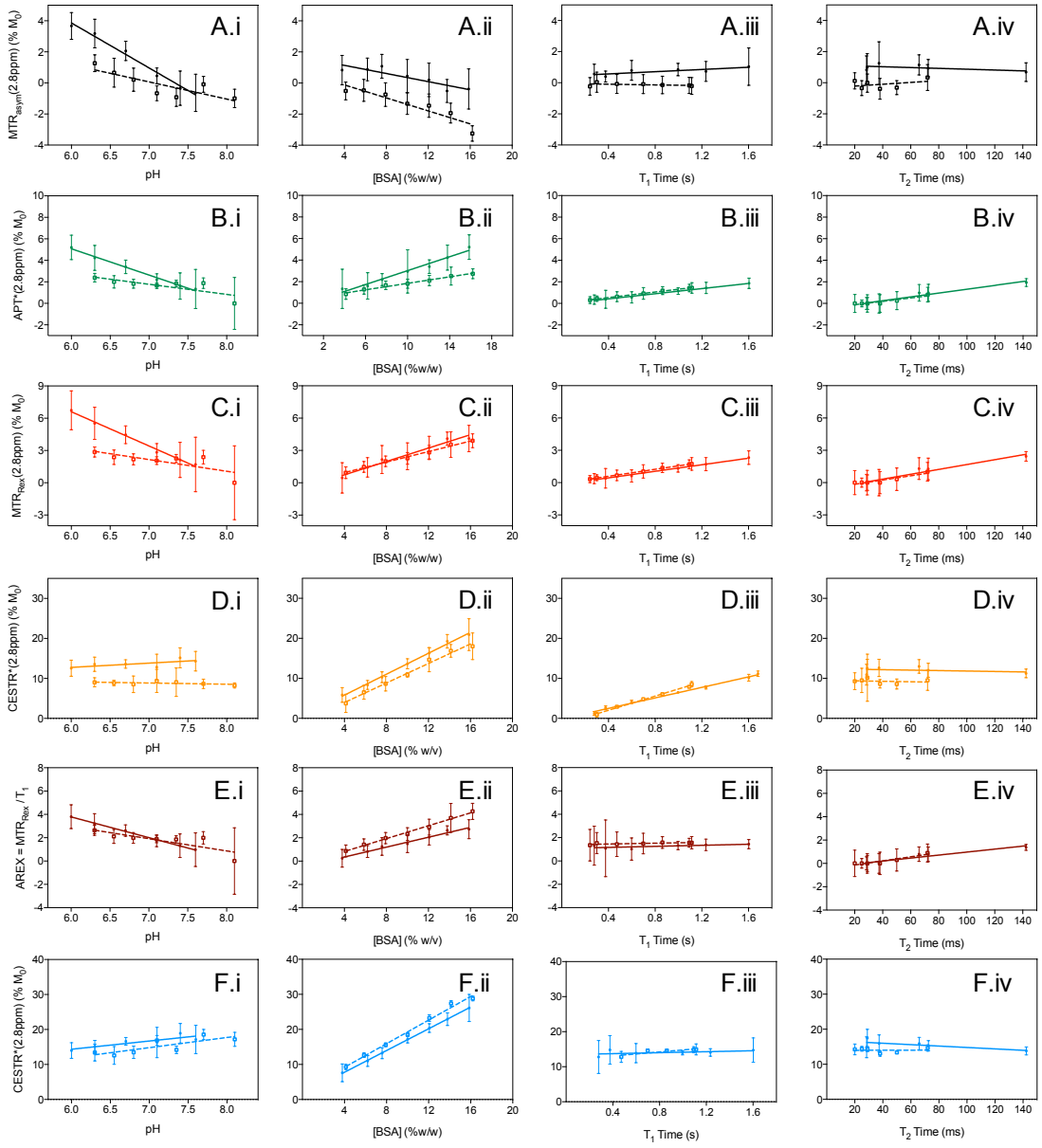

Figure 3.5: Linear regression relationships of MTR_{asym} (A), APT* (B), MTR_{Rex} (C), CESTR* calculated with default T_1/T_2 priors (D), AREX (E) and CESTR* calculated with measured T_1/T_2 priors (F) as a function of pH (i), BSA content (ii), T_1 time (iii), and T_2 time (iv) for the CEST effect at 2.8 ppm in phantoms containing 8 % *w/v* BSA and PCA extract from 4T1-GFP cells (solid circles) and naïve mouse brains (open squares). Solid and dashed lines are the fitted linear regression relationships to tumour and naïve mouse brain phantoms, respectively.

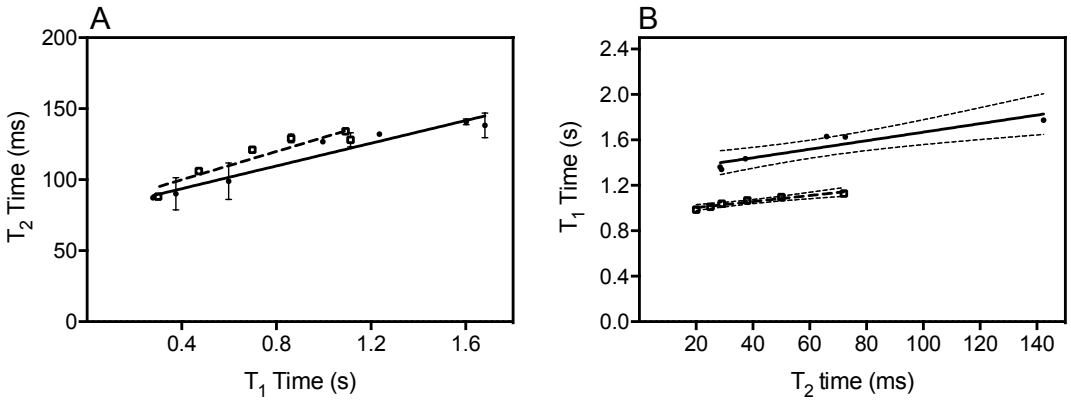

Figure 3.6: The measured variation in T_2 time for varying concentration of gadolinium-DTPA to adjust T_1 time (A) and T_1 time for varying concentration of iron nanoparticles to adjust T_2 time (B), for tumour (solid circles) and naïve mouse brain (open squares) phantoms. Solid and dashed lines show the linear regression of both relationships for tumour and naïve brain phantoms, respectively. In all cases a significant variation in both relaxation times is measured, highlighting the difficulty in altering relaxation times independently with contrast agents. However, the variation in T_1 with varying iron nanoparticle concentration to change T_2 was four times less (76% change in T_2 *vs.* 18% change in T_1). Similarly, the variation in T_2 as gadolinium-DTPA was added to adjust T_1 time was much less (78% change in T_1 *vs.* 34% change in T_2). Hence, the T_1 and T_2 times were treated as remaining constant for increasing concentration of iron nanoparticles and gadolinium-DTPA, respectively, since the change in the target relaxation time was at least twice that of the other relaxation time.

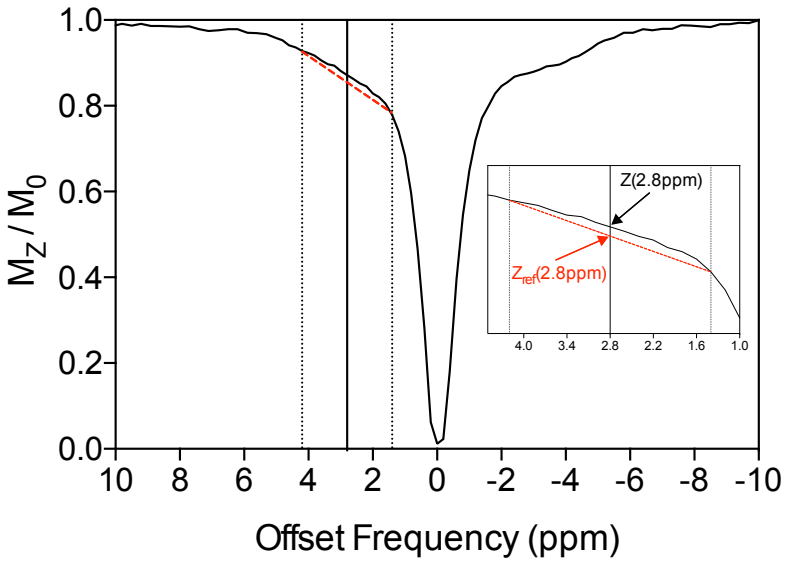

Figure 3.7: Raw Z-spectrum for a tumour phantom with T_2 relaxation time of 29 ms, showing that at such short T_2 relaxation times the broadening of the water lineshape in the Z-spectrum prevents the delineation of any discernible CEST peak at 2.8 ppm, hence giving Z_{ref}(2.8 ppm) < Z(2.8 ppm), and negative APT* and MTR_{Rex} values.

measurements showed minimal sensitivity to serial variation in both T_1 and T_2 time (Fig. 3.5F.iii - iv). As expected, AREX was not significantly sensitive to variations in T_1 time, but did vary with T_2 time. Notably, CESTR* with measured T_1/T_2 priors was the only metric to show no significant dependence on T_1 or T_2 time in either phantom model, indicating the specificity of CESTR* to measuring changes in only the CEST pool properties).

Correlation analysis between the experimentally measured CEST effects and the theoretically calculated CEST effects from Eq. 3.1, yielded the highest R^2 value (0.88) for CESTR* with measured T_1/T_2 priors (Fig. 3.8F). This high R^2 value means that CESTR* with measured T_1/T_2 priors is dependent only on pH and protein concentration. MTR_{asym}, APT*, MTR_{Rex} and CESTR* with default T_1/T_2 priors (Fig. 3.8A-D) display a constant calculated CEST effect in many cases, because these metrics do not directly account for the effects of T_1 or T_2 variations. For this reason it is difficult to use these metrics for pH estimation. One contributing factor to the low R^2 values observed for MTR_{asym} (0.53), MTR_{Rex} (0.14) and APT* (0.45) may be the significant difference in linear regression gradients between tumour and naïve brain phantom models as pH is varied. However, it is unlikely that this is the only factor since AREX and CESTR* with default T_1/T_2 priors both display similarly low R^2 values (0.48 and 0.07 respectively) with non-significant differences between phantom models. On this basis, the optimal metric was found to be CESTR* with measured T_1/T_2 priors.

3.3.4 Measurement of phantom pH

Differences in the experimentally measured CESTR* (with measured T_1/T_2 priors) values from each phantom were measured and tested for statistical significance. A total of 28 ΔCESTR* values were found to be significant. For these differences, the experimentally measured ΔpH and the calculated ΔpH using a re-arrangement of Eq. 3.1 were correlated (Fig. 3.9). These findings validate CESTR* as a reliable measure of ΔpH by CEST MRI, with a root mean square deviation for the correlation in Fig. 3.9 — and expected quantitative pH accuracy — of 0.6 pH units for the case of no variation in protein concentration.

Further, considering the data points in distinct groups based on the magnitude of the Experimental ΔpH value, CESTR* correctly predicted the sign of ΔpH in 94% of cases (16/17) where Experimental ΔpH < -0.6 pH units and 100% of cases where Experimental ΔpH > 0.6 pH units (3/3). For the group where Experimental ΔpH was within ± 0.6 pH units of zero, CESTR* was successful in 75% of cases (6/8).

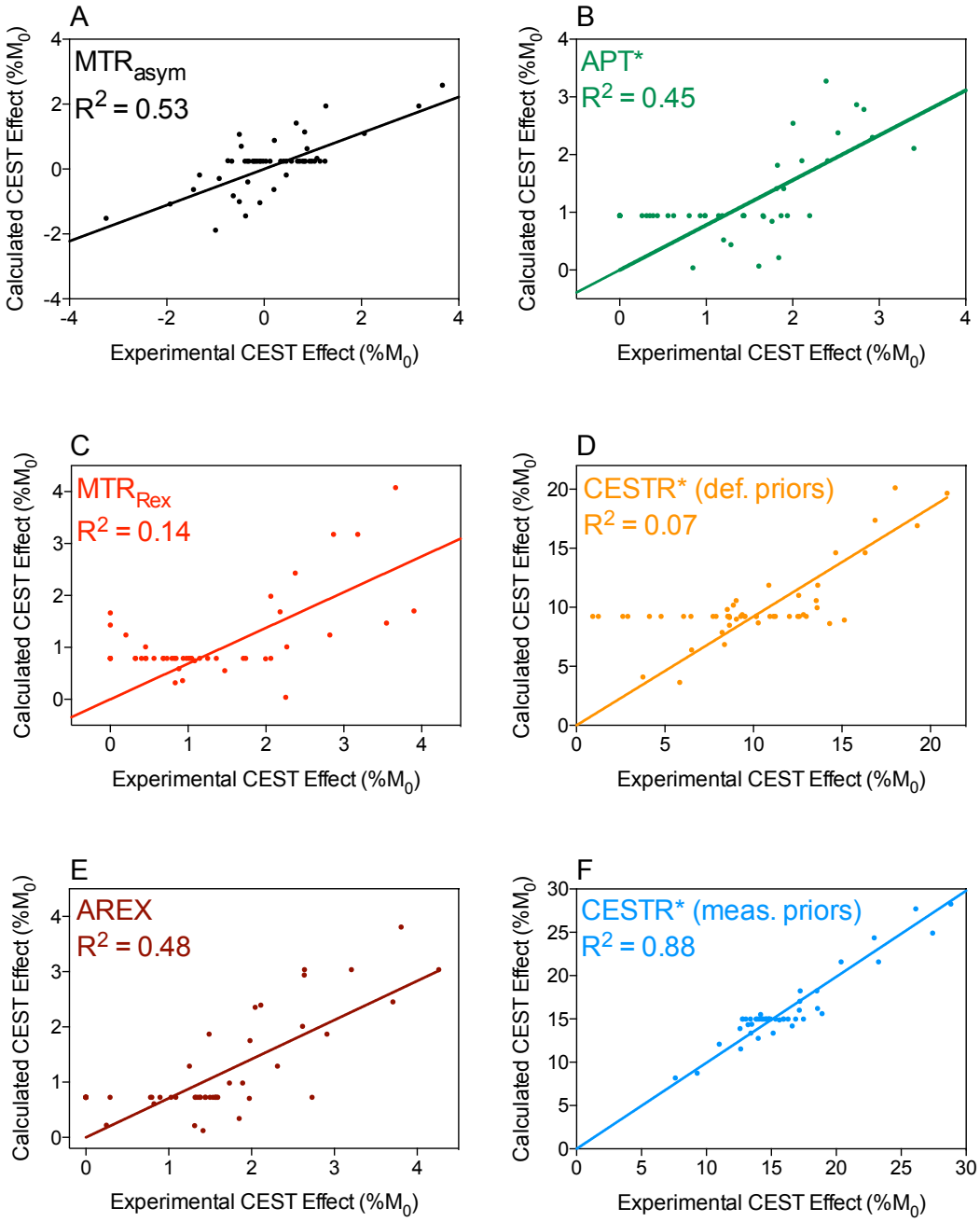

Figure 3.8: Correlations between calculated CEST effects from equation 3.6 and the experimentally measured CEST effects in each phantom as measured by each analysis metric: MTR_{asym} (A), APT* (B), MTR_{Rex} (C), CESTR* calculated with default T_1/T_2 priors (D), AREX (E), and CESTR* calculated with measured T_1/T_2 priors (F). R^2 values are: MTR_{asym} = 0.53, MTR_{Rex} = 0.14, APT* = 0.45, CESTR* with default priors = 0.07, AREX = 0.48, and CESTR* with measured priors = 0.88.

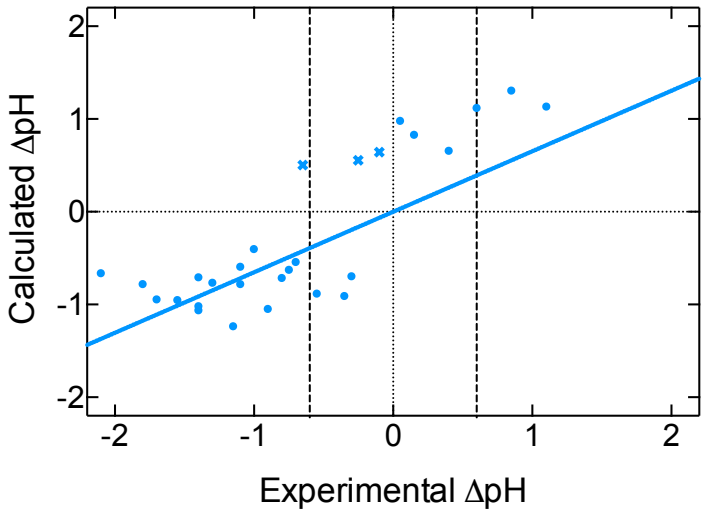

Figure 3.9: Correlation between ΔpH calculated using a rearrangement of Eq. 3.1 for statistically significant ΔCESTR* measurements between phantoms, and the ΔpH experimentally measured by pH probe. The R_2 value is 0.61. Cross markers indicate the data points where CESTR* incorrectly predicted the sign of the pH change.

3.4 Discussion

The current study examined the sensitivity and specificity of various CEST MRI quantification methods, in novel phantom models that closely reflect the intracellular environment of brain metastases and naïve mouse brain. In contrast to all other metrics, CESTR* with measured T_1/T_2 priors was found to be sensitive only to variations in pH and [BSA] in both tumour and naïve brain phantom models. Thus, CESTR* can remove the effect of T_1 and T_2 from the CEST measurement, which are known to vary with pathological changes *in vivo* [189], allowing a more accurate quantification of the CEST effect. Therefore, this study found that CESTR* with measured T_1 and T_2 priors is the most specific metric for quantification of CEST MRI data. CESTR* with measured T_1/T_2 priors can be applied robustly both between samples, and between voxels within a single experiment, to measure pH differences with an accuracy of 0.6 pH units in these phantoms.

Other studies have suggested that the T_1 contamination of the CEST signal is counteracted by changes in water content *in vivo*, and that the CEST contrast in tumours originates from a higher mobile protein concentration [190]. If this is the case, it may be difficult to quantify pH in tumours as both the pH and protein concentration may be changing simultaneously. However, as shown by this study and others [117, 191], T_1 correction is absolutely necessary for reliable, specific quantification of the CEST signal, regardless of the counteracting effect of water content. Assuming that the effects of T_1 and water content perfectly cancel may lead to inaccurate

quantification of CEST effects *in vivo* in pathologies where only one of these parameters changes.

MTR_{asym} measured from our phantoms decreased as the protein concentration increased, contrary to previous studies [101, 135, 188]. This discrepancy can be explained by the difference in saturation parameters used in the studies. In this study, a 7.8 s pulse train with CW equivalent power 0.8 µT was employed, which is preferentially sensitive to slowly exchanging protons. The effect of these saturation parameters is to enhance the NOE effects seen from the BSA and extracted metabolites in the phantoms. As the protein concentration increases, these NOE effects increase more than the CEST effects at 2.8 ppm, leading to a decreasing MTR_{asym}. Other studies employing BSA phantoms [184] or *in vivo* [101, 138] all used much shorter pulse trains (4 s) and higher powers (1.3 – 1.5 µT), which are less sensitive to the slowly exchanging NOE effects.

Other methods not examined in this study can also be used to quantify the various contributions to a measured CEST effect, such as qCEST [179]. However, qCEST separates the contributions of labile proton exchange rate and concentration to the Z-spectrum by measuring the CEST effect as a function of the saturation power. When applied to a clinical setting this approach is impractical owing to acquisition duration and specific absorption rate (SAR) concerns. In addition, the phantom model used in this study does not include a contribution from macromolecular magnetization transfer, which may remain as a confounding issue in interpreting changes in CEST metrics *in vivo*. However, macromolecular magnetization transfer effects can be accounted for by CESTR* with measured T_1/T_2 priors by including another pool in the BayCEST fitting algorithm.

One major result of this phantom study is that CESTR* measurement is dependent on a good choice of prior values for T_1 and T_2 times used by the BayCEST fitting algorithm. This dependency implies that there is insufficient information in a single Z-spectrum for the BayCEST algorithm to accurately estimate water T_1 and T_2 times when provided with generic, rather than individually measured, values for the prior distributions. The CESTR* metric with default T_1/T_2 priors has been used to identify the ischemic penumbra in acute stroke patients [48], and to generate quantitative pH maps in healthy volunteers and acute stroke patients [126]. The apparent success of these pH maps (i.e. that the anticipated drop in pH was observed in known stroke regions) may be due to the relative lack of variation in T_1 across the healthy brain and in the acute stage of stroke compared to tumours. In addition, the simulated CESTR* *vs.* pH calibration in that study was generated using a constant amide concentration of 100 mM in both healthy brain and stroke regions.

Assumptions of constant T_1 and amide concentration, however, may not be valid when assessing tumours. Consequently, accurate estimations of both the T_1 relaxation time and labile proton concentration are necessary for reliable pH quantification in tumours using CESTR*. Whilst T_1

is easy to measure *in vivo*, the labile proton concentration is much harder to quantify reliably. This phantom study has shown that CESTR*, with knowledge of the T_1 time and labile proton concentration, provides a means for immediate, quantitative and non-invasive pH measurement, with an accuracy of 0.6 pH units based on the root mean square deviation of Fig. 3.9. However, as the ΔpH measurements in Fig. 3.9 were made on phantoms with known BSA concentration, application of this method *in vivo* is limited. Importantly, the non-significant difference in sensitivities of CESTR* to pH in tumour and normal brain phantoms implies that no manual tumour segmentation should be necessary when evaluating the pH of tumours using CESTR* *in vivo*.

Extracellular pH acidifications of the order of 0.6 pH units are not uncommon in tumours *in vivo* [23]. Though intracellular pH changes of this order are rare, there are numerous cellular environments (mitochondria and other organelles) where the pH is very alkaline, and which may contribute to the CEST signal by virtue of the majority of their protein content being largely mobile [192, 193]. The exact contribution of each of these compartments to the CEST signal measured *in vivo* remains to be elucidated.

3.5 Conclusion

Novel, realistic phantom models of the *in vivo* intracellular environment of brain metastases and naïve mouse brain have been developed to determine an analysis metric for quantification of CEST-MRI data that is sensitive to only labile proton exchange rate and concentration. It has been demonstrated that the CESTR* metric with T_1 and T_2 time compensation overcomes many challenges facing interpretation of CEST MRI data. When combined with prior knowledge of protein concentration, CESTR* with T_1/T_2 compensation allows quantification of pH differences with a mean accuracy of 0.6 pH units. These results suggest that CEST MRI may enable pH differences between tumour and normal tissue to be quantified *in vivo* without the need for exogenous contrast agents.

Chapter 4

Further development of CESTR*

Contents

4.1 Introduction . . . 68
4.2 Methods . . . 69
4.2.1 Simulations . . . 69
4.2.2 Performance of model based analysis & dependency of CESTR* on labile pool parameters . . . 70
4.2.3 Effect of noise on model based analysis . . . 70
4.2.4 *In vivo* dataset . . . 72
4.2.5 Model based analysis of CEST data . . . 72
4.2.6 isoCESTR* method . . . 73
4.3 Results . . . 74
4.3.1 Performance of model based analysis . . . 74
4.3.2 CESTR* is a degenerate metric . . . 80
4.3.3 Effect of noise on model based analysis . . . 84
4.3.4 CESTR* measurements from *in vivo* data . . . 87
4.3.5 Feasibility of isoCESTR* method . . . 88
4.4 Discussion . . . 90
4.5 Conclusion . . . 92

4.1 Introduction

The successful identification of CESTR* as an optimally sensitive and specific analysis metric for CEST MRI data motivates further investigation and development of the model based analysis method. Several studies have already interrogated the ability of the model based analysis to quantify the labile proton concentration and exchange rate from simulated data [125], found an optimal sampling schedule for the model based analysis to accurately quantify the CEST effect [194], evaluated the equivalence of a continuous pulse approximation to pulsed saturation in the model based algorithm [100], and compared the model-based analysis method with other quantification metrics in hyperacute stroke patients [126].

However, the ability of the model based analysis method to quantify labile proton concentration and exchange rate from noisy *in vivo* data has not been investigated thoroughly. Previous studies investigating the accuracy of these parameter estimates found amide proton concentration values in white matter and gray matter of 370 ± 10 mM and 350 ± 20 mM, respectively [125]. However, these estimates disagree with other CEST MRI literature which found amide proton concentrations in the range *ca.* 100 mM [89, 101], and are likely to be an overestimate of the true amide proton concentration, based on biologically plausible and expected values[1].

As was shown in the previous chapter, CESTR* is dependent only on labile proton concentration and exchange rate when analysed with T_1 and T_2 priors set as measured values. This result is also evident from studying the theoretical derivation of the CESTR* metric from the results of the Bayesian model based analysis. BayCEST actually estimates the labile proton concentration and exchange rate directly from the data. Hence, since CESTR* is a secondary output of the Bayesian model, systematic data-driven overestimation of either labile proton concentration or exchange rate may lead to inaccurate quantification of the CEST effect size by CESTR*.

In this chapter, therefore, the accuracy of the labile proton concentration and exchange rate values that are estimated by BayCEST is examined. The accuracy was determined by comparing the model fitted parameter values with ground truth (from simulated data) or biologically plausible values (from *in vivo* data). Subsequently, the relationship between labile proton concentration, exchange rate and calculated CESTR* was investigated, as well as the extent to which CESTR* provides an accurate measurement of the true CEST effect. The extent to which noise in CEST data affects these parameter estimates, and the consequent CESTR* values measured, was investigated, and the suitability of CESTR* as a measurement of true CEST effect size *in vivo* determined. Finally, an extension of the CESTR* analysis metric — isoCESTR* — is introduced, which utilises the understanding of the CESTR* metric and independent measurements to improve the specificity of the CESTR* metric.

[1] A thorough analysis of why this estimate is likely to be biologically implausible is given in Section 5.4.5

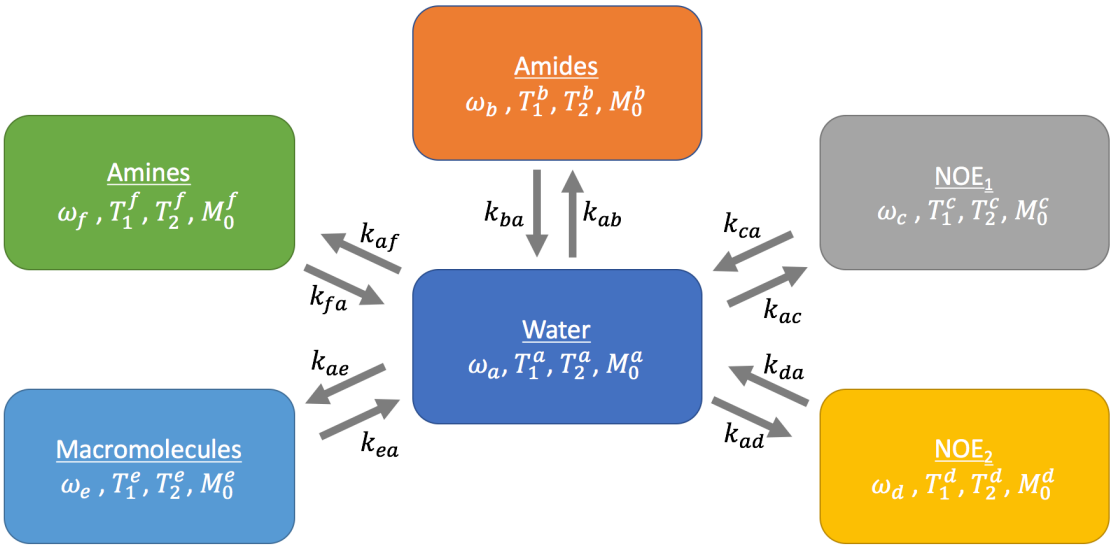

Figure 4.1: Schematic of realistic six pool model used to evaluate dependency of CESTR* on labile pool parameters and evaluate the performance of the BayCEST model based analysis method. Parameter values used are in the main text.

4.2 Methods

4.2.1 Simulations

A realistic six pool model of the *in vivo* intracellular environment probed by CEST MRI was used to generate simulated Z-spectra. A schematic of the six pool model implemented is shown in Fig. 4.1. Simulated data were generated using a numerical solution to the Bloch-McConnell equations assuming a 2 s continuous wave saturation pulse with RF power 0.55 µT in a B_0 field of 9.4 T. A total of $N = 202$ saturation frequencies were simulated, with 200 equally distributed between ± 10 ppm and two used for normalisation of $M_Z = 1$ at ± 300 ppm.

Initially, for the purposes of determining the performance of the BayCEST model based analysis (see Section 4.2.2), amide proton concentration was varied as $M_0^b = 0 - 1000$ mM in steps of 100 mM, and amide proton exchange rate was varied as $k_{ba} = 2.22 - 222$ Hz in logarithmic steps (corresponding to variation of pH between 6 – 8 in steps of 0.2 pH units; conversion between pH and k_{ba} was $k_{ba} = 5.57 \times 10^{pH-6.4}$ [89]) to provide a total of 121 Z-spectra. A second, narrower range of amide proton concentrations ($M_0^b = 50 - 200$ mM in steps of 25 mM) and pH (6.5 – 7.5 in steps of 0.25 pH units) was also used to generate $n = 35$ Z-spectra that reflect the range of parameters expected to be encountered *in vivo*.

4.2.2 Performance of model based analysis & dependency of CESTR* on labile pool parameters

In order to evaluate the performance of the BayCEST algorithm, the labile pool parameters estimated by the BayCEST algorithm were compared to the ground truth values from simulated Z-spectra using the six-pool simulation described in Section 4.2.1. If the BayCEST algorithm accurately measures the true CEST effect size through Bayesian fitting of the Bloch-McConnell equations, the ratio of the estimated amide proton pool parameters to their simulated ground truth values would be equal to 1 over the full range of parameters simulated. The mean ratio of fitted to ground truth parameter values from all simulated Z-spectra was measured and compared to a hypothetical value of 1 using a one-sample t-test.

The performance of the BayCEST algorithm to quantify the CEST effect from *in vivo* data was also assessed by examining the biological feasibility of the labile pool parameters estimated. Section 4.2.4 has further details concerning the acquisition protocol of the *in vivo* data. In addition, goodness of fit between the simulated or *in vivo* data x_i and model fitted Z-spectra y_i was quantified using the residual deviation, shown in equation Eq. 4.1 [195], where N is the number of offset frequencies sampled in the Z-spectrum.

$$RD = 100 \cdot \sqrt{\frac{\sum_i^N (x_i - y_i)^2}{N}} \tag{4.1}$$

As well as investigating the ability of the BayCEST algorithm to accurately fit the amide pool parameters, CESTR* was calculated from the fitted amide proton concentration and exchange rate as described in Section 4.2.5. The dependency of CESTR* on the simulated labile proton concentration and exchange rate was investigated by quantifying CESTR* from each of the 121 simulated Z-spectra generated using the six-pool simulation described in Section 4.2.1. The ability of the BayCEST algorithm to accurately quantify the size of the CEST effect was determined by comparing the measured CESTR* to the ground truth CESTR* from the known simulation parameters. Additionally, to demonstrate the degeneracy of the CESTR* metric, the CESTR* from many combinations of amide proton concentration and exchange rate was measured and a three-dimensional plot of amide proton concentration, exchange rate and CESTR* generated.

4.2.3 Effect of noise on model based analysis

The effect of noise on the results of the model based analysis was investigated by generating noisy simulated Z-spectra to adequately reflect the Z-spectra acquired *in vivo*. Since noise *in vivo* can originate from physiological variation of biophysical parameters between voxels as well as

Name	**Pool A Water**	**Pool B Amides**	**Pool C NOE 1**	**Pool D NOE 2**	**Pool E MT**	**Pool F Amines**
ω_i (ppm)	0	3.5	-3.0	-1.6	-2.30	2.0
M_0^i (mM)	112000	120 ± 10	800 ± 10	400 ± 10	11200 ± 200	35 ± 3
k_{ia} (Hz)	-	28 ± 3	50 ± 0	50 ± 0	13 ± 3	410 ± 50
T_1^i (s)	1.60 ± 0.15	1 ± 0	1 ± 0	1 ± 0	1 ± 0	1 ± 0
T_2^i (ms)	42 ± 3	2 ± 0	0.5 ± 0	1 ± 0	$(7.5 \pm 2) \times 10^{-3}$	10 ± 0

Table 4.1: Simulation parameters used in the Monte Carlo simulation of Z-spectra to realistically reflect the physiological noise affecting *in vivo* data.

inherent random noise in the system, both sources of variation are included in the simulated data.

A Monte Carlo approach to simulating Z-spectra was adopted to accurately model the physiological variation present *in vivo*. Each parameter in the Bloch-McConnell equations was defined by a normal distribution and many instances of the simulation repeated. For each instance of the simulation, the parameters were selected randomly from their defined normal distributions. The mean and standard deviation of the normal distributions for each parameter in the six pool model is shown in Table 4.1. Parameters were selected based on previous literature [89, 117, 125, 126, 196, 197]. The number of instances (200) was chosen to reflect the typical size of a region of interest used in *in vivo* analysis.

Random noise was added by adding a random offset η to each Z-spectrum data point using Eq. 4.2, where ε is a user-defined noise level normalised to the unsaturated water signal M_Z. Noise levels of $\varepsilon = 0$, 1, 2, 3, 4, 5, 6, 7, 8, 9, 10, 15, 20, 25, 30, 35 were studied, each with 200 Z-spectra, to determine the value of ε at which the model based analysis can no longer adequately quantify CEST effects.

$$\eta = \frac{\varepsilon}{2} \cdot (\text{rand}[0, 1] - 1) \tag{4.2}$$

All 3200 Z-spectra (200 instances $\times$ 16 ε values) were analysed with the BayCEST algorithm with amide proton concentration prior information included (see Section 4.2.5). The model fitted parameters were compared to the ground truth values for all 3200 Z-spectra, and the goodness of fit of the fitted Z-spectrum to the raw data quantified by Eq. 4.1.

4.2.4 *In vivo* dataset

An *in vivo* dataset was used to examine the accuracy of the model fitted values for labile proton concentration and exchange rate. The *in vivo* dataset was obtained from a Berlin Druckrey IX (BDIX) rat implanted with 1×10^6 ENU1506 cells via intracerebral injection into the left striatum of the brain (injection volume 1 µl, injection co-ordinates 1 mm anterior, 3 mm lateral from bregma, 3.5 mm depth). The CEST MRI pulse sequence was identical to that simulated, with the exception of a pulsed saturation scheme being used instead of continuous wave. The pulsed saturation scheme was made up of 50 saturation pulses, each one comprising a 20 ms gaussian RF pulse with flip angle $184°$ followed by a 20 ms crusher gradient, for a total saturation duration of 2 s with equivalent continuous wave RF power 0.55 µT. Following saturation, an EPI readout with FOV = $32\,\mathrm{mm} \times 32\,\mathrm{mm}$ measured the Z-magnetisation. Other sequence parameters were TR = $5\,\mathrm{s}$, TE $= 27\,\mathrm{ms}$, 1 average, 10 slices, slice thickness $= 2\,\mathrm{mm}$, in-plane resolution $500\,\mu\mathrm{m} \times 500\,\mu\mathrm{m}$. A total of 51 measurements were made following saturation at the following offset frequencies relative to water: -300, -4.1, -3.8, -3.5, -3.2, -2.9, -2.6, -2.3, -2, -1.7, -1.5, -1.2, -0.9, -0.6, -0.3, 0, 0.3, 0.6, 0.9, 1.2, 1.5, 1.6, 1.7, 1.8, 1.9, 2, 2.1, 2.4, 2.7, 2.9, 3.1, 3.2, 3.3, 3.4, 3.5, 3.6, 3.7, 3.8, 3.9, 4.1, 5, 7, 9.7, 13.5, 19, 26, 37, 51, 72, 100, 300 ppm.

In addition, T_1 and T_2 relaxation times were determined voxelwise using inversion recovery (TR = 10 s, TE = 8.22 ms, inversion time (TI) varied in 9 steps from 13.14 ms to 8 s, signals fitted to $M_Z = M_0\left(1 - 2e^{-\frac{\mathrm{TI}}{T_1}}\right)$) and spin echo (TR = 10 s, TE varied in 10 steps from 30 ms to 160 ms, signals fitted to $M_Z = M_0 e^{-\frac{\mathrm{TE}}{T_2}}$) experiments, respectively. In both cases the same spin-echo EPI readout used for CEST imaging was used to acquire images.

4.2.5 Model based analysis of CEST data

All Z-spectra were analysed using the Bayesian model based analysis method (BayCEST), whereby data are fit to the Bloch-McConnell equations with each parameter assigned a Bayesian prior value and an associated precision. Simulated and *in vivo* data were fit to a three pool model comprising water protons, amide protons with a resonance frequency 3.5 ppm upfield from water, and a pool with resonance frequency –2.41 ppm representing the combination of MT and NOE effects. Two versions of the BayCEST model were implemented: one with prior values defined for the exchange rate, T_1 time and T_2 time of each pool (the 'original' BayCEST algorithm), and one which also defined a prior value on the amide proton concentration of 100 mM with precision 204 mM (the 'new' BayCEST algorithm).

CESTR* was then calculated by simulating an ideal two pool system comprising water and the labile pool of interest. In all cases in this chapter, CESTR* at 3.5 ppm for amide protons is reported. Since the results of the previous chapter show that CESTR* is only a good estimator of

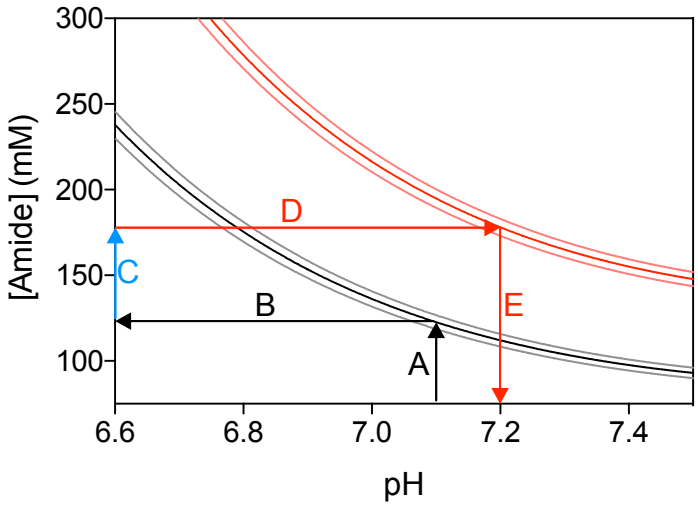

Figure 4.2: Demonstration of the generalised isoCESTR* method. The solid black and red lines represent mean CESTR* values from two tissue regions, and dashed lines are the 95% CI on these mean values. Assuming a pH in tissue region 1 (arrow A), the amide proton concentration of tissue 1 can be estimated from the measured CESTR* (arrow B). By measuring the difference in amide proton concentration between the two tissue regions independently of CEST MRI (arrow C), it is then possible to use the CESTR* in tissue region 2 (arrow D) to estimate the pH of tissue region 2 (arrow E).

the CEST effect size when analysed with accurate T_1 and T_2 prior information, each simulated Z-spectrum was analysed with T_1 and T_2 priors set equal to the actual value it was simulated with. T_1 and T_2 priors for *in vivo* data were set based on the average T_1 and T_2 time in the whole brain. In both simulated and *in vivo* data analysis, T_1 and T_2 were left as parameters to be estimated by the model. *In vivo* data were analysed voxelwise, but with T_1 and T_2 priors the same for each voxel.

4.2.6 isoCESTR* method

In order to enable quantification of the underlying physiological parameters that contribute to CESTR*, an extension to the analysis method — isoCESTR* — was developed. The isoCESTR* method is summarised in Fig. 4.2. The isoCESTR* lines represent the mean (solid line) and 95% CI (dotted line) of CESTR* measurements from two tissue regions. Assuming a pH in tissue region 1, the amide proton concentration of tissue 1 can be estimated from the measured CESTR*. By measuring the difference in amide proton concentration between the two tissue regions independently of CEST MRI, it is then possible to use the CESTR* in tissue region 2 to estimate the pH of tissue region 2. To be able to find isoCESTR* lines in amide proton concentration/pH space, over 500,000 noise-free Z-spectra were simulated using varying amide proton concentration and pH, and CESTR* calculated from each.

	Healthy Brain — pH 7.10					
Name	**Pool A Water**	**Pool B Amides**	**Pool C NOE 1**	**Pool D NOE 2**	**Pool E MT**	**Pool F Amines**
ω_i (ppm)	0	3.5	-3.0	-1.6	-2.30	2.0
M_0^i (mM)	112000 ± 0	120 ± 10	800 ± 10	400 ± 10	11200 ± 200	35 ± 3
k_{ia} (Hz)	-	28 ± 3	50 ± 0	50 ± 0	13 ± 3	410 ± 50
T_1^i (s)	1.60 ± 0.15	1 ± 0	1 ± 0	1 ± 0	1 ± 0	1 ± 0
T_2^i (ms)	42 ± 3	2 ± 0	0.5 ± 0	1 ± 0	$(7.5 \pm 2) \times 10^{-3}$	10 ± 0

Table 4.2: Parameters for simulation of healthy brain tissue. The exchange constants k_{ba} and k_{fa} (i.e. amides and amines) were determined from the defined pH.

	Tumour — pH 7.20					
Name	**Pool A Water**	**Pool B Amides**	**Pool C NOE 1**	**Pool D NOE 2**	**Pool E MT**	**Pool F Amines**
ω_i (ppm)	0	3.5	-3.0	-1.6	-2.30	2.0
M_0^i (mM)	112000 ± 0	168 ± 20	1120 ± 50	560 ± 25	5200 ± 200	49 ± 3
k_{ia} (Hz)	-	35 ± 3	50 ± 0	50 ± 0	20 ± 3	520 ± 50
T_1^i (s)	2.30 ± 0.20	1 ± 0	1 ± 0	1 ± 0	1 ± 0	1 ± 0
T_2^i (ms)	35 ± 3	2 ± 0	0.5 ± 0	1 ± 0	$(12.5 \pm 2) \times 10^{-3}$	10 ± 0

Table 4.3: Parameters for simulation of tumour tissue. The exchange constants k_{ba} and k_{fa} (i.e. amides and amines) were determined from the defined pH.

The feasibility of this general method was determined by applying it to realistic simulations of healthy brain and tumour tissue. The simulations comprised the same six pool model as used in Fig. 4.1, but with simulation parameters altered to realistically reflect healthy brain and tumour tissue. The values assigned to each parameter were defined as normal distributions in a similar way to the simulations of Section 4.2.3, and a single random noise level of $\varepsilon = 10$ used. Parameters for healthy brain and tumour simulations are shown in Table 4.2 and Table 4.3, respectively, and are taken from literature [89, 117, 125, 126, 196, 197].

4.3 Results

4.3.1 Performance of model based analysis

In order to evaluate the performance of the BayCEST algorithm, the fitted labile pool parameters were compared to the ground truth values from the six pool simulation described in Fig. 4.1. Z-spectra (total $n = 121$) were simulated for every combination of parameters within a range of pH values (6.0 – 8.0 , $n = 11$) and amide proton concentrations (0 – 1000 mM, $n = 11$). Figure 4.3

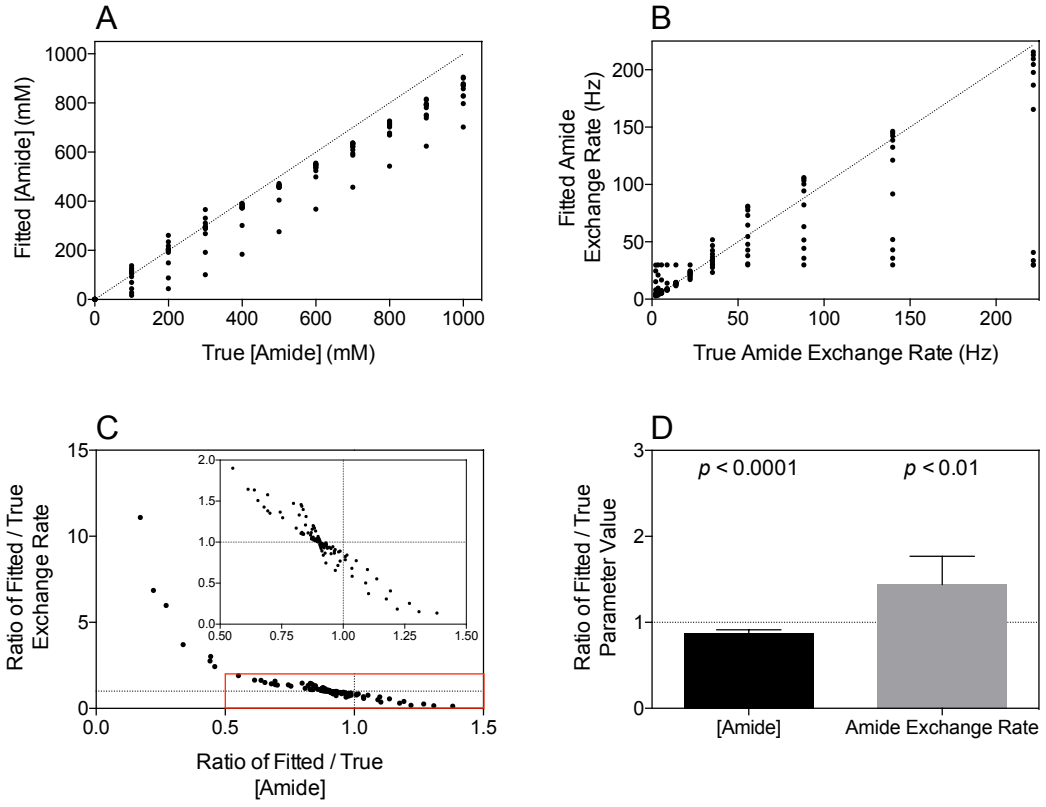

Figure 4.3: Comparison of fitted and true parameter values for amide proton concentration (A) and exchange rate (B) for all 121 Z-spectra simulated. An inverse correlation between the ratio of estimated amide proton concentration and exchange rate to their ground truth values is measured (C), and over the full range of parameters simulated the BayCEST algorithm systematically underestimates amide proton concentration and overestimates amide proton exchange rate (D).

shows the relationships between fitted and ground truth values of amide proton concentration (Fig. 4.3A) and exchange rate (Fig. 4.3B) for all 121 Z-spectra, as well as the identity line. Figure 4.3C demonstrates an inverse correlation between the ratio of estimated amide proton concentration and exchange rate to their ground truth values — the greater the underestimation of amide proton concentration, the greater the overestimation of amide proton exchange rate. If the BayCEST algorithm were performing well, a cluster of data points centred on the ordinate (1,1) would be expected. Figure 4.3D shows that over the full range of parameters simulated, amide proton concentration was significantly underestimated (mean $\pm$ 95% CI = 0.88 ± 0.04, $p < 0.0001$ for t-test comparing to a hypothetical value of 1) and amide proton exchange rate significantly overestimated (mean $\pm$ 95% CI = 1.4 ± 0.3, $p < 0.01$ for t-test comparing to a hypothetical value of 1).

The BayCEST algorithm was subsequently applied to *in vivo* data in order to evaluate the ability of CESTR* to adequately measure the size of CEST effects *in vivo*. The measured CESTR*

map from the example *in vivo* data is shown in Fig. 4.4A, along with parameter value maps for amide proton concentration (Fig. 4.4B) and exchange rate (Fig. 4.4C). A residual deviation map is shown in Fig. 4.4D to demonstrate the goodness of fit of the model across the brain.

The average amide proton concentration that is estimated by the BayCEST algorithm was $1 \pm 2\,\mathrm{M}$ (mean $\pm$ s.d., Fig. 4.4B), while the average amide exchange rate was $20 \pm 9\,\mathrm{Hz}$ (mean $\pm$ s.d., Fig. 4.4C) corresponding to a pH of 7.0 ± 0.2. An amide proton concentration this high *in vivo* is biologically implausible and is likely an overestimate of the true value. Similarly the estimated pH from the amide exchange rate is likely an underestimate of the true *in vivo* pH, though is, at least, in a biologically realistic range. This underestimate of exchange rate is expected from the inverse correlation between estimated exchange rate and concentration seen in Fig. 4.3C. The average residual deviation (RD) was $RD = 4 \pm 2\%$ (mean $\pm$ s.d.), demonstrating an acceptable model fitting performance across the brain.

The biologically implausible overestimate of amide proton concentration casts doubt over the accuracy of the resulting CESTR* value as a descriptor of the true *in vivo* CEST effect. However, since the fitted amide proton concentration values are an output from a Bayesian model fitting algorithm, the model may be improved with an informative prior value of the expected amide proton concentration with an associated uncertainty on this estimate. A new version of the BayCEST algorithm, with an informative prior estimate of amide proton concentration of $100 \pm 204\,\mathrm{mM}$ (mean $\pm$ s.d.), was compiled and used to analyse the same *in vivo* dataset shown in Fig. 4.4. The results of the new analysis of *in vivo* data are shown in Fig. 4.5.

The new BayCEST algorithm applied to the same *in vivo* dataset outputs an average amide proton concentration of $300 \pm 100\,\mathrm{mM}$ (mean $\pm$ s.d.) and an average amide exchange rate of $40 \pm 10\,\mathrm{Hz}$ (mean $\pm$ s.d.), corresponding to a pH of 7.3 ± 0.1. Crucially, the model fitted Z-spectra in each voxel are still good fits to the raw data, with a residual deviation calculated using Eq. 4.1 of $RD = 4 \pm 2\%$ (compared to $RD = 4 \pm 2\%$ for the original BayCEST algorithm).

Obviously, because an *in vivo* dataset is being analysed, it is impossible to know the ground truth amide proton concentration and exchange rate values that should be returned by the BayCEST algorithm. However, it can be determined whether adding a prior estimate of amide proton concentration affects the accuracy of the model fit by applying the new BayCEST algorithm to simulated data where the ground truth values are known.

The new BayCEST algorithm with an informative prior amide proton concentration value was used to fit simulated data generated using the six-pool model, and an analysis identical to Fig. 4.3 performed. The results of this analysis are shown in Fig. 4.6, demonstrating that the new BayCEST algorithm has an additional bias introduced to the modelling process from the prior

amide proton concentration information. The amide proton concentration is underestimated and the amide proton exchange rate overestimated to a greater extent than with the original BayCEST algorithm across the entire range of simulated Z-spectra (Fig. 4.6).

However, it should be noted that the ranges of parameters simulated in Fig. 4.3 and Fig. 4.6 do not adequately represent the environments encountered *in vivo*. The amide proton concentration *in vivo* has been approximated as 100 mM, while the *in vivo* pH is tightly regulated to within a narrow range within healthy tissue (pH 7.0 – 7.2), which implies the amide proton exchange rate is equally stable. Even in diseased tissue, amide proton concentration is likely to stay within the range 50 – 200 mM, and pH will remain regulated to within pH 6.5 – 7.5

This narrower range of biologically plausible amide proton parameters was used to simulate another $n = 35$ Z-spectra and the model performance analysis repeated to determine the performance of the BayCEST algorithm within a more realistic range of parameters. Figure 4.7 shows the performance of the new BayCEST algorithm with informative prior information on the amide proton concentration, demonstrating that the algorithm estimates amide pool parameters accurately over the full range of biologically plausible parameters (Fig. 4.7D). In particular, the fitted amide proton concentrations in Fig. 4.7A show good agreement with the identity line. An inverse correlation between the ratio of estimated amide proton concentration and exchange rate to their ground truth values is still measured (Fig. 4.7C).

For completeness, the original BayCEST algorithm without informative prior information on the amide proton concentration was also used to analyse the simulated data generated in a biologically realistic parameter range. The result of this analysis is shown in Fig. 4.8. The similarity of Fig. 4.7 and Fig. 4.8 implies that the inclusion of the amide proton concentration prior in the new BayCEST algorithm does not significantly alter the modelling process within the range of parameters encountered *in vivo*.

In summary, the performance of the BayCEST model-fitting procedure has been evaluted by determining the accuracy of the model-fitted parameters compared to simulated ground-truth values. Two BayCEST algorithms have been used, one with informative prior information of the amide proton concentration (the 'new' BayCEST algorithm) and one without (the 'original' BayCEST algorithm). Over a wide range of parameters, both algorithms performed poorly, underestimating amide proton concentration and overestimating exchange rate. Over a narrower range of parameters encountered *in vivo*, both algorithms performed well, accurately estimating both amide proton concentration and exchange rate. However, when applied to actual *in vivo* data, only the new BayCEST algorithm returned amide proton concentration values that are physiologically feasible. This result suggests that the noise in the *in vivo* data drives overestimation of the amide proton concentration when analysed using the old BayCEST algorithm.

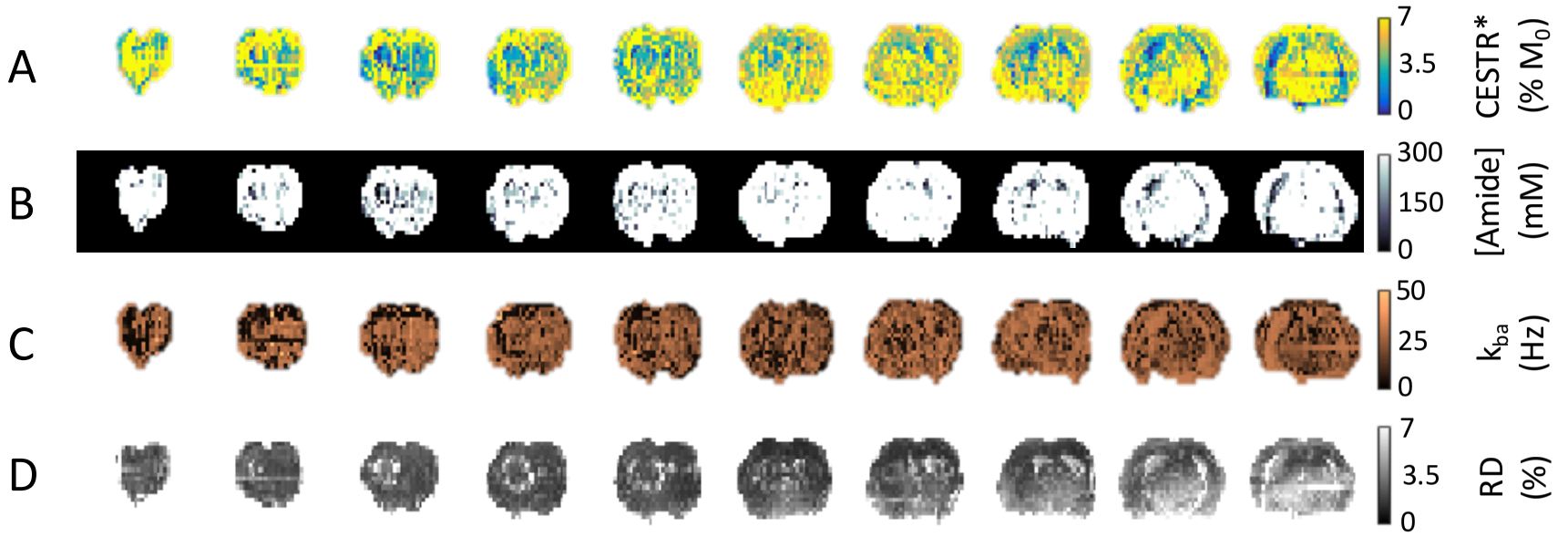

Figure 4.4: CESTR* (A), amide concentration (B), and amide exchange rates (C) estimated from the BayCEST algorithm applied to *in vivo* data. The residual deviation (D) shows acceptable goodness of fit across the brain, but the estimated amide concentration (B) is far above physiologically relevant values.

Figure 4.5: CESTR* (A), amide concentration (B), and amide exchange rates (C) estimated from the same *in vivo* data analysed in Fig. 4.4 analysed with the new BayCEST algorithm with amide proton concentration information included. The residual deviation (D) is still as good as the original algorithm, but the estimated amide pool parameters are in a more biologically realistic range.

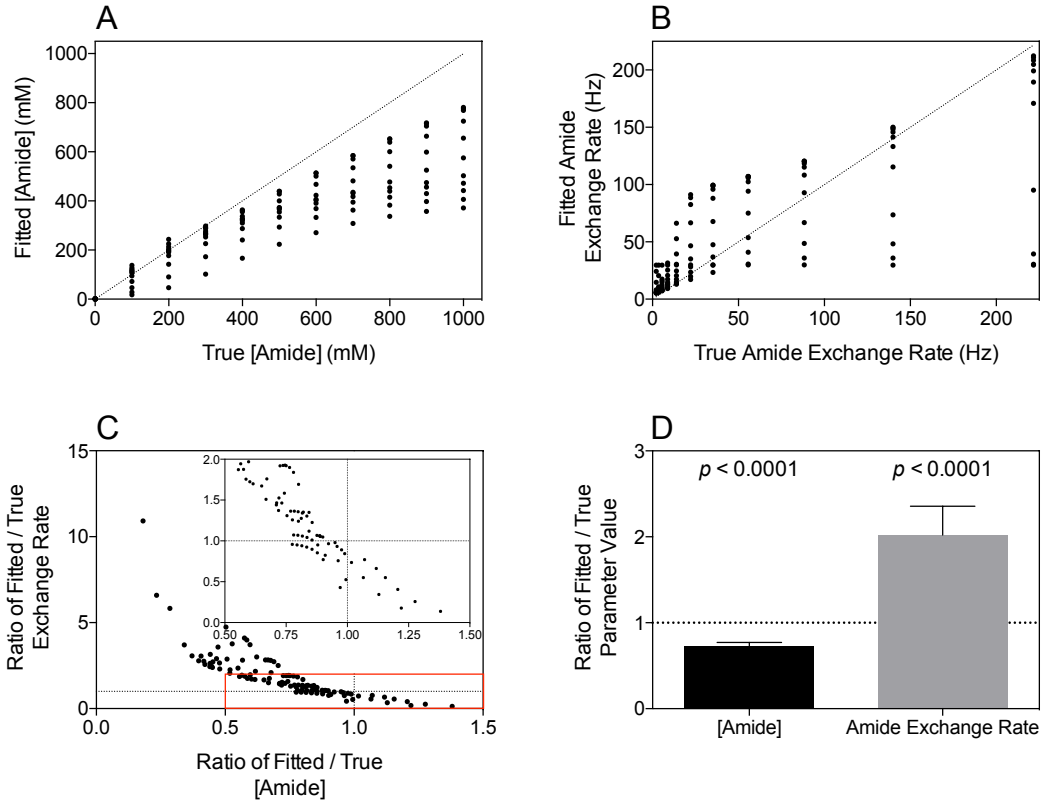

Figure 4.6: Comparison of fitted and true parameter values for amide proton concentration (A) and exchange rate (B) for all 121 Z-spectra simulated analysed using a BayCEST algorithm with informative prior information for the amide proton concentration. An inverse correlation between the ratio of estimated amide proton concentration and exchange rate to their ground truth values is still measured (C), and the additional prior information in the new BayCEST algorithm leads to greater underestimation of the amide proton concentration and greater overestimation of the amide proton exchange rate from simulated Z-spectra over a wide range of amide proton parameters (D).

4.3.2 CESTR* is a degenerate metric

Figure 4.9 shows the variation of CESTR* as a function of simulated amide proton concentration for different exchange rates (Fig. 4.9A) and exchange rate with different concentrations (Fig. 4.9B) in the simulated model. CESTR* monotonically grows linearly as a function of simulated amide proton concentration up to 1 M. Conversely, CESTR* exponentially approaches a fixed maximum value as a function of amide proton exchange rate. The gradient of the monotonic linear relationship between CESTR* and amide proton concentration is in turn dependent on the amide proton exchange rate, and the plateau CESTR* value reached when increasing amide proton exchange rate depends on the amide proton concentration.

It is evident from Fig. 4.9 that CESTR* is a degenerate metric — many combinations of simulated amide proton concentration and exchange rate will result in the same measured CESTR* value.

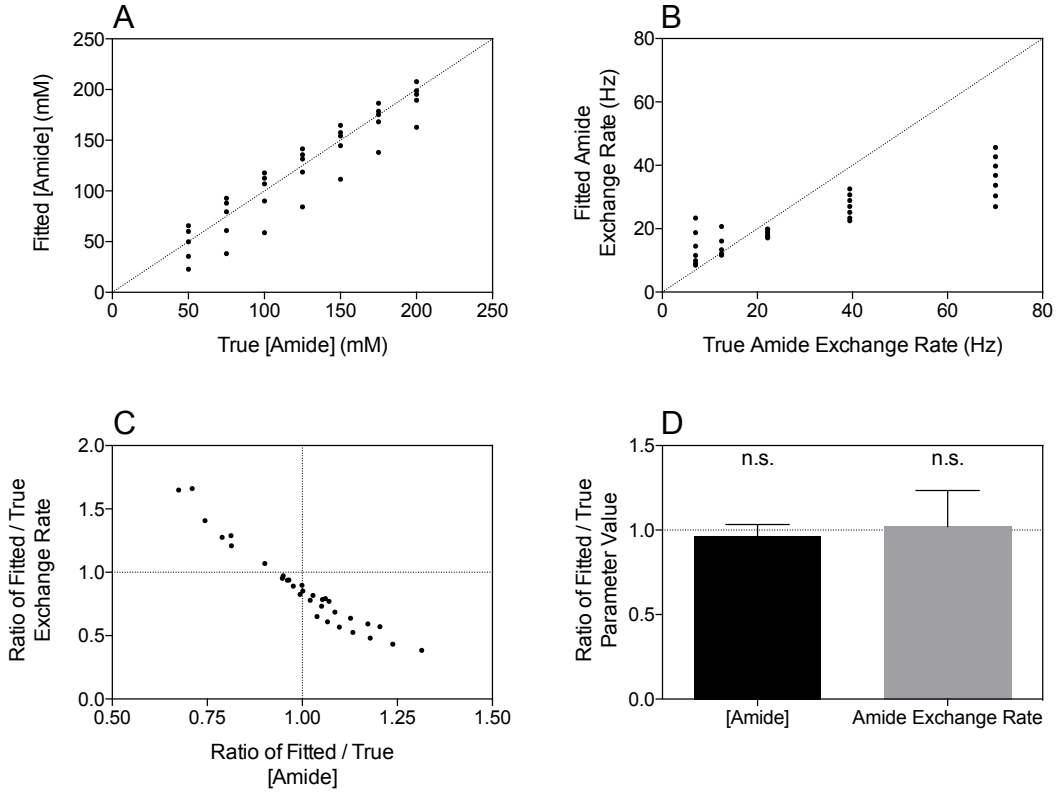

Figure 4.7: Comparison of fitted and true parameter values for amide proton concentration (A) and exchange rate (B) for 35 Z-spectra in a biologically plausible parameter range, analysed using the new BayCEST algorithm with informative prior information for the amide proton concentration. In particular, the fitted amide proton concentrations in (A) show good agreement with the identity line. An inverse correlation between the ratio of estimated amide proton concentration and exchange rate to their ground truth values is still measured (C), though within a narrower range than those seen in Fig. 4.3 and Fig. 4.6. Over the full parameter range, both the amide proton concentration and exchange rate are accurately estimated (D).

Figure 4.10 demonstrates this clearly, where arcing lines of constant CESTR* (henceforth referred to as 'isoCESTR* lines'[2]) can be delineated.

The degenerate behaviour of CESTR* as a function of amide proton concentration and exchange rate is a result of the manner in which the CESTR* metric is calculated. The amide proton concentration and exchange rate are parameters directly estimated by the BayCEST algorithm. Hence, as the simulated amide proton concentration increases, we expect the fitted amide proton concentration to also increase and cause a consequential increase in CESTR*. Similarly as the amide proton exchange rate varies, the BayCEST estimated exchange rate should also vary. However, in the current measurement paradigm where, for example, differences in CESTR* between pathological and normal tissue are measured, it is impossible to be able to determine

[2]In the same manner as lines of constant pressure are known as isobars, and lines of constant temperature are known as isotherms in meterology.

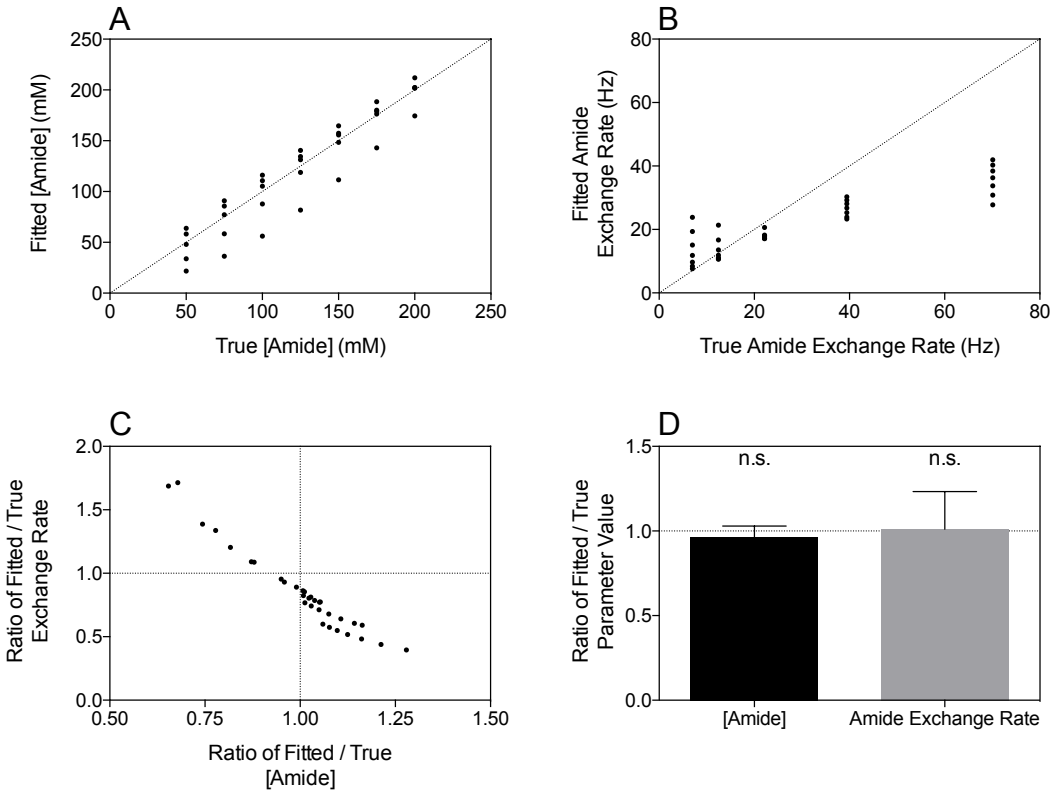

Figure 4.8: Comparison of fitted and true parameter values for amide proton concentration and exchange rate for 35 Z-spectra in a biologically plausible parameter range, analysed using the original BayCEST algorithm. The original BayCEST algorithm estimates amide pool parameters accurately, demonstrating that no additional bias has been introduced to the modelling process by adding a prior value to the amide proton concentration.

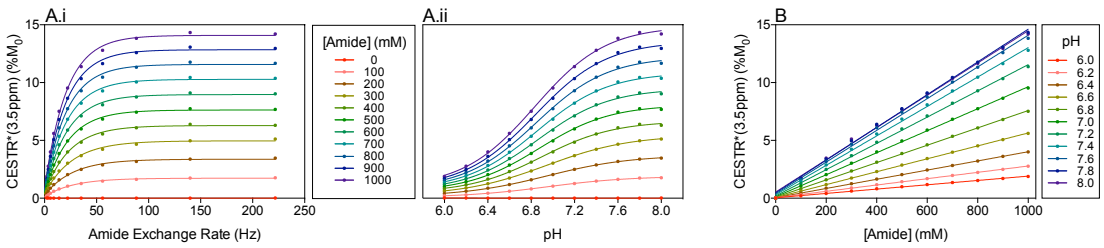

Figure 4.9: Variation of CESTR* as a function of amide proton exchange rate for different concentrations (A.i), pH for different concentrations (A.ii), and amide concentrations for different pH/exchange rates (B). Lines in the graphs show either the fitted exponential growth (A.i,ii) or linear (B) curve.

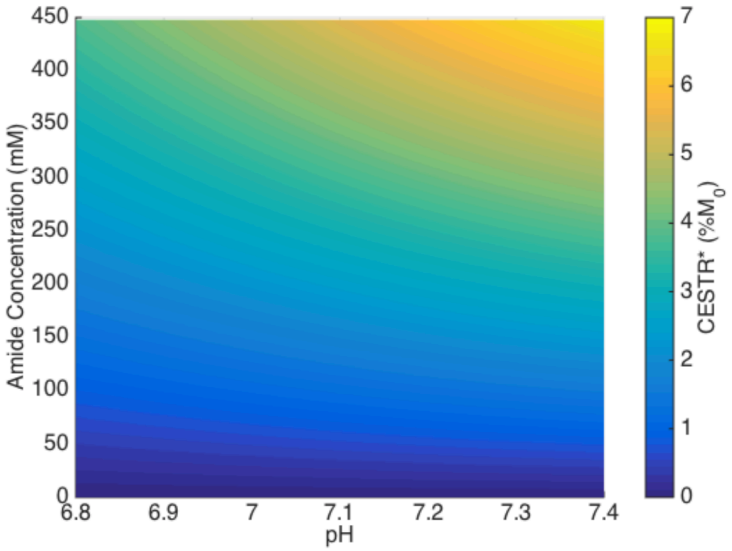

Figure 4.10: CESTR* is a degenerate metric — many different combinations of simulated amide proton concentration and exchange rate lead to the same measured CESTR* value.

whether the change in CESTR* is a change in labile proton concentration or exchange rate. Thus, it becomes important to establish whether CESTR* accurately reflects the true size of the CEST effect.

Figure 4.11 shows the comparison between the calculated and true CESTR* values for the 121 parameter combinations simulated for the two BayCEST algorithms used in Section 4.3.1. Both models fail to accurately estimate the true CESTR* (derived based on the known simulation parameters) over the full range of parameters simulated. However, in the range of parameters expected *in vivo* (the same range used in Fig. 4.7 and Fig. 4.8), which approximately corresponds to $0\,\%\,\mathrm{M}_0 <$ CESTR* $< 7\,\%\,\mathrm{M}_0$, both models perform equally well and accurately measure the true CESTR* in simulated data.

Figure 4.11 demonstrates that CESTR* is a degenerate but consistent metric to accurately quantify the size of CEST effects. However, different CESTR* values were measured from the *in vivo* dataset used in Section 4.3.1 depending on the BayCEST algorithm used to analyse the same data. Since both algorithms seem to accurately measure the true CEST effect size, and accurately determine the amide proton concentration and exchange rate in simulated data corresponding to the range expected *in vivo*, the difference in measured CESTR*, amide proton concentration and exchange rate observed *in vivo* likely derives from the additional noise in *in vivo* data that is not present in simulated data.

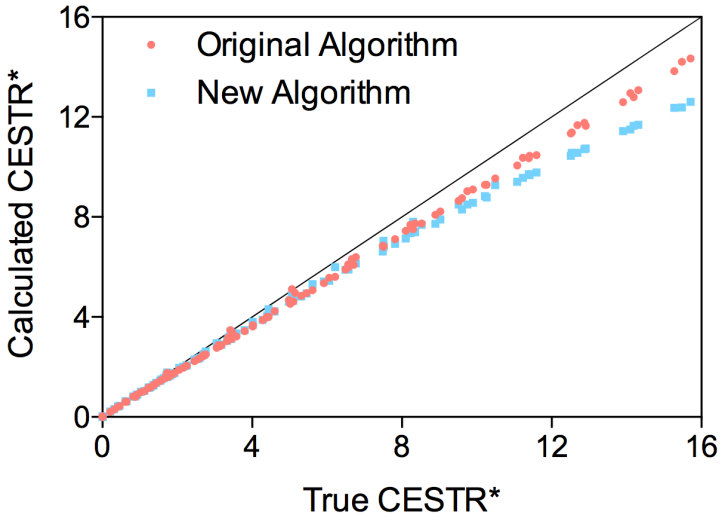

Figure 4.11: Comparison between CESTR* measured using the original or new BayCEST algorithm and the true CESTR* determined from the known ground truth simulation parameters. The simulation parameters were the same as those used in Fig. 4.9, generating 121 individual Z-spectra over a wide range of amide proton concentration and exchange rates.

4.3.3 Effect of noise on model based analysis

The effect of noise in data analysed using the BayCEST algorithm was determined by adding random noise to Z-spectra simulated using the Monte Carlo approach outlined in Section 4.2.3, and evaluating the variability in amide proton concentration, exchange rate and CESTR*. Examples of raw clean data, noisy data, and the model fitted Z-spectra are shown in Fig. 4.12 for $\varepsilon = 0, 3, 10, 20, 35$. Noise levels of $\varepsilon > 35$ were not investigated as the noise masked any clear CEST effects (Fig. 4.12). This exercise was repeated for both the original and new BayCEST algorithms.

Assuming that the CESTR* measured with $\varepsilon = 0$ is the best estimate of CESTR*, and evaluating the accuracy of the CESTR* estimate derived from the new BayCEST algorithm relative to this value, it is clear that as ε increases the measured CESTR* remains accurate up to $\varepsilon = 35$, but with decreasing precision (Fig. 4.13A). The origin of this decrease in precision can be attributed to the decreased precision on the estimated amide proton concentration as ε increases (Fig. 4.13B). The estimated CESTR* for all ε values up to $\varepsilon = 25$ is not significantly different from the $\varepsilon = 0$ value (one-way ANOVA followed by Dunnett's multiple comparison test comparing CESTR* at each ε noise level to CESTR* with $\varepsilon = 0$, $p > 0.05$). For $\varepsilon = 30$, CESTR* is significantly overestimated ($p < 0.05$ with Dunnett's multiple comparison correction).

While CESTR* measured using the new algorithm was not significantly different from the $\varepsilon = 0$ value up to $\varepsilon = 25$, a similar statistical comparison of CESTR* measurements from the original BayCEST algorithm showed that at $\varepsilon = 7$ the CESTR* measured was significantly lower

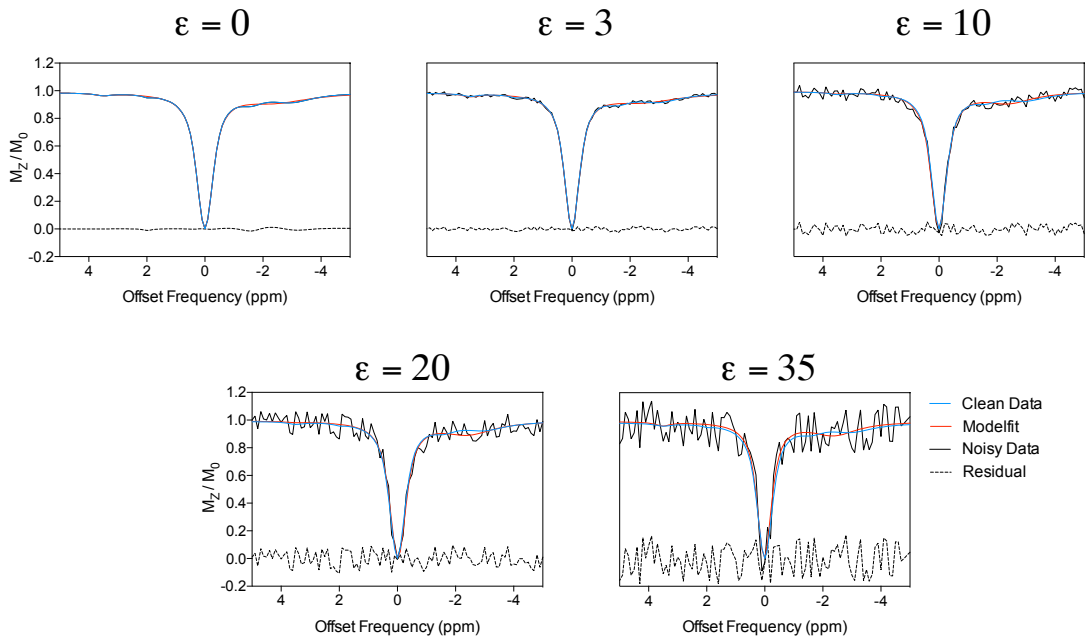

Figure 4.12: Example of typical simulated Z-spectra, with random noise added, for five different random noise levels ε.

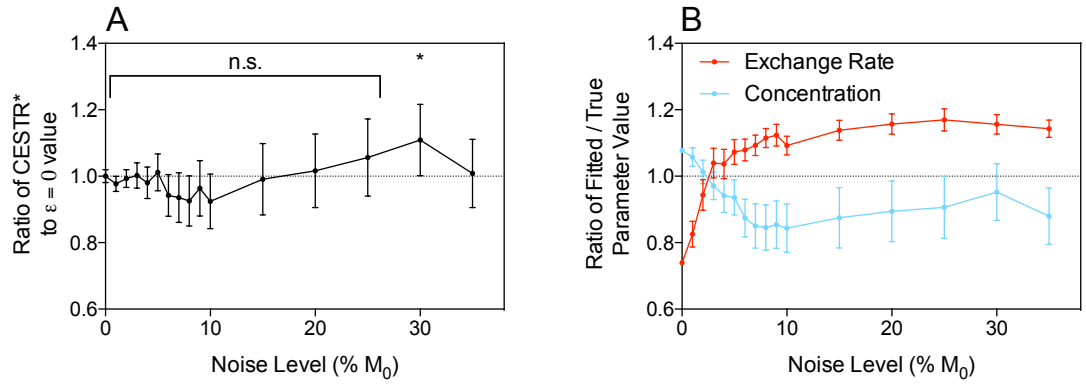

Figure 4.13: Ratio of CESTR* calculated using the new BayCEST algorithm relative to the value calculated with $\varepsilon = 0$ vs. noise level (A) indicating that while the precision of the estimated CESTR* decreases as ε increases, the accuracy of the CESTR* value is retained until $\varepsilon = 30$. The decrease in precision can be attributed to the decreased precision on the estimated amide proton concentration and exchange rate (B). Error bars are 95% CI on the mean value measured from $n = 200$ Z-spectra. * and n.s. signify $p < 0.05$ and $p > 0.05$, respectively, from one-way ANOVA followed by Dunnett's multiple comparison test comparing CESTR* at each ε noise level to CESTR* with $\varepsilon = 0$.

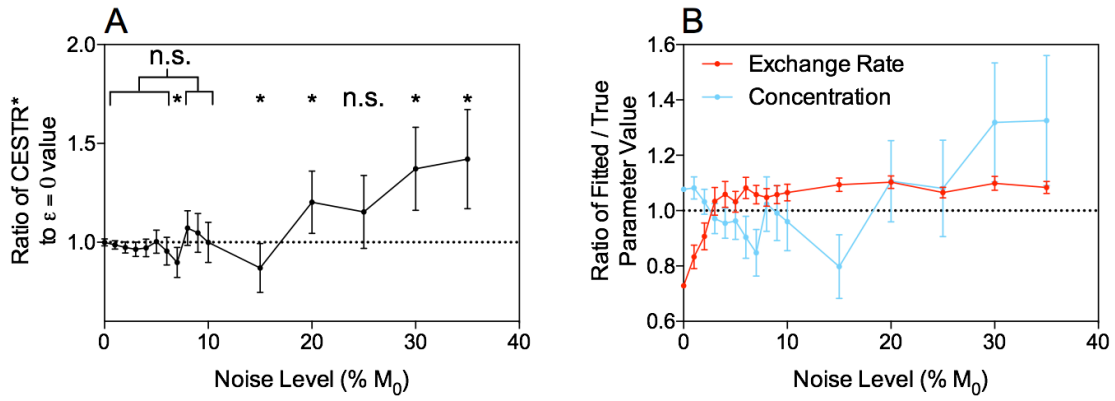

Figure 4.14: Ratio of CESTR* calculated using the old BayCEST algorithm relative to the value calculated with $\varepsilon = 0$ vs. noise level (A) indicating that, similar to the new BayCEST algorithm the precision of the estimated CESTR* decreases as ε increases. However, the measured CESTR* is no longer accurate for $\varepsilon = 7$, indicating that the old BayCEST algorithm handles noisy data much more poorly than the new BayCEST algorithm. The decrease in precision an inaccurate estimate of CESTR* can be attributed to the decreased precision and inaccurate estimate of the estimated amide proton concentration and exchange rate (B). Error bars are 95% CI on the mean value measured from $n = 200$ Z-spectra. * and n.s. signify $p < 0.05$ and $p > 0.05$, respectively, from one-way ANOVA followed by Dunnett's multiple comparison test comparing CESTR* at each ε noise level to CESTR* with $\varepsilon = 0$.

than the $\varepsilon = 0$ value (Fig. 4.14A). Additionally, CESTR* was underestimated when $\varepsilon = 15$, and overestimated when ε =20, 30, 35. These results suggest that the original BayCEST algorithm is much less robust to measuring accurate CESTR* values from noisy data, which explains the overestimation of amide proton concentration (and subsequent inaccurate CESTR* measurement) from the noisy *in vivo* data in Fig. 4.4.

Figure 4.13B and Fig. 4.14B reveal the inverse relationship between the estimated amide proton concentration and exchange rate, which was found in a previous study of the model based analysis in non-noisy data [125]. The inverse relationship is present at all values of ε, but 'crosses over' at $\varepsilon = 3$ in both models, where the amide proton concentration and exchange rate are both estimated with maximal accuracy. This effect is likely an artefact of the non-linearity of the Bayesian model used to estimate the concentration and exchange rate.

Since the new BayCEST algorithm was more resilient to the noise in *in vivo* datasets, this algorithm was used to establish a threshold RD. The RD between the model fitted Z-spectrum and simulated data increases as ε increases, as expected (Fig. 4.15). The RD is not 0 for a noise level of 0 because the simulated Z-spectrum is simulated with 6 pools, but the BayCEST algorithm only fits 3 pools, reflecting the way that we would interrogate *in vivo* data without *a priori* knowledge of the proton pools in the tissue. This effect is shown by the non-zero residual plot in the $\varepsilon = 0$ plot of Fig. 4.12.

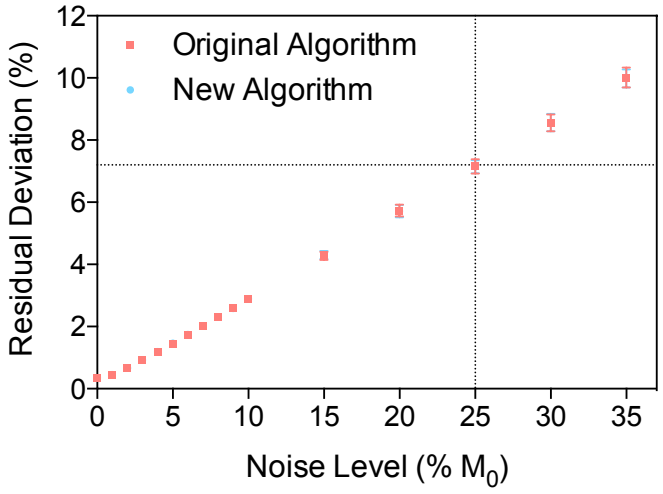

Figure 4.15: RD vs ε showing the expected increase in RD as ε increases. The threshold RD value of $RD = 7.2 \pm 0.2\%$ is derived from this being the RD value for $\varepsilon = 25$, the last ε value for which CESTR* is still accurately estimated in Fig. 4.13A.

The threshold RD value was defined corresponding to the minimum ε value that results in a significantly different CESTR* estimation from the CESTR* estimate with $\varepsilon = 0$. Since CESTR* is only significantly overestimated at $\varepsilon = 30$, the threshold RD value is $RD = 7.2 \pm 0.2\,\%$, which corresponds to $\varepsilon = 25$. If the original BayCEST algorithm results were used to define a threshold RD value, the result would be $RD = 1.75 \pm 0.06\,\%$ corresponding to $\varepsilon = 6$. This value is lower than the average RD calculated from the *in vivo* dataset in Fig. 4.4 ($RD = 4 \pm 2\,\%$), suggesting that the CESTR*, amide proton concentration and exchange rate calculated from *in vivo* data using the original BayCEST algorithm are indeed inaccurate.

4.3.4 CESTR* measurements from *in vivo* data

The results of the previous section have shown that noise affects the accuracy of the model fitted parameters, but not necessarily the resulting CESTR* value that is calculated so long as the model fits the data sufficiently well. In addition, the precision on the CESTR* value that is calculated decreases as noise level increases. It is, therefore, now possible to determine whether quantification of CEST effects by CESTR* is possible from *in vivo* data by determining whether the new BayCEST algorithm fits data sufficiently well.

Figure 4.5D in Section 4.3.1 shows the residual deviation of the new BayCEST model fitted Z-spectrum compared to the raw data within the *in vivo* data set examined in this chapter. Examples of well-fitted (low RD) and poorly-fitted (high RD) voxels are shown in Fig. 4.16A and B, respectively. In addition, Fig. 4.16C shows the cumulative frequency of RD values across the

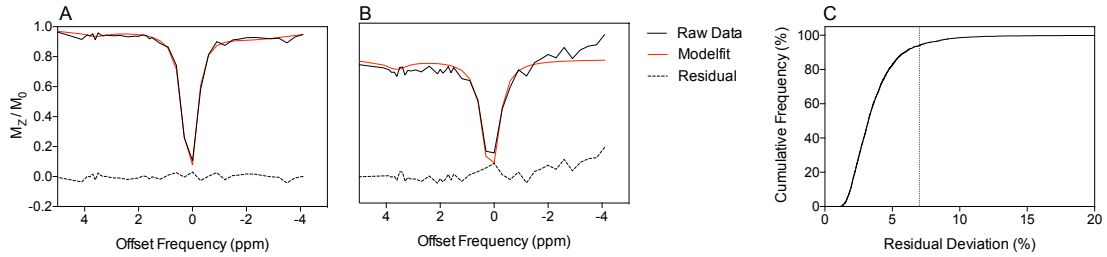

Figure 4.16: Example model fitted Z-spectra and raw data for a well fitted (A, $RD = 1.5\%$) and poorly fitted (B, $RD = 5.9\%$) voxel in the *in vivo* dataset. The cumulative frequency of RD values across the full brain volume (C) shows that 94% of voxels are fitted with $RD < 7\%$.

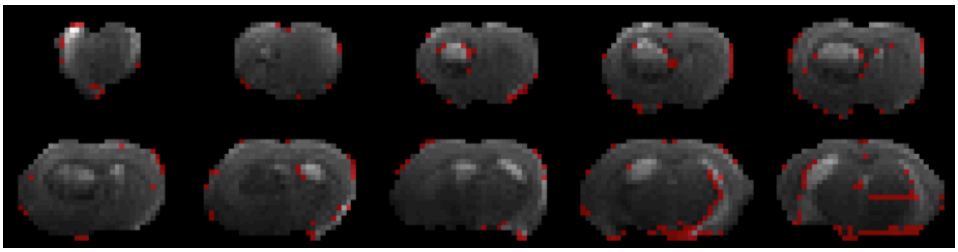

Figure 4.17: Spatial distribution of voxels within the example *in vivo* dataset that are above the $RD > 7\%$ threshold value. Voxels with $RD > 7\%$ are shown in red overlaid on an anatomical reference to visualise that most of the affected voxels are near tissue boundaries (either at the edge of the brain or the edge of the implanted tumour) or in imaging slices far away from the centre of the coil and so likely to suffer from B_1 inhomogeneity effects. Voxels at tissue boundaries, particularly near the ventricles or the implanted tumour, may suffer from partial volume effects and contain a higher proportion of CSF, which may contribute to the poor fitting of the BayCEST model.

in vivo data set shown in Fig. 4.5D, demonstrating that 94% of voxels are fitted with a $RD < 7\%$, and so provide sufficiently accurate estimates of CESTR*.

The location of the 6% of voxels that do not meet the threshold RD value is shown in the binary map in Fig. 4.17. These voxels are predominantly located at a tissue boundary (either between brain and the implanted tumour, or the brain and extracerebral tissue) or in the imaging slices furthest from the isocentre of the magnet, and so most likely to suffer from B_1 inhomogeneity effects.

4.3.5 Feasibility of isoCESTR* method

The previous results have demonstrated that the CESTR* calculated from an *in vivo* dataset is an accurate reflection of the true CEST effect size. However, converting CESTR* into a quantitative physiological parameter such as amide proton concentration or pH remains a non-trivial problem. Since two unknown elements (concentration and pH) control the size of the one measurable (CESTR*), without extra information it is impossible to deconvolve CESTR* into its constituent physiological parameters.

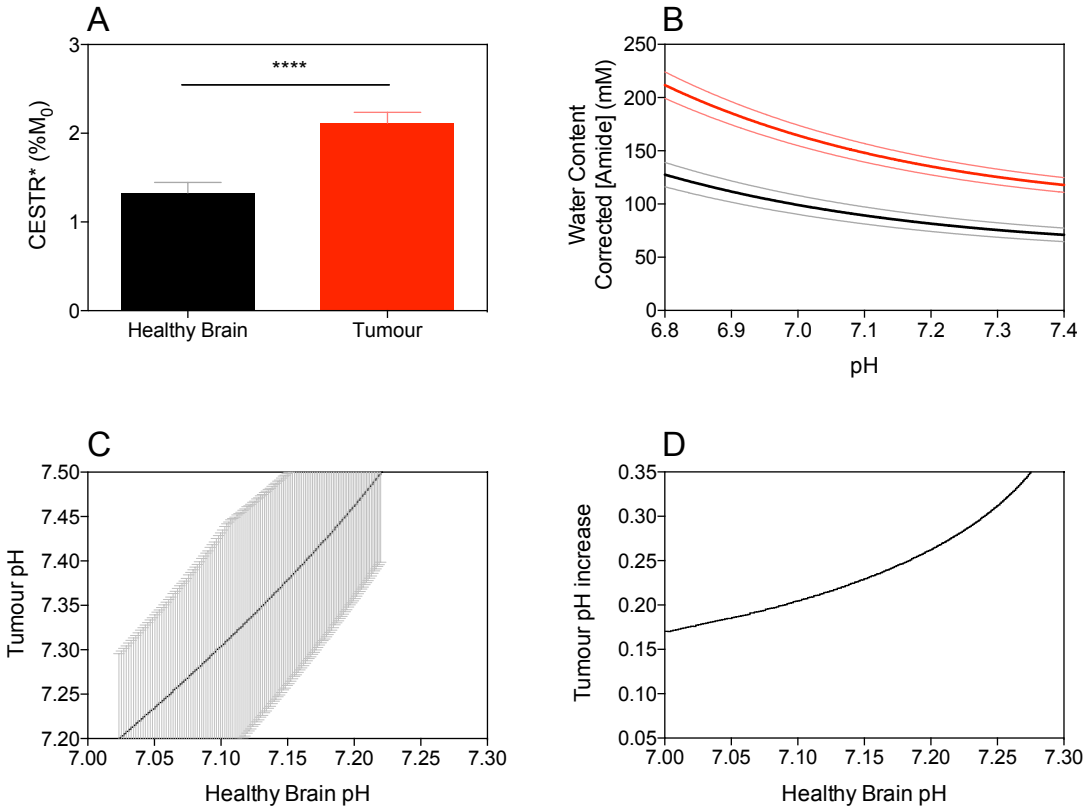

Figure 4.18: CESTR* in simulated tumour tissue is significantly higher than in simulated healthy brain tissue (A) using the parameters in Table 4.2 and Table 4.3 (unpaired two-tailed t-test, $p < 0.0001$, mean $\pm$ 95% CI from 200 iterations of simulation plotted). The isoCESTR* lines for healthy brain and tumour CESTR* values show the degeneracy in CESTR* measurement (B). By following the isoCESTR* method in Fig. 4.10, tumour pH can be estimated. This tumour pH estimate depends on the starting healthy brain pH assumption. (C) shows the actual tumour pH values estimated for each healthy brain pH assumed, with error bars showing the 95% CI. (D) shows the estimated increase in pH in the tumour over the same range of assumed healthy brain pH values. The average increase in pH in tumour compared to healthy brain over the whole range is 0.26 ± 0.06.

However, since the CESTR* metric is dependent on these parameters in a predictable way (Fig. 4.10), by making some basic assumptions about the parameters in question it is possible to convert the measured CESTR* values in two different regions of interest into physiological parameters. Simulations of healthy brain and tumour tissue using the parameters in Table 4.2 and Table 4.3, respectively, were used to measure CESTR* (Fig. 4.18A). Fig. 4.18B shows the two isoCESTR* lines of the measured CESTR* in healthy brain and tumour tissue. Assuming a pH of 7.1 in the healthy tissue, which is reasonable given the expectation that pH is well-regulated in healthy tissue, it is possible to estimate the amide proton concentration in healthy tissue from the CESTR* value measured ($88 \pm 8\,\mathrm{mM}$, error propagated from CESTR* measurement).

By then assuming a certain amide proton concentration change in tumour tissue (increase of

40% [190] giving tumour amide concentration of $120 \pm 10\,\mathrm{mM}$), it is possible to estimate a tumour pH of 7.3 ± 0.3 using the CESTR* measurement of tumour tissue.

Since this pH estimate is dependent on the initial starting value of healthy tissue pH, the isoCESTR* method was repeated for variable healthy tissue assumed pH (Fig. 4.18C,D). Across the full physiological range of pH 7.0 - 7.3 in healthy tissue, the estimated tumour pH change was 0.26 ± 0.06, indicating the relative insensitivty of the isoCEST method to the starting healthy tissue pH value.

4.4 Discussion

The results of this chapter demonstrate that the BayCEST model based algorithm is a suitable method to use for quantification of the size of the CEST effect *in vivo*. This has been proven by applying the BayCEST algorithm to ideal simulated data (without noise added), realistic simulated data (with physiological and random sources of noise accounted for), and an example *in vivo* dataset. An extension to the BayCEST model based analysis method — isoCESTR* — has been developed and its ability to deconvolve the measured CESTR* value into the physiological sources of CEST effect demonstrated.

The suitability of voxelwise application of the BayCEST algorithm was demonstrated by comparing the goodness of fit of the model fitted Z-spectrum in the *in vivo* dataset to a threshold value determined from realistic simulated data with noise added. The goodness of fit was quantified using the residual deviation (Eq. 4.1), which has been used previously in Magnetisation Transfer studies as a measurement of goodness of fit of model based analysis methods [195]. Equation 4.1 inherently applies an equal weighting to each data point within a Z-spectrum to determine the goodness of fit of the model fitted Z-spectrum. However, since most of the information for the labile pool properties comes from the data points at the resonance frequency of the labile protons [194], quantification of the goodness of fit of BayCEST fitted Z-spectra by Eq. 4.1 — and in turn drawing inferences about the accuracy of the calculated CESTR* value — may be inappropriate. An alternative strategy may be to use Eq. 4.1 restricted only to those offset frequencies that contribute most information about the labile pool parameters to the model, or derive sensitivity functions in a similar approach to previous studies [194] and use these functions as weighting factors in the calculation of RD. This in turn may introduce a bias, however, since the accuracy of a model that fits to all data points would be quantified based on its performance across a very narrow range.

A number of assumptions have been made when using simulated data to judge the ability of the BayCEST algorithm to accurately quantify CESTR*. Firstly, the labile pool parameters for all proton pools have been assumed or extrapolated from previous MRI studies [89, 117, 125,

126, 196, 197]. Better estimates of these parameters, particularly the concentrations of protons in each pool, may be elucidated using advanced biochemical or proteomic methods. Secondly, a six pool model has been used, which may not adequately reflect the complex biochemical environment *in vivo*. This simplification is necessary, however, as modelling of the exchange properties of individual protons on specific molecules within an *in vivo* voxel over the timescales necessary to model a CEST MRI experiment is beyond current computational capabilities. Finally, it has been assumed that only the intracellular space contributes to the measured CEST signal. This simplification is motivated by the theory that only protein molecules that are tumbling sufficiently quickly contribute to the amide proton CEST MRI signal, and these proteins are likely to be located predominantly within the cytoplasm of cells [89]. However, it is known that extracellular matrix proteins also contribute to the CEST signal [190]. In addition, there is no biophysical reason why quickly tumbling side chains of proteins attached to cellular membranes could not also contribute to the measured CEST MRI signal. Ignoring the known *in vivo* tissue compartmentalisation in the simulations has more of an effect on the accuracy of the tumour simulations in Section 4.3.5, since the biochemical environments of the intra- and extracellular spaces in tumours are very different. The effect of compartmentalisation on the CEST MRI signal is investigated further in Chapter 6.

The accurate determination of parameters to ensure optimally realistic simulations is a crucial limitation of all simulation studies. It is also a limiting factor in validation of CESTR* as an appropriate method for quantifying CEST effect size *in vivo*, since the true value of amide proton concentration and exchange rate are not known *a priori*. Nevertheless, it can be confidently concluded that the new BayCEST algorithm with the amide proton concentration prior set to 100 mM is a better algorithm than without a prior value on amide proton concentration, because the returned fitted Z-spectra are equally good fits to the data, but with more physiologically realistic amide concentration values (300 mM *vs.* 1 M). These amide concentration estimates agree with values output from the BayCEST algorithm when applied to human *in vivo* data sets [125].

The proposed isoCESTR* methodology also goes some way to evaluating the ability of the CESTR* metric to quantify the biological source of variation that results in an altered CEST effect, though it does require assumptions and independent measurements to be obtained for successful application. The independent measurements could either be pH by, for example, ^{31}P MRS, or amide proton concentration by measuring the bulk protein concentration using a bicinchoninic acid (BCA) assay and making assumptions concerning the distribution of amide protons on protein molecules. Measuring pH by ^{31}P MRS is non-invasive, but the spatial and temporal resolution of the pH measurements is poor and extra hardware is required to make the measurements. Measuring the amide proton concentration by BCA assay is easier in that

extra equipment is not needed, but the necessity of acquiring tissue biopsies makes it an invasive measurement. It may be possible to non-invasively assess amide proton concentration by ^{1}H MRS, but this method is likely to measure signals that are also sensitive to amide exchange rate and, so, are not a truly independent measurement of concentration.

Degeneracy between the amide proton concentration and exchange rate still exists in the quantification of the CESTR* values. This issue is inherent in the model based algorithm implemented, and can only be eradicated by fixing one parameter based on an assumption about the biology in the pathology that is being studied. This strategy would require independent measurements of either parameter, however, which are also required for the isoCESTR* method. In addition, the correlation between amide proton concentration and exchange rate tend to counteract one another (overestimation in one parameter leads to underestimation in the other), and does not seem to affect the accuracy of the measured CESTR* value from simulated data including physiological and random sources of noise. Since the isoCESTR* method has the added benefit of not requiring *a priori* knowledge in the fitting stage of the analysis, it is likely to be more advantageous to use isoCESTR* with independent measurements than to fix a parameter in the fitting stage of the analysis.

The dependence of CESTR* on the simulated noise level found in Section 4.3.3 is not surprising. The accuracy of the CESTR* value remains good, and not significantly different from ideal (non-noisy) data as the noise level increases, but the precision of the estimated CESTR* decreases. This decrease in precision reflects the increased variability in the parameters the model fitting algorithm returns (amide proton concentration and exchange rate). This dependence of CESTR* on noise has implications for the application of BayCEST to *in vivo* data. Individual voxel CESTR* values are likely to be fairly imprecise and comparison of individual voxel values may be inappropriate. However, grouping CESTR* values according to biologically similar environments (e.g. healthy areas of brain tissue, regions of tumour) serves to reduce this imprecision and enable region of interest based comparisons of CESTR* values. This is a more ideal scenario than averaging of the raw data within these regions of interest before fitting with BayCEST, as information concerning biological heterogeneity is retained that would otherwise be lost.

4.5 Conclusion

The work described in this chapter has investigated the ability of the BayCEST algorithm to accurately quantify the size of CEST effect in simulated and *in vivo* data. It was shown that the original BayCEST algorithm accurately quantifies the size of the CEST effect in simulated data with amide proton exchange parameters expected *in vivo*, and the agreement between simulated and fitted concentration and exchange rate was good. However, when BayCEST was applied to

an example *in vivo* dataset, unphysiological amide proton concentration values were returned by BayCEST despite the model fitted Z-spectrum agreeing with the data.

To alleviate this issue, the algorithm was modified to include informative prior information about the amide proton concentration, with no decrease in model fitting performance. The new BayCEST algorithm was then shown to accurately quantify the CEST effect from simulated data with physiological and random sources of noise, and a threshold goodness of fit value found to determine which CESTR* values could be reliably used. Measurement of the goodness of fit between the new BayCEST algorithm fitted Z-spectra and *in vivo* data revealed that voxelwise fitting of *in vivo* data is possible, with 94% of voxels from the example *in vivo* dataset studied having a reliably quantified CESTR* value. Subsequently, the sensitivity of CESTR* as a CEST quantification metric to labile proton concentration and exchange rate in simulations was investigated. Finally, the isoCESTR* methodology was introduced and its ability to deconvolve CESTR* into the relevant physiological parameters demonstrated.

Chapter 5

Elucidation of the source of the CEST MRI signal *in vivo*

Contents

5.1 Introduction . . . 96
5.2 Methods . . . 97
5.2.1 Brain metastasis animal model . . . 97
5.2.2 Ischaemic stroke animal model . . . 97
5.2.3 Hypopharyngeal squamous cell carcinoma animal model . . . 99
5.2.4 MRI experiments . . . 99
5.2.5 MRI data analysis . . . 102
5.2.6 Region of interest definitions . . . 104
5.2.7 Subcellular fractionation & protein concentration measurements . . . 106
5.2.8 Histology . . . 107
5.2.9 pH estimation using isoCESTR* . . . 110
5.3 Results . . . 110
5.3.1 Brain metastasis experiment . . . 110
5.3.2 Ischaemic stroke experiment . . . 117
5.3.3 Atovaquone treatment experiment . . . 121
5.4 Discussion . . . 126
5.4.1 Histological measurement of protein concentration . . . 127
5.4.2 Brain metastasis experiment . . . 128
5.4.3 Ischaemic stroke experiment . . . 131
5.4.4 Atovaquone treatment experiment . . . 132
5.4.5 Accuracy of amide proton concentration estimates by isoCESTR* . . . 133
5.5 Conclusion . . . 135

5.1 Introduction

The previous two chapters have both focussed on addressing the lack of specificity in CEST MRI. This issue is of particular importance when using CEST MRI *in vivo* since it impacts the ability to make inferences of the *in vivo* biochemical or biophysical environment.

Preclinical and clinical CEST MRI studies have usually attributed the altered signal in tumours to their increased cytosolic protein concentration [101, 121, 190, 198]. However, a number of other studies have cast doubt on this interpretation, instead claiming that CEST MRI signal changes in tumours are a product of an altered T_1 relaxation time in these tissues [117, 118]. In addition, the water content in tumours varies somewhat from normal tissue, which affects quantification of the CEST MRI signals, and the metabolic phenotype of tumour cells tends to alter the intra- and extracellular pH in their microenvironment [13, 22]. These factors combine to make CEST MRI of tumours at best a protein-weighted imaging modality, with limited scope for absolute quantification of protein concentration or pH changes, until the complex interplay between these four factors can be deconvolved.

Similarly, CEST MRI studies of ischaemic stroke have predominantly focussed on the pH-weighted nature of the measured signals [56, 89, 199], largely ignoring any concomitant changes in tissue water content, protein concentration, or T_1 time. The simplification that all CEST MRI signal changes originate from pH changes in ischaemic stroke is likely an invalid one, especially given the known changes in protein synthesis in severely ischaemic areas [44]. To date, this component of stroke pathology has not been examined thoroughly with CEST MRI.

In this chapter, three different animal models of human disease were used to elucidate the source of the CEST MRI signal *in vivo*. The relative contributions of protein concentration and pH to changes in CEST MRI signals were investigated using animal models of brain metastasis (ENU1564 cells injected intracerebrally) and ischaemic stroke (occlusion of the middle cerebral artery). In addition, the ability to modulate measured CEST MRI signals was studied using a subcutaneous model of hypoxic hypopharyngeal squamous cell carcinoma treated with atovaquone, an anti-malarial drug which has recently been shown to alleviate tumour hypoxia [36]. In all three experiments, *ex vivo* tissue characterisation using immunohistochemical and biochemical methods was performed as well as *in vivo* CEST MRI. The aim of this chapter is to draw conclusions regarding the sources of the CEST MRI signal *in vivo* by combining this *in vivo* and *ex vivo* information.

5.2 Methods

All animal procedures were conducted in line with the Animal (Scientific Procedures) Act 1986 (UK), and were approved by the Home Office (UK).

5.2.1 Brain metastasis animal model

Female Berlin Druckrey IX (BDIX) rats (180 – 340 g; $n = 15$; Charles River, UK) underwent surgery to induce cerebral tumours as a model of brain metastasis[1]. Rats were anaesthetised with 3 % isoflurane and maintained with 2 – 3 % isoflurane carried in 30 % oxygen and 70 % nitrogen throughout surgery. Core body temperature was monitored by rectal probe and maintained at 37 °C using a heating pad (Harvard Apparatus, UK). Respiration was monitored using a respiration balloon (Biopac, UK) and maintained at approximately 40 breaths/min through modulation of the isoflurane concentration. The fur on the scalp was removed using clippers. Rats were placed on a stereotactic frame to fully immobilise the head, and a midline incision made in the scalp. The bregma point was identified, a burr hole drilled in the skull, and 1×10^6 ENU1564 cells in 1 µl PBS injected using a micro capilliary. The intracerebral injection was made in the left striatum of the brain (co-ordinates 1 mm anterior, 3 mm lateral from bregma, 3.5 mm depth). Following injection, the scalp was sutured and animals recovered with appropriate analgesia. MRI experiments (see Section 5.2.4) were performed four weeks post-injection.

Immediately following MRI experiments, rats were split into two groups. One group ($n = 10$) were sacrified under terminal anaesthesia by transcardial perfusion-fixation with 0.9 % heparinised saline, followed by periodate-lysine-paraformaldehyde (PLP) containing 0.025 % glutaraldehyde. The brains of these animals were collected for further immunohistochemical processing (see Section 5.2.8). The remaining rats ($n = 5$) were sacrified under terminal anaesthesia by transcardial perfusion with 0.9 % heparinised saline. The brains of these rats were extracted and sliced into 2 mm slices using an ice cold rat brain matrix (Braintree Scientific, USA). Tissue biopsies of the tumour and contralateral brain tissue were taken for subcellular fractionation and protein concentration quantification (see Section 5.2.7). The biopsies were snap-frozen in liquid nitrogen and stored at –80 °C until further processing.

5.2.2 Ischaemic stroke animal model

Six male Sprague-Dawley rats (290 – 325 g; Charles River, UK) underwent surgery[2] to occlude the middle cerebral artery with an intraluminal filament. Rats were anaesthetized with 4 % isoflurane and maintained with 1.5 – 2 % isoflurane carried in 30 % oxygen and 70 % nitrogen.

[1] Surgeries were performed by Dr. James Larkin with assistance (cell preparation, monitoring animal anaesthetic, animal preparation etc.) from the author.

[2] Surgeries were performed by Dr. Brad Sutherland.

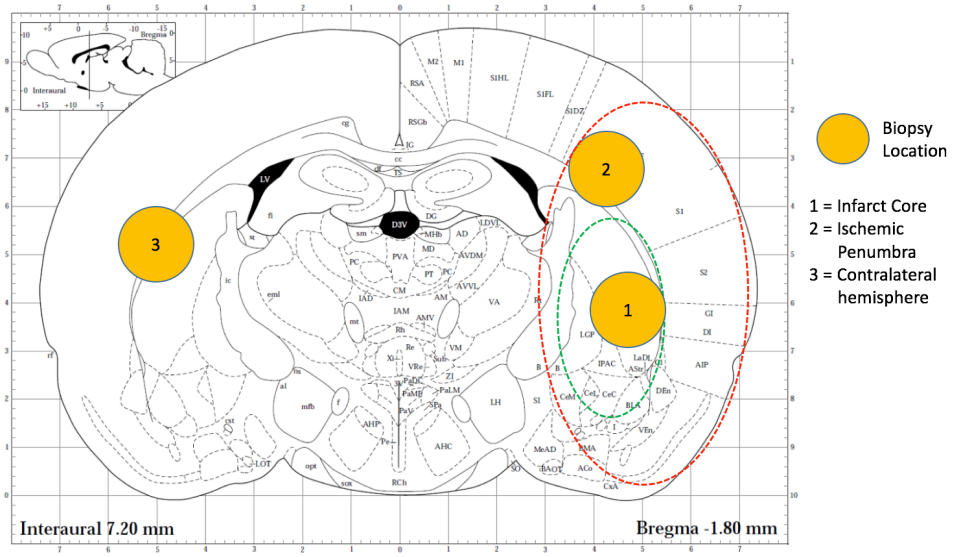

Figure 5.1: Approximate locations of the biopsies collected from infarct core (1), penumbra (2) and contralateral (3) tissue. The green and red outlines represent the ADC and CBF deficits, respectively, in acquired MRI data (see Section 5.2.5).

Core body temperature was monitored by rectal probe and maintained at 37 °C using a heating pad (Harvard Apparatus, UK). Respiration was monitored using a respiration balloon (Biopac, UK) and maintained at approximately 40 breaths/min through modulation of the isoflurane concentration. A midline incision was made in the neck and the right external and common carotid arteries (CCA) were isolated and permanently ligated. After temporary ligation of the right internal carotid artery (ICA), an arteriotomy was made in the CCA and a 4-0 filament with a silicon tip (Doccol, USA) was inserted and advanced up the ICA to occlude the origin of the right MCA, noted by the resistance felt on advancement of the filament. After securing the filament in place, the rat was sutured and transferred for MRI experiments (see Section 5.2.4).

After MRI had been completed (2.5 – 3 h post-MCAO), three rats were sacrificed under terminal anaesthesia by transcardial perfusion-fixation with 0.9 % heparinised saline, followed by PLP containing 0.025 % glutaraldehyde. The brains of these animals were collected for further immunohistochemical processing (see Section 5.2.8). The remaining three rats were sacrified under terminal anaesthesia by transcardial perfusion with 0.9 % heparinised saline. The brains of these rats were extracted and sliced into 2 mm slices using an ice cold rat brain matrix (Braintree Scientific, USA). The fourth slice of each brain (approximately 1.8 mm posterior to bregma) was used to obtain 1 mm diameter biopsies from the core infarct, penumbra and a contralateral sample from a similar brain region. The core infarct and penumbral regions were identified using the MRI data (see Section 5.2.5); Fig. 5.1 shows approximate locations of tissue samples taken. The biopsies were snap-frozen in liquid nitrogen and stored at –80 °C until further processing.

5.2.3 Hypopharyngeal squamous cell carcinoma animal model

Female BALB/c nude mice (age 55 – 70 d; $n = 21$; Charles River, UK) were implanted with subcutaneous tumours on their left flank[3]. Tumours were induced by injection of 1×10^6 FaDu cells in matrigel. Once tumours reached a volume of $100\,\mathrm{mm}^3$, animals were randomly split into Atovaquone-treated ($n = 10$) or control ($n = 11$) groups. Atovaquone is an anti-malarial drug which has recently been shown to reduce the oxygen consumption rate (OCR) of cancer cells *in vitro* and *in vivo*by more than 80%, consequently reducing tumour hypoxia and increasing sensitivity to radiotherapy treatments [36]. The mechanism by which Atovaquone reduces OCR is through inhibition of mitochondrial complex III [36]. Atovaquone is an FDA-approved agent with a good safety profile, it is cleared through the liver after 50 – 84 h, and is not metabolised *in vivo* to a significant extent [36]. It is currently under investigation for alleviation of hypoxia in patients with non-small cell lung carcinoma as part of the ATOM trial at the University of Oxford[4].

Atovaquone was administered in drinking water ($50\,\mathrm{mg\,kg^{-1}\,d^{-1}}$) with 2% dimethyl sulfoxide (DMSO) and 0.1% carboxymethylcellulose. Control animals were treated with DMSO and carboxymethylcellulose only. After 7 days of treatment, MRI was performed on each mouse (see Section 5.2.4.3).

Following MRI, $n = 5$ Atovatuone-treated animals and $n = 6$ control animals were injected intraperitoneally with $0.01\,\mathrm{ml\,g^{-1}}$ EF5 (2-(2-Nitro-1H-imidazol-1-yl)-N-(2,2,3,3,3-pentafluoropropyl) acetamide) and sacrificed under terminal anaesthesia by transcardial perfusion-fixation with 0.9 % heparinised saline, followed by PLP containing 0.025 % glutaraldehyde. The tumours of these animals were carefully excised for further immunohistochemical processing (see Section 5.2.8). The remaining animals ($n = 5$ in each group) were sacrificed following MRI under terminal anaesthesia without perfusion of any kind, and their tumours excised and stored at −80 °C until being used for subcellular fractionation and biochemical protein concentration measurement (see Section 5.2.7).

5.2.4 MRI experiments

All MRI experiments were performed using a 9.4 T spectrometer (Agilent). Animals were anaesthetised with 2 – 3 % isoflurane delivered in a mixture of 30 % oxygen and 70 % nitrogen. Respiration was monitored using a respiration balloon and maintained at approximately 60 breaths/min for mice and 40 breaths/min for rats. Rectal temperature was maintained in all animals at 37 °C using a resistive heating pad (Harvard Apparatus, UK).

[3]Tumour induction procedure and animal monitoring was performed by James Coates.
[4]https://clinicaltrials.gov/ct2/show/NCT02628080

5.2.4.1 Brain metastasis experiment

A 72 mm diameter volume transmit coil and 4-channel surface receive array (Rapid Biomedical) were used. Prior to placement of the animal in the MRI scanner, a tail vein was cannulated to allow for injection of contrast agents throughout imaging. Animals were placed in a prone position and the head immobilised using ear and tooth bars in a custom-made cradle. B_0 inhomogeneity was minimised by ensuring that the head of the animal was placed at magnet isocentre and performing an automated gradient shimming sequence[5] on a voxel covering the brain tissue within the imaging area.

The CEST MRI pulse sequence used was identical to the one described in Section 4.2.4. A pulsed saturation scheme of 50 saturation pulses was used, with each pulse comprising a 20 ms gaussian RF pulse with flip angle 184° followed by a 20 ms crusher gradient, for a total saturation duration of 2 s with equivalent continuous wave RF power 0.55 µT. Following saturation, an EPI readout with FOV = $32\,\mathrm{mm} \times 32\,\mathrm{mm}$ measured the Z-magnetisation. Other sequence parameters were TR = $5\,\mathrm{s}$, TE = $27\,\mathrm{ms}$, 1 average, 10 slices, slice thickness = $1\,\mathrm{mm}$, in-plane resolution $500\,\mu\mathrm{m} \times 500\,\mu\mathrm{m}$. A total of 51 measurements were made following saturation at the following offset frequencies relative to water: $-300, -4.1, -3.8, -3.5, -3.2, -2.9, -2.6, -2.3, -2, -1.7, -1.5, -1.2, -0.9, -0.6, -0.3, 0, 0.3, 0.6, 0.9, 1.2, 1.5, 1.6, 1.7, 1.8, 1.9, 2, 2.1, 2.4, 2.7, 2.9, 3.1, 3.2, 3.3, 3.4, 3.5, 3.6, 3.7, 3.8, 3.9, 4.1, 5, 7, 9.7, 13.5, 19, 26, 37, 51, 72, 100, 300\,\mathrm{ppm}$.

T_1 and T_2 relaxation times were determined voxelwise in all three experiments using inversion recovery (TR = 10 s, TE = 8.22 ms, inversion time (TI) varied in 9 steps from 13.14 ms to 8 s, signals fitted to $M_Z = M_0\left(1 - 2e^{-\frac{\mathrm{TI}}{T_1}}\right)$) and spin echo (TR = 10 s, TE varied in 10 steps from 30 ms to 160 ms, signals fitted to $M_Z = M_0 e^{-\frac{\mathrm{TE}}{T_2}}$) experiments, respectively. In both cases the same spin-echo EPI readout used for CEST imaging was used to acquire images. The slice plan for T_1 and T_2 mapping was identical to CEST MRI to enable coregistration of the images.

B_1 inhomogeneity was measured using a 3D actual flip angle imaging (AFI) pulse sequence ($\mathrm{TR}_1 = 12\,\mathrm{ms}$, $\mathrm{TR}_2 = 120\,\mathrm{ms}$, TE = 2 ms). T_1-weighted gradient echo anatomical imaging was performed before and after injection of gadolinium contrast agent (Omniscan, GE Healthcare, USA) to elucidate the extent of blood-brain barrier breakdown (TR = 500 ms, TE = 20 ms, same slice plan as CEST MRI but with in-plane resolution $125\,\mu\mathrm{m} \times 125\,\mu\mathrm{m}$). High resolution T_2-weighted fast spin echo imaging ($\mathrm{TR} = 3\,\mathrm{s}$, TE = 51 ms, same resolution as T_1-weighted) was also performed for anatomical reference.

[5]The automated gradient shimming sequence was written and implemented by Dr. Paul Kinchesh and Dr. Sean Smart.

5.2.4.2 Ischaemic stroke experiment

The same hardware, animal positioning, and B_0 shimming as used in the brain metastasis experiment were used for the ischaemic stroke experiment, with the exception of tail vein cannulation. CEST, T_1, T_2 and B_1 mapping acquisitions as described in Section 5.2.4.1 were performed twice for each animal, timed such that CEST data were acquired approximately 1 h and 2 h post occlusion of the middle cerebral artery. High resolution T_2 weighted fast spin echo imaging was also performed with same acquisition parameters as described in Section 5.2.4.1.

Additionally, Apparent Diffusion Coefficient (ADC) was measured using trace diffusion weighted images with diffusion b-values of 1000 s mm^{-2} and 0 s mm^{-2}, both with TR = 3 s, TE = 43 ms, and the same FOV and slice pattern as the CEST MRI sequence. Multiphase pseudocontinuous arterial spin labelling (pCASL) was performed to measure cerebral blood flow (CBF). Labelling of blood was achieved with a train of 600 µs Hanning-shaped RF pulses spaced 600 µs apart, flip angle 40°, with eight phases spaced 45° apart between 0° and 315°. Label duration was 1.4 s (TR = 4 s), and post-labelling delay (to allow for labelled blood to flow to the brain and generate ASL signal) set at 550 ms. The EPI readout and slice plan was the same as used for the CEST MRI.

5.2.4.3 Atovaquone treatment experiment

A 26 mm volume coil was used to image mice, which were placed in a supine position in the coil. Insulation was placed between the animal and coil to prevent excessive heat loss from the animal and provide a small level of immobilisation. Core body temperature was monitored by rectal probe and maintained at 37 °C using a heating pad (Harvard Apparatus, UK). Respiration was monitored using a respiration balloon (Biopac, UK) and maintained at approximately 60 breaths/min through modulation of the isoflurane concentration.

CEST MRI was performed using a multi-slice gradient echo sequence [200] (TR = 195 ms, TE = 1.4 ms, Fig. 5.2) with respiration-gating and reacquisition of data corrupted by a breath. Z-spectra were acquired using a CEST pulse flip angle 180°, CEST pulse duration 20 ms, and 37 frequency offsets (–5.1 – 5.1 ppm in 0.3 ppm steps, plus $\pm 500\,\mathrm{ppm}$ for normalisation). For 10 mice (5 each from Atovaquone-treated or control groups), mice were euthanised after CEST MRI and repositioned for non-respiration-gated T_1 and T_2 mapping with acquisition parameters described in Section 5.2.4.1. This T_1 and T_2 mapping was performed to provide accurate priors for subsequent BayCEST analysis of the CEST MRI data (see Section 5.2.5), and was performed post-mortem because no respiration-gated T_1 or T_2 mapping sequence was available at the time of performing the experiments.

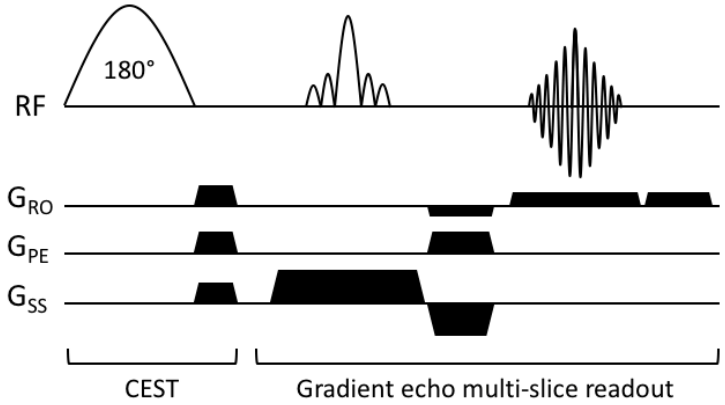

Figure 5.2: Respiration gated CEST MRI pulse sequence implemented for the atovaquone experiment.

5.2.5 MRI data analysis

CEST MRI data were quantified using the CESTR* metric. Acquired data were fit to the Bloch-McConnell equations using the modified BayCEST algorithm with an amide proton concentration prior of 100 mM, as used in Section 4.3.2. A 3-pool model model comprising of water, amide protons at 3.5 ppm, and a combined NOE+MT pool at –2.41 ppm was fit. In all cases, CESTR* was used to quantify the CEST effect of amide protons at 3.5ppm. T_1 and T_2 correction was applied by allowing the BayCEST algorithm to fit T_1 and T_2 from the data, with prior values set based on the average T_1 and T_2 times within the imaging region ('regional priors'). In the brain metastasis experiment, the effect of implementing voxelwise T_1 and T_2 correction based on the acquired T_1 and T_2 maps was investigated by comparing CESTR* values with voxelwise and regional priors.

Regions of interest were used to measure the mean $\pm$ standard deviation CESTR* within regions of biologically similar tissue (see Section 5.2.6). In the brain metastasis and ischaemic stroke experiments, contralateral hemisphere ROIs were defined to represent normal healthy brain tissue and used to normalise the CESTR* in each diseased ROI. The relative CESTR* (rCESTR*) values in ROIs for each animal were combined using a random effects model to generate a weighted mean that accounts not only for the size of the ROI in each animal, but also the variability of CESTR* within the ROI.

The random effects model [201] calculates a weighted groupwise mean, $\bar{x}$, across all animals according to Eq. 5.1 where Y_i is the mean rCESTR* value observed in each animal and n is the number of animals.

$$\bar{x} = \frac{\sum_{i=1}^{n} W_i Y_i}{\sum_{i=1}^{k} W_i} \tag{5.1}$$

The weighting applied to each animal's result is determined by $W_i = \frac{1}{V_i + \tau^2}$, where V_i captures the variance of rCESTR* within each animal and τ^2 represents the variance between animals. Within-animal variance is given by $V_i = \frac{\sigma^2}{k}$ for an rCESTR* measurement with standard deviation σ^2 from a region of interest comprising k voxels. Note that from this definition of V_i, larger regions of interest contribute more information to the final group-wise result than smaller regions of interest. Between-animal variance is computed according to the DerSimonian and Laird method, outlined in equations Eq. 5.2, where $\bar{y}$ is the so-called fixed effect weighted mean, defined in a similar way to $\bar{x}$ in Eq. 5.1 but with weightings defined by $W_i = \frac{1}{V_i} = \frac{k}{\sigma^2}$.

$$\tau^2 = \frac{Q - (n-1)}{C} \qquad Q = \sum_{i=1}^{n} \frac{(Y_i - \bar{y})^2}{V_i} \qquad C = \sum W_i - \frac{\sum W_i^2}{W_i} \tag{5.2}$$

In the atovaquone treatment experiment, since no normal 'control' tissue is present for the xenograft tumour model used in this experiment, rCESTR* values cannot be calculated for individual mice. In addition, the tumours display large amounts of heterogeneity both within and between animals, making usual region of interest statistics less informative. Instead, the absolute CESTR* values for all voxels within every tumour in both groups were calculated and the cumulative frequency of CESTR* values across both groups was compared using the Kolmogorov-Smirnov test, with statistical significance defined as $p < 0.05$.

The ADC was calculated from the DWI acquisitions with diffusion b-values of $b_1 = 1000\,\mathrm{s\,mm^{-2}}$ and $b_0 = 0\,\mathrm{s\,mm^{-2}}$ using Eq. 5.3.

$$\mathrm{ADC} = -\frac{\ln(S_{b1}/S_{b0})}{b_1} \tag{5.3}$$

CBF was calculated from the multi-phase pCASL acquisitions by fitting the raw pCASL data using a custom version of `BASIL` [124] with a modified Fermi function of the form in Eq. 5.4. α and β were 66 and 21, respectively. Resultant mean magnetisation maps were processed with `oxford_asl` to produce relative CBF maps, which were then calibrated using calibration images acquired with no ASL. Brain and blood T_1 were set as $1.53\,\mathrm{s}$ and $2.3\,\mathrm{s}$, respectively, in `oxford_asl`, with inversion efficiency of 0.85 [202] [6].

$$f(x) = -2\left[\frac{1}{1 + \exp^{(|x|-\alpha)/\beta}} + 1\right] \tag{5.4}$$

[6] ADC and CBF analysis was performed using in-house MATLAB scripts written by Dr. James Larkin.

B_1 field homogeneity was determined by the actual flip angle imaging method [203], where the actual flip angle α is calculated according to Eq. 5.5, with r defined as the ratio of the two acquired signals, $r = \frac{S_2}{S_1}$, and $n = \frac{\mathrm{TR}_2}{\mathrm{TR}_1}$ for $\mathrm{TR}_1 = 12\,\mathrm{ms}$ and $\mathrm{TR}_2 = 120\,\mathrm{ms}$. A threshold value of B_1 field inhomogeneity of < 10% across the entire imaging region was used, and was readily observed in all experiments owing to the small field of view and RF coil geometry.

$$\alpha \approx \arccos \frac{rn - 1}{n - r} \tag{5.5}$$

5.2.6 Region of interest definitions

5.2.6.1 Brain metastasis experiment

The model of brain metastasis used here is known to reflect the heterogeneity present in human brain metastasis [182]. Intracerebrally injected ENU1564 tumours tend to grow rapidly and with a poor vascular network, resulting in a rim of infiltrating tumour cells (which frequently appears hyperintense on post-gadolinium injection images, indicating blood-brain barrier breakdown) and a core of necrotic tissue and cellular debris. The high resolution T_1-weighted post-Gd anatomical images were used to manually segment the abnormality volume, defined as areas of tissue enclosed within an area of hyperintense signal in the injected hemisphere.

To ensure the identified abnormality volume was correctly segmented into the two tissue types (infiltrating tumour and necrotic tissue), an automated tissue segmentation algorithm was implemented. The T_1 time measured from the inversion recovery experiment was used as a tissue classifier, where tissue with T_1 < 1.6 s was classified as healthy brain, tissue with 1.6 s < T_1 < 2.2 s was tumour, and tissue with T_1 > 2.2 s was necrotic. The automatic segmentation was verified and adjusted manually to ensure that a consistent 'rim-core' pattern was present in the full tumour volume.

A region of interest of similar size and cerebral location to the tumour on the contralateral hemisphere was defined for the purposes of calculating relative CESTR* (rCESTR*) values within animals. CESTR* within the tumour rim and core regions were normalised to the CESTR* of the contralateral hemisphere within each animal and reported as relative CESTR* (rCESTR*) values. This approach allows for more robust groupwise comparison of CESTR* within tissue locations. rCESTR* values within the tumour rim and tumour core regions were compared to a hypothetical value of 1 using a one-sample t-test, with statistical significance defined as $p < 0.05$.

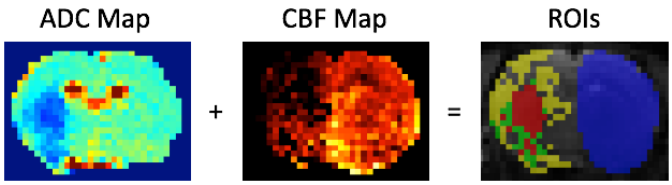

Figure 5.3: Example of defined ROIs in animals following ischaemic stroke. Blue = contralateral hemisphere; red = infarct core; green = infarct growth; yellow = oligemia.

5.2.6.2 Ischaemic stroke experiment

The MCAO model is a well-used and consistent model of ischaemic stroke in rats, fully recapitulating a number of cellular processes seen in human ischaemic stroke [204]. The regions most commonly studied in human stroke are tissue that is infarct at presentation (infarct core), tissue that goes on to infarct over time (infarct growth), and tissue that has restricted blood flow but never becomes infarcted (oligemia). These regions of interest were defined in rats as:

- Infarct Core (IC): ADC < 620 $mm^2\,s^{-1}$ at 1 h post-MCAO and 2 h post-MCAO
- Infarct Growth (IG): ADC > 620 $mm^2\,s^{-1}$ at 1 h post-MCAO but ADC < 620 $mm^2\,s^{-1}$ at 2 h post-MCAO
- Oligemia (OG): ADC > 620 $mm^2\,s^{-1}$ at 2 h post-MCAO and CBF < 20 ml/100g/min at 1 h

The threshold values here are taken from a previous clinical study [48]. The generated binary masks (see Fig. 5.3) for these regions of interests were manually inspected and any erroneous voxels (at the edge of the brain or in the contralateral hemisphere) removed. The contralateral hemisphere was defined for the purposes of calculating rCESTR* within animals, and the rCESTR* value reported for each region of interest. rCESTR* values within each region were compared to a hypothetical value of 1 using a one-sample t-test, with statistical significance defined as $p < 0.05$.

5.2.6.3 Atovaquone treatment experiment

The whole tumour region was segmented manually with guidance from the high resolution T_2-weighted imaging. As described in Section 5.2.5, no normal 'control' tissue was present to allow calculation of rCESTR* values. The absolute CESTR* values for all voxels within every tumour in both groups were calculated and the cumulative frequency of CESTR* values across both groups was compared using the Kolmogorov-Smirnov test, with statistical significance defined as $p < 0.05$.

5.2.7 Subcellular fractionation & protein concentration measurements

The *ex vivo* tissue biopsies collected during each experiment were subjected to the same subcellular fractionation and protein concentration measurement protocol. This protocol involved homogenising the tissue in a volume of lysis buffer scaled to the tissue weight in a glass Dounce homogeniser at wet ice bath temperature. If lysis buffer volumes were too small to permit reliable homogenisation using a Dounce homogeniser, a motorised pestle was used in a wet ice chilled 1.5 ml microcentrifuge tube.

The lysis buffer was part of the Subcellular Protein Fractionation Kit for Tissues (Thermo Scientific, UK; catalog number 87790)[7] and was doped with protease inhibitor immediately prior to homogenisation (Halt Protease Inhibitor Cocktail, 100x; Thermo Scientific, UK). Following homogenisation in the lysis buffer and spinning in a centrifuge at $500 \times g$ for 5 min at 4 °C, the supernatant (cytoplasmic fraction) was removed and stored at –20 °C until further use. The pellet was resuspended in PBS and mixed until homogenous, then stored at –20 °C until further use, yielding cytoplasmic and non-cytoplasmic protein fractions from all tissue samples.

The protein concentration within these fractions was quantified by bicinchoninic acid (BCA) assay [205]. The BCA assay, similar to the Bradford or Lowry assays, is a biochemical method for determining total protein concentration within a sample. A BCA assay kit (Pierce BCA Assay Kit, Thermo Scientific, catalog number 23225) was used according to manufacturer's instructions. Briefly, 25 µl of sample was mixed with 200 µl of working BCA solution (containing BCA, sodium carbonate, sodium bicarbonate, sodium tartrate, and copper(II) sulfate pentahydrate) in triplicate in a 96 well plate. Following an incubation period of 30 min at room temperature, the absorption at 562 nm was measured. The absorption within a well is proportional to the amount of protein in the well, and through calibration to a known set of standard protein concentrations (using BSA as the protein), absolute protein concentrations were calculated.

The protocol was performed on all available subcellular fractions from the biopsies from each animal. Mean and standard deviation protein concentrations were taken from the triplicate measurements, and were combined across animals and cellular locations to give groupwise protein concentration estimates across all animals. Total protein concentrations were also derived from the sum of the two fractions. The protein concentrations were compared using an unpaired two-tailed t-test in brain metastasis and atovaquone experiments, and a one-way ANOVA with Tukey's post-hoc test corrected for multiple comparisons in the ischaemic stroke experiment, with statistical significance defined as $p < 0.05$.

[7] The exact constituents of the lysis buffer are unfortunately not published by Thermo Scientific.

5.2.8 Histology

Histology enables interrogation of tissues at the cellular and molecular level. Despite its invasive nature, it allows very specific and sensitive tissue characterisation to be performed. Tissue which had been perfused-fixed was further fixed by submersion in PLP containing 0.025 % glutaraldehyde for 8 h followed by 30 % *w/v* sucrose overnight for cryopreservation. The tissue was then embedded in optimal cutting temperature compound (OCT-Tissue Tek, VWR International Ltd, Lutterworth, UK) and frozen in an isopentane dry ice bath. Tissue was stored at −80 °C until it was sectioned at 10 µm thickness using a cryostat[8]. Sectioned tissue was stored at −20 °C until being used for staining.

As well as more standard immunohistochemical and immunofluorescent procedures involving functionalisation of the tissue using antibodies, a more straightforward stain to evaluate bulk protein concentration at histological resolution using Coomassie Brilliant Blue G-250 was employed in all three experiments. Coomassie is a dye often used to stain proteins in biochemical techniques such as polyacrylamide gel electrophoresis (PAGE) and the Bradford assay, where the intensity of the dye is proportional to the amount of protein present [206]. It is less widely used as a histological marker of protein concentration, though has been employed in quantitative autoradiography studies [207]. With associated standards of a known protein concentration (e.g. from tissue homogenates as in [207]), quantitative estimates of protein concentration at a histological resolution are possible.

Frozen sections were thawed for 20 min at room temperature and rehydrated in distilled water. The thawed sections were stained for protein in 1.25 % *w/v* Coomassie Brilliant Blue G-250 dye (Thermo Scientific, UK; catalog number 20279) in 0.9 % NaCl with 0.5 % Tween for 30 min. Addition of Tween ensures that cellular membranes are permeabilised to allow the dye to enter cells and stain for intracellular proteins. The sections were destained by washing in PBS for $3 \times 15\,\mathrm{min}$ or until the destain solution ran clear.

Protein concentration standards were generated using a fresh-frozen naïve Wistar rat brain perfused with 0.9 % NaCl. Briefly, the whole frozen rat brain was thawed and homogenised into a paste using a pestle and mortar at wet ice temperature. Serial dilutions of homogenate were generated by adding the homogenate to PBS in ratios of 0:1, 1:1, 2:1, 4:1, 12:1, 20:1, 50:1, 100:1 PBS:brain. The dilutions were mixed thoroughly and an aliquot taken for protein concentration measurement by BCA assay (as described in Section 5.2.7)[9]. The remaining homogenate was frozen in an isopentane dry ice bath and stored at −80 °C until they were embedded in OCT,

[8] Sectioning of tissue in the brain metastasis experiment was performed by Manon Simard, in the ischaemic stroke experiment by Claire Bristow, and in the atovaquone treatment experiment by James Coates.

[9] Assistance with preparing the dilutions of tissue homogenate and quantifying their protein concentration by BCA assay was provided by Dr. Vanessa Johannsen

Parameter Name	Best Fit Value ± 95% CI
B_{max}	32.76 ± 6.00
K_d	0.02891 ± 0.02479
N_S	3.910 ± 0.719
BG	21.97 ± 3.50

Table 5.1: Best fit values for the one-site binding equation in Eq. 5.6 to convert transformed blue RGB intensities, I, into quantitative protein concentration measurements.

sectioned, and stained in the same way as tissue sections.

Stained tissue was imaged at $20\times$ magnification using a Leica Biosystem ScanScope CS2 scanner (Aperio, ePathology Solutions, Milton Keynes, UK). The images were analysed using a combination of Image Scope (ePathology Solutions), ImageJ (Fiji; www.fiji.sc) and MATLAB (MathWorks) to measure the intensity of the blue RGB channel in the scanned images. Regions of interest were drawn on each tissue section with guidance from immunohistochemical staining of adjacent tissue sections, and the intensity of the blue RGB channel converted into quantitative protein concentration measurement using a calibration curve.

Calibration standard curves to convert blue RGB intensity to quantitative protein concentration were generated from the protein concentration measurements by BCA assay of the tissue homogenates. Six replicate tissue homogenates were used for BCA and blue RGB intensity measurements. To minimise experimental error, the calibration slides were stained at the same time as tissue slides. Blue RGB intensities were linearly transformed according to $I = 255 -$ Blue RGB Value to make the data more intuitive (i.e. higher number indicates more protein). These transformed blue RGB values were plotted against the BCA-derived protein concentrations (Fig. 5.4) and a one-site binding equation of the form Eq. 5.6 fitted to the data. B_{max} is the maximum specific transformed blue RGB value, K_d is the equilibrium binding constant of Coomassie dye to protein, N_s is the slope of the nonspecific binding of Coomassie to protein, and BG is the amount of background Coomassie staining. The best fit values of all fitted parameters are shown in Table 5.1. The equation was then rearranged to a quadratic in [Prot] (Eq. 5.7), solved using the quadratic formula, and the positive solution only kept since negative protein concentrations are impossible (Eq. 5.8).

$$I = \frac{B_{max} \times [\text{Prot}]}{K_d + [\text{Prot}]} + N_s \times [\text{Prot}] + \text{BG} \tag{5.6}$$

$$3.91[\text{Prot}]^2 + [\text{Prot}](54.84 - I) + 0.02891(21.97 - I) = 0 \tag{5.7}$$

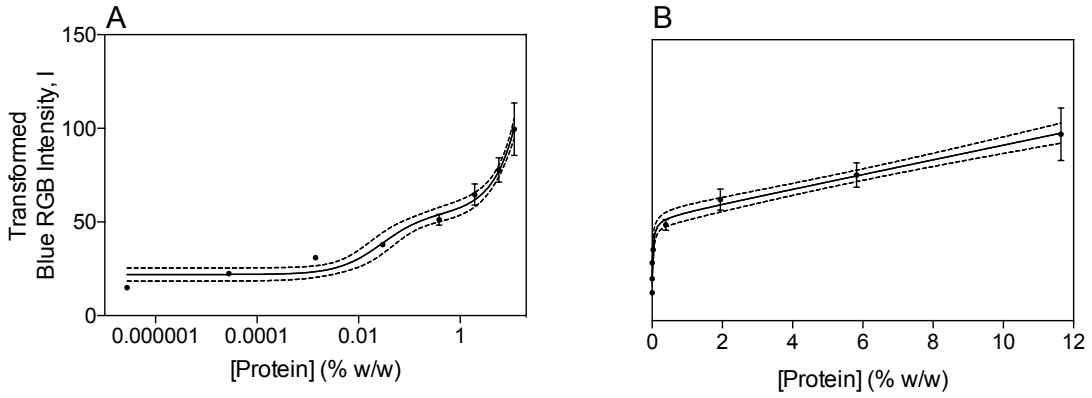

Figure 5.4: Coomassie standard curve to show conversion between transformed blue RGB intensity to protein concentration. The two panels show the same data but on a logarithimic (A) or linear (B) x-axis. The best fit line is Eq. 5.6 with parameters having the values shown in Table 5.1. R^2 of the fit is 0.9418. Dashed line shows 95% CI of the fit.

$$[\text{Prot}] = \frac{\sqrt{I^2 - 109I + 2997} + I - 54.84}{7.82} \tag{5.8}$$

5.2.8.1 Brain metastasis experiment

Sections from animals in the brain metastasis experiment were stained[10] for the endothelial cell marker CD31 (AF3628, R&D Systems, UK) and the hypoxia marker pimonidazole (Hypoxyprobe, USA). The digitised images (identical imaging procedure to slides stained for Coomassie) were used as guidance for defining areas of infiltrating tumour or necrotic tisue for protein concentration measurements by Coomassie.

5.2.8.2 Ischaemic stroke experiment

Sections from animals in the ischaemic stroke experiment were stained[11] for the neuronal marker NeuN (anti-NeuN antibody, MAB377, Merck Millipore, UK). The digitised images (identical imaging procedure to slides stained for Coomassie) were used as guidance for defining areas of infarct core for protein concentration measurements by Coomassie.

5.2.8.3 Atovaquone treatment experiment

Sections from tumours from animals in the atovaquone treatment experiment were stained[12] for the hypoxia marker EF5 (gift from the laboratory of Cameron Koch, University of Pennsylvania, USA) and the cellular nucleus marker DAPI (D9542, Sigma Aldrich, USA). The distribution of DAPI and EF5 within the tumour sections was visualised by immunofluorescence using a Nikon

[10]Staining of brain metastasis sections for CD31 and pimonidazole was completed by Manon Simard.
[11]Staining of ischaemic stroke sections for NeuN was completed by Dr. Manuel Sarmiento Soto.
[12]Staining of FaDu tumour sections for DAPI and EF5 was completed by James Coates.

Eclipse 90i microscope (Nikon, Japan), and used to investigate the effect of atovaquone treatment on hypoxia within tumours. In addition, EF5 staining was used as guidance to delineate hypoxic areas in tumours and measure the protein concentration in hypoxic areas by Coomassie staining.

5.2.9 pH estimation using isoCESTR*

The isoCESTR* method described in Section 4.2.6 was used with the CESTR* measurements made in all three experiments to estimate the pH in the examined regions of interest. A normal tissue pH of 7.11 was assumed [89] in the isoCESTR* procedure with CESTR* results from the brain metastasis and ischaemic stroke experiments. Errors in pH were propagated based on the 95% CI of the CESTR* measurements. Data to draw the isoCESTR* lines are generated using 500,000 simulated Z-spectra (simulated using 1001 relative amide proton concentrations of $0-0.004$ and 501 amide exchange rates of $0-100$ Hz), meaning it is possible to correct for potential differences in the water content in tumour regions. Relative amide proton concentrations were converted to absolute amide proton concentrations by multiplying by the *in vivo* water proton concentration (112 M), and the water content of the tissue from which CESTR* was measured (0.84 ml water /ml brain for healthy brain, 0.87 ml water /ml brain in tumours [101]). The water content of healthy brain was used in ischaemic stroke isoCESTR* pH measurements, as water content changes in the ischaemic stroke lesion are not expected at such acute timescales [89]. Compensating for differences in water content between pathologic and healthy tissue ensures that all concomitant factors have been accounted for, and any difference in *in vivo* CESTR* that is not owing to a change in the protein concentration measured *ex vivo* is likely to originate from pH differences.

5.3 Results

5.3.1 Brain metastasis experiment

5.3.1.1 CEST MRI Results

A CESTR* map of a representative rat from the brain metastasis experiment is shown in Fig. 5.5A, as well as a high-resolution post-Gd T_1-weighted image for anatomical reference (Fig. 5.5B). The infiltrating tumour rim is evident as a hyperintense region in the post-Gd T_1-weighted images, whereas the necrotic core region appears hypo- to isointense. Distinguishing between the two tissue regions using the CESTR* maps is more difficult, but regions of localised hyperintense CESTR* in the tumour rim are evident (Fig. 5.5A). The residual deviation (RD) map in Fig. 5.5C shows an acceptable model fitting performance across the whole brain, with only 131/4049 voxels (3.2 %) fitted with $RD > 7\%$. The location of these voxels is shown in Fig. 5.5D.

Over all animals, the relative CESTR* (rCESTR*) in tumour rim tissue was significantly elevated

compared to contralateral tissue (rCESTR* = 1.10 ± 0.09, mean $\pm$ 95% CI, 1347 voxels, $p < 0.05$ from one-sample t-test compared to a hypothetical mean of 1), as was the necrotic core tissue (rCESTR* = 1.14 ± 0.10, mean $\pm$ 95% CI, 1475 voxels, $p < 0.05$ from one-sample t-test compared to a hypothetical mean of 1). The groupwise measurements from all animals are shown in Fig. 5.6.

5.3.1.2 CESTR* with and without voxelwise T_1 and T_2 correction

The results presented in Section 5.3.1.1 were analysed with the BayCEST algorithm with 100 mM amide proton concentration prior, identical to the analysis performed in Section 4.3.4. T_1 and T_2 correction was implemented by allowing T_1 and T_2 to be estimated from the CEST MRI data, with priors set as the same value for each voxel. Since T_1 and T_2 were measured voxelwise in the same slice plan as the CEST MRI data, it was possible to test whether voxelwise variation of the T_1 and T_2 priors has any impact on quantification of CESTR* *in vivo* in the brain metastasis experiment.

Figure 5.7 shows the effect of adding voxelwise priors for both T_1 and T_2 on the measured rCESTR* within the tumour rim and necrotic core regions of interest from every animal. With both T_1 and T_2 priors varying voxelwise, the measured rCESTR* is not significantly different from the rCESTR* measured without voxelwise prior variation. As a result, voxelwise variation of T_1 and T_2 priors was not used for any further *in vivo* analyses.

5.3.1.3 Protein concentration measurements

Quantitative protein concentration measurements made by BCA assay of the cytoplasmic and non-cytoplasmic fractions of biopsied tissue are shown in Fig. 5.8. No significant difference in cytoplasmic, non-cytoplasmic or total protein concentration was evident between the biopsied tumour and healthy brain ($p > 0.05$ as determined by two-tailed unpaired t-test). However, since the T_1-weighted high-resolution anatomical imaging revealed the expected intratumoral heterogeneity (Fig. 5.5B), the protein concentration measurements may be biased by mixed tissue types (i.e. necrotic as well as proliferative) being assayed in the same sample.

Quantitative cytoplasmic protein concentration measurements of the ENU tumour model were instead made using Coomassie staining and imaging with histological resolution. Example sections through a tumour volume of a single rat are shown in Fig. 5.9A, as well as zoomed regions of the tumour rim, necrotic core and contralateral hemisphere from a single section in Fig. 5.9B,C, and D, respectively. These sections show a clear pattern of lighter blue staining (corresponding with lower cytoplasmic protein concentration) in the necrotic core areas, darker blue staining in the tumour rim areas, and an intermediate level of blue staining in the contralateral hemisphere. This relationship is maintained over all sections and all animals (Fig. 5.9E; 18 sections per animal

Figure 5.5: CESTR* map of a representative rat from the brain metastasis experiment (A), with high-resolution T_1-weighted spin echo image after gadolinium contrast agent injection (B), showing the typical extent of tumour burden and rim-core pattern within these tumour-bearing rats. The residual deviation map (C) shows an acceptable model fitting performance across the whole brain, with the location of the $RD > 7\%$ voxels restricted mainly to the edge of the brain (D).

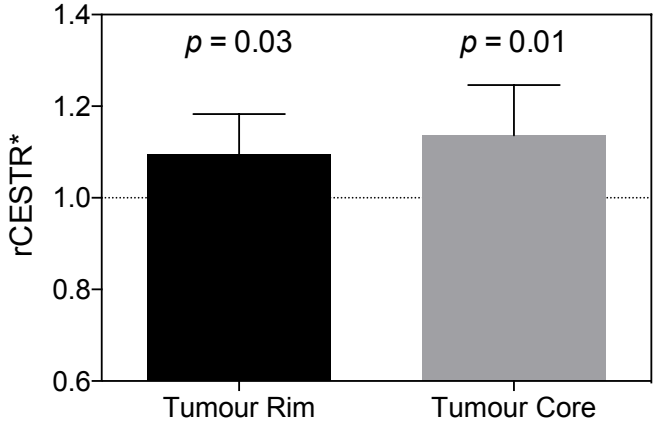

Figure 5.6: rCESTR* values from tumour rim and necrotic tumour core regions in all animals in the brain metastasis experiment. p values show significance level of a one-sample t-test comparing to a hypothetical mean of 1. Error bars are 95% CI. The number of voxels for each tissue type is $n = 1347$ for tumour rim, $n = 1475$ for tumour core.

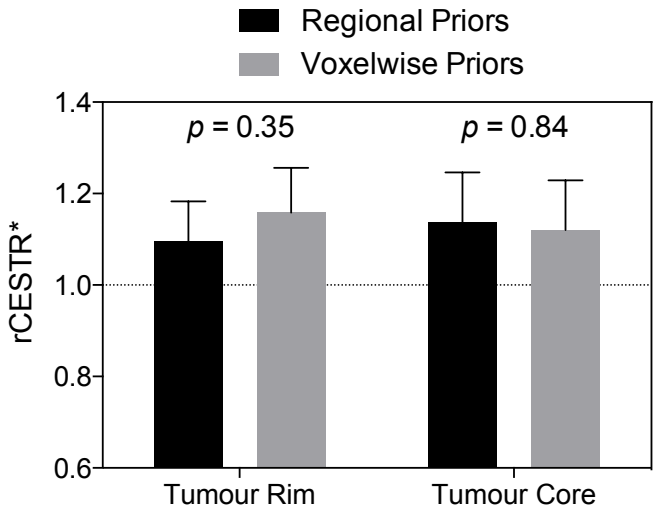

Figure 5.7: Comparison of rCESTR* in tumour rim and core with regional or voxelwise T_1 and T_2 priors. There is no significant difference in rCESTR* in either tumour rim or core, implying that regional T_1 and T_2 priors for the whole brain are suitable for CESTR* quantification. p values show significance level of a t-test between the rCESTR* value calculated with regional or voxelwise priors within each region with Bonferroni's correction for multiple comparisons. The number of voxels for each tissue type is $n = 1347$ for tumour rim, $n = 1475$ for tumour core.

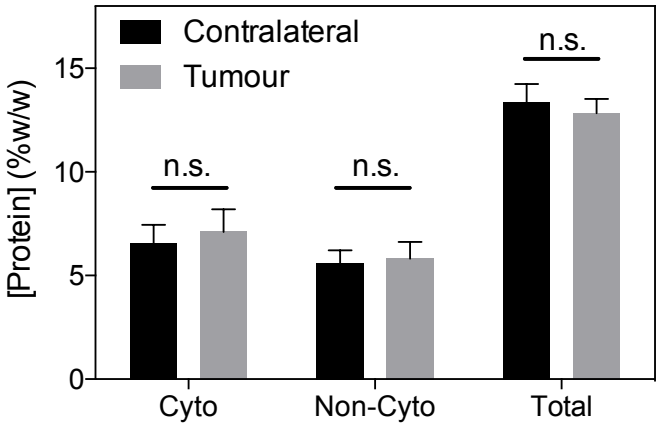

Figure 5.8: Cytoplasmic (left), non-cytoplasmic (middle) and total (right) protein concentrations measured by BCA assay of biopsied tissue from the contralateral healthy brain (black, $n = 5$) and tumour (grey, $n = 5$) of animals with brain metastasis. Statistical comparison was unpaired t-test comparing contralateral and tumour protein concentration in each fraction, n.s. signifies $p > 0.05$.

taken throughout the tumour) with regions of interest of tumour and necrotic tissue guided by stains for hypoxia (pimonidazole) and blood vessels (CD31) in adjacent sections (Fig. 5.10). In addition, it is interesting to note the areas of localised lighter stain in the contralateral hemisphere region (Fig. 5.9D) that may reflect myelinated white matter fibre tracts, which are known to have a lower protein concentration than surrounding brain tissue [208].

5.3.1.4 Estimation of tumour pH by isoCESTR*

The isoCESTR* lines for the healthy contralateral brain and tumour rim tissue are shown in Fig. 5.11. The isoCESTR* lines plotted refer to the average contralateral CESTR* ($3.43 \pm 0.10\,\%\,\mathrm{M_0}$) and tumour rim CESTR* ($1.10 \times 3.43 \pm 0.10\,\%\,\mathrm{M_0} = 3.77 \pm 0.09\,\%\,\mathrm{M_0}$) from all animals. The increase in cytoplasmic protein concentration in tumour rim tissue compared to healthy brain tissue is an absolute increase of 0.83 % *w/w* (Fig. 5.9E), which is a relative increase of 10 % ($100 \times \frac{9.05\,\%\,w/w}{8.20\,\%\,w/w} - 100\% = 10\,\%$).

Using the isoCESTR* method of Section 4.2.6, assuming a healthy brain pH = 7.11 [89] and using the relative increase of cytoplasmic protein concentration in tumour tissue of 10 %, the tumour pH in ENU tumours is estimated to be 7.14 ± 0.01. Errors were propagated based on the 95% CI of the CESTR* values in Fig. 5.11.

Based on the CESTR* one would expect to measure if there were no pH change in the tumour (red cross-marked point in Fig. 5.11, which corresponds with CESTR* = 3.64 % $\mathrm{M_0}$), it was estimated that approximately 66 % of the observed CESTR* change is owing to protein concentration changes, with the remaining 34 % a result of pH changes in the tumour.

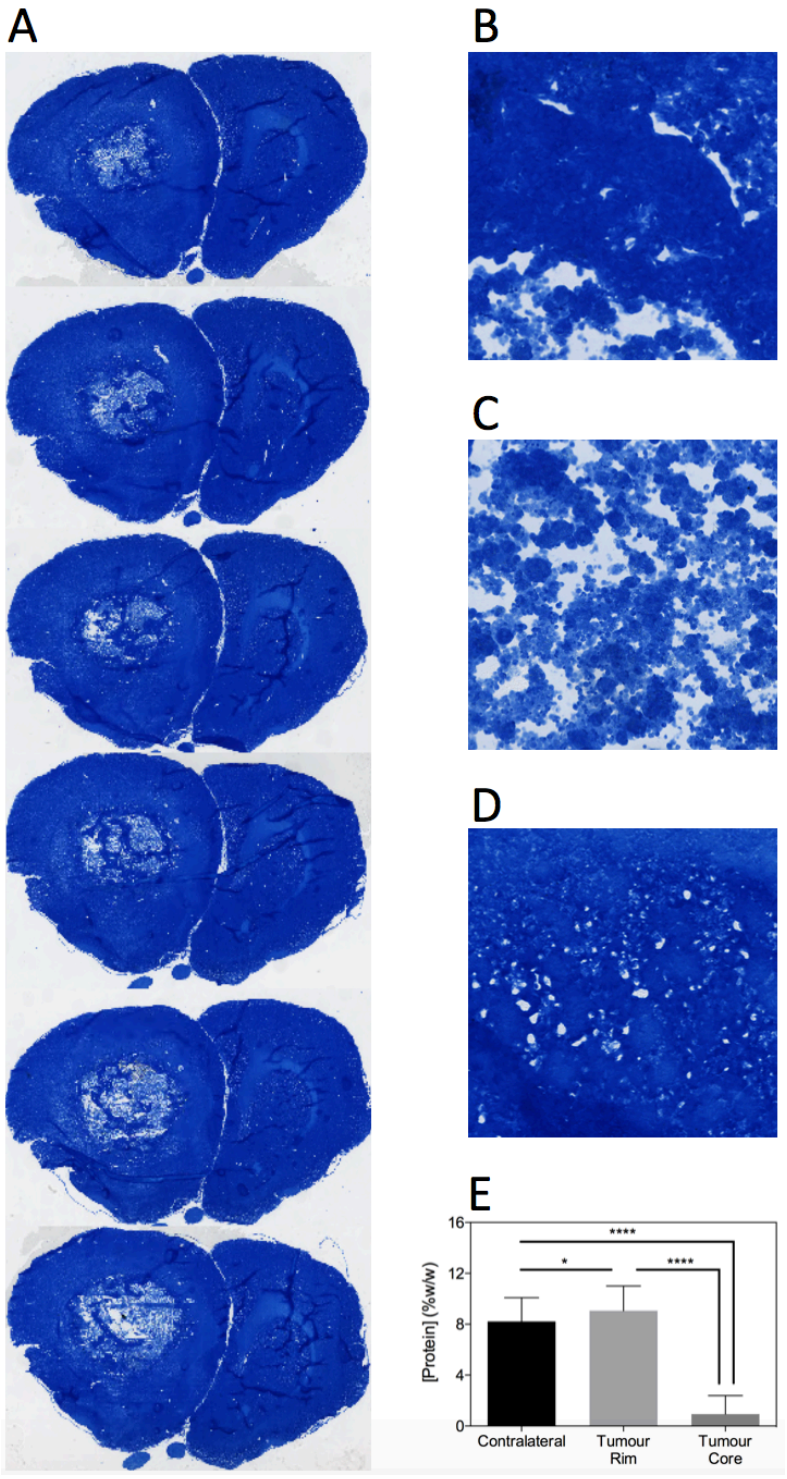

Figure 5.9: Example of Coomassie stained sections through a tumour from a representative rat (A), as well as zoomed ($200\times$ magnification) regions of tumour rim (B), tumour core (C) and contralateral (D) tissue. Groupwise quantitative protein concentration measurements (E) show that tumour rim has significantly higher protein content than contralateral tissue, whereas tumour core has significantly lower protein concentration than contralateral tissue. **** = $p < 0.0001$, ** = $p < 0.01$ from one-way repeated measures ANOVA followed by Tukey's multiple comparison test to compare protein concentrations in each tissue region.

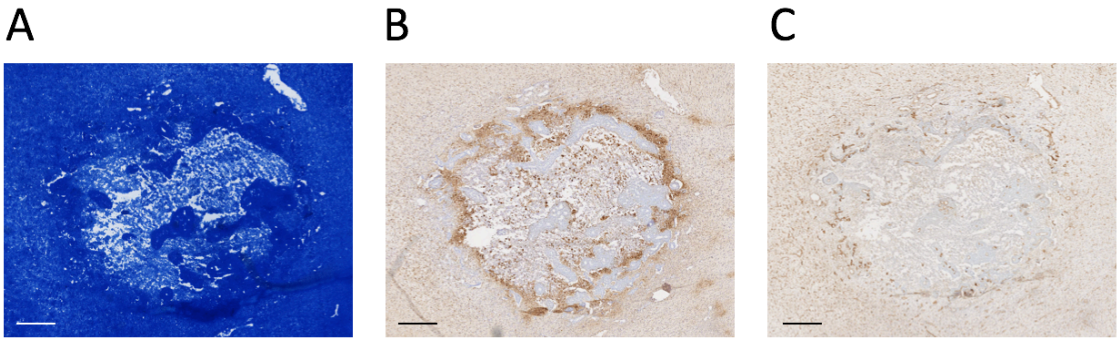

Figure 5.10: Comparison of adjacent tissue sections stained for Coomassie to show protein concentration (A), pimonidazole to show hypoxia (B), and CD31 to show blood vessels (C). Regions of high protein concentration (dark blue in A) correlate with regions of hypoxia (dark brown in B), indicating that these areas are likely to be infiltrating tumour rim. In addition, areas of cellular necrosis are visible in the hypoxia and CD31 stained images (no brown stain in B, C) which correlate with areas of lighter Coomassie stain, indicating a lower protein concentration. Scale bar = 500 µm.

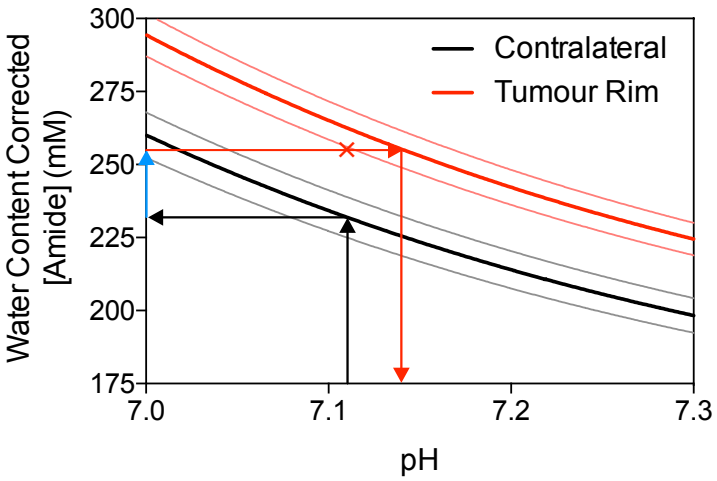

Figure 5.11: Demonstration of the isoCESTR* method to measure the pH of ENU tumours. Using the relative increase in protein concentration in the tumour rim tissue measured by Coomassie staining (10 %), a tumour pH of 7.14 ± 0.01 is measured. The red cross shows the CESTR* value that would be expected with no pH change in the tumour, indicating that approximately 66 % of the observed CESTR* change is owing to protein concentration changes, with the remaining 34 % a result of pH changes in the tumour.

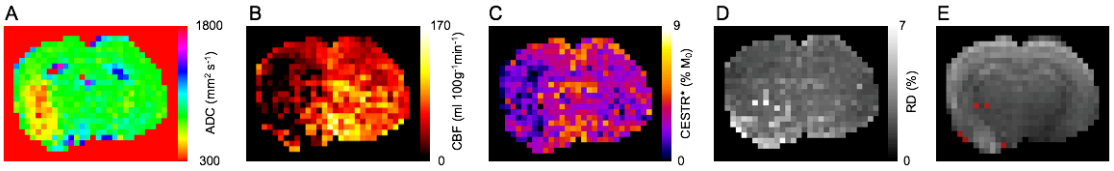

Figure 5.12: Multiparametric maps of a representative rat in the ischaemic stroke experiment, showing ADC (A), CBF (B), CESTR* (C) and the residual deviation of the model-fitted Z-spectra (D) at 2 h post-MCAO. Very few voxels are fitted with $RD > 7\%$, and are mainly at the edge of the brain (E).

5.3.2 Ischaemic stroke experiment

5.3.2.1 CEST MRI Results

The imaging for one rat was compromised[13], which delayed imaging by approximately 30 min. As a result, this animal was excluded from analysis in the 1 h timepoint, but was included for the 2 h timepoint. The CESTR*, CBF and ADC maps at 2 h post-MCAO from a single slice of a representative rat in the ischaemic stroke experiment are shown in Fig. 5.12A, B and C, respectively, as well as the residual deviation map showing the model fitting performance of BayCEST in Fig. 5.12D. The decrease in ADC associated with the infarct core area is evident, as is the larger perfusion deficit in the CBF map. The difference in CBF and ADC lesion areas is the commonly-defined diffusion-perfusion mismatch. A clear decrease in CESTR* is evident within the stroke lesion, and the residual deviation map shows adequate model-fitting performance across the whole brain, with 94/4655 voxels (2%) fitted with $RD > 7\%$. The location of these voxels is shown in Fig. 5.12E.

Figure 5.13 shows the rCESTR* value for each region across all animals at 1 h (Fig. 5.13A) and 2 h (Fig. 5.13B) post-MCAO. At 1 h post-MCAO, the infarct core showed a significantly decreased CESTR* compared to healthy tissue (rCESTR* = 0.7 ± 0.1, mean $\pm$ 95% CI, $n = 1289$ total voxels, $p < 0.0001$ from one-sample t-test comparing to hypothetical value of 1), as did the oligemic tissue (rCESTR* = 0.88 ± 0.07, mean $\pm$ 95% CI, $n = 3237$ total voxels, $p = 0.001$ from one-sample t-test comparing to hypothetical value of 1). At 2 h post-MCAO, the oligemic tissue has normalised (i.e. not significantly different from 1 as determined by one-sample t-test), while the infarct growth region showed a decreased CESTR* value (rCESTR* = 0.83 ± 0.09, mean $\pm$ 95% CI, $n = 576$ total voxels, $p = 0.001$ from one-sample t-test comparing to hypothetical value of 1). The infarct core tissue maintained a significantly decreased CESTR* value (rCESTR* = 0.7 ± 0.1, mean $\pm$ 95% CI, $n = 1289$ total voxels, $p < 0.0001$ from one-sample t-test comparing to hypothetical value of 1).

[13]The automatic calculation of the water-fat frequency offset did not complete correctly within VnmrJ, leading to on-resonant saturation prior to magnetisation readout instead of fat suppression.

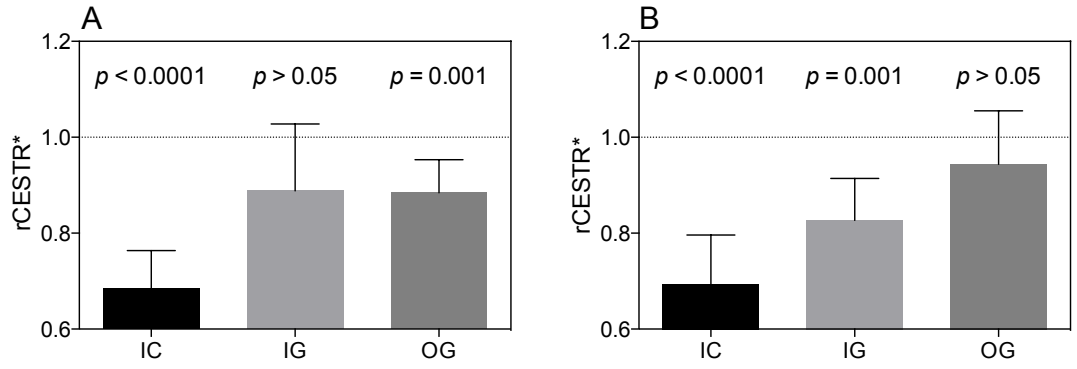

Figure 5.13: rCESTR* values (weighted mean ± 95% CI) in infarct core (IC), infarct growth (IG) and oligemia (OG) ROIs at 1 h (A) and 2 h (B) post-MCAO. p values are for one-sample t-test comparing to a hypothetical mean of 1. The number of voxels in each ROI was $n = 1289$ for IC, $n = 576$ for IG and $n = 3237$ for OG.

5.3.2.2 Protein concentration measurements

Quantitative protein concentrations measured by BCA assay of cytoplasmic and non-cytoplasmic fractions of tissue biopsied from the infarct core, ischaemic penumbra and contralateral hemisphere (sampled as shown in Fig. 5.1) are shown in Fig. 5.14A and Fig. 5.14B, respectively. Cytoplasmic protein concentration in the infarct core was significantly reduced compared to ischaemic penumbra or healthy tissue ($p < 0.05$ as determined by Tukey's post-hoc test following one-way ANOVA). Non-cytoplasmic protein concentration, likely dominated by cellular membrane associated proteins, was significantly elevated in infarct core tissue compared to ischaemic penumbra and contralateral tissue ($p < 0.05$ as determined by Tukey's post-hoc test following one-way ANOVA). Crucially, the cytoplasmic protein concentration in the ischaemic penumbral tissue region, which corresponds approximately with the infarct growth region of interest in the MRI results of Section 5.3.2.1, was not reduced compared to the healthy contralateral tissue. Since rCESTR* was quantified for amide protons, which are likely to be on the backbone and sidechains of mobile proteins and peptides in the cytoplasm, this result implies that the reduced rCESTR* seen at 2 h post-MCAO in the infarct growth region was likely driven by pH alterations alone. In addition, the decreased protein concentration in the infarct core implies that the reduced rCESTR* in the infarct core region was likely a result of simultaneous changes in pH and cytoplasmic protein concentration.

Further quantitative protein concentration measurements were made in animals with ischaemic stroke using Coomassie staining and imaging with histological resolution. Example sections through a region of ischaemic stroke in a representative rat are shown in Fig. 5.15A, as well as zoomed regions of the infarct core and contralateral hemisphere from a single section in Fig. 5.15B. These sections show a clear lighter blue staining (corresponding with lower cyto-

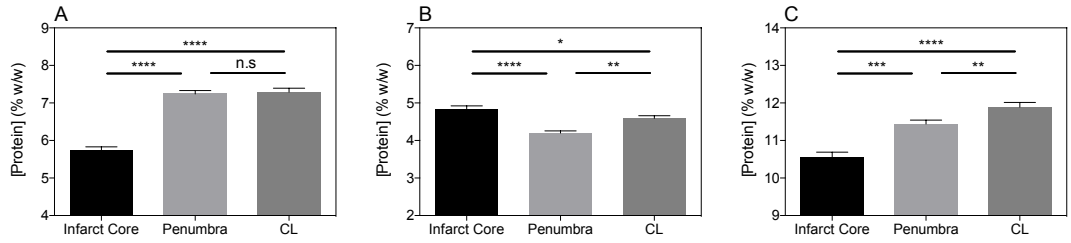

Figure 5.14: Cytoplasmic (A), non-cytoplasmic (B) and total (C) protein concentrations measured by BCA assay in each tissue region biopsied from $n = 3$ animals with ischaemic stroke. The total protein values displayed are summed from the cytoplasmic and non-cytoplasmic fractions. * = $p < 0.05$, ** = $p < 0.01$, *** = $p < 0.001$, **** = $p < 0.0001$ for Tukey's corrected multiple comparison test following one-way ANOVA.

plasmic protein concentration) in the infarct core than the contralateral hemisphere. However, significant amounts of tissue damage is also evident, likely a result of improper freezing of the tissue (see Section 5.4.3).

To reduce the effect of the tissue damage on the quantification of the blue RGB intensity within the infarct core and contralateral hemisphere, a custom MATLAB script was written to remove background pixels from the calculation of average blue RGB intensity. An RGB threshold was defined as RGB = (200,200,200) using a histogram analysis of a whole tissue section. Pixels with RGB above the threshold (i.e. more white) were replaced by 0 values, and the average blue RGB intensity within the region of interest then calculated using a combination of `mean` and `nonzeros` functions in MATLAB.

The blue RGB intensity of only the tissue within regions of interest comprising the infarct core and contralateral healthy tissue was quantified in all sections of all animals ($n = 25$ sections total throughout the stroke lesion in all animals), and converted to quantitative protein concentrations. The measured protein concentration in the infarct core was significantly lower than the contralateral hemisphere (Fig. 5.15C). Regions of interest of ischaemic core were guided by stains for healthy neurons (NeuN) in adjacent sections (Fig. 5.16).

5.3.2.3 Estimation of pH in infarct core

The isoCESTR* lines for the healthy contralateral brain and infarct core tissue are shown in Fig. 5.17. The CESTR* values plotted are the average from all animals (contralateral CESTR* = $3.43 \pm 0.10\,\%\,\mathrm{M_0}$, infarct core CESTR* ($0.7 \times 3.43 = 2.40 \pm 0.09\,\%\,\mathrm{M_0}$)). The absolute decrease in cytoplasmic protein concentration in infarct core tissue compared to healthy brain tissue as measured by BCA assay was 1.56 % *w/w* (Fig. 5.14), whereas by Coomassie staining was 5.5 % *w/w* (Fig. 5.15). These correspond to relative protein concentration decreases of 21 % or 69 % for BCA or Coomassie measurements, respectively.

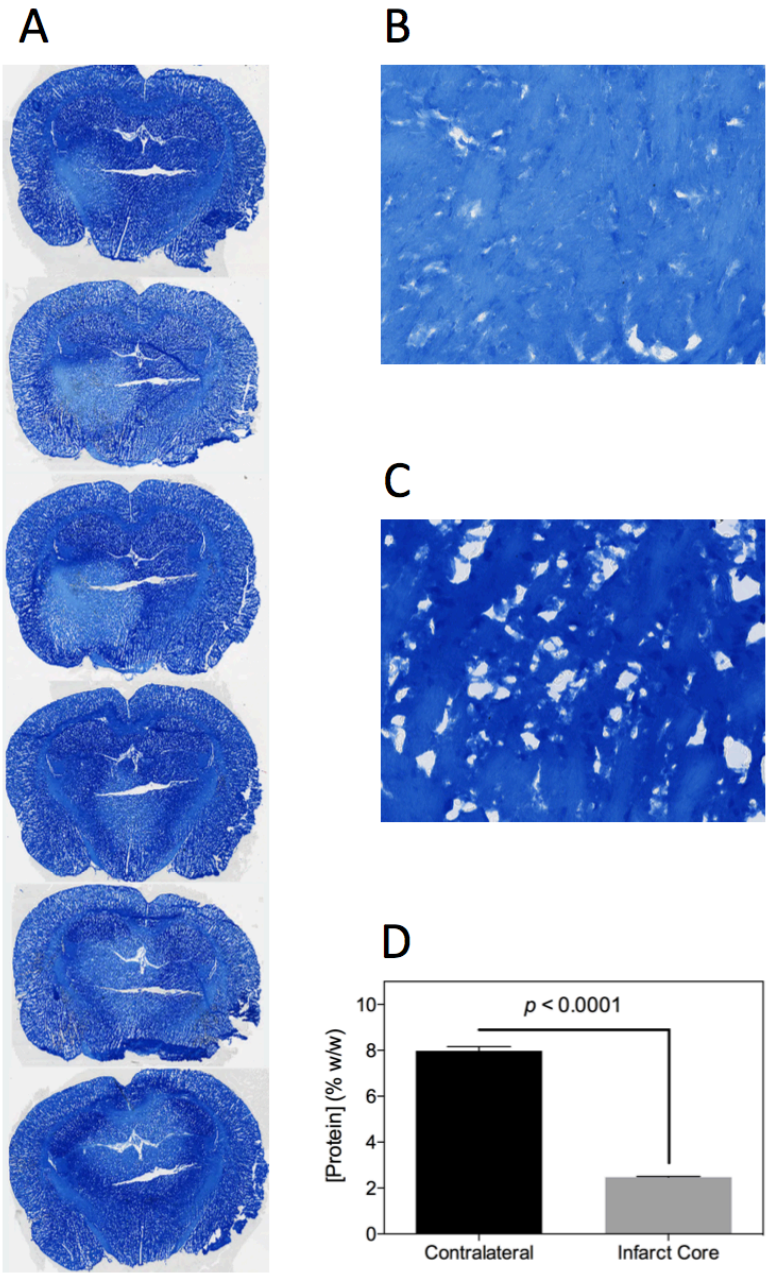

Figure 5.15: Example of Coomassie stained sections through a stroke lesion from a representative rat (A), as well as zoomed ($200\times$ magnification) regions of infarct core (B) and contralateral hemisphere (C) tissue. Groupwise quantitative protein concentration measurements (D) show that the infarct core has significantly lower protein content than contralateral tissue. p value is from unpaired t-test between contralateral ($n = 25$) and infarct core ($n = 25$) regions as defined by NeuN staining of adjacent tissue sections.

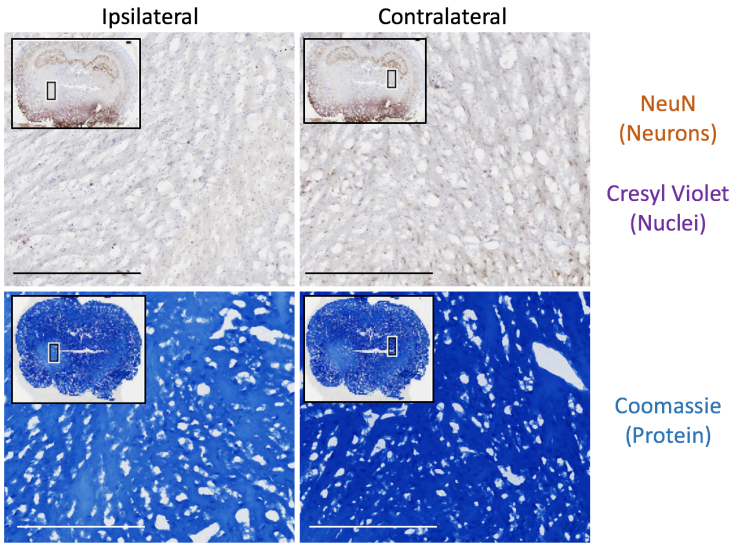

Figure 5.16: Verification that the infarct core lesion identified on Coomassie by lower protein concentration is the infarct core by staining an adjacent tissue section with NeuN. Absence of brown staining in the ipsilateral hemisphere is indicative of neuronal death associated with the infarct core region. Scale bar = 500 µm.

Using the isoCESTR* method of Section 4.2.6, assuming a healthy brain pH = 7.11 [89] and using the relative decrease of cytoplasmic protein concentration in infarct core tissue of 21 % as measured by BCA assay, the pH in the infarct core is estimated to be 6.98 ± 0.02. Errors were propagated based on the 95% CI of the CESTR* values in Fig. 5.17.

Based on the CESTR* expected if no pH change in the infarct core region occurred (cross-marked point in Fig. 5.17), it was estimated that 68 % of the observed CESTR* change was owing to protein concentration changes, with the remaining 32 % a result of pH changes in the infarct core.

5.3.3 Atovaquone treatment experiment

5.3.3.1 CEST MRI Results

CESTR* maps for a single slice through the tumours of representative mice in the atovaquone treated and control groups are shown in Fig. 5.18. The heterogeneity within the tumour is evident, which made analysis of these tumours difficult using the simple region of interest approaches adopted for the brain metastasis and ischaemic stroke experiments. In addition, there was no contralateral or adjacent normal tissue to use as within-animal control for calculation of rCESTR*. Cumulative frequency distributions for voxelwise CESTR* values within each group of animals are shown in Fig. 5.19. A statistically significant difference was evident between these cumulative frequency distributions ($p < 0.001$ as determined by Kolmogorov-Smirnov test), indicating that the median CESTR* in atovaquone treated animals was significantly reduced

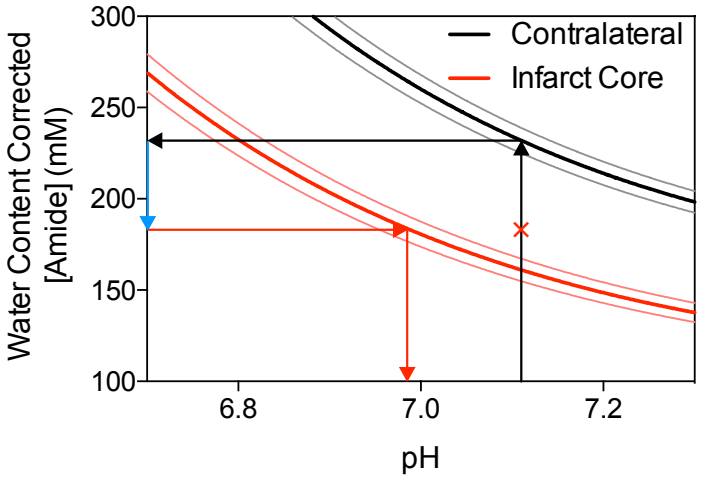

Figure 5.17: Demonstration of the isoCESTR* method to measure the pH of infarct core region of ischaemic stroke. Using the relative decrease in protein concentration in the infarct core region measured by BCA assay (20 %), an infarct core pH of 6.98 ± 0.02 is estimated. The red cross shows the CESTR* value that would be expected with no pH change in the infarct core, indicating that approximately 68 % of the observed CESTR* change is owing to protein concentration changes, with the remaining 32 % a result of pH changes in the infarct core.

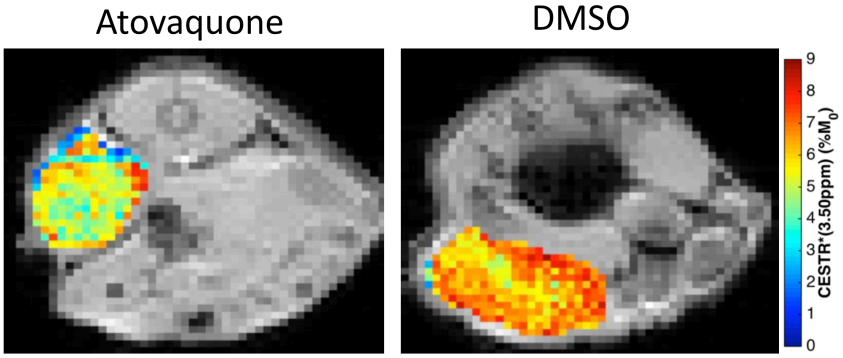

Figure 5.18: Representative CESTR* maps from mice in the atovaquone treated and control (DMSO treated) groups.

compared to control animals. The reduction in median CESTR* may originate from either a reduced protein concentration or pH in atovaquone treated animals.

5.3.3.2 Protein concentration measurements

Quantitative protein concentration measurements of cytoplasmic and non-cytoplasmic fractions of the subcellular fractionated tumours from atovaquone treated and control animals made by BCA assay are shown in Fig. 5.20. No significant difference in cytoplasmic protein concentration was found as a result of the atovaquone treatment ($p > 0.05$ as determined by two-tailed unpaired t-test), but a significant increase in non-cytoplasmic protein was evident ($p < 0.05$ as determined by unpaired two-tailed t-test). This result implies that the reduction in CESTR* seen

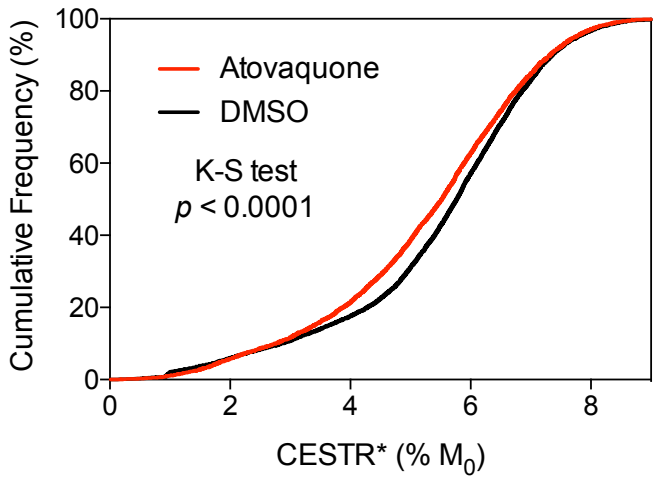

Figure 5.19: Cumulate frequency distributions for CESTR* values within the atovaquone treated and control groups of mice. The two distributions are significantly different ($p < 0.0001$ as determined by Kolmogorov-Smirnov test).

in atovaquone treated animals was a result of a change in pH, rather than a change in cytoplasmic protein concentration, since CESTR* quantified for amide protons is expected to be sensitive only to cytoplasmic protein concentration. The increase in non-cytoplasmic protein concentration in atovaquone treated animals may reflect a reduction in necrotic cells within the treated tumours. A greater number of intact cells within the tumour would likely result in a greater concentration of membrane bound (i.e. non-cytoplasmic) proteins. Since the xenograft tumours are known to be heterogeneous, and the protein concentration measurements by BCA assay do not retain information on this heterogeneity, protein concentration measurements using Coomassie and histological imaging were also made.

Figure 5.21 shows example Coomassie stained sections from atovaquone treated (Fig. 5.21A) and control (Fig. 5.21B) animals. The blue RGB intensity in the images is similar and relatively homogenous, indicating that the protein concentration in the two sections is similar. The blue RGB intenstiy across all sections in all animals ($2-3$ sections per animal taken throughout the tumour, $n = 22$ total for atovaquone animals, $n = 15$ for control) was measured and converted using the standard curve in Fig. 5.4 to give the protein concentration measurements in atovaquone treated and control animals shown in Fig. 5.21C. In agreement with BCA assay derived protein concentration measurements, no significant difference was measured ($p > 0.05$ as determined by two-tailed unpaired t-test). Since the protein concentration in atovaquone treated tumours is not significantly different to DMSO treated tumours, this implies that the CESTR* change observed is wholy a result of a change in pH.

Further histological characterisation of the tumours was performed using immunofluores-

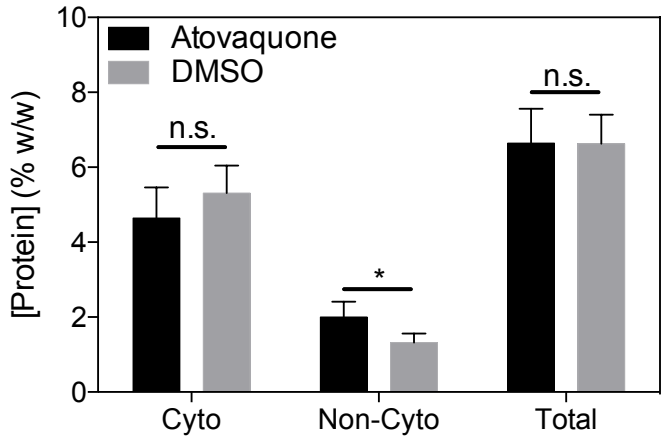

Figure 5.20: Cytoplasmic (left), non-cytoplasmic (middle) and total (right) protein concentrations measured by BCA assay of tumour tissue recovered from mice treated with atovaquone (black, $n = 5$) or DMSO (grey, $n = 5$). The total protein values displayed are summed from the cytoplasmic and non-cytoplasmic fractions. Protein concentrations in each region were compared by unpaired two-tailed t-test, with Bonferroni correction for multiple comparisons. * = $p < 0.05$, n.s. = $p > 0.05$.

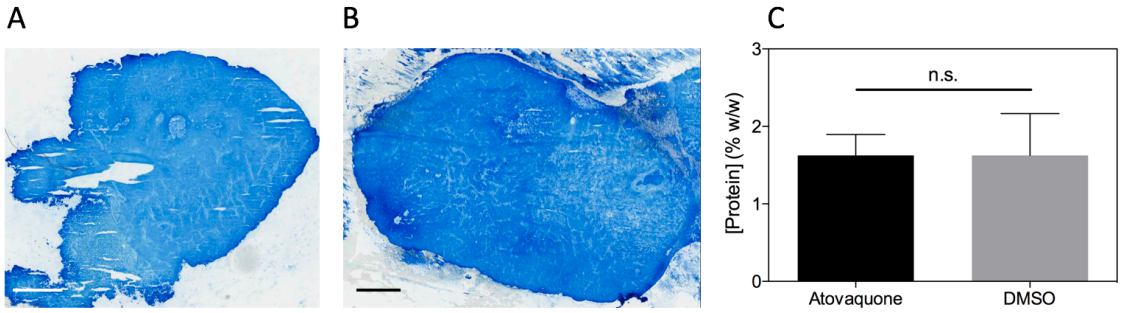

Figure 5.21: Examples of Coomassie stained sections from tumours in atovaquone treated (A) and control (B) mice. No significant difference was evident in protein concentration measured by Coomassie staining of all sections from all animals (C, $n = 22$ atovaquone group, $n = 15$ control group, n.s. = $p > 0.05$ from unpaired two-tailed t-test). Scale bar = 1 mm.

cence to evaluate the extent to which tumour hypoxia was alleviated in atovaquone treated animals. Example immunofluorescence images are shown in Fig. 5.22A, with areas of tumour hypoxia shown in green in the EF5 images and cellular areas shown blue in the DAPI images. Quantitation of the normalised intensity of EF5 staining shows a significant reduction of hypoxia in atovaquone treated animals compared to control (Fig. 5.22B, unpaired t-test, $p < 0.05$). In addition, comparison of the Coomassie stained sections with adjacent sections stained for EF5 shows that the protein concentration was lower in areas likely to be necrotic (lighter blue in Coomassie correlates with areas of no EF5/DAPI staining), but was relatively homogenous in areas of heterogenous hypoxia (Fig. 5.22C).

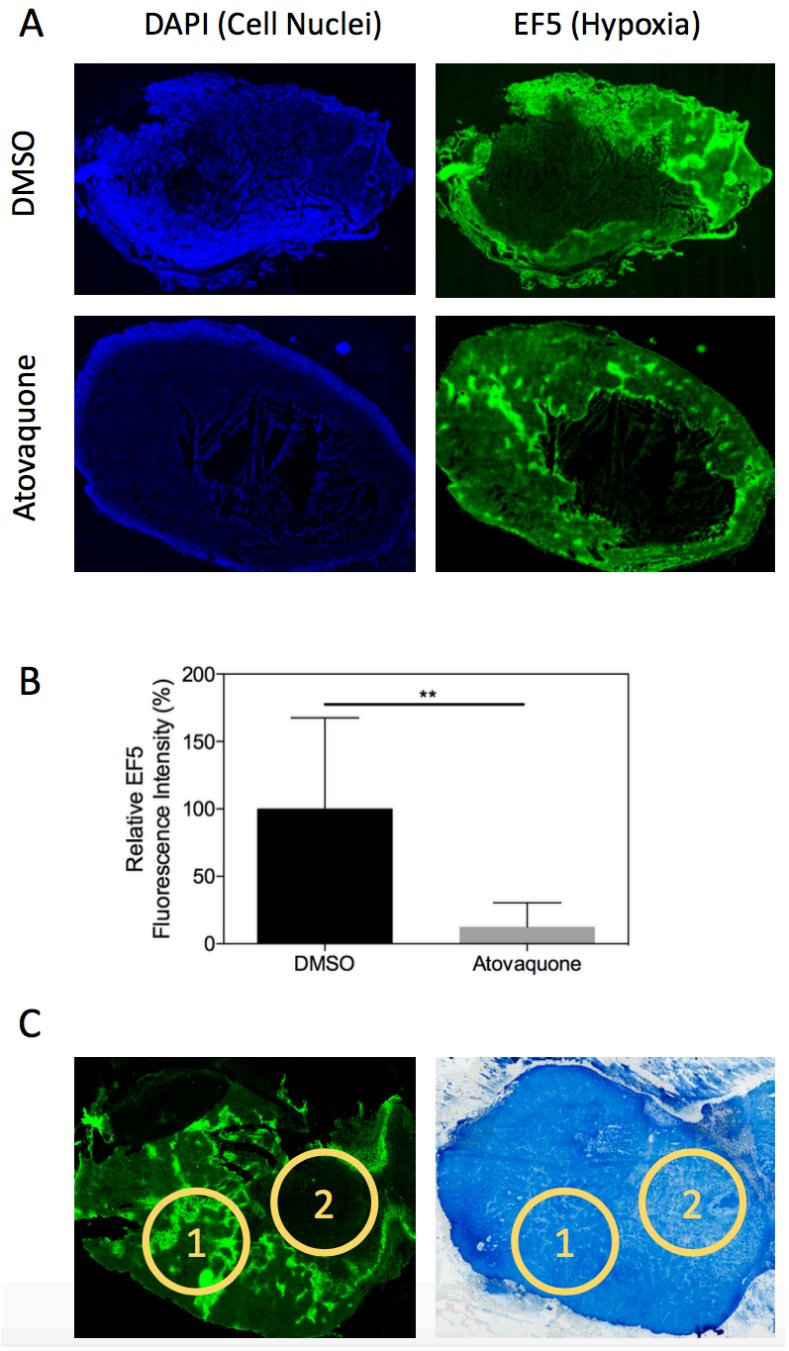

Figure 5.22: A: Example immunofluorescence images from DMSO and atovaquone treated animals showing cellular nuclei in blue (DAPI) and areas of hypoxia in green (EF5). B: Quantification of EF5 fluorescence intensity across all animals reveals a significant decrease in intensity in atovaquone treated animals (** = $p < 0.01$, unpaired two-tailed t-test, $n = 9$ measurements in both groups from five atovatuone-treated animals and six DMSO-treated animals), corresponding to a decrease in tumour hypoxia. C: Comparison of EF5 and Coomassie staining in DMSO treated mouse reveals that protein concentration is not correlated with hypoxia. Region 1 identifies an area of heterogenous EF5 staining, indicating heterogenous hypoxia in the tumour, whereas region 2 highlights an area of likely necrosis based on the complete lack of EF5 staining. Region 1 in the Coomassie is comparatively homogenous, suggesting that protein concentration is not significantly altered with hypoxia. Region 2 is shown in the Coomassie with a slightly lighter stain, possibly indicating a reduction in protein concentration in the necrotic area.

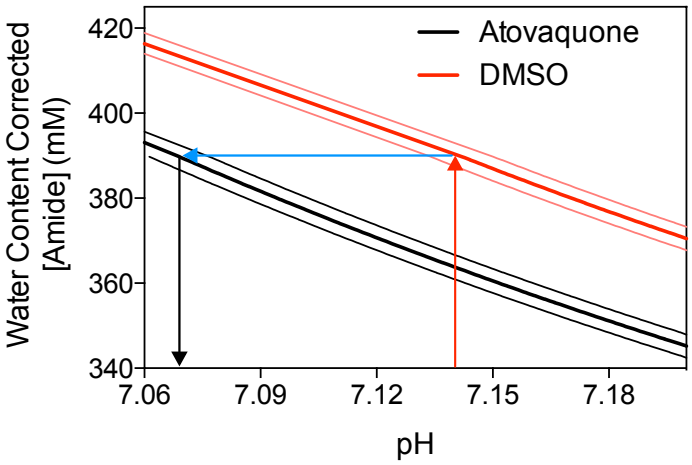

Figure 5.23: Demonstration of the isoCESTR* method to measure the change in tumour pH due to atovaquone treatment. Since no significant difference in protein concentration was measured by BCA assay (Fig. 5.20) or Coomassie staining (Fig. 5.21), the difference in measured CESTR* was assumed to be derived from an altered tumour pH only. A change in tumour pH due to atovaquone treatment of -0.07 pH units was estimated (errors propagated from the 95% CI on CESTR* measurements).

5.3.3.3 Estimation of pH change in atovaquone treated animals

Based on the change in mean CESTR* value in atovaquone treated animals compared to control (CESTR* = $5.27 \pm 0.04\,\%\,\mathrm{M_0}$ in atovaquone animals, $5.46 \pm 0.04\,\%\,\mathrm{M_0}$ in control animals, mean $\pm$ 95% CI) and using these values in an isoCESTR* analysis (Fig. 5.23), a change in tumour pH due to atovaquone treatment of -0.07 pH units to pH 7.07 ± 0.01 (errors propagated from the 95% CI on CESTR* measurements) was estimated. This pH change has been estimated assuming a control tumour pH of 7.14, as measured for tumour pH of ENU brain metastasis in Section 5.3.1.4. This change in pH may reflect an alteration in tumour metabolism following alleviation of hypoxia in areas of the tumours.

5.4 Discussion

The results of this chapter provide new insights into the source of *in vivo* CEST MRI signal changes in the two most common applications studied in preclinical and clinical settings, cancer and ischaemic stroke. Previous studies have interpreted changes in CEST signal in tumours as originating solely from the increased intracellular protein content, and in stroke as from only an intracellular acidosis [56, 89, 101, 199, 209]. The results of this chapter show that whilst these processes contribute to the observed changes in *in vivo* CEST MRI signals, concomitant changes in pH in tumours and protein content in infarcted stroke regions make quantification of the physiological parameters of interest difficult.

In addition, it has been shown for the first time that alterations in the observed CEST MRI signal can be induced through alteration of the tumour microenvironment in a hypoxic xenograft model of hypopharyngeal squamous cell carcinoma. The observed change in CESTR* was consistent with an alteration in pH occuring at the same time as alleviation of hypoxia in tumours, and implies that CEST MRI may enable non-invasive visualisation of the effect of hypoxia-modifying treatments.

5.4.1 Histological measurement of protein concentration

One novelty of the work presented in this chapter is the combination of protein concentration measurements derived from a histological approach with *in vivo* CEST MRI measurements to assist in the interpretation of the *in vivo* CEST MRI signals. The measurement of protein concentration using a Coomassie stain is not in itself a novel concept, and is used routinely in standard biochemical techniques to visualise protein bands in SDS-PAGE. However, its use in histology is less widespread, and to the author's knowledge has never been combined with *in vivo* MRI data.

Certain difficulties arise when trying to use histology in combination with MRI. The CEST MRI readout employed *in vivo* encompasses the entire tumour or stroke volume. Practical considerations make histology of the entire tumour or stroke volume difficult. The two orders of magnitude difference in the tissue thickness probed by the two methods would mean that 1000 tissue sections would have to be combined to cover the same volume of the MRI data. Even for the relatively small studies described in this chapter, processing this much tissue is impractical. This shortcoming was alleviated somewhat by measuring the protein concentration from histological sections taken from different locations within the tumour or stroke lesion volume.

Calibrating the protein concentration measurements using a gold standard biochemical (BCA assay) method is important for the histological measurement of protein concentration. The calibration method employed in this chapter is similar to a previous study [207]. However, differences in tissue thickness between the standards and the experimental tissue sections will contribute to differences in absolute Coomassie present in the tissue sections. The concentration standards were stained in the same batch of Coomassie at the same time as the experimental tissue, and digitised in the same way, so the experimental conditions were as identical as possible. However, natural variation in staining intensity from subtle differences in tissue thickness and morphology will lead to differences in absolute blue RGB values between the tissue standards and the tissue sections.

The above factors may explain some of the differences seen between protein concentration measurements made by BCA assay or Coomassie staining. In the brain metastasis experiment,

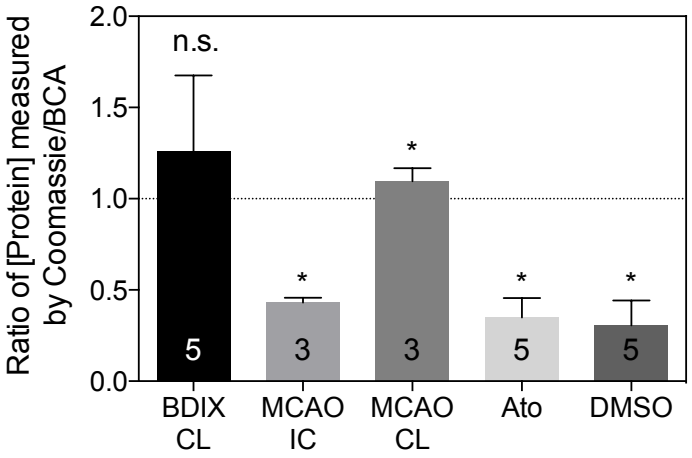

Figure 5.24: Comparison of protein concentrations measured by Coomassie and BCA assay methods for the tissue samples that are able to be directly compared across all three experiments in this chapter. Mean $\pm$ 95% CI are plotted for the ratio of protein concentration measured by Coomassie and BCA assay methods. * signifies a result significantly different ($p < 0.05$) from 1 as determined by a one-sample t-test. Numbers in each bar are the number of animals in each group used for the t-test.

a significant difference in protein concentration was measured between tumour rim, tumour core and contralateral tissue in Coomassie staining, whereas no difference was measured by BCA assay. This result is thought to reflect the additional information concerning tumour heterogeneity that is preserved by measuring protein concentration using Coomassie staining, but is lost when using the BCA assay.

However, in the stroke and atovaquone treatment experiments, whilst the same pattern of protein concentration measurements was preserved between BCA assay and Coomassie staining (less protein in infarct core areas in the stroke experiment; equivalent protein concentration in atovquone or control groups in the atovaquone experiment), the absolute protein concentration measurements were significantly different (Fig. 5.24). In fact, only the contralateral hemisphere protein concentration measurement in the brain metastasis experiment showed good agreement between Coomassie staining and BCA assay. Whilst further methodological refinements may improve the measurement of protein concentration by Coomassie staining, it should also be noted that this comparison assumes that the tissue is identical in the two measurements. This assumption may be invalid if the tissue biopsy for the BCA assay was affected by partial volume effects.

5.4.2 Brain metastasis experiment

The brain metastasis animal model employed in this experiment recapitulates the heterogeneity present in human brain metastases, both in terms of within tumour heterogeneity and between

animals. Aiming to measure the protein concentration of these tumours by taking a single biopsy and processing for BCA assay, therefore, is likely to result in estimations of protein concentration that are not a true reflection of the infiltrating tumour tissue. The partial voluming effect of biopsying an unknown proportion of infiltrating tumour along with necrotic tissue is evident in the different results for protein concentration measurement by BCA assay or Coomassie staining. The mapping of protein concentration with histological resolution through staining with Coomassie is a preferred option for retaining the heterogeneity information present within these, and likely other, tumours.

The measurement of protein concentration this way found a significantly higher protein concentration in the tumour rim than in the contralateral hemisphere, but a significantly reduced protein concentration in the necrotic core. The tumour rim *in vivo* rCESTR* measurement was elevated, as expected based on the protein concentration measurement and previous literature in tumour-bearing animals [101, 121]. The necrotic tumour core, however, displayed an elevated *in vivo* rCESTR* despite the lower protein concentration measured by Coomassie staining.

Whilst initially this result may seem troublesome, clinical CEST MRI studies have also measured elevated CEST MRI signals in suspected necrotic or cystic portions of tumours [136], which are attributed to an increased proportion of mobile proteins in these areas [210, 211]. These proteins may not be retained within the fixed and sectioned tissue used for Coomassie staining since acellular tissue areas are difficult to retain throughout the sectioning and staining process. The absence of tissue renders in the Coomassie staining as a complete absence of staining, which will bias the protein concentration measurements in tumour core regions of interest. This limitation of measuring protein concentration by Coomassie staining is inherent to the procedure of histology, but arguably still provides more information than a simple BCA assay from a tumour biopsy.

In addition, the protein concentration measurement results by BCA assay presented in this chapter agree with previous measurements from a 9L glioma animal model [117]. This result implies that a BCA assay may not capture the full heterogeneity of the 9L model, and perhaps future protein concentration measurements of this model using the Coomassie staining procedure described in this chapter would be beneficial.

The invasive nature of histology limits the clinical translatability of the method. One may also wonder whether a technique that requires biopsying a tumour to measure the pH of the same tumour is worthwhile. The proposed technique for histological measurement of protein concentration, and the associated estimation of pH by isoCESTR*, is not necessarily meant for clinical *translation*, however, but merely to aid in the *interpretation* of CEST MRI. Whereas prior clinical studies have interpreted the CEST MRI signal in terms of changes in intracellular protein

content in isolation, in reality the CEST MRI signal change in tumours is also affected by pH changes. As long as the CEST MRI signal quantification technique employed is sufficiently sensitive to both protein concentration and pH changes, the measured *in vivo* CEST signal will be a combination of both effects.

The estimated pH change in the tumour regions have not been independently validated. The best candidate method for performing these validations would be ^{31}P MRS as it probes the same intracellular space that the CEST MRI signal has been assumed to report on. Unfortunately, no ^{31}P RF coil with sufficient performance was available at the time of performing the experiments. The limitations of ^{31}P MRS may still prevent reliable validation of the CESTR*-derived pH estimates, however, since it is likely it would only be possible to acquire a spectrum from a single voxel covering the entire infiltrating tumour and necrotic tissue area. The influence of partial voluming within this voxel would likely serve to make the pH estimate not suitable for validation of pH measurements within only the infiltrating tumour region.

Other pH validation methods such as fluorescent imaging [192] or pH-sensitive diaCEST agents [142] may be possible, but these rely on exogenous tracers reaching the target tissue in sufficient concentration to provide a signal. Histology of the implanted ENU tumours shows them to be very poorly perfused with an abnormal vascular network, which would likely mean the exogenous tracers would not reach the tissue in sufficient quantity. Whilst diaCEST agents have been used with some success to measure tumour pH in xenograft models of breast cancer [142], to date there is no example of an exogenous diaCEST agent being used to estimate the pH of a tumour implanted in the brain. Pilot studies completed by colleagues before the author began their DPhil, using iopamidol to measure pH in a different animal model (DAOY cells implanted in the medulla as a model of medulloblastoma), demonstrated that iopamidol does not accumulate in tumours in sufficient concentration to provide a CEST signal, despite breakdown of the blood brain barrier (personal communication, Dr. Sébastien Serres).

As such, the isoCESTR*-derived pH estimates can only be compared to previous literature estimates of pH in brain metastasis. It has been assumed here that the pH measured is an intracellular pH as the CEST MRI signal reports predominantly on the intracellular environment. This assumption is likely to be invalid, however, given that the extracellular space can also contribute to the signal. The effect of tissue compartmentalisation is investigated fully in Chapter 6. Nevertheless, assuming the pH estimate is weighted to the intracellular space, the pH_i measurement in this study is in line with previous intracellular alkalosis measurements made in cell lines, animal experiments and patients [22–24, 62, 183, 212].

5.4.3 Ischaemic stroke experiment

To the author's knowledge, the work presented in this chapter represents the first time that the effect of altered protein concentration has been investigated as a contributing factor to CEST MRI signal changes in ischaemic stroke. Whilst again the measurement of protein concentration is an invasive procedure, thereby limiting its clinical translatability, these experiments do improve understanding of the origin of CEST MRI signals in ischaemic stroke patients in the clinic. Importantly, and most excitingly for clinical applications, the protein concentration did not change in the ischaemic penumbra region, but the CESTR* decreases relative to contralateral healthy tissue. This result implies that the signal change in this region reflects a pH change alone, suggesting that this tissue is metabolically stressed and informing on tissue regions that could be recovered if treatment is delivered promptly. The measured reduction in cytoplasmic protein concentration in the infarct core is consistent with existing literature from other preclinical ischaemic stroke experiments [44], which observed a cessation of protein synthesis in tissue regions with blood flow of less than 20 ml/100g/min. Additionally, the decreased blood flow in these tissue regions would also imply a decreased concentration of blood-associated proteins, such as albumin, which may contribute to the decreased CEST MRI signals observed in oligemic tissue. It is unlikely that this factor is dominant, however, since the vascular volume of a voxel is far smaller than the brain parenchyma volume.

Frustratingly, the preparation of tissue to be used for histological processing was compromised in the ischaemic stroke experiment, resulting in extensive damage to the structure of the tissue. It is likely that the damage was caused by improper cryopreservation of the tissue, and the formation of ice crystals when freezing the tissue. As a result, tissue structures were damaged, causing the well-known 'swiss cheese' appearance. This tissue damage made quantification and analysis of the resultant histological images more difficult. Nevertheless, for the purposes of Coomassie staining for quantification of protein concentration, all of the tissue remained in place (albeit distorted), so a simple thresholding of white background pixels from the digitised section images (as was implemented in this study) can be used.

Even so, the agreement of Coomassie and BCA protein concentration measurements in the ischaemic stroke experiment is poor (Fig. 5.24). Using the isoCESTR* method with Coomassie derived protein concentration changes yields unphysiological pH values in the infarct core. In addition, the accuracy of the infarct core pH measurement using isoCESTR* with BCA derived protein concentration changes may be questioned; more acidotic pH measurements have been made by other methods in infarct regions of ischaemic stroke [44, 213, 214]. This disagreement may be a result of experimental differences, particularly since the MRI data in this work were acquired in the very acute stages of ischaemic stroke.

5.4.4 Atovaquone treatment experiment

To the author's knowledge, the results of the atovaquone treatment study presented in this chapter represent the first instance of CEST MRI being used to visualise changes in tumour hypoxia. The dependence of the CEST MRI signal, as quantified by CESTR*, on hypoxia was verified through extensive *ex vivo* tissue characerisation. Analysis of CEST MRI by CESTR* was performed using T_1 and T_2 priors based on *ex vivo* measurements of the T_1 and T_2 time, rather than *in vivo*, as no respiration gated relaxation mapping sequence was available at the time of the study. Whilst post-mortem T_1 and T_2 times in the tumour will likely be different from the *in vivo* values, the magnitude of the difference is unlikely to have had any effect on the accuracy of the CESTR* quantification of the CEST MRI signal.

The measured range of CESTR* values within tumours in both the atovaquone treated and control groups was quite wide ($0-8\,\%\,M_0$). The assumption made during the isoCESTR* analysis was that the amide proton concentration across the whole tumour volume is constant. Extending the isoCESTR* analysis to individual voxels, this assumption would imply an unphysiological range of pH values. This result highlights one key limitation of the isoCESTR* method, already mentioned in the previous chapter, that it can only be applied on an ROI basis.

Additionally, this result highlights the known invalidity of the assumption of a constant amide proton concentration across the whole tumour volume, as was visualised by histology of Coomassie stained tissue sections. Integration of the regional variation of amide proton concentration to the isoCESTR* method is limited by the difficulties of co-registering histology and MRI data. Despite the extensive *ex vivo* tissue characterisation performed as part of all three experiments in this study, no effort was made to co-register the histological and MRI images. Differences in tissue orientation between the MRI and histological sectioning make the co-registration of these types of images difficult unless the tissue itself is well-structured (e.g. the brain). As such, only full tumour volume measurements can be matched to the *ex vivo* tissue measurements, rather than investigating the heterogeneity present within the CEST MRI and histological images.

The direction of the CESTR* change in atovaquone treated animals compared to control is that expected if there were an intracellular acidification to normal levels. Hypoxia and pH are inextricably linked within the tumour microenvironment [13], with hypoxia being associated with expression of pH-regulating proteins, including carbonic anhydrase IX (CAIX) [196]. CAIX maintains the transmembrane pH gradient between intra- and extracellular environments in hypoxic tumours, promoting proliferation via an alkalotic intracellular pH and invasion and metastasis by an acidic extracellular pH [215, 216]. By shifting the tumour to a more normoxic microenvironment through treatment with atovaquone, CAIX expression is restricted and the pH

regulation of the tissue in turn shifts to a more acidic intracellular pH and alkaline extracellular pH.

5.4.5 Accuracy of amide proton concentration estimates by isoCESTR*

In theory, it is possible to directly measure amide proton concentration from a protein concentration measurement made by BCA assay or Coomassie staining by making assumptions about the size, structure and conformation of the proteins measured, as well as the abundance of amide protons within protein molecules. For instance, an equation of the form Eq. 5.9 relates a measured amount of protein Pg, from a brain tissue biopsy of mass Bg, to the estimated molar amide proton concentration [NH]. In Eq. 5.9, N_A is Avagadro's constant ($6.023 \times 10^{23}\,\mathrm{mol}^{-1}$), N^p_{NH} is the number of amide protons per protein molecule, M_P is the molar mass of protein, $N^p_{H_2O}$ is the number of water protons in the brain tissue sample, WC is the water content of the brain tissue sample, [H_2O] is the molar concentration of water (112 M), and EF is the exchangeable fraction of amide protons available for chemical exchange.

$$[\mathrm{NH}] = \left(\frac{\frac{\mathrm{P}}{M_P} \times N_A \times N^p_{NH}}{N^p_{H_2O}} \right) \times \mathrm{WC} \times \mathrm{EF} \times [\mathrm{H_2O}] \tag{5.9}$$

Since the BCA assay permits absolute quantitation of protein amount, and the mass of a brain tissue biopsy is known, further simplifications of Eq. 5.9 can be made. For instance, using the density of brain of 1.05 g brain / ml brain [89] and density of water of $1\,\mathrm{g\,ml}^{-1}$, it can be determined that in a brain tissue mass of 1 mg there is 0.8 µl water with mass 0.8 mg. In this mass of water there are $0.8\,\mathrm{mg}/18.01528 = 0.444\,\mu\mathrm{mol}$ of water, which can be used to calculate $0.444\,\mu\mathrm{mol} \times N_A = 2.67 \times 10^{19}$ molecules or $N^p_{H_2O} = 2 \times 2.67 \times 10^{19} = 5.34 \times 10^{19}$.

Since P is measured and N_A, [H_2O] and WC are all known from literature, the only remaining factors to calculate before estimates of [NH] can be made are N^p_{NH}, M_P and EF. EF is a difficult parameter to estimate directly, but reasonably good estimates of N^p_{NH} and M_P can be made by making assumptions concerning the "average" protein in the brain[14]. The median length of a human protein is 375 amino acid residues [217], and the molar mass and abundance profile within the human proteome of each amino acid is known (see Table 5.2). Assuming the abundance of amino acid residues within the average protein is identical to that seen across the full proteome, and inspecting the structure of each amino acid to determine how many amide groups are in each one, the number of amide groups per average protein can be calculated. For an average protein which is 375 amino acid residues long, 374 amide groups would be expected in the protein

[14]The author recognises the absolute horror with which Biochemists would react to this sentiment, and understands their disgust of the elimination of their field with one fell swoop. The "average protein" in CEST MRI reflects a similar idea to the "spherical cow in a vaccuum" — a necessary albeit unrealistic assumption.

Letter code	Amino Acid Name	Abundance (%)†	Molar Mass (g mol^{-1})	Amides in R group	Residues in Avg Protein*	Amides Overall
A	Alanine	7.19	89.09	0	28	0
C	Cysteine	2.81	121.16	0	12	0
D	Aspartic Acid	5.29	133.10	0	22	0
E	Glutamic Acid	6.38	147.13	0	22	0
F	Phenylalanine	3.82	165.19	0	15	0
G	Glycine	7.05	75.07	0	28	0
H	Histidine	2.77	155.15	1	11	11
I	Isoleucine	4.08	131.17	0	14	0
K	Lysine	6.46	146.19	0	27	0
L	Leucine	8.74	131.17	0	29	0
M	Methionine	2.00	149.21	0	7	0
N	Asparagine	3.99	132.12	0	17	0
P	Proline	5.69	115.13	0	19	0
Q	Glutamine	4.21	146.14	0	14	0
R	Arginine	4.94	174.20	2	16	32
S	Serine	8.18	105.09	0	30	0
T	Threonine	5.77	119.12	0	23	0
V	Valine	6.40	117.15	0	26	0
W	Trytophan	1.29	204.23	1	5	5
Y	Tyrosine	2.97	181.19	0	12	0

Table 5.2: Table of amino acid residues within the human proteome and their relative abundance. † The abundance listed is the average from two independent analyses in [218] and [219]. * The number of residues of each amino in the average protein was calculated based on the assumption that the average protein is 375 residues long.

backbone, 11 amide groups from histidine sidechains, 32 amide groups from arginine sidechains, and 5 amide groups from tryptophan sidechains, giving a total $N^p_{NH} = 422$. In addition, using the abundance of each amino acid as a weighting factor to sum up their individual molar masses, the molar mass of an average protein can be calculated as $M_P = 48\,328\,\mathrm{g\,mol^{-1}}$.

An estimate of EF can be made from studies examining the solvent accessibility of amide protons within individual model proteins. For instance, one study using MALDI-TOF mass spectrometry of example globular (thrombin) and nonglobular (IκBα) proteins estimated an exchangeable fraction of around 20% [220]. A separate study employing molecular dynamic simulations of ubiquitin suggests 25% of amino acid residues are solvent accessible [221]. However, a separate method to estimate EF from CEST MRI data is to use the amide proton concentration [NH] found in healthy brain tissue in the brain metastasis and ischaemic stroke experiments and use a rearranged version of Eq. 5.9 to solve for EF. For a healthy brain pH of 7.11 [89] and a healthy brain tissue CESTR* of $3.43 \pm 0.10\,\%\,\mathrm{M_0}$, the estimated water content corrected amide proton concentration was [NH] = 232 mM (Fig. 5.11). A rearranged version of Eq. 5.9, with the average contralateral protein concentration of $6.9 \pm 0.9\,\%\,w/w = 69\,\mu\mathrm{g}$ in a hypothetical 1 mg tissue biopsy from the ischaemic stroke and brain metastasis experiments, gives an exchangeable fraction of approximately 35 % estimated using CEST MRI data (Eq. 5.10).

$$\begin{aligned} \mathrm{EF} &= \frac{M_P \times [\mathrm{NH}] \times N^p_{H_2O}}{N_A \times N^p_{NH} \times \mathrm{WC} \times \mathrm{P} \times [\mathrm{H_2O}]} \\ &= \frac{48\,328\,\mathrm{g\,mol^{-1}} \times 232\,\mathrm{mM} \times 5.348 \times 10^{19}}{6.023 \times 10^{23}\,\mathrm{mol^{-1}} \times 422 \times 0.87 \times 69\,\mu\mathrm{g} \times 112\,\mathrm{M}} \\ &= 35\% \end{aligned} \tag{5.10}$$

While EF = 35 % is slightly higher than the estimates of EF from molecular dynamic simulations or mass spectrometry, it is at least of similar order of magnitude and represents a reasonable estimate of the proportion of amide protons available for chemical exchange within a tissue region. Following a similar process but instead using [NH] = 350 mM, as was previously determined from analysis of CEST MRI data collected in human white matter using the BayCEST algorithm, EF = 53 % is calculated. This exercise shows the likelihood that [NH] = 350 mM is biologically implausible since independent measurements of EF are in the range 20 – 25 %. Using EF = 25 % as calculated from molecular dynamic simulations [221], an amide proton concentration of 165 mM is estimated, approximately 71% the value estimated by isoCESTR*.

Unfortunately validation of these estimates is likely to only be possible using molecular dynamic simulations of a particular model protein with CEST measurements from a homogenous sample of that same protein. Nevertheless, it is an interesting exercise in validation of the isoCESTR* method and determining order of magnitude estimates of amide proton concentrations *in vivo* from *ex vivo* protein concentration measurements.

Finally, this section also explicitly highlights alterations of protein conformation and structure as further biophysical sources of changes in *in vivo* CEST MRI signals. The CEST MRI signal will be altered if only EF in Eq. 5.9 changes between healthy and pathologic tissue. This signal dependency has been investigated in well-controlled NMR studies [146, 147, 222], but has yet to be fully explored *in vivo*. The CESTR* and BCA assay protein concentration results of the tumour core region in the brain metastasis experiment suggest that perhaps an increase in the exchanging fraction of amide protons is the source of the increased CESTR* signal, since the BCA assay measures an identical protein concentration to healthy tissue. This mechanism is consistent with known protein physiology within cystic regions of tumours, which are more hydrolysed and are comprised of smaller peptide fragments than in healthy tissue [223].

5.5 Conclusion

The methods and results presented in this chapter represent:

- the first time that imaging of Coomassie staining at histological resolution has been used in combination with *in vivo* MRI;
- the first time that changes in protein concentration in ischaemic stroke have been studied as a source of altering the CEST MRI signal; and
- the first time that alleviation of tumour hypoxia has been imaged using CEST MRI.

The results of this chapter provide new insight into the source of the *in vivo* CEST MRI signal by combining *in vivo* CEST MRI measurements with *ex vivo* measurements of protein concentration. Through doing this, it was estimated that approximately 66 % and 68 % of observed CEST MRI signal changes in brain metastasis and ischaemic stroke, respectively, is due to a change in protein concentration. Consequently, quantitative estimates of pH in brain metastasis and ischaemic stroke lesions were made using a novel isoCESTR* method.

Chapter 6

Separation of intra- and extracellular CEST effects

Contents

6.1 Introduction . . . 138
6.2 Methods . . . 139
6.2.1 Simulations . . . 139
6.2.2 DiffusionCEST Pulse Sequence . . . 141
6.2.3 Sample Preparation . . . 142
6.2.4 NMR Experiments . . . 145
6.2.5 Data Analysis . . . 145
6.3 Results . . . 147
6.3.1 Simulations . . . 147
6.3.2 GUVs . . . 149
6.3.3 Cells . . . 150
6.3.4 Post-mortem animals . . . 153
6.4 Discussion . . . 155
6.5 Conclusion . . . 158

6.1 Introduction

The amide proton CEST effects observed *in vivo* are predominantly assumed to originate from the intracellular space [89]. This assumption is based on the knowledge that the majority of amide protons found *in vivo* are located on the backbone and side chains of polypeptides and protein molecules, and these proteins are generally found in the intracellular environment [224]. In addition, the T_2 relaxation time of the amide protons must be long enough to be observed in the CEST spectrum, and this only occurs for amide protons on relatively quickly tumbling molecules in the fluid intracellular space. Proteins associated with cellular membranes or the extracellular matrix are generally in a more solid-like environment, resulting in a slower tumbling rate and fast T_2 relaxation time.

While this assumption seems a plausible and reasonable one to aid and simplify the interpretation of *in vivo* CEST spectra, it has never been thoroughly and rigorously validated. Since the ability of CEST to measure a signal from *in vivo* amide protons is predominantly limited by the T_2 relaxation time of those protons, there is nothing preventing extracellular amide protons contributing to the measured *in vivo* signals; the extracellular environment *in vivo* is still predominantly liquid-state from an NMR perspective. Quantifying the contribution of extracellular amides to the CEST MRI signal would be particularly beneficial in studying tumours, which are characterised by an altered metabolic phenotype leading to intracellular alkalosis and extracellular acidosis [212].

Specifically quantifying intra- and extracellular signals in NMR and MRI has been attempted previously by applying diffusion-weighting to pulse sequences [158, 160, 225, 226]. Signals that are sensitive to the degree of motion restriction imposed by a cellular membrane can be measured by applying diffusion-weighting to a given pulse sequence with sufficiently long diffusion time between the diffusion-encoding gradients. Intracellular specific signals have previously been recorded in NMR spectroscopy of live cells [158]. However, such studies are typically done using very idealised samples, ignoring the complications that arise when dealing with *in vivo* environments.

One such complication for separating intra- and extracellular signals *in vivo* is transmembrane exchange of water. While the fraction of intracellular water *in vivo* is within the range of 60 – 80 %[**Ackerman1983**], individual water molecules are in a constant state of transfer between intra- and extracellular locations. Not only can water diffuse across the cell membrane since it is a relatively small molecule, but it is also actively transported across the membrane by proteins, such as those in the aquaporin family. If the transmembrane (also known as transcytolemmal to refer specifically to exchange across the cell membrane) exchange rate is sufficiently fast then the separation of intra- and extracellular water populations may not be possible as they will be

well-mixed. Estimates of the transcytolemmal exchange rate vary with cell type and whether the measurements are made *in vivo* or in less physiologically relevant settings [172, 227–230].

In this chapter, the aim was to develop a novel method that allows separation of intra- and extracellular CEST spectra, in order to quantify the proportion of CEST signal originating from each physical space. Realistic simulations of normal and tumour tissue are used to demonstrate and investigate the effect of compartmentalisation on Z-spectra. The novel method developed — termed 'diffusionCEST' — was applied to well-controlled samples of cellular mimicking giant unilamellar vesicles (GUVs) to validate the ability of the method to separate CEST spectra based on physical location. The method was subsequently applied to samples of homogenously suspended cells and post-mortem mouse brain for further validation, and to evaluate the performance of the method to reliably separate the CEST spectra from intra- and extracellular environments. Finally, quantitative estimates of the proportion of CEST signals arising from the intracellular and extracellular spaces of complex biologically relevant samples were made.

6.2 Methods

6.2.1 Simulations

Several separate simulations of standard CEST MRI pulse sequences were implemented as part of this study. The first simulation was used to investigate the effect of tissue compartmentalisation on Z-spectra by simulating two six-pool systems representing the intra- and extracellular spaces, with a transcytolemmal exchange term between the two water populations. A diagram of the simulated system is shown in Fig. 6.1. Normal brain tissue and tumour tissue were both simulated, with parameter values given in Table 6.1 and Table 6.2, respectively. The parameter values used in the simulations are taken from previous literature [89, 117, 125, 126, 196, 197]. For tumour tissue, the concentration increase of protons in the amide, amine and NOE pools was assumed to be 10%, as measured in Chapter 5. The CESTR* metric was used to quantify the CEST effect from amide protons at 3.5 ppm.

Simulations were also done where each parameter that differed between tumour and normal tissue was varied in turn, with all other parameters kept at their normal brain values, to evaluate the extent to which each parameter contributed to the overall CESTR* signal change. These simulations all used the same Monte Carlo method used in Chapter 4 to include physiological and random sources of noise. Standard deviations on each parameter were set to the values displayed in Table 6.1 and Table 6.2, and 200 instances of the simulations run, to reflect biological variability. To capture the effect of random noise in the Z-spectra, Eq. 4.2 was used to add random noise on to each iteration of the simulation with $\varepsilon = 1.5\,\%\,\mathrm{M}_0$.

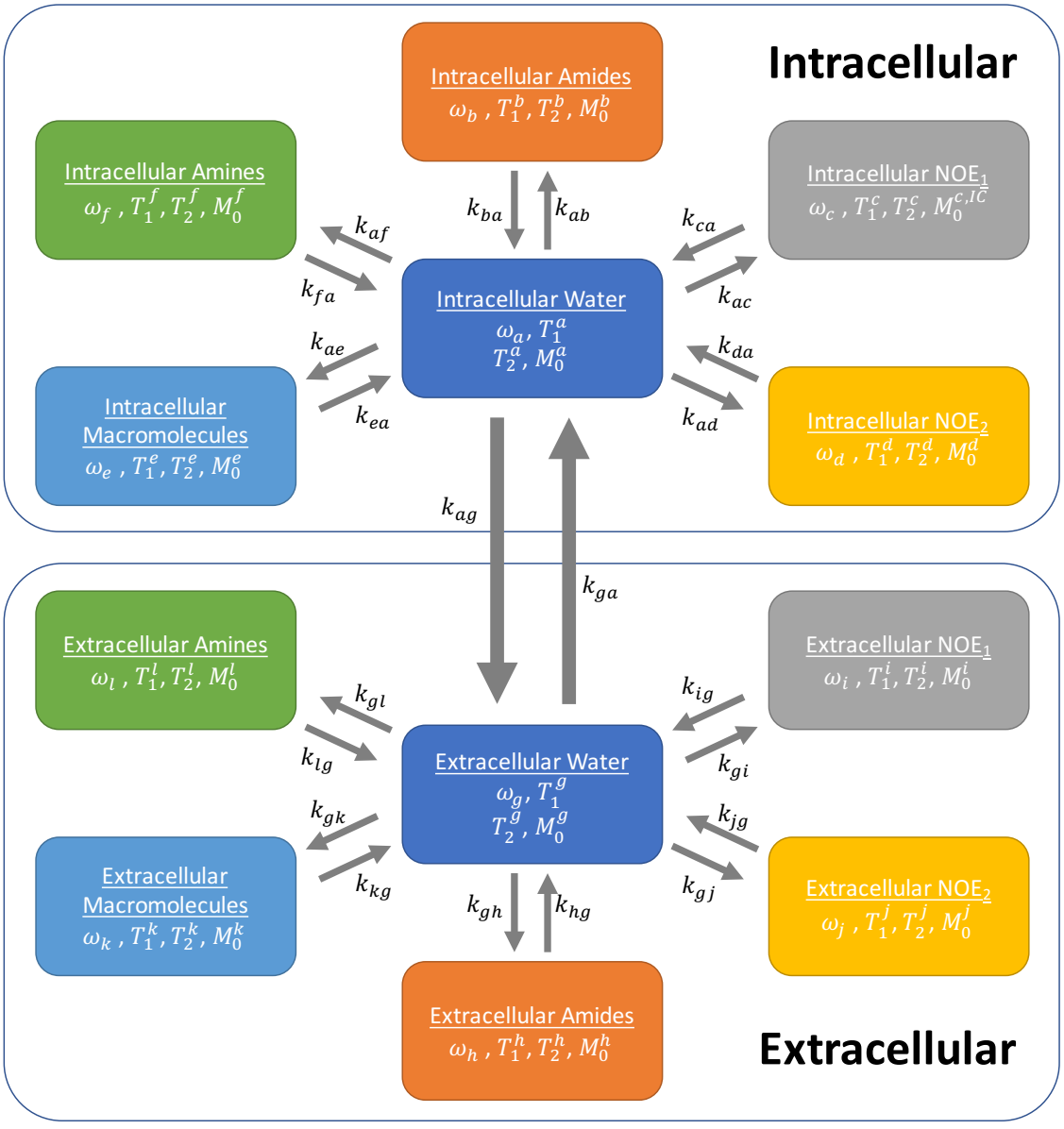

Figure 6.1: Schematic of realistic model used to determine the extent to which each evaluate dependency of CESTR* on labile pool parameters and evaluate the performance of the BayCEST model based analysis method. Parameter values used are in Table 6.1 and Table 6.2 for healthy and tumour tissue, respectively.

	Intracellular — pH 7.11						Extracellular — pH 7.11					
Name	**Pool A IC Water**	**Pool B Amides**	**Pool C NOE 1**	**Pool D NOE 2**	**Pool E MT**	**Pool F Amines**	**Pool G EC Water**	**Pool H Amides**	**Pool I NOE 1**	**Pool J NOE 2**	**Pool K MT**	**Pool L Amines**
ω_i (ppm)	0	3.5	-3.0	-1.6	-2.30	2.0	0	3.5	-3.0	-1.6	-2.30	2.0
M_0^i (mM)	89600	80 ± 6	533 ± 13	266 ± 13	3733 ± 17	23 ± 2	22400	40 ± 3	267 ± 7	133 ± 7	7467 ± 33	12 ± 1
$k^*_{ia,g}$ (Hz)	-	29 ± 3	50 ± 0	50 ± 0	13 ± 3	420 ± 50	5.0 ± 0.2	29 ± 3	50 ± 0	50 ± 0	13 ± 3	420 ± 50
T_1^i (s)	1.60 ± 0.15	1 ± 0	1 ± 0	1 ± 0	1 ± 0	1 ± 0	1.60 ± 0.15	1 ± 0	1 ± 0	1 ± 0	1 ± 0	1 ± 0
T_2^i (ms)	42 ± 3	2 ± 0	0.5 ± 0	1 ± 0	$(7.5 \pm 2) \times 10^{-3}$	10 ± 0	42 ± 3	2 ± 0	0.5 ± 0	1 ± 0	$(7.5 \pm 2) \times 10^{-3}$	10 ± 0

Table 6.1: Simulation parameters used to reflect Z-spectra acquired from normal brain. The intracellular proportion of amide, amine and NOE protons was assumed to be 2/3, whereas the intracellular proportion of MT protons was assumed to be 1/3. * Pools B — F exchanged only with the intracellular water (pool A) and pools H — L exchanged only with extracellular water (pool G). The transcytolemmal exchange rate between intracellular and extracellular water is denoted as k_{ga}.

	Intracellular — pH 7.30						Extracellular — pH 6.70					
Name	**Pool A Water**	**Pool B Amides**	**Pool C NOE 1**	**Pool D NOE 2**	**Pool E MT**	**Pool F Amines**	**Pool G Water**	**Pool H Amides**	**Pool I NOE 1**	**Pool J NOE 2**	**Pool K MT**	**Pool L Amines**
ω_i (ppm)	0	3.5	-3.0	-1.6	-2.30	2.0	0	3.5	-3.0	-1.6	-2.30	2.0
M_0^i (mM)	89600	88 ± 6	586 ± 13	293 ± 13	1733 ± 17	25 ± 2	22400	44 ± 3	294 ± 7	146 ± 7	3467 ± 33	13 ± 1
$k^*_{ia,g}$ (Hz)	-	44 ± 5	50 ± 0	50 ± 0	20 ± 3	650 ± 80	5.0 ± 0.2	11 ± 2	50 ± 0	50 ± 0	20 ± 3	160 ± 20
T_1^i (s)	2.30 ± 0.15	1 ± 0	1 ± 0	1 ± 0	1 ± 0	1 ± 0	2.30 ± 0.15	1 ± 0	1 ± 0	1 ± 0	1 ± 0	1 ± 0
T_2^i (ms)	35 ± 3	2 ± 0	0.5 ± 0	1 ± 0	$(12.5 \pm 2) \times 10^{-3}$	10 ± 0	35 ± 3	2 ± 0	0.5 ± 0	1 ± 0	$(12.5 \pm 2) \times 10^{-3}$	10 ± 0

Table 6.2: Simulation parameters used to reflect Z-spectra acquired from tumour tissue. The intracellular proportion of amide, amine and NOE protons was assumed to be 2/3, whereas the intracellular proportion of MT protons was assumed to be 1/3. * Pools B — F exchanged only with the intracellular water (pool A) and pools H — L exchanged only with extracellular water (pool G). The transcytolemmal exchange rate between intracellular and extracellular water is denoted as k_{ga}.

Further fully deterministic simulations (i.e. with standard deviations on parameters and ε set to 0) were run for normal and tumour tissue paramater combinations with variable transcytolemmal exchange rate, in order to determine the extent to which this parameter affects the Z-spectra and CESTR* measured in both tissues. The CEST sequence simulated comprised a continuous wave saturation with B_1 = 1.17 µT (corresponding to 50 Hz) for 2 s. The overall water pool Z-magnetisation (i.e. $M_Z = M_Z^A + M_Z^G$) was used for plotting Z-spectra and model fitting to reflect the measurement made in typical CEST MRI acquisitions.

6.2.2 DiffusionCEST Pulse Sequence

The novel diffusionCEST NMR/MRI pulse sequence is shown in Fig. 6.2. The pulse sequence comprises a standard stimulated echo acquisition mode (STEAM) diffusion pulse sequence with an additional CEST encoding module inserted during the diffusion time delay, Δ. The basic premise is to sensitise the magnetisation to both diffusion and CEST signals in the same pulse sequence. By acquiring Z-spectra for a range of diffusion weightings, it may then be possible to separate CEST effects into intra- and extracellular spaces based on the differing diffusion properties in these environments. Using a STEAM sequence means that long Δ times can be

implemented, which enables longer CEST saturation durations to be used, therefore enhancing the CEST signal encoding, and ensures that the measured signal is sensitive to restriction effects of cellular boundaries. In addition, the signal decay during the Δ time is governed by T_1 decay, which occurs on a much slower timescale than the T_2 relaxation decay that governs the signal evolution in the Δ of spin echo diffusion sequences. Whilst the stimulated echo diffusion sequence loses a factor of two of SNR compared to spin echo sequences, the T_1 signal decay and ability to use long Δ times, which also allows a CEST signal to be encoded onto the signal, makes stimulated echo diffusion a suitable candidate for the diffusionCEST pulse sequence.

The pulse sequence was first implemented on a 14 T verical bore NMR spectrometer (Agilent)[1]. The CEST encoding module comprised a single continuous wave RF pulse of duration $T_{sat} = 500\,\mathrm{ms}$ and saturation power $B_1 = 1.17\,\mu\mathrm{T}$. The diffusion time $\Delta = 513\,\mathrm{ms}$, diffusion gradient duration $\delta = 2\,\mathrm{ms}$, TR = 2 s, TE = 20 ms, mixing time (TM) = 500 ms. CEST spectra were measured using 52 evenly spaced saturation frequency offsets for $\Omega = \pm 5\,\mathrm{ppm}$, with signal following saturation at $\Omega = 300\,\mathrm{ppm}$ used for normalisation. Each CEST spectrum was acquired with a different diffusion gradient strength G_D applied along the z-axis. G_D was varied as $G_D = 4 - 54\,\mathrm{G\,cm^{-1}}$ (diffusion b-value = 200 – 42 000 s mm^{-2}) in quadratically spaced steps, for a total of 264 recorded signals in a total acquisition time of 8 min 48 s.

Subsequently, the pulse sequence was implemented on a 9.4 T horizontal bore preclinical MRI scanner (Agilent). The CEST saturation scheme was implemented on the 9.4 T scanner as a pulsed saturation scheme. Each pulse module comprised a 19 ms gaussian pulse with flip angle 180°, followed by a 1 ms crusher gradient. The 20 ms pulse module was repeated $N = 25$ times for a total saturation time of $T_{sat} = 500\,\mathrm{ms}$ with equivalent continuous wave saturation power $B_1 = 0.63\,\mu\mathrm{T}$. CEST spectra were measured using 42 evenly spaced saturation frequency offsets between the limits $\Omega = \pm 5\,\mathrm{ppm}$, with signal following saturation at $\Omega = 300\,\mathrm{ppm}$ used for normalisation. G_D was varied as 3 – 35 G cm^{-1} in 7 logarithmically spaced steps for each CEST spectrum, giving diffusion b-values between 99 – 18 000 s mm^{-2} with $\Delta = 513\,\mathrm{ms}$ and $\delta = 2\,\mathrm{ms}$. TR, TE and TM were the same as at 14 T. Gradients were applied along the x-, y- and z-axis simultaneously.

6.2.3 Sample Preparation

In order to determine whether the diffusionCEST pulse sequence can separate CEST effects based on compartmentalisation, a number of *in vitro* and *ex vivo* samples were studied.

[1]The diffusionCEST pulse sequence was implemented on the 14 T verical bore NMR spectrometer by Gogulan Karunanithy.

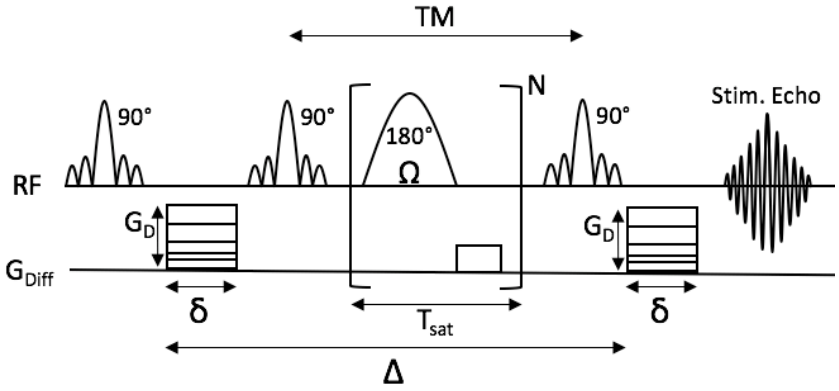

Figure 6.2: DiffusionCEST pulse sequence. The pulse sequence comprises a standard stimulated echo acquisition mode (STEAM) diffusion pulse sequence with an additional CEST encoding module inserted during the diffusion time delay, Δ.

6.2.3.1 Giant Unilamellar Vesicles (GUVs)

Giant unilamellar vesicles (GUVs) are cellular mimics manufactured by rolling a lipid bilayer into a spherical shell with a diameter of $\mathcal{O}(10\,\mu\mathrm{m})$. GUVs were used in this study to replicate the cellular membrane boundary between the intra- and extracellular spaces, and two separate CEST visible molecules placed within and outside the GUVs. By applying the diffusionCEST pulse sequence to a sample of GUVs, we are able to determine whether separation of intra- and extra-GUV CEST spectra is possible. In this study, 200 mM sucrose was encapsulated within the GUVs, which were then suspended in a solution of 20 % *w/w* bovine serum albumin (BSA). Since sucrose and BSA demonstrate different CEST effects, this model system serves as a good test sample to discover the ability of the diffusionCEST pulse sequence, and associated analysis method (see Section 6.2.5), to separate the intra- and extracellular CEST spectra.

GUVs were produced using a recently-developed cost-effective method[2] [231]. Briefly, a solution of 1,2-Dioleoyl-sn-glycero-3-phosphocholine (DOPC, Avanti Polar Lipids, 1 mg ml^{-1} in chloroform) and cholesterol (Sigma-Aldrich, 10 mg ml^{-1} in chloroform) was prepared to achieve a 1:3 molar ratio and was then pipetted (25 µl per electrode) onto nine pairs of stainless steel electrodes. After allowing the chloroform to evaporate overnight, the electrodes were immersed in 200 mM sucrose at room temperature. A signal generator was used to apply a 4.87 Vpp, 10 Hz sinusoidal wave signal for two hours to induce vesicle swelling. Subsequently, the frequency of excitation was lowered to 5 Hz for 30 minutes to facilitate vesicle detachment.

The GUV-rich solutions were then transferred to a 50 ml tube filled with 27 ml PBS and allowed to sediment overnight. An aliquot of concentrated GUV solution was added to an equal volume

[2]GUVs were manufactured by Valerio Pereno and Dr. Luca Bau in the Institute of Biomedical Engineering, University of Oxford. The details of the manufacturing protocol presented here are courtesy of Valerio Pereno.

of 20 % *w/w* BSA in PBS doped with D_2O, and the resulting solution transferred to a 5 mm inner diameter NMR tube for use in the 14 T spectrometer. To minimise the shear stress experienced by the GUVs, the end of the pipette tip was cut to a 2 mm inner diameter. The size and concentration of the GUVs was determined using a Zeiss LSM 780 microscope and a purpose-built MATLAB routine that detects the GUVs using the `imfindcircles` function[3].

6.2.3.2 Cells

Two separate cellular samples were prepared for use in the 14 T NMR spectrometer. The first was a simple suspension of 4T1-GFP (mouse mammary carcinoma) cells in PBS. Cells were cultured as a monolayer in Dulbecco's Modified Eagle's Medium (DMEM; Sigma Aldrich, UK) at 37 °C, and passaged when necessary until a sufficient number were available for harvest. Cells were detached from the culture flask using trypsin (Sigma Aldrich, UK), all available cells pooled into a single tube and a cell pellet formed by spinning in a centrifuge (1000×*g*, 5 min at 4 °C). Cells were subsequently resuspended in PBS, counted using a Countess™ II FL Automated Cell Counter, and transferred to an NMR tube.

In addition, homogenous suspensions of 4T1-GFP cells with varying cell number were prepared. Cell management and preparation was identical to the PBS samples. Samples comprising 1.2, 2.3, 4.6, and 9.3 $\times 10^6$ cells were made by combining the necessary volume of cells with PBS and matrigel. Matrigel is a commonly-used mixture of extracellular matrix proteins that is liquid at low temperature (4 °C), but becomes gelatinous above approximately 10 °C, thus slowing cell sedimentation when the cells are in an NMR tube. Samples were prepared at 4 °C and homogeneity ensured by mixing the cells, PBS and matrigel well. The mixture was rapidly transferred to a chilled NMR tube and submerged in a water bath at 37 °C to quickly form a homogenous gel sample within the NMR tube.

6.2.3.3 Post-mortem animals

Two separate post-mortem animal samples were prepared to evaluate the diffusionCEST pulse sequence in a more complex and physiologically relevant environment. The first was brain tissue from a naïve Wistar rat placed into an NMR tube. Briefly, a single female Wistar rat was sacrificed by overdose of pentobarbitol delivered intraperitoneally. The head was removed, brain exposed and removed from the skull, and then an NMR tube inserted through the brain to insert tissue into the tube. This process was repeated until sufficient tissue was within the NMR tube, with minimal structural integrity retained. The tissue was pushed to the bottom of the NMR tube and used in the vertical bore 14 T spectrometer.

[3]The MATLAB routine was written by Valerio Pereno.

The second post-mortem sample was intact whole mouse brain from a naïve BALB/c mouse. A single female BALB/c mouse was sacrificed by overdose of pentobarbitol delivered intraperitoneally and placed inside the 9.4 T preclinical MRI scanner. A 26 mm volume transmit/receive coil (Rapid Technologies) was used for imaging and spectroscopy. Following localisation scans and shimming, a single voxel covering the whole brain was defined for acquiring diffusionCEST signals.

6.2.4 NMR Experiments

Stimulated echo diffusion experiments without any CEST signal encoding during the diffusion time delay Δ were performed on samples in the 14 T spectrometer to verify the presence of two water populations in each sample[4]. The acqusition details were identical to the diffusionCEST pulse sequence, with the exception of no CEST signal encoding module during the mixing time. The stimulated echo diffusion experiment without CEST encoding was repeated with $\Delta = 0.1-0.5\,\mathrm{s}$ in 0.1 s steps. This so-called 'variable Δ' dataset was fitted to a complex biophysical model of the signal evolution as Δ varies (see Section 6.2.5) to determine diffusion coefficients and volume fractions from the water populations present in each sample, as well as the rate of exchange of water between the two populations.

6.2.5 Data Analysis

Data acquired using the diffusionCEST sequence were analysed using a simple biexponential description of the signal variation as a function of diffusion b-value[5]. Each signal, S, in (b, Ω) variable space was fitted globally to the biexponential signal model in Eq. 6.1, where each signal acquired with CEST saturation at offset frequency Ω is fitted with identical diffusion coefficients, $D_{1,2}$. $f_{1,2}$ represent the volume fractions of the two water populations, and Ω is the offset frequency of the CEST saturation pulses in the diffusionCEST pulse sequence. b refers to the diffusion b-value, which is defined as $b = \gamma^2 G^2 \delta^2 (\Delta - {}^{\delta}/_{3})$, where $\gamma = 267.5 \times 10^6\,\mathrm{rad\,s^{-1}\,T^{-1}}$ is the gyromagnetic ratio of the proton, G is the diffusion gradient strength, and δ and Δ are defined as in Fig. 6.2. The two water populations separated by the biexponential model were assigned to the intra- and extracellular spaces, and a Z-spectrum for each population plotted. The CEST effect in each Z-spectrum was quantified using the $\mathrm{MTR_{asym}}$ metric rather than CESTR* because the aim of this study was merely to determine whether non-zero CEST effects could be measured using the diffusionCEST pulse sequence, for which the $\mathrm{MTR_{asym}}$ metric suffices. The proportion of the CEST signal originating from the intracellular compartment was quantified by $\frac{\mathrm{MTR^{IC}_{asym}}}{\mathrm{MTR^{IC}_{asym}}+\mathrm{MTR^{EC}_{asym}}}$.

[4]NMR experiments on the 14 T spectrometer were performed by Gogulan Karunanithy, with sample preparation and production performed by the author.

[5]The analysis script for diffusionCEST and variable Δ data was an in-house custom python script written by Gogulan Karunanithy and Dr. Andrew Baldwin.

$$S(b,\Omega) = f_1(\Omega)e^{D_1 b} + f_2(\Omega)e^{D_2 b} \tag{6.1}$$

The intracellular diffusion coefficient was used to estimate the cell radius by using the relationship between mean square displacement, x and diffusion coefficient (Eq. 6.2), where Δ is the diffusion time in the diffusionCEST pulse sequence. Assuming water does not move across the cellular boundary, in the limit of large Δ the mean square displacement of water x can be used as an estimate for the cellular radius because the predominant factor determining the diffusion coefficient in this limit is the restriction of motion of water protons by cellular membranes.

$$x = \sqrt{2D_I\Delta} \tag{6.2}$$

One key limitation of the biexponential signal model is that the two water populations identified cannot be assigned definitively to intra- and extracellular water. Data acquired from experiments with varied Δ were fit to a more complex biophysical model of the diffusion signal (Eq. 6.3) in order to determine whether the two water populations identified from the biexponential model correspond to intra- and extracellular water. Equation 6.3 is the model proposed in [232] that describes the expected diffusion signal from a system with physically restrictive boundaries such as cellular membranes. In this model, R is the cell radius and α_m is the mth root of the equation $\alpha_m R J'_{3/2}(\alpha_m R) - \frac{1}{2}J_{3/2}(\alpha_m R) = 0$ where $J_{3/2}(\alpha_m R)$ denotes a Bessel function of the first kind. δ, Δ, and b are all as defined previously. This model was used to estimate the intracellular diffusion coefficient, D_I, and cell radius, R. Note that while the sum in Eq. 6.3 is to ∞, only the first 10 terms were used to reduce computational time.

$$\ln(S(b,\Omega)) = \frac{-2b}{\delta^2(\Delta - \delta/3)}\sum_{m-1}^{\infty}\frac{1}{\alpha_m^2(\alpha_m^2R^2-2)}\times \\ \left(\frac{2\delta}{\alpha_m^2 D} - \frac{2 + e^{-\alpha_m^2 D\delta} - 2e^{-\alpha_m^2 D\delta} - 2e^{-\alpha_m^2 D\Delta} + e^{-\alpha_m^2 D(\Delta+\delta)}}{(\alpha_m^2 D)^2}\right) \tag{6.3}$$

The estimated D_I value was then used with Eq. 6.4 to estimate D_I^*, D_E^* and f_E^*, the intra- and extracellular diffusion coefficients, respectively, and extracellular water volume fraction in the presence of exchange across a restrictive boundary. Equation 6.4 originates from the concept of the "diffusigraphic shutter speed" [172], where $k_{ex} = k_{ga} + k_{ag}$ and q is the diffusion q-value defined by $b = (2\pi q)^2\Delta$. These biophysical models, particularly Eq. 6.3, have been used in previous diffusion studies to measure cellular radius, intracellular water fraction, and other biophysical parameters of interest [177].

$$
\begin{aligned}
D_I^* &= \frac{1}{2}(D_I + D_E + q^{-2}k_{ex} + \sqrt{(D_E - D_I + q^{-2}(k_{ag} - k_{ga}))^2 + \frac{4k_{ag}k_{ga}}{q^4}} \\
D_E^* &= \frac{1}{2}(D_I + D_E + q^{-2}k_{ex} - \sqrt{(D_E - D_I + q^{-2}(k_{ag} - k_{ga}))^2 + \frac{4k_{ag}k_{ga}}{q^4}} \\
f_E^* &= \frac{1}{D_E^* - D_I^*}(f_I D_I + f_E D_E - D_I^*)
\end{aligned}
\tag{6.4}
$$

6.3 Results

6.3.1 Simulations

Simulated Z-spectra for normal brain and tumour tissue are shown in Fig. 6.3, along with the model fitted Z-spectra from the BayCEST fitting and its residual. The mean $\pm$ 95 % confidence interval CESTR* measured from the normal brain simulation was $2.62 \pm 0.05\,\%\,\mathrm{M_0}$, compared to the tumour CESTR* of $3.16 \pm 0.05\,\%\,\mathrm{M_0}$ (rCESTR* = 1.21 ± 0.03). Table 6.3 gives the measured CESTR* and rCESTR* values for each simulation run, where each parameter that was different between normal and tumour tissue was varied in turn to determine the extent to which each parameter affected the quantification of CESTR*.

Table 6.3 suggests that intra- and extracellular pH, amide and MT proton concentration, and the T_2 time of the MT protons are the dominant factors in driving the difference between CESTR* measured in normal and tumour tissue. Importantly, and as expected, the acidic extracellular pH in tumour tissue acts to reduce the measured CESTR*, also reducing the possible contrast in CESTR* images and affecting the accuracy of any pH measurements made using the isoCESTR* method introduced in Chapter 4. This result motivates the separation of intra- and extracellular

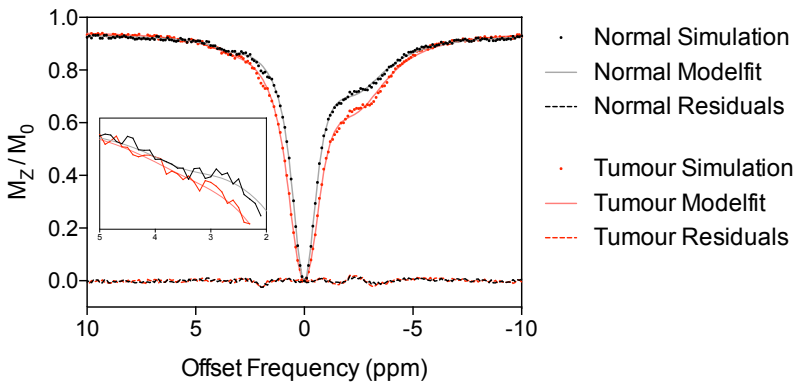

Figure 6.3: Example Z-spectra for the simulations of normal (black) and tumour (red) tissue, along with the model fitted Z-spectra from BayCEST and the fitting residual.

Simulation Ref	CESTR* (% M_0)	ΔCESTR* (% M_0)	rCESTR*	ΔrCESTR*	*p* value
Normal Tissue	2.62 ± 0.05	0.00 ± 0.07	1.00 ± 0.03	0.00 ± 0.04	1
Tumour Tissue	3.16 ± 0.05	0.54 ± 0.07	1.21 ± 0.03	0.21 ± 0.04	< 0.0001
Vary pHi	3.34 ± 0.06	0.72 ± 0.08	1.27 ± 0.03	0.27 ± 0.04	< 0.0001
Vary pHe	2.22 ± 0.04	-0.40 ± 0.06	0.85 ± 0.02	-0.15 ± 0.03	< 0.0001
Vary [Amide]	2.92 ± 0.05	0.30 ± 0.07	1.11 ± 0.03	0.11 ± 0.04	< 0.0001
Vary [MT]	2.53 ± 0.05	-0.09 ± 0.07	0.96 ± 0.02	-0.04 ± 0.04	0.0019
Vary [Amine]	2.63 ± 0.04	0.01 ± 0.06	1.01 ± 0.02	0.01 ± 0.04	0.433
Vary [NOE]	2.61 ± 0.05	-0.01 ± 0.07	1.00 ± 0.03	0.00 ± 0.04	1
Vary k_{MT}	2.67 ± 0.04	0.05 ± 0.07	1.02 ± 0.03	0.02 ± 0.04	0.1177
Vary MT T_2	2.97 ± 0.04	0.36 ± 0.06	1.14 ± 0.03	0.14 ± 0.04	< 0.0001
Vary T_1	2.53 ± 0.04	-0.09 ± 0.06	0.97 ± 0.02	-0.03 ± 0.03	0.0977
Vary T_2	2.63 ± 0.05	0.01 ± 0.07	1.00 ± 0.03	0.00 ± 0.04	1
Σ Vary		0.86 ± 0.07		0.33 ± 0.04	

Table 6.3: CESTR* and rCESTR* values for each deterministic simulation to determine the extent to which each parameter contributes to the measured CESTR* difference between simulated normal and tumour tissue.

Z-spectra in order to make more accurate and biologically meaningful measurements of tumour pH.

Deterministic simulation of normal and tumour tissue, whilst varying the transcytolemmal exchange rate, revealed the extent to which transytolemmal exchange affects the quantification of CESTR* (Fig. 6.4). Whilst the variation of CESTR* over a fairly wide range of transcytolemmal exchange rates (50 Hz) is of the order 0.1 % M_0 in both normal and tumour tissue, a clear variation of CESTR* is evident at slower exchange rates $0\,\text{Hz} < k_{ga} < 10\,\text{Hz}$ before an eventual plateau for $k_{ga} > 20\,\text{Hz}$. This result implies that, as expected, at faster transcytolemmal exchange rates the compartmentalisation of the water pools is masked as the compartments are well-mixed. Consequently, any differences in the CEST pool parameters between the intra- and extracellular spaces are no longer discernible. In addition, the effect of the extracellular acidification in the tumour tissue acts to reduce the measured CESTR* as the effect of transcytolemmal exchange increases.

Figure 6.3 and Fig. 6.4 demonstrate that tissue compartmentalisation is an important factor when acquiring Z-spectra from complex *in vivo* tissue, and that as long as the transcytolemmal exchange rate is of the order 1 – 10 Hz, it may be possible to separate the intra- and extracellular Z-spectra.

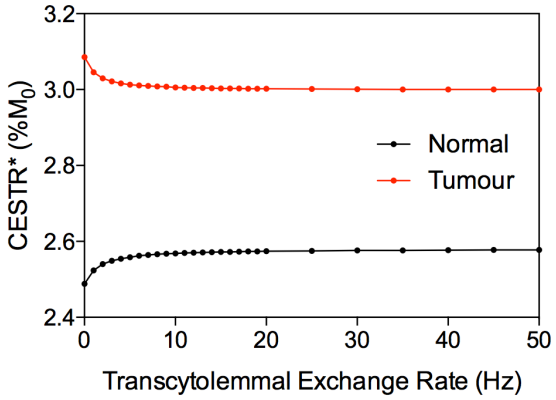

Figure 6.4: Variation of CESTR* as a function of transcytolemmal exchange in deterministic simulation of normal and tumour tissue.

6.3.2 GUVs

Figure 6.5A shows the two Z-spectra measured using the diffusionCEST pulse sequence and biexponential model for analysis, demonstrating the distinctness of the two spectra. Figure 6.5B shows the quantification of CEST effect in the GUV sample by MTR_{asym}, demonstrating a prominent CEST effect at 1.2 ppm in the intracellular spectrum, and broad effects centered at 2.8 ppm and 1.2 ppm in the extracellular spectrum. Qualitatively comparing the separated Z-spectra to the control Z-spectra (Fig. 6.5C) and MTR_{asym} curves of (Fig. 6.5D) 200 mM sucrose and 10 % *w/w* BSA, it is apparent that the intracellular spectrum is dominated by the sucrose signal, whereas the extracellular signal is dominated by BSA, with evidence of some sucrose in the extracellular space. The extracellular sucrose is an expected observation owing to the preparation method of the GUV samples. Note also that the lack of NOE saturation in the extracellular spectrum of Fig. 6.5A is likely owing to differences in the CEST preparation between the GUV and control samples.

Table 6.4 displays the measured diffusion characteristics for each compartment as estimated by the biexponential model, showing an order of magnitude difference in diffusion coefficient between the two spaces. This result is likely owing to the restriction placed on the intracellular water by the GUV boundary. Analysis of the variable Δ dataset (Fig. 6.6) analysed with Eq. 6.3 estimates intra- and extracellular diffusion coefficients that are in agreement with biexponential model measurements. The water volume fraction measurements using the complex model are larger than the biexponential model. This discrepancy is perhaps a result of using the complex biophysical model that accounts for diffusion within restricted spaces as well as exchange between intra- and extracellular spaces to analyse the variable Δ dataset. The cellular radius of $9.2 \pm 0.2\,\mu m$ was in agreement with the size of the GUVs as measured by microscopy (diameter = $20 \pm 5\,\mu m$, mean $\pm$ s.d. Fig. 6.7). The transcytolemmal water exchange rate measured was

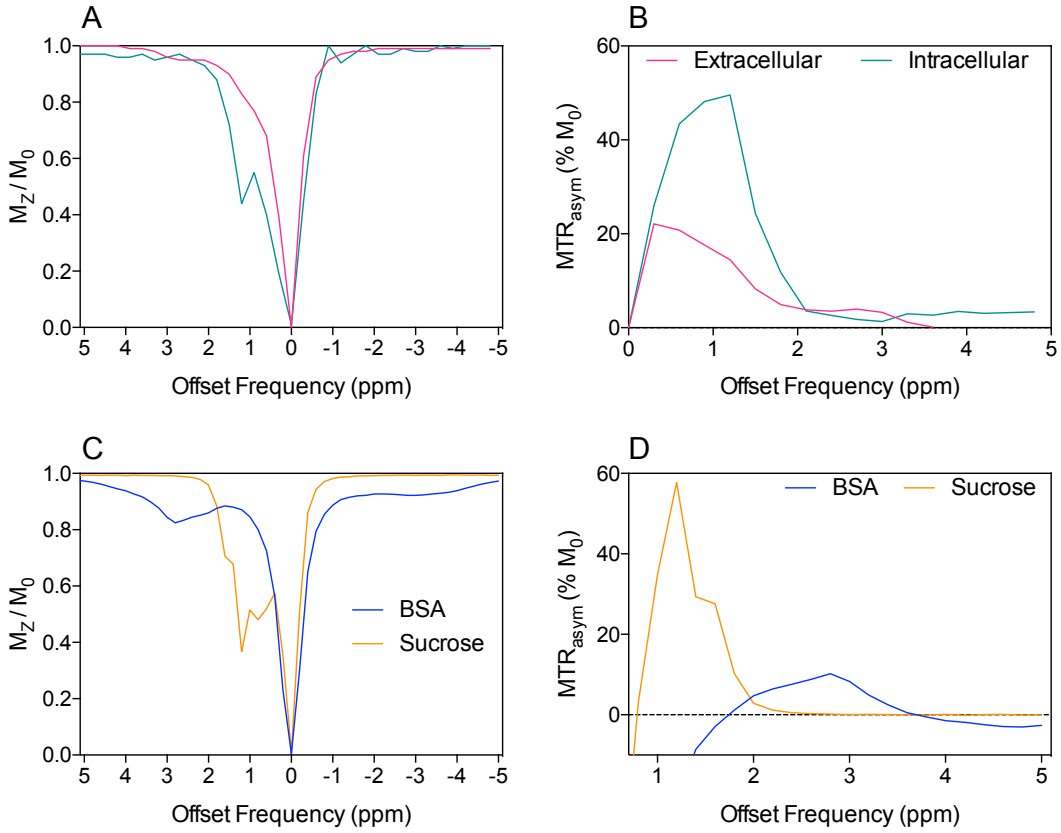

Figure 6.5: Separated intra- and extracellular Z-spectra (A) and MTR_{asym} curves (B) for GUVs. Comparison with the control Z-spectra (C) and MTR_{asym} curves (D) of BSA and sucrose reveals that the Z-spectrum from the intracellular space of GUVs is dominated by sucrose, and the extracellular space is a combination of sucrose and BSA effects.

Model	D_I (cm^2 s^{-1})	f_I (%)	D_E (cm^2 s^{-1})	f_E (%)	Cell Radius (µm)
Biexp (Eq. 6.1)	$1.0 \pm 0.1 \times 10^{-6}$	1.7 ± 0.3	$1.25 \pm 0.05 \times 10^{-5}$	98.3 ± 0.6	10 ± 1
Complex (Eq. 6.3)	$1.4 \pm 0.1 \times 10^{-6}$	4.8 ± 0.7	$1.30 \pm 0.04 \times 10^{-5}$	95.2 ± 0.7	9.2 ± 0.2

Table 6.4: Biexponential and complex model diffusion results for GUVs.

5.5 ± 0.3 Hz, which is within the range of exchange rates required to discriminate between intra- and extracellular CEST spectra.

6.3.3 Cells

With the diffusionCEST method demonstrated as a way to separate CEST spectra based on compartmentalisation of water, the pulse sequence was applied to various samples of increasing biological relevance to the *in vivo* environment. Figure 6.8 shows the separated Z-spectra from intra- and extracellular compartments of a sample of 4T1-GFP cells suspended in PBS, and Table 6.5 displays the measured diffusion characteristics of the various fractions compared to

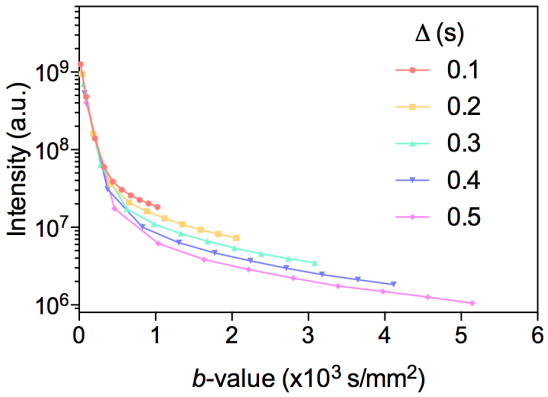

Figure 6.6: Variable Δ dataset acquired from a sample of GUVs in the 14 T NMR spectrometer.

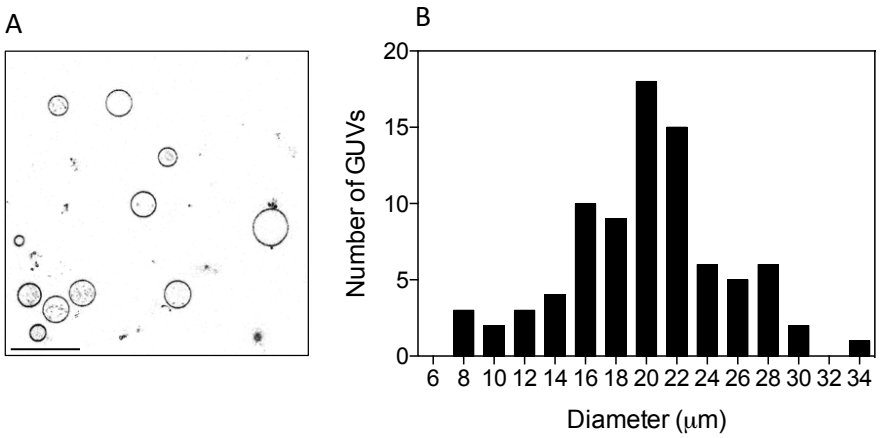

Figure 6.7: A: Microscope image of GUVs, scale bar = 50 µm. B: Frequency distribution of GUV diameters measured from three aliquots of concentrated GUV solution, $n = 84$ total GUVs identified. The mean $\pm$ s.d. diameter was $20 \pm 5\,\mu\text{m}$.

Model	D_I (cm^2 s^{-1})	f_I (%)	D_E (cm^2 s^{-1})	f_E (%)	Cell Radius (µm)
DiffusionCEST	0.63×10^{-6}	9	1.2×10^{-5}	91	8
van Zijl *et. al.* [158]	1.1×10^{-6}	0.8	2.4×10^{-5}	99.2	6

Table 6.5: Comparison of diffusion characteristics of cells suspended in PBS acquired using diffusionCEST and a similar sample used in a previous study.

literature estimates using a similar sample. No significant CEST effects are measured in the extracellular spectrum, with the only non-zero MTR_{asym} values being exhibited in the intracellular spectrum. In addition, the diffusion characteristics measured by diffusionCEST agree reasonably well with diffusion measurements made from a similar sample in previous literature, though discrepancies between the estimated water fractions may reflect the different cell types and experimental set ups.

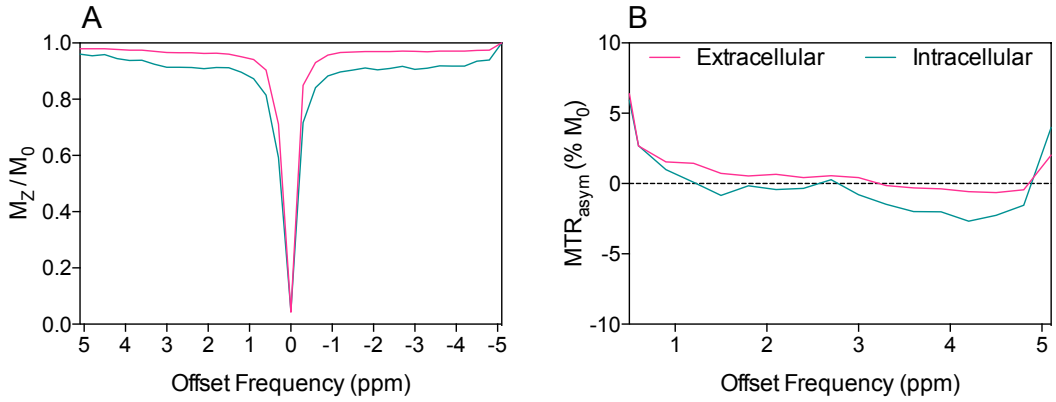

Figure 6.8: Separated intra- and extracellular Z-spectra (A) and MTR_{asym} curves (B) from 4T1-GFP cells suspended in PBS. The only non-zero CEST effects in the MTR_{asym} curves are in the intracellular space.

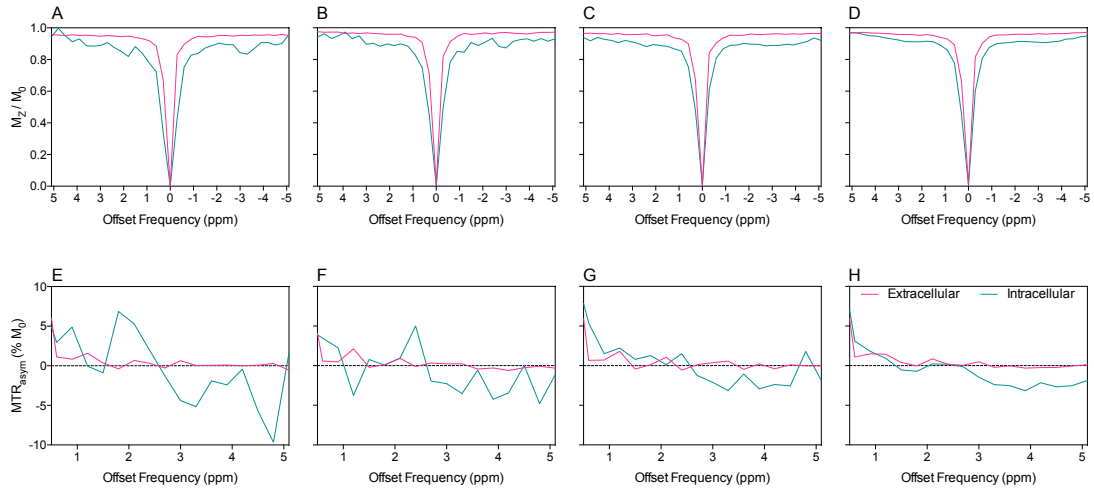

Figure 6.9: Separated intra- and extracellular Z-spectra (A,B,C,D) and MTR_{asym} curves (E,F,G,H) from homogenously suspended 4T1-GFP cells in matrigel with varying cell number (A,E = 1.2×10^6; B,F = 2.3×10^6; C,G = 4.6×10^6; D,H = 9.3×10^6). Note as the number of cells increases, the SNR of the intracellular Z-spectrum and MTR_{asym} curve increases.

The second sample used comprised a set of NMR tubes containing a variable number of cells. Figure 6.9 shows the intra- and extracellular Z-spectra and MTR_{asym} curves for each sample, demonstrating that as the number of cells in the sample increased, so did the intracellular spectrum SNR. In addition, Table 6.6 shows the results of the diffusion characteristics from each sample, demonstrating that there is a correlation between the number of cells in the sample and the estimated intracellular fraction of water, and that the diffusion coefficients of the intra- and extracellular spaces are consistently estimated in an expected range for all samples.

Fig. 6.10 shows the result of fitting the complex model (Eq. 6.3) to a variable Δ dataset acquired from a sample containing 9.3×10^6 cells. The estimated cell radius of $10.30 \pm 0.03\,\mu m$ is smaller

Cell Number	D_I ($cm^2\,s^{-1}$)	f_I (%)	D_E ($cm^2\,s^{-1}$)	f_E (%)	Cell Radius (μm)
1.2×10^6	0.35×10^{-6}	0.1	1.6×10^{-5}	99.9	40
2.3×10^6	0.41×10^{-6}	0.3	1.4×10^{-5}	99.7	37
4.6×10^6	0.86×10^{-6}	0.4	1.6×10^{-5}	99.6	40
9.3×10^6	0.32×10^{-6}	1.0	1.2×10^{-5}	99.0	35

Table 6.6: Diffusion properties of cells suspended in matrigel samples. Note that as cell number in the sample increases, so does the estimated fraction of intracellular water, whilst the intra- and extracelluar diffusion coefficients and cell radius estimates remain in agreement for all samples.

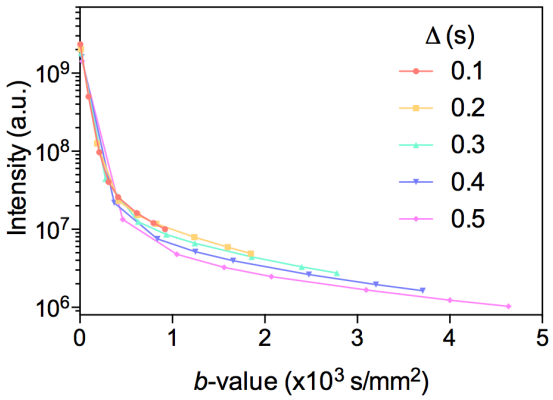

Figure 6.10: Variable Δ dataset acquired from a sample of 4T1-GFP cells suspended in matrigel in the 14 T NMR spectrometer.

than that estimated using the biexponential model, but of the same order of magnitude and in agreement with the expected cellular radius for 4T1-GFP cells. In addition, the intra- and extracellular diffusion coefficients estimated by the complex model ($D_I = 6.5 \pm 0.2 \times 10^{-6}\,cm^2\,s^{-1}$, $D_E = 1.37 \pm 0.02 \times 10^{-5}\,cm^2\,s^{-1}$) are of a similar order of magnitude to those estimated with the biexponential model and in excellent agreement for D_E. The estimated intracellular water fraction from the complex model was $f_I = 26.5 \pm 0.4\,\%$, which is much larger than that estimated by the biexponential model. Similarly to the GUV sample, this discrepancy may be a result of the complex biophysical model accounting for diffusion within restricted spaces as well as exchange between intra- and extracellular spaces. Crucially, Eq. 6.3 measures the transcytolemmal exchange rate as $5.24 \pm 0.05\,Hz$, which is in the range of values (estimated from simulations) required for the intra- and extracellular Z-spectra to be separable.

6.3.4 Post-mortem animals

Subsequently, the diffusionCEST method was applied to complex systems that more closely reflect the *in vivo* environment. The first sample used was brain tissue from a naïve female Wistar rat, randomly inserted into a 5 mm diameter NMR tube. The two separated Z-spectra

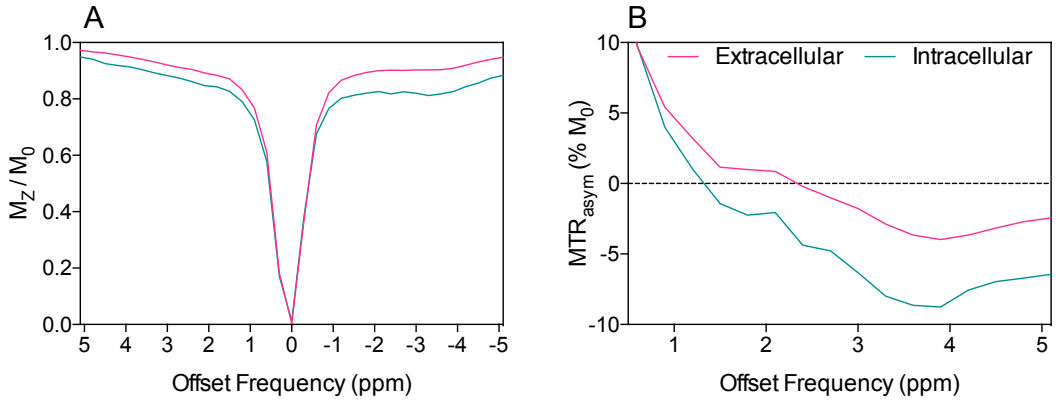

Figure 6.11: Separated intra- and extracellular Z-spectra (A) and MTR_{asym} curves (B) from rat brain tissue in an NMR tube. Non-zero CEST effects were present in both intra- and extracellular spaces.

Model	D_I ($cm^2\,s^{-1}$)	f_I (%)	D_E ($cm^2\,s^{-1}$)	f_E (%)	Cell Radius (µm)
DiffusionCEST	0.4×10^{-6}	7	2.3×10^{-6}	93	7
Assaf & Cohen [159]	0.08×10^{-6}	2	2.7×10^{-6}	98	2

Table 6.7: Comparison of diffusion characteristics of the rat brain tissue acquired using diffusionCEST and a similar sample used in a previous study.

from this sample are shown in Fig. 6.11A, with MTR_{asym} quantification in Fig. 6.11B, and the diffusion characteristics of the compartments shown in Table 6.7. The diffusion coefficients and volume fractions are of similar order of magnitude to previous studies using a similar sample. MTR_{asym} quantification of the separated Z-spectra suggests that, for the CEST effect from amide protons at 3.5 ppm, the intracellular space contributes the majority of the signal ($\frac{MTR^{IC}_{asym}}{MTR^{IC}_{asym}+MTR^{EC}_{asym}} = \frac{-8.6\,\%\,M_0}{-3.6\,\%\,M_0+-8.6\,\%\,M_0} = 70\,\%$).

Figure 6.12A shows the separated Z-spectra and Fig. 6.12B the MTR_{asym} quantification from the intact post-mortem whole mouse brain, which show qualitative similarity to those recorded from the rat brain tissue in Fig. 6.11. Table 6.8 also shows the similarity of the diffusion characteristics of the intact post-mortem mouse brain to a similar sample used in a previous study. The estimated contribution of the intracellular space to the overall CEST signal in the intact whole post-mortem mouse brain sample is approximately $\frac{MTR^{IC}_{asym}}{MTR^{IC}_{asym}+MTR^{EC}_{asym}} = \frac{-5.3\,\%\,M_0}{-2.3\,\%\,M_0+-5.3\,\%\,M_0} = 70\,\%$, in agreement with the rat brain tissue estimate.

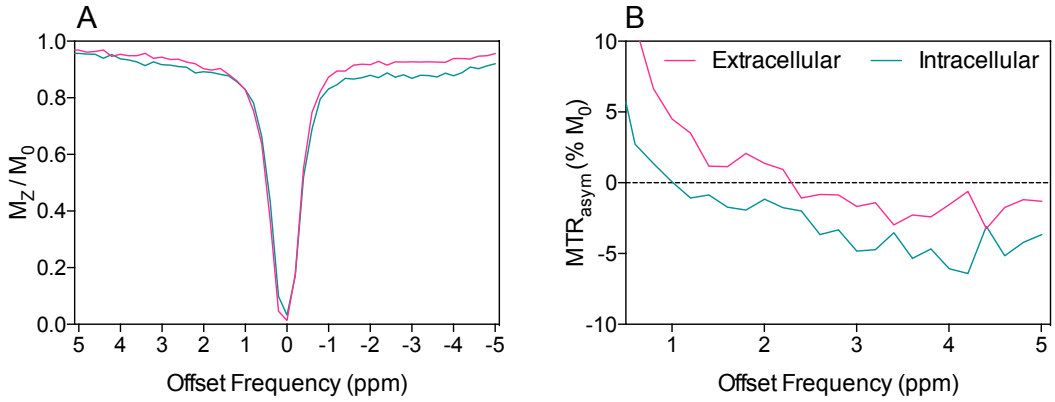

Figure 6.12: Separated intra- and extracellular Z-spectra (A) and MTR_{asym} curves (B) from intact post-mortem mouse brain. Non-zero CEST effects were present in both intra- and extracellular spaces.

Model	D_I ($cm^2\,s^{-1}$)	f_I (%)	D_E ($cm^2\,s^{-1}$)	f_E (%)	Cell Radius (µm)
DiffusionCEST	1.4×10^{-6}	15	8.5×10^{-6}	85	12
Niendorf *et. al.* [161]	1.7×10^{-6}	17	8.2×10^{-6}	83	2

Table 6.8: Comparison of diffusion characteristics of intact post-mortem mouse brain tissue acquired using diffusionCEST and a similar sample used in a previous study.

6.4 Discussion

The results of this chapter demonstrate that it is possible, through use of a novel NMR/MRI pulse sequence, to discriminate between intra- and extracellular CEST effects. The novel method — termed diffusionCEST — was first validated in a well-controlled sample of cellular mimicking GUVs, subsequently tested in cellular and tissue samples, and finally used to estimate the proportion of CEST signal originating from the intracellular space in complex brain tissue samples. These results mark the first measurement of separated intra- and extracellular CEST effects, and demonstrate the proof-of-concept that may enable quantification of intra- and extracellular biophysical parameters (such as protein concentration or pH) *in vivo* using CEST MRI.

One novel result from this chapter which has not been previously reported or systematically investigated is the effect of tissue compartmentalisation on the Z-spectrum. A previous study looked at the contribution of transcytolemmal exchange and different T_1 relaxation times in the intra- or extracellular spaces [233]. However, that study did not investigate variation in other physiological parameters, such as pH or protein concentration, which also contribute to changes in the Z-spectrum. The multi compartmental nature of tissue is especially important when studying tumours *in vivo* as their metabolic phenotype leads to vastly different intra- and extracellular biochemical environments compared to healthy tissue. Here it has been demonstrated that the

extracellular acidification present in tumours serves to counteract the increase in CESTR* that would be measured from an increased intracellular protein concentration, decreasing the CEST contrast between tumour and healthy tissue. Measuring only the intracellular CEST signal may therefore enable more accurate tumour delineation based on the elevated intracellular protein concentration in infiltrating tumour regions.

In the simulations used to motivate the quantification of separate intra- and extracellular CEST spectra in Section 6.3.1, a number of assumptions were made. Firstly, the proportion of protons participating in amide, amine and NOE exchange pathways that are intracellular has been assumed to be $^2/_3$, whereas the proportion of protons contributing to the MT effect that are intracellular has been assumed as $^1/_3$. Additionally, these proportions have been assumed to be unchanged between normal and tumour tissue. These assumptions are difficult to verify independently. The rationale behind choosing these values was that amide, amine and NOE protons are typically associated with proteins and peptides in a mobile (i.e. freely tumbling) environment, which is more likely to be found in the cytoplasm than in the extracellular matrix. In addition, the large membrane-associated macromolecules which contribute to the MT pool are likely to exhibit similar mobility (i.e. slow tumbling rate, more solid-like) to proteins in the extracellular matrix, which provides tissue with support and structure. It may be possible to use a more advanced proteomics approach from tissue samples to provide more robust estimates of the proportion of each proton pool associated with each cellular location, but for the purposes of demonstrating the importance of tissue compartmentalisation on the Z-spectrum, the values chosen suffice.

One major limitation of the diffusionCEST pulse sequence relates to the signal-to-noise ratio of the measurements. Since diffusion and CEST are both 'signal destructive' modalities (i.e. both methods encode information as a decrease in the measured signal intensity), difficulties may arise in observing signals from systems where the intrinsic SNR is low. In these cases, it may not be possible to probe sufficiently high diffusion b-values to obtain separate intra- and extracellular CEST spectra. Whilst these SNR limitations were not an issue for the well-controlled samples used in this chapter, and the high B_0 field strengths used, they may prevent effective translation of the diffusionCEST method to lower magnetic field strengths and *in vivo* environments.

A crucial component to being able to separate intra- and extracellular CEST effects relates to the effect of transcytolemmal exchange. If intra- and extracellular CEST effects are to be separated, water must reside within the cell for a sufficiently long time to be encoded with a measurable CEST signal from *only* intracellular molecules. A number of measurements of the intracellular water lifetime, or the transcytolemmal exchange rate, have been made using diffusion-based MRI methods, with measurements of the intracellular water lifetime ranging from 120 ms in cell

suspension [227] to approximately 550 ms *in vivo* [229]. One recent study also found a difference between the intracellular water lifetime of two different brain cell types, with an intracellular water lifetime of 750 ms in neurons and 570 ms in astrocytes [228]. The measurements made of transcytolemmal exchange rate in this chapter correspond to intracellular water lifetimes in 4T1-GFP cells of 191 ms or in GUVs of 182 ms, in agreement with other intracellular water lifetime measurements made in cell suspension samples [227]. The consensus of these measurements is that a CEST pulse of 500 ms during the diffusion delay Δ, as implemented in the diffusionCEST sequence in this chapter, is likely sufficient to encode a CEST signal on the water whilst it resides in the intracellular or extracellular space in complex biological tissues.

A number of the samples used in this chapter have been used in previous diffusion studies investigating compartmentalisation of tissue. In particular, cell suspension NMR studies are very popular, with advanced perfusion systems now in place in some groups to enable culturing of cells within the NMR spectrometer. The study used as the literature comparison in this chapter [158] utilised such a perfusion system to separate the intra- and extracellular signal contributions using diffusion-weighted spectroscopy. Unfortunately, no such perfusion system was available to the author. Brain tissue with minimal structural integrity has also been used in the past in an NMR tube as a model of the *in vivo* environment [159].

One major result of this chapter is that the contribution of the intracellular compartment to the overall CEST signal in complex biologically relevant samples was estimated as 70 % both in brain tissue and whole brain. This value is in broad agreement with independent calculations of the expected proportion of proteins that reside in the cytoplasm of cells [224]. The average proportion of protein in the cytoplasm from the tissue biopsies collected for the work presented in Chapter 5 was measured to be $62 \pm 3\,\%$, in agreement with the estimate of 70 % of the CEST signal originating from the intracellular space. This result represents the first time that the validity of the assumption that the CEST effect *in vivo* is dominated by the intracellular compartment has been tested. Whilst this result suggests that *in vivo* CEST signals are weighted toward the intracellular environment, the interpretation of *in vivo* CEST MRI data should be approached with caution if the aim is absolute quantitation of biophysical parameters such as amide proton concentration or pH. More complex analysis and acquisition methodologies may be needed to deconvolve *in vivo* CEST signals, particularly in pathologies that are known to induce different biophysical microenvironments in the intra- and extracellular spaces (e.g. tumours).

Finally, the biexponential signal model used to analyse the diffusionCEST data has a significant limitation in that it is a mathematical model of the signal; it does not inherently provide a framework to infer information on the physical properties of the system. The complex biophysical model used to analyse the variable Δ datasets in this chapter is based on deriving the physical

properties of a system comprising diffusion of water within restricted spaces, as well as exchange between two water populations. It can be used to verify and assign some of the results from the biexponential fitting method. However, whilst the complex model allows more information to be obtained about the physical properties of the sample, it is limited by the much greater number of free parameters that must be fitted in the analysis. These parameters may have high levels of correlation that can lead to over-fitting of the data, with subsequent implications on the accuracy of the measurements made. The modelling of the diffusion signal from various tissues is an area of ongoing research in the diffusion NMR/MRI community, and attempts have been made by a number of research groups to develop analysis methodologies to extract parameters such as cell radius or intracellular water fraction [177, 178].

6.5 Conclusion

The aim of this chapter was to assess the possibility of separating intra- and extracellular CEST effects. A novel NMR/MRI pulse sequence combining a stimulated echo diffusion sequence with CEST saturation — diffusionCEST — was developed and implemented on two separate spectrometers. A number of *in vitro* and *ex vivo* samples were used to validate the sequence, determine its ability to separate CEST spectra, and finally estimate the proportion of CEST signal originating from the intracellular space in complex tissue samples as approximately 70 %. This 70 % value is in agreement with independent calculations of the expected proportion of proteins that reside in the cytoplasm of cells. These results mark the first measurement of separate intra- and extracellular CEST effects, and demonstrate the proof-of-concept that may enable quantification of intra- and extracellular biophysical parameters (such as protein concentration or pH) *in vivo* using CEST MRI.

Chapter 7

Conclusions, Criticisms, and Future Work

Contents

7.1 Conclusions . . . 160
7.2 Criticisms & Future Work . . . 160
7.2.1 Effect of protein conformation on CEST signal . . . 160
7.2.2 Validation of pH estimates made using isoCESTR* . . . 161
7.2.3 Application of diffusionCEST with imaging readout . . . 162
7.2.4 Modification of tumour pH using glucose . . . 162
7.2.5 Subregional analysis of tumours . . . 163
7.2.6 Minimal data required for accurate model fitting results . . . 164
7.3 Closing Remarks . . . 164

7.1 Conclusions

This thesis has focussed on the development of CEST MRI as an *in vivo* pH measurement modality. To facilitate this development, three areas were identified where progress must be made before CEST MRI can be successfully and reliably applied to measure tissue pH *in vivo*.

Chapter 3 outlined work to develop a quantification metric for CEST MRI data that is specific only to modifications in the exchange dynamics of a labile proton population, with no contamination from other factors such as the water relaxation times. Using novel, realistic phantom models of the *in vivo* intracellular environment of brain metastases and naïve mouse brain, the CESTR* metric with T_1 and T_2 time compensation was found to be such a quantification metric. Chapter 4 detailed steps to enable the application of CESTR* to reliably quantify *in vivo* CEST MRI data, taking advantage of the Bayesian nature of the analysis methodology to ensure accurate quantification of CEST MRI data. The isoCESTR* method was also introduced and its ability to deconvolve CESTR* changes into changes in the relevant physiological parameters demonstrated.

In order to determine the proportion of the CEST MRI signal changes in pathology that arise from pH or protein concentration alterations, the isoCESTR* method was applied to three different *in vivo* models of disease in Chapter 5. A method of measuring protein concentration by histology with unparalleled spatial resolution was used in combination with the *in vivo* MRI data for the first time, and estimates were made of the proportion of CESTR* change that is attributable to protein concentration changes in brain metastasis and ischaemic stroke. Further, CESTR* was used to image the alleviation of tumour hypoxia for the first time.

Finally, a proof-of-principle study presented in Chapter 6 demonstrated how CEST effects specific to the intra- and extracellular spaces may be separable. A novel pulse sequence was developed and tested using a number of well-controlled *in vitro* and *ex vivo* samples to estimate that approximately 70 % of the CEST signal measured *in vivo* originates from the intracellular compartment.

7.2 Criticisms & Future Work

7.2.1 Effect of protein conformation on CEST signal

The phantom models in Chapter 3 were more representative of the *in vivo* environment than *in vitro* models that have been used previously to investigate CEST MRI quantification metrics, and the primary factors that contribute to the CEST effect were investigated in an iterative manner. However, one variable that was not accounted for was protein conformation, which would

alter the number of protons available for chemical exchange. As discussed in Section 2.2.5.1 and Section 5.4.5, the measured CEST signal is a function of the *effective* concentration of labile protons, which may be less than the total concentration of those protons, since some protons may not be solvent accessible. Previous studies have examined the dependence of Z-spectra and other CEST quantification metrics on protein conformation [146, 147], but this exercise should be repeated for the CESTR* metric identified as optimal in this work. The development of CEST MRI as a measurement of protein conformation is an avenue of research that holds great promise, particularly for clinical translation, since a number of neurodegenerative diseases are known to exhibit changes in protein conformation status before clinical symptoms manifest [234]. Further work is also required to elucidate whether the concentration of proteins involved in disease-related conformational change is sufficient for them to be detected using CEST MRI, and whether conformational changes in one protein can be distinguished from another (e.g. to separate between conformational changes of Huntingdin and Beta Amyloid proteins to differentiate between Huntingdon's and Alzhiemer's disease, respectively.)

7.2.2 Validation of pH estimates made using isoCESTR*

While the isoCESTR* method introduced in Chapter 4 and applied in Chapter 5 enables deconvolution of changes in CESTR* into alterations of its constituent factors (labile proton concentration and exchange rate, or equivalently protein concentration and pH), it is predicated on making independent, *ex vivo* measurements of protein concentration from tissue biopsies. The clinical translatability of such a method is limited since biopsy samples are not readily available in all cases. However, if a library of protein concentrations and their corresponding CESTR* values can be built up from previous patient biopsies with a sufficiently tight correlation, it may be possible to use this information to determine the pH of a tumour where biopsy is not possible. Alternatively, assessing the protein concentration of a number of tumour types using Coomassie staining of tissue microarrays would enable elucidation of the typical protein concentration (with an associated uncertainty) in various tumour types. Thus, pH estimation using isoCESTR* may be possible without tissue biopsy, so long as the standard deviation of measured protein concentrations within each tumour type is small.

An alternative strategy would be to independently measure pH and infer protein concentration measurements from the CEST MRI data, but current strategies to measure pH *in vivo* are restricted to ^{31}P spectroscopy methods. Unfortunately, at the time of completing the experiments, no ^{31}P RF coil was available to the author to pursue this strategy, or to verify the pH estimates made using the isoCESTR* method with *ex vivo* protein concentration measurements. A ^{31}P coil compatible with the 9.4 T MRI system has now been manufactured, and is in the process of being optimised for use *in vivo* to validate the isoCESTR* pH estimates.

7.2.3 Application of diffusionCEST with imaging readout

The diffusionCEST pulse sequence developed in Chapter 6 was implemented with a spectroscopic readout, which restricts the spatial information that can be obtained. In principle, however, the signal acquisition can be amended to provide a stimulated echo imaging readout using a fast imaging readout method (e.g. echo planar imaging). The limiting factor is likely to be the available signal-to-noise ratio, especially if attempting to acquire Z-spectra with large diffusion b-values and long CEST saturation times. This low SNR may necessitate many signal averages, resulting in long acquisition times that may preclude *in vivo* application of the method.

7.2.4 Modification of tumour pH using glucose

Studies in animals and humans have shown that glucose causes an acidification of pH_e in tumour tissue but not in normal healthy tissue [235–238]. The mechanism by which this acidification occurs is thought to be tumour-specific uptake of glucose increasing metabolic activity, with a consequential increase in lactate production. This lactate is extruded from the tumour cells to maintain an alkalotic pH_i, leading to a tumour specific acidification in pH_e. The glucose loads used in previous experiments have varied from a bolus intravenous injection in mice [238], systemic infusion in rats [236], or oral administration in humans [235, 237].

This alteration in tumour pH_e may be detectable using CEST MRI. The proposed experiment would involve measuring a full Z-spectrum before and after glucose administration, with concurrent blood glucose measurements. Importantly, the post-glucose administration Z-spectrum must be acquired when a plateau in blood glucose concentration has been reached, and it must be maintained at the same value throughout Z-spectrum sampling. Since protein concentration in the tumour can be assumed to be unaltered by the introduction of glucose, with suitable control for changes in T_1 and T_2 relaxation times (such as by quantifying the CEST effect using CESTR*), any observed change in the CEST signal from amide protons after glucose administration can be attributed to the pH_e change. Crucially, this experiment would differ from a glucoCEST or Dynamic Glucose Enhanced (DGE) acquisition because the CEST effect from *amide* protons would be investigated, rather than the CEST effect directly attributable to glucose.

Several factors would need to be accounted for to determine the extent to which the amide proton CEST effect may be able to inform on pH_e changes in the tumour following glucose administration. In particular, the CEST effect caused by glucose may overlap with the signal from amide protons. The extent to which the quantification of the amide CEST signal may be contaminated by this effect may be determined using phantom models of a protein with varying glucose concentrations and pH values. Additionally, the CEST effect caused by glucose must be accounted for in the BayCEST model in the post-glucose Z-spectrum. The correlation between

exchanging pools in the BayCEST model must be fully investigated to ensure that introducing an additional exchanging pool does not adversely affect the quantification of the amide CEST signal. The signal change may also be too small to be readily measured since the pH change induced by the glucose load is restricted to the extracellular space only. The results of Chapter 6 suggest this space contributes only 30% of the CEST MRI signal *in vivo*. Realistic simulations of the intra- and extracellular environment *in vivo*, such as those used in Chapter 6, may be able to provide information on the feasibility of the proposed experiment to discern tumour pH_e related changes in the amide CEST signal. Further additional measurements of arterial blood pH and blood glucose level would need to be made throughout and following the glucose administration. Finally, a DGE CEST MRI acquisition during glucose administration may be required to ensure glucose administration leads to an increase in glucose concentration specifically in the tumour.

7.2.5 Subregional analysis of tumours

Measuring tumour heterogeneity is an active area of research in many MRI fields. One recent example of heterogeneity imaging utilised dynamic contrast enhanced (DCE) MRI to identify tumour subregions based on voxels sharing similar perfusion properties derived from gadolinium uptake curves [239]. Similar subregional methods have been applied in the same preclinical model of brain metastasis used in Chapter 5, using multiphase pseudocontinuous arterial spin labelling (MP-pCASL) MRI data to optimise the acquisition of MP-pCASL in rats [240]. Regional acquisition and analysis methods have already been employed in CEST MRI in the form of CEST-SLAM acquisition strategies, with the aim being to speed up acquisition and analysis methods in biologically similar tissue. However, CEST-SLAM removes any information concerning tumour heterogeneity, and may mask interesting and biologically meaningful differences in the CEST spectrum within the tumour region. An as-yet unexplored, but potentially powerful regional analysis method, would be to identify areas of tissue with similar CEST spectra using a partial least squares discriminant analysis (PLSDA) method, as implemented in [239]. This algorithm may identify tissue categories with spectrally similar profiles in anatomically corresponding areas, potentially leading to improvements in tumour delineation. A strength of this method is that the tissue classification is completely unbiased since it is driven by the raw CEST spectrum within each imaging voxel rather than processed maps of CESTR* or other physiological parameters.

Subsequent application of biophysical models to the data within the identified subregions (for example, fitting the average CEST spectrum within the region with BayCEST and analysing the CEST effects using CESTR*) may enable further characterisation of the defined subregions into biologically meaningful categories (e.g. proliferative tumour, hypoxic tumour, necrosis, peritumoral oedema, etc.). Combining these subregions identified using CEST MRI with those

identified through other modalities (DCE, MP-pCASL, diffusion MRI, T_1 and T_2 relaxation mapping) may strengthen such conclusions about the physiological relevance of the subregions. This analysis strategy is part of a wider shift in tumour imaging that focuses on tissue function as opposed to anatomy or volume.

7.2.6 Minimal data required for accurate model fitting results

The identification of the effect of noisy data on the BayCEST model fitting analysis completed in Chapter 4 builds on previous literature examining and optimising the BayCEST algorithm. Specifically, an optimal distribution of frequencies to be sampled when acquiring a Z-spectrum has been identified [194], a continuous approximation to a pulsed saturation scheme verified as suitable for the model-fitting process [100], and CESTR* revealed as a quantification metric with reduced variance compared to other methods in hyperacute stroke patients [126]. The optimal sampling schedule identified in [194] recommends placing many sampling points around the water frequency and the labile pool of interest, but this study normalised the overall number of acquisitions to be identical to a previously implemented evenly distributed sampling scheme.

Thus far, the minimal data required for the BayCEST algorithm to return accurate estimates of the parameters of interest (labile proton exchange rate and concentration for a given proton pool) has not been investigated. The extent to which the number of samples can be reduced, though still be optimally placed around the resonance frequency of water and the labile proton pool of interest, remains to be seen, and is an interesting problem to pursue. Even with the efforts to speed up acquisition of Z-spectrum data through novel acquisition strategies (discussed in Section 2.2.4), the best way to improve imaging efficiency is simply to reduce the number of data points acquired. If accurate BayCEST model fitted parameters are achievable with a minimally sampled Z-spectrum, this may lead to a significant decrease in acquisition time for CEST MRI data.

7.3 Closing Remarks

This thesis has focussed on the development and application of CEST MRI as an *in vivo* pH measurement tool. An optimal method for quantification of CEST MRI data (CESTR*) was identified, and the isoCESTR* extension developed. The isoCESTR* method was applied to three separate animal models of human disease, and measurements made of the pH of brain metastasis and ischaemic stroke *in vivo*. Additionally, the pH change induced by alleviation of tumour hypoxia was measured, and the separability of Z-spectra from intra- and extracellular environments demonstrated using a novel pulse sequence. Altered metabolic phenotypes, with consequential alterations in tissue pH, are commonplace in a number of pathologies, and pH

is so far under-utilised as a physiological parameter of interest in the clinic. It is hoped that the work presented here goes some way to improving the understanding of CEST effects from endogenous sources, and exploiting these effects for measurement of tissue pH.

Bibliography

[1] S. P. L. Sørensen, "Über die Messung und die Bedeutung der Wasserstoffionenkonzentration bei enzymatischen Prozessen", *Biochemische Zeitschrift*, vol. 21, no. 72, p. 131, 1909.

[2] A. K. Covington, R. G. Bates and R. A. Durst, "Definition of pH scales, standard reference values, measurement of pH and related terminology (Recommendations 1984)", *Pure and Applied Chemistry*, vol. 57, no. 3, pp. 531–542, 1985.

[3] J. A. Mindell, "Lysosomal Acidification Mechanisms", *Annual Review of Physiology*, vol. 74, no. 1, pp. 69–86, 2012.

[4] X. Yao and J. G. Forte, "Cell Biology of Acid Secretion by the Parietal Cell", *Annual Review of Physiology*, vol. 65, no. 1, pp. 103–131, 2003.

[5] W. F. Boron, "Regulation of intracellular pH", *AJP: Advances in Physiology Education*, vol. 28, no. 4, pp. 160–179, 2004.

[6] D. W. Piper and B. H. Fenton, "pH stability and activity curves of pepsin with special reference to their clinical importance", *Gut*, vol. 6, 1965.

[7] J. M. Berg, J. L. Tymoczko and L. Stryer, "Making a Fast Reaction Faster: Carbonic Anhydrases", in *Biochemistry*, 5th, W H Freeman, 2002, ch. 9.2.

[8] J. A. Kellum, "Determinants of blood pH in health and disease.", *Critical Care*, vol. 4, no. 1, pp. 6–14, 2000.

[9] A. Roos and W. Boron, "Intracellular pH.", *Physiological Reviews*, vol. 61, no. 2, pp. 296–434, 1981.

[10] Cancer Research UK, *Cancer Statistics for the UK - www.cancerresearchuk.org*.

[11] UK Government, *2010 to 2015 government policy: Cancer research and treatment - www.gov.uk*.

[12] D. Hanahan and R. A. A. Weinberg, "The Hallmarks of Cancer", *Cell*, vol. 100, no. 1, pp. 57–70, 2000.

[13] D. Hanahan and R. A. Weinberg, "Hallmarks of cancer: The next generation", *Cell*, vol. 144, no. 5, pp. 646–674, 2011.

[14] O. Warburg, "The metabolism of tumours. Investigations from the Kaiser-Wilhelm Institute for Biology, Berlin-Dahlem. Edited by Otto Warburg, Kaiser-Wilhelm Institute for Biology, Berlin-Dahlem. Translated from the German edition, with accounts of additional recent res", *British Journal of Surgery*, vol. 19, no. 73, pp. 168–168, 1931.

[15] T. Belhocine, K. Spaepen, M. Dusart, C. Castaigne, K. Muylle, P. Bourgeois, D. Bourgeois, L. Dierickx and P. Flamen, "18FDG PET in oncology: the best and the worst", *International Journal of Oncology*, vol. 28, no. 5, pp. 1249–61, 2006.

[16] M. G. Vander Heiden, L. C. Cantley and C. B. Thompson, "Understanding the Warburg Effect: The Metabolic Requirements of Cell Proliferation", *Science*, vol. 324, no. 5930, pp. 1029–1033, 2009.

[17] V. R. Potter, "The biochemical approach to the cancer problem.", *Federation proceedings*, vol. 17, no. 2, pp. 691–7, 1958.

[18] D. G. Smith and R. G. Sturmey, "Parallels between embryo and cancer cell metabolism", *Biochemical Society Transactions*, vol. 41, no. 2, 2013.

[19] Y. Pylayeva-Gupta, E. Grabocka and D. Bar-Sagi, "RAS oncogenes: weaving a tumorigenic web", *Nature Reviews Cancer*, vol. 11, no. 11, pp. 761–774, 2011.

[20] D. L. Kaplans and W. F. Boron, "Long-term Expression of c-H-rus Stimulates Na-H and Na+-dependent C1-HCO3 Exchange in NIH-3T3 Fibroblasts*", *The Journal of Biological Chemistry*, vol. 269, no. 6, pp. 4116–4124, 1994.

[21] N. C. Denko, "Hypoxia, HIF1 and glucose metabolism in the solid tumour", *Nature Reviews Cancer*, vol. 8, no. 9, pp. 705–713, 2008.

[22] R. J. Gillies, N. Raghunand, G. S. Karczmar and Z. M. Bhujwalla, "MRI of the tumor microenvironment.", *Journal of Magnetic Resonance Imaging*, vol. 16, no. 4, pp. 430–50, 2002.

[23] R. J. Gillies, N. Raghunand, M. L. Garcia-Martin and R. A. Gatenby, "pH imaging. A review of pH measurement methods and applications in cancers.", *IEEE Engineering in Medicine and Biology Magazine*, vol. 23, no. 5, pp. 57–64, 2004.

[24] R. J. Gillies, Z. Liu and Z. Bhujwalla, "31P-MRS measurements of extracellular pH of tumors using 3-aminopropylphosphonate", *American Journal of Physiology - Cell Physiology*, vol. 267, no. 1, pp. C195–203, 1994.

[25] I. F. Tannock and D. Rotin, "Acid pH in Tumors and Its Potential for Therapeutic Exploitation", *Cancer Research*, vol. 49, no. 16, pp. 4373–4384, 1989.

[26] A. McIntyre, S. Patiar, S. Wigfield, J.-L. Li, I. Ledaki, H. Turley, R. Leek, C. Snell, K. Gatter, W. S. Sly, R. D. Vaughan-Jones, P. Swietach and A. L. Harris, "Carbonic anhydrase IX promotes tumor growth and necrosis in vivo and inhibition enhances anti-VEGF therapy.", *Clinical Cancer Research*, vol. 18, no. 11, pp. 3100–11, 2012.

[27] S Matsuyama and J. C. Reed, "Mitochondria-dependent apoptosis and cellular pH regulation", *Cell Death and Differentiation*, vol. 7, no. 12, pp. 1155–1165, 2000.

[28] W. H. Moolenaar, L. H. Defize and S. W. De Laat, "Ionic signalling by growth factor receptors.", *The Journal of Experimental Biology*, vol. 124, pp. 359–73, 1986.

[29] M. Stubbs, P. M. McSheehy, J. R. Griffiths and C. Bashford, "Causes and consequences of tumour acidity and implications for treatment", *Molecular Medicine Today*, vol. 6, no. 1, pp. 15–19, 2000.

[30] R. J. Gillies, R Martinez-Zaguilana, E. P. Petersona and R Peronab, "Role of Intracellular pH in Mammalian Cell Proliferation", *Cellular Physiology and Biochemistry*, vol. 2, pp. 159–179, 1992.

[31] L. Yadav, N. Puri, V. Rastogi, P. Satpute and V. Sharma, "Tumour Angiogenesis and Angiogenic Inhibitors: A Review.", *Journal of Clinical and Diagnostic Research*, vol. 9, no. 6, XE01–XE05, 2015.

[32] W. R. Wilson and M. P. Hay, "Targeting hypoxia in cancer therapy", *Nature Reviews Cancer*, vol. 11, no. 6, pp. 393–410, 2011.

[33] J. J. Connell, G. Chatain, B. Cornelissen, K. A. Vallis, A. Hamilton, L. Seymour, D. C. Anthony and N. R. Sibson, "Selective permeabilization of the blood-brain barrier at sites of metastasis.", *Journal of the National Cancer Institute*, vol. 105, no. 21, pp. 1634–43, 2013.

[34] B. P. Mahoney, N. Raghunand, B. Baggett and R. J. Gillies, "Tumor acidity, ion trapping and chemotherapeutics I. Acid pH affects the distribution of chemotherapeutic agents in vitro", *Biochemical Pharmacology*, vol. 66, pp. 1207–1218, 2003.

[35] S. Goel, A. H.-K. Wong and R. K. Jain, "Vascular Normalization as a Therapeutic Strategy for Malignant and Nonmalignant Disease", *Cold Spring Harbor Perspectives in Medicine*, vol. 2, no. 3, 2012.

[36] T. M. Ashton, E. Fokas, L. A. Kunz-Schughart, L. K. Folkes, S. Anbalagan, M. Huether, C. J. Kelly, G. Pirovano, F. M. Buffa, E. M. Hammond, M. Stratford, R. J. Muschel, G. S. Higgins and W. G. McKenna, "The anti-malarial atovaquone increases radiosensitivity by alleviating tumour hypoxia", *Nature Communications*, vol. 7, p. 12 308, 2016.

[37] J. Bernier, E. J. Hall and A. Giaccia, "Timeline: Radiation oncology: a century of achievements", *Nature Reviews Cancer*, vol. 4, no. 9, pp. 737–747, 2004.

[38] E. J. Hall and A. J. Giaccia, *Radiobiology for the Radiologist*, 7th. Lippincott Williams & Wilkins, 2006, p. 546.

[39] R. L. Tanner, N. A. Baily and J. W. Hilbert, "High-energy proton depth-dose patterns.", *Radiation Research*, vol. 32, no. 4, pp. 861–74, 1967.

[40] Y. Rong and J. Welsh, "Basics of particle therapy II biologic and dosimetric aspects of clinical hadron therapy.", *American Journal of Clinical Oncology*, vol. 33, no. 6, pp. 646–9, 2010.

[41] J Haveman, "The influence of pH on the survival after X-irradiation of cultured malignant cells. Effects of carbonylcyanide-3-chlorophenylhydrazone.", *International Journal of Radiation Biology and related studies in Physics, Chemistry, and Medicine*, vol. 37, no. 2, pp. 201–5, 1980.

[42] M. L. Freeman and E. Sierra, "An Acidic Extracellular Environment Reduces the Fixation of Radiation Damage", *Radiation Research*, vol. 97, no. 1, p. 154, 1984.

[43] J. L. Wike-Hooley, J Haveman and H. S. Reinhold, "The relevance of tumour pH to the treatment of malignant disease", *Radiotherapy and Oncology*, vol. 2, no. 343, pp. 366–343, 1984.

[44] K. Hossmann, "Viability thresholds and the penumbra of focal ischemia", *Annals of Neurology*, vol. 36, no. 4, pp. 557–565, 1994.

[45] Stroke, *State of the Nation - Stroke Statistics*, 2016.

[46] M. A. Yenari and H. S. Han, "Neuroprotective mechanisms of hypothermia in brain ischaemia", *Nature Reviews Neuroscience*, vol. 13, no. 4, p. 267, 2012.

[47] K.-A. Hossmann, "Pathophysiological basis of translational stroke research", *Folia Neuropathologica*, vol. 47, no. 3, pp. 213–227, 2005.

[48] G. W. J. Harston, Y. K. Tee, N. Blockley, T. W. Okell, S. Thandeswaran, G. Shaya, F. Sheerin, M. Cellerini, S. Payne, P. Jezzard, M. Chappell and J. Kennedy, "Identifying the ischaemic penumbra using pH-weighted magnetic resonance imaging.", *Brain*, vol. 138, no. Pt 1, pp. 36–42, 2015.

[49] T. Peisker, B. Koznar, I. Stetkarova and P. Widimsky, "Acute stroke therapy: A review", *Trends in Cardiovascular Medicine*, vol. 27, no. 1, pp. 59–66, 2017.

[50] T. Reffelmann and R. A. Kloner, "The 'no-reflow' phenomenon: basic science and clinical correlates.", *Heart (British Cardiac Society)*, vol. 87, no. 2, pp. 162–8, 2002.

[51] M. Nour, F. Scalzo and D. S. Liebeskind, "Ischemia-reperfusion injury in stroke.", *Interventional neurology*, vol. 1, no. 3-4, pp. 185–99, 2013.

[52] W Hacke, M Kaste, C Fieschi, R von Kummer, A Davalos, D Meier, V Larrue, E Bluhmki, S Davis, G Donnan, D Schneider, E Diez-Tejedor and P Trouillas, "Randomised double-blind placebo-controlled trial of thrombolytic therapy with intravenous alteplase in acute ischaemic stroke (ECASS II). Second European-Australasian Acute Stroke Study Investigators.", *Lancet*, vol. 352, no. 9136, pp. 1245–51, 1998.

[53] B. J. Kim, H. G. Kang, H.-J. Kim, S.-H. Ahn, N. Y. Kim, S. Warach and D.-W. Kang, "Magnetic resonance imaging in acute ischemic stroke treatment.", *Journal of Stroke*, vol. 16, no. 3, pp. 131–45, 2014.

[54] M. Goyal, B. K. Menon and C. P. Derdeyn, "Perfusion imaging in Acute ischemic stroke: Let Us Improve the Science before Changing Clinical Practice", *Radiology*, vol. 266, no. 266, pp. 16–21, 2013.

[55] S. J. Warach, M. Luby, G. W. Albers, R. Bammer, A. Bivard, B. C. Campbell, C. Derdeyn, J. J. Heit, P. Khatri, M. G. Lansberg, D. S. Liebeskind, C. BLM Majoie, M. P. Marks, B. K. Menon, K. W. Muir, M. W. Parsons, A. Vagal, A. J. Yoo, A. V. Alexandrov, J.-C. Baron, D. J. Fiorella, A. J. Furlan, J. Puig, P. D. Schellinger, M. Wintermark and C. to Max Wintermark, "Acute Stroke Imaging Research Roadmap III Imaging Selection and Outcomes in Acute Stroke Reperfusion Clinical Trials Consensus Recommendations and Further Research Priorities MAS; for the Stroke Imaging Research (STIR) and VISTA-Imaging Investigators*", *Stroke*, vol. 47, p. 1389, 2016.

[56] P. Z. Sun, J. Zhou, W. Sun, J. Huang and P. C. van Zijl, "Detection of the Ischemic Penumbra Using pH-Weighted MRI", *Journal of Cerebral Blood Flow & Metabolism*, vol. 27, no. 6, pp. 1129–1136, 2007.

[57] Y. Guo, I. Y. Zhou, S. T. Chan, Y. Wang, E. T. Mandeville, T. Igarashi, E. H. Lo, X. Ji and P. Z. Sun, "pH-sensitive MRI demarcates graded tissue acidification during acute stroke pH specificity enhancement with magnetization transfer and relaxation-normalized amide proton transfer (APT) MRI", *NeuroImage*, vol. 141, pp. 242–249, 2016.

[58] F. Chen and Y.-C. Ni, "Magnetic resonance diffusion-perfusion mismatch in acute ischemic stroke: An update.", *World Journal of Radiology*, vol. 4, no. 3, pp. 63–74, 2012.

[59] M.-L. Garcia-Martin, G. Herigault, C. Remy, R. Farion, P. Ballesteros, J. A. Coles, S. Cerdan, A. Ziegler, M. L. García-Martín, G Hérigault, C Rémy, R. Farion, P. Ballesteros, J. A. Coles, S Cerdán and A. Ziegler, "Mapping Extracellular pH in Rat Brain Gliomas in Vivo by H Magnetic Resonance Spectroscopic Imaging: Comparison with Maps of Metabolites", *Cancer Research*, vol. 61, no. 17, pp. 6524–6531, 2001.

[60] L. J. Henderson, "Concerning the relationship between the strength of acids and their capacity to preserve neutrality", *American Journal of Physiology*, vol. 21, no. 2, 1908.

[61] F Ohta, K Moritake, T Kagawa, M Fukuda and A Fukuma, "Intracellular pH regulation of normal rat brain: 31P-MRS study.", *Acta neurochirurgica. Supplementum*, vol. 51, pp. 25–7, 1990.

[62] M. Rata, S. L. Giles, N. M. DeSouza, M. O. Leach and G. S. Payne, "Comparison of three reference methods for the measurement of intracellular pH using 31P MRS in healthy volunteers and patients with lymphoma", *NMR in Biomedicine*, vol. 27, no. 2, pp. 158–162, 2014.

[63] F. A. Gallagher, M. I. Kettunen, S. E. Day, D.-E. Hu, J. H. Ardenkjaer-Larsen, R. i. t. Zandt, P. R. Jensen, M. Karlsson, K. Golman, M. H. Lerche and K. M. Brindle, "Magnetic resonance imaging of pH in vivo using hyperpolarized 13C-labelled bicarbonate.", *Nature*, vol. 453, no. 7197, pp. 940–3, 2008.

[64] A. Z. Lau, J. J. Miller and D. J. Tyler, "Mapping of intracellular pH in the in vivo rodent heart using hyperpolarized [1-13C]pyruvate", *Magnetic Resonance in Medicine*, vol. 77, no. 5, pp. 1810–1817, 2017.

[65] G. V. Martinez, X. Zhang, M. L. García-Martín, D. L. Morse, M. Woods, A. D. Sherry and R. J. Gillies, "Imaging the extracellular pH of tumors by MRI after injection of a single cocktail of T1 and T2 contrast agents.", *NMR in Biomedicine*, vol. 24, no. 10, pp. 1380–91, 2011.

[66] M. L. Garcia-Martin, G. V. Martinez, N. Raghunand, A. D. Sherry, S. Zhang and R. J. Gillies, "High resolution pHe imaging of rat glioma using pH-dependent relaxivity", *Magnetic Resonance in Medicine*, vol. 55, no. 2, pp. 309–315, 2006.

[67] C. Olchowy, K. Cebulski, M. Łasecki, R. Chaber, A. Olchowy, K. Kałwak and U. Zaleska-Dorobisz, "The presence of the gadolinium-based contrast agent depositions in the brain and symptoms of gadolinium neurotoxicity - A systematic review", *PLOS ONE*, vol. 12, no. 2, S. Mohapatra, Ed., e0171704, 2017.

[68] S. Koda, J. Goodwin, V. V. Khramtsov, H. Fujii and H. Hirata, "Electron paramagnetic resonance-based pH mapping using spectral-spatial imaging of sequentially scanned spectra.", *Analytical Chemistry*, vol. 84, no. 8, pp. 3833–7, 2012.

[69] A. L. Vavere, G. B. Biddlecombe, W. M. Spees, J. R. Garbow, D. Wijesinghe, O. A. Andreev, D. M. Engelman, Y. K. Reshetnyak and J. S. Lewis, "A Novel Technology for the Imaging of Acidic Prostate Tumors by Positron Emission Tomography", *Cancer Research*, vol. 69, no. 10, pp. 4510–4516, 2009.

[70] M. N. Loja, Z. Luo, D Greg Farwell, Q. C. Luu, P. J. Donald, D. Amott, A. Q. Truong, R. F. Gandour-Edwards and N Nitin, "Optical molecular imaging detects changes in extracellular pH with the development of head and neck cancer.", *International Journal of Cancer*, vol. 132, no. 7, pp. 1613–23, 2013.

[71] R. M. Henderson, P. B. Bell, R. D. Cohen, C. Browning and R. A. Iles, "Measurement of intracellular pH with microelectrodes in rat kidney in vivo", *American Journal of Physiology*, vol. 250, no. 2 Pt 2, F203–9, 1986.

[72] D. G. Gadian, *NMR and its applications to living systems*. Oxford: Oxford University Press, 1995, p. 283.

[73] M. H. Levitt, *Spin dynamics : basics of nuclear magnetic resonance*. 2001, p. 714.

[74] M. A. Bernstein, K. F. King and X. J. Zhou, *Handbook of MRI pulse sequences*. Academic Press, 2004, p. 1017.

[75] D. W. McRobbie, E. A. Moore and M. J. Graves, *MRI from picture to proton*. Cambridge University Press, 2007, p. 394.

[76] R. W. Brown, Y.-C. N. Cheng, E. M. Haacke, M. R. Thompson and R. Venkatesan, *Magnetic resonance imaging : physical properties and sequence design*. Wiley, 2014, p. 978.

[77] J. Ashman, B. Badelek, G. Baum, J. Beaufays, C. Bee, C. Benchouk, I. Bird, S. Brown, M. Caputo, H. Cheung, J. Chima, J. Ciborowski, R. Clifft, G. Coignet, F. Combley, G. Court, G. D'Agostini, J. Drees, M. Düren, N. Dyce, A. Edwards, M. Edwards, T. Ernst, M. Ferrero, D. Francis, E. Gabathuler, J. Gajewski, R. Gamet, V. Gibson, J. Gillies, P. Graftström, K. Hamacher, D. Von Harrach, P. Hayman, J. Holt, V. Hughes, A. Jacholkowska, T. Jones, E. Kabuss, B. Korzen, U. Krüner, S. Kullander, U. Landgraf, D. Lanske, F. Lettenström, T. Lindqvist, J. Loken, M. Matthews, Y. Mizuno, K. Mönig, F. Montanet, J. Nassalski, T. Niinikoski, P. Norton, G. Oakham, R. Oppenheim, A. Osborne, V. Papavassiliou, N. Pavel, C. Peroni, H. Peschel, R. Piegaia, B. Pietrzyk, U. Pietrzyk, B. Povh, P. Renton, J. Rieubland, A. Rijllart, K. Rith, E. Rondio, L. Ropelewski, D. Salmon, A. Sandacz, T. Schröder, K. Schüler, K. Schultze, T.-A. Shibata, T. Sloan, A. Staiano, H. Stier, J. Stock, G. Taylor, J. Thompson, T. Walcher, S. Wheeler, W. Williams, S. Wimpenny, R. Windmolders, W. Womersley and K. Ziemons, "A measurement of the spin asymmetry and determination of the structure function g1 in deep inelastic muon-proton scattering", *Physics Letters B*, vol. 206, no. 2, pp. 364–370, 1988.

[78] F. Bloch, "Nuclear Induction", *Physical Review*, vol. 70, no. 7-8, pp. 460–474, 1946.

[79] A. Saupe and G. Englert, "High-Resolution Nuclear Magnetic Resonance Spectra of Orientated Molecules", *Physical Review Letters*, vol. 11, no. 10, pp. 462–464, 1963.

[80] S. D. Wolff and R. S. Balaban, "Magnetization transfer contrast (MTC) and tissue water proton relaxation in vivo.", *Magnetic Resonance in Medicine*, vol. 10, no. 1, pp. 135–44, 1989.

[81] R. M. Henkelman, G. J. Stanisz and S. J. Graham, "Magnetization Transfer in MRI: a review.", *NMR in Biomedicine*, vol. 14, no. 2, pp. 57–64, 2001.

[82] C. J. Gallagher and S. A. Moszkowski, "Coupling of Angular Momenta in Odd-Odd Nuclei", *Physical Review*, vol. 111, no. 5, pp. 1282–1290, 1958.

[83] E. Brunner, "Residual dipolar couplings in protein NMR", *Concepts in Magnetic Resonance*, vol. 13, no. 4, pp. 238–259, 2001.

[84] K. Wüthrich, *NMR of proteins and nucleic acids*. Wiley, 1986.

[85] E. E. Kwan and S. G. Huang, "Structural elucidation with NMR spectroscopy: Practical strategies for organic chemists", *European Journal of Organic Chemistry*, no. 16, pp. 2671–2688, 2008.

[86] S. Arrhenius, "Über die Dissociationswärme und den Einfluss der Temperatur auf den Dissociationsgrad der Elektrolyte", *Zeitschrift für Physikalische Chemie*, vol. 4, no. 1, 1889.

[87] K. M. Ward and R. S. Balaban, "Determination of pH using water protons and chemical exchange dependent saturation transfer (CEST).", *Magnetic Resonance in Medicine*, vol. 44, no. 5, pp. 799–802, 2000.

[88] P. C. van Zijl and N. N. Yadav, "Chemical exchange saturation transfer (CEST): what is in a name and what isn't?", *Magnetic Resonance in Medicine*, vol. 65, no. 4, pp. 927–948, 2011.

[89] J. Zhou, J. F. Payen, D. A. Wilson, R. J. Traystman and P. C. van Zijl, "Using the amide proton signals of intracellular proteins and peptides to detect pH effects in MRI", *Nature Medicine*, vol. 9, no. 8, pp. 1085–1090, 2003.

[90] E. Liepinsh and G. Otting, "Proton exchange rates from amino acid side chains - Implications for image contrast", *Magnetic Resonance in Medicine*, vol. 35, no. 1, pp. 30–42, 1996.

[91] M. Zaiss and P. Bachert, "Chemical exchange saturation transfer (CEST) and MR Z-spectroscopy in vivo: a review of theoretical approaches and methods.", en, *Physics in Medicine and Biology*, vol. 58, no. 22, R221–69, 2013.

[92] J. Hua, C. K. Jones, J. Blakeley, S. A. Smith, P. C. M. van Zijl and J. Zhou, "Quantitative description of the asymmetry in magnetization transfer effects around the water resonance in the human brain.", *Magnetic Resonance in Medicine*, vol. 58, no. 4, pp. 786–93, 2007.

[93] S. D. Swanson, D. I. Malyarenko, M. L. Fabiilli, R. C. Welsh, J.-F. Nielsen and A. Srinivasan, "Molecular, dynamic, and structural origin of inhomogeneous magnetization transfer in lipid membranes", *Magnetic Resonance in Medicine*, vol. 77, no. 3, pp. 1318–1328, 2017.

[94] S. Zhang, P. Winter, K. Wu and A. D. Sherry, "A Novel Europium(III)-Based MRI Contrast Agent", *Journal of the American Chemical Society*, vol. 123, no. 7, pp. 1517–1518, 2001.

[95] D. L. Longo, W. Dastrù, G. Digilio, J. Keupp, S. Langereis, S. Lanzardo, S. Prestigio, O. Steinbach, E. Terreno, F. Uggeri and S. Aime, "Iopamidol as a responsive MRI-chemical exchange saturation transfer contrast agent for pH mapping of kidneys: In vivo studies in mice at 7 T", *Magnetic Resonance in Medicine*, vol. 65, no. 1, pp. 202–211, 2011.

[96] J. Flament, F. Geffroy, C. Medina, C. Robic, J.-F. Mayer, S. Mériaux, J. Valette, P. Robert, M. Port, D. Le Bihan, F. Lethimonnier and F. Boumezbeur, "In vivo CEST MR imaging of U87 mice brain tumor angiogenesis using targeted LipoCEST contrast agent at 7 T", *Magnetic Resonance in Medicine*, vol. 69, no. 1, pp. 179–187, 2013.

[97] T. K. Stevens, K. K. Palaniappan, R. M. Ramirez, M. B. Francis, D. E. Wemmer and A. Pines, "HyperCEST detection of a 129Xe-based contrast agent composed of cryptophane-A molecular cages on a bacteriophage scaffold", *Magnetic Resonance in Medicine*, vol. 69, no. 5, pp. 1245–1252, 2013.

[98] H. M. McConnell, "Reaction Rates by Nuclear Magnetic Resonance", *The Journal of Chemical Physics*, vol. 28, no. 3, pp. 430–431, 1958.

[99] Z. Zu, K. Li, V. A. Janve, M. D. Does and D. F. Gochberg, "Optimizing pulsed-chemical exchange saturation transfer imaging sequences.", *Magnetic Resonance in Medicine*, vol. 66, no. 4, pp. 1100–8, 2011.

[100] Y. K. Tee, A. A. Khrapitchev, N. R. Sibson, S. J. Payne and M. A. Chappell, "Evaluating the use of a continuous approximation for model-based quantification of pulsed chemical exchange saturation transfer (CEST).", *Journal of Magnetic Resonance*, vol. 222, pp. 88–95, 2012.

[101] J. Zhou, B. Lal, D. A. Wilson, J. Laterra and P. C. van Zijl, "Amide proton transfer (APT) contrast for imaging of brain tumors", *Magnetic Resonance in Medicine*, vol. 50, no. 6, pp. 1120–1126, 2003.

[102] C. K. Jones, M. J. Schlosser, P. C. M. van Zijl, M. G. Pomper, X. Golay and J. Zhou, "Amide proton transfer imaging of human brain tumors at 3T.", *Magnetic Resonance in Medicine*, vol. 56, no. 3, pp. 585–92, 2006.

[103] T Shah, L Lu, K. M. Dell, M. D. Pagel, M. A. Griswold and C. A. Flask, "CEST-FISP: a novel technique for rapid chemical exchange saturation transfer MRI at 7 T.", *Magnetic Resonance in Medicine*, vol. 65, no. 2, pp. 432–7, 2011.

[104] Y. Zhang, H.-Y. Heo, S. Jiang, D.-H. Lee, P. A. Bottomley and J. Zhou, "Highly accelerated chemical exchange saturation transfer (CEST) measurements with linear algebraic modeling.", *Magnetic Resonance in Medicine*, vol. 76, no. 1, pp. 136–44, 2016.

[105] H.-Y. Heo, Y. Zhang, D.-H. Lee, S. Jiang, X. Zhao and J. Zhou, "Accelerating chemical exchange saturation transfer (CEST) MRI by combining compressed sensing and sensitivity encoding techniques", *Magnetic Resonance in Medicine*, vol. 77, no. 2, pp. 779–786, 2017.

[106] Z. Dai, J. Ji, G. Xiao, G. Yan, S. Li, G. Zhang, Y. Lin, Z. Shen and R. Wu, "Magnetization transfer prepared gradient echo MRI for CEST imaging.", *PloS one*, vol. 9, no. 11, e112219, 2014.

[107] E. A. Randtke, J. C. Granados, C. M. Howison, M. D. Pagel and J. Cárdenas-Rodríguez, "Multislice CEST MRI improves the spatial assessment of tumor pH", *Magnetic Resonance in Medicine*, vol. 78, no. 1, pp. 97–106, 2017.

[108] H. Y. Heo, C. K. Jones, J. Hua, N. Yadav, S. Agarwal, J. Zhou, P. C. M. van Zijl and J. J. Pillai, "Whole-brain amide proton transfer (APT) and nuclear overhauser enhancement (NOE) imaging in glioma patients using low-power steady-state pulsed chemical exchange saturation transfer (CEST) imaging at 7T", *Journal of Magnetic Resonance Imaging*, vol. 44, no. 1, pp. 41–50, 2016.

[109] U. Katscher and P. Börnert, "Parallel RF transmission in MRI", *NMR in Biomedicine*, vol. 19, no. 3, pp. 393–400, 2006.

[110] D. Liu, R. Xue, J. Zhou, J. An, X. Miao and D. J. Wang, "Using Simultaneous Multi-Slice Excitation to Accelerate CEST Imaging", in *Proceedings 22nd Scientific Meeting, International Society for Magnetic Resonance in Medicine*, 2014, p. 3294.

[111] J. Zhou, D. A. Wilson, P. Z. Sun, J. A. Klaus and P. C. M. Van Zijl, "Quantitative description of proton exchange processes between water and endogenous and exogenous agents for WEX, CEST, and APT experiments.", *Magnetic Resonance in Medicine*, vol. 51, no. 5, pp. 945–52, 2004.

[112] R. J. Harris, T. F. Cloughesy, L. M. Liau, P. L. Nghiemphu, A. Lai, W. B. Pope and B. M. Ellingson, "Simulation, phantom validation, and clinical evaluation of fast pH-weighted molecular imaging using amine chemical exchange saturation transfer echo planar imaging (CEST-EPI) in glioma at 3 T", *NMR in Biomedicine*, vol. 29, no. 11, pp. 1563–1576, 2016.

[113] P. S. Tofts, "PD: Proton Density of Tissue Water", in *Quantitative MRI of the Brain*, P. Tofts, Ed., John Wiley & Sons, Ltd, 2003, pp. 83–109.

[114] K. M. Ward, A. H. Aletras and R. S. Balaban, "A new class of contrast agents for MRI based on proton chemical exchange dependent saturation transfer (CEST)", *Journal of Magnetic Resonance*, vol. 143, no. 1, pp. 79–87, 2000.

[115] T. Jin, P. Wang, X. Zong and S.-G. Kim, "MR imaging of the amide-proton transfer effect and the pH-insensitive nuclear overhauser effect at 9.4 T.", *Magnetic Resonance in Medicine*, vol. 69, no. 3, pp. 760–70, 2013.

[116] M. Zaiss and P. Bachert, "Exchange-dependent relaxation in the rotating frame for slow and intermediate exchange – modeling off-resonant spin-lock and chemical exchange saturation transfer.", *NMR in Biomedicine*, vol. 26, no. 5, pp. 507–18, 2013.

[117] J. Xu, M. Zaiss, Z. Zu, H. Li, J. Xie, D. F. Gochberg, P. Bachert and J. C. Gore, "On the origins of chemical exchange saturation transfer (CEST) contrast in tumors at 9.4 T.", *NMR in Biomedicine*, vol. 27, no. 4, pp. 406–16, 2014.

[118] M. Zaiss, J. Xu, S. Goerke, I. S. Khan, R. J. Singer, J. C. Gore, D. F. Gochberg and P. Bachert, "Inverse Z-spectrum analysis for spillover-, MT-, and T1 -corrected steady-state pulsed CEST-MRI - application to pH-weighted MRI of acute stroke.", *NMR in Biomedicine*, vol. 27, pp. 240–252, 2014.

[119] K. L. Desmond, F. Moosvi and G. J. Stanisz, "Mapping of amide, amine, and aliphatic peaks in the CEST spectra of murine xenografts at 7 T", *Magnetic Resonance in Medicine*, vol. 71, no. 5, pp. 1841–1853, 2014.

[120] C. K. Jones, D. Polders, J. Hua, H. Zhu, H. J. Hoogduin, J. Zhou, P. Luijten and P. C. M. van Zijl, "In vivo three-dimensional whole-brain pulsed steady-state chemical exchange saturation transfer at 7 T.", *Magnetic Resonance in Medicine*, vol. 67, no. 6, pp. 1579–89, 2012.

[121] H. Y. Heo, Y. Zhang, S. Jiang, D. H. Lee and J. Zhou, "Quantitative assessment of amide proton transfer (APT) and nuclear overhauser enhancement (NOE) imaging with extrapolated semisolid magnetization transfer reference (EMR) signals: II. Comparison of three EMR models and application to human brain glioma at", *Magnetic Resonance in Medicine*, vol. 75, no. 4, pp. 1630–1639, 2016.

[122] K. L. Desmond and G. J. Stanisz, "Understanding quantitative pulsed CEST in the presence of MT.", *Magnetic Resonance in Medicine*, vol. 67, no. 4, pp. 979–90, 2012.

[123] N. Geades, B. A. E. Hunt, S. M. Shah, A. Peters, O. E. Mougin and P. A. Gowland, "Quantitative analysis of the z-spectrum using a numerically simulated look-up table: Application to the healthy human brain at 7T", *Magnetic Resonance in Medicine*, vol. 78, no. 2, pp. 645–655, 2016.

[124] M. Chappell, A. Groves, B. Whitcher and M. Woolrich, "Variational Bayesian Inference for a Nonlinear Forward Model", *IEEE Transactions on Signal Processing*, vol. 57, no. 1, pp. 223–236, 2009.

[125] M. A. Chappell, M. J. Donahue, Y. K. Tee, A. A. Khrapitchev, N. R. Sibson, P. Jezzard and S. J. Payne, "Quantitative Bayesian model-based analysis of amide proton transfer MRI", *Magnetic Resonance in Medicine*, vol. 70, no. 2, pp. 556–567, 2013.

[126] Y. K. Tee, G. W. J. Harston, N Blockley, T. W. Okell, J Levman, F Sheerin, M Cellerini, P Jezzard, J Kennedy, S. J. Payne and M. A. Chappell, "Comparing different analysis methods for quantifying the MRI amide proton transfer (APT) effect in hyperacute stroke patients.", *NMR in Biomedicine*, vol. 27, no. 9, pp. 1019–29, 2014.

[127] J. Zhou and P. C. van Zijl, "Chemical exchange saturation transfer imaging and spectroscopy", *Progress in Nuclear Magnetic Resonance Spectroscopy*, vol. 48, no. 2-3, pp. 109–136, 2006.

[128] A. D. Sherry and M. Woods, "Chemical Exchange Saturation Transfer Contrast Agents for Magnetic Resonance Imaging", en, *Annual Review of Biomedical Engineering*, vol. 10, pp. 391–411, 2008.

[129] E. Vinogradov, A. D. Sherry and R. E. Lenkinski, "CEST: From basic principles to applications, challenges and opportunities", *Journal of Magnetic Resonance*, vol. 229, pp. 155–172, 2013.

[130] F. Kogan, H. Hariharan and R. Reddy, "Chemical Exchange Saturation Transfer (CEST) Imaging: Description of Technique and Potential Clinical Applications.", *Current Radiology Reports*, vol. 1, no. 2, pp. 102–114, 2013.

[131] G. Liu, X. Song, K. W. Y. Chan and M. T. McMahon, "Nuts and bolts of chemical exchange saturation transfer MRI.", *NMR in Biomedicine*, vol. 26, no. 7, pp. 810–28, 2013.

[132] P. Z. Sun, G. Xiao, I. Y. Zhou, Y. Guo and R. Wu, "A method for accurate pH mapping with chemical exchange saturation transfer (CEST) MRI", *Contrast Media and Molecular Imaging*, vol. 11, no. 3, pp. 195–202, 2016.

[133] P. Z. Sun, E. Wang and J. S. Cheung, "Imaging acute ischemic tissue acidosis with pH-sensitive endogenous amide proton transfer (APT) MRI–correction of tissue relaxation and concomitant RF irradiation effects toward mapping quantitative cerebral tissue pH.", *NeuroImage*, vol. 60, no. 1, pp. 1–6, 2012.

[134] P. Z. Sun, Y. Murata, J. Lu, X. Wang, E. H. Lo and A. G. Sorensen, "Relaxation-compensated fast multislice amide proton transfer (APT) imaging of acute ischemic stroke.", *Magnetic Resonance in Medicine*, vol. 59, no. 5, pp. 1175–82, 2008.

[135] J. Zhou, "Amide Proton Transfer Imaging of the Human Brain", *Magnetic Resonance Neuroimaging: Methods and Protocols*, vol. 711, pp. 227–237, 2011.

[136] J. Zhou, H. Zhu, M. Lim, L. Blair, A. Quinones-Hinojosa, S. A. Messina, C. G. Eberhart, M. G. Pomper, J. Laterra, P. B. Barker, P. C. M. van Zijl and J. O. Blakeley, "Three-Dimensional Amide Proton Transfer MR Imaging of Gliomas: Initial Experience and Comparison With Gadolinium Enhancement", *Journal of Magnetic Resonance Imaging*, vol. 38, no. 5, pp. 1119–1128, 2013.

[137] J. Zhou, X. Hong, X. Zhao, J. H. Gao and J. Yuan, "APT-weighted and NOE-weighted image contrasts in glioma with different RF saturation powers based on magnetization transfer ratio asymmetry analyses", *Magnetic Resonance in Medicine*, vol. 70, no. 2, pp. 320–327, 2013. arXiv: NIHMS150003.

[138] J. Zhou, E. Tryggestad, Z. Wen, B. Lal, T. Zhou, R. Grossman, S. Wang, K. Yan, D.-X. Fu, E. Ford, B. Tyler, J. Blakeley, J. Laterra and P. C. M. van Zijl, "Differentiation between glioma and radiation necrosis using molecular magnetic resonance imaging of endogenous proteins and peptides.", *Nature Medicine*, vol. 17, no. 1, pp. 130–4, 2011.

[139] H. Mehrabian, K. L. Desmond, H. Soliman, A. Sahgal and G. J. Stanisz, "Differentiation between Radiation Necrosis and Tumor Progression Using Chemical Exchange Saturation Transfer", *Clinical Cancer Research*, vol. 23, no. 14, pp. 3667–3675, 2017.

[140] B. Ma, J. O. Blakeley, X. Hong, H. Zhang, S. Jiang, L. Blair, Y. Zhang, H. Y. Heo, M. Zhang, P. C. M. van Zijl and J. Zhou, "Applying amide proton transfer-weighted MRI to distinguish pseudoprogression from true progression in malignant gliomas", *Journal of Magnetic Resonance Imaging*, vol. 44, no. 2, pp. 456–462, 2016.

[141] E. A. Randtke, L. Q. Chen, L. R. Corrales and M. D. Pagel, "The Hanes-Woolf linear QUESP method improves the measurements of fast chemical exchange rates with CEST MRI.", *Magnetic Resonance in Medicine*, vol. 71, no. 4, pp. 1603–12, 2014.

[142] L. Q. Chen, C. M. Howison, J. J. Jeffery, I. F. Robey, P. H. Kuo and M. D. Pagel, "Evaluations of extracellular PH within in vivo tumors using acidocest MRI", *Magnetic Resonance in Medicine*, vol. 72, no. 5, pp. 1408–1417, 2014.

[143] S. Walker-Samuel, R. Ramasawmy, F. Torrealdea, M. Rega, V. Rajkumar, S. P. Johnson, S. Richardson, M. Gonçalves, H. G. Parkes, E. Arstad, D. L. Thomas, R. B. Pedley, M. F. Lythgoe and X. Golay, "In vivo imaging of glucose uptake and metabolism in tumors.", en, *Nature Medicine*, vol. 19, no. 8, pp. 1067–72, 2013.

[144] M Rivlin, J Horev, I Tsarfaty and G Navon, "Molecular imaging of tumors and metastases using chemical exchange saturation transfer (CEST) MRI", *Scientific Reports*, vol. 3, p. 3045, 2013.

[145] X. Xu, K. W. Chan, L. Knutsson, D. Artemov, J. Xu, G. Liu, Y. Kato, B. Lal, J. Laterra, M. T. McMahon and P. C. van Zijl, "Dynamic glucose enhanced (DGE) MRI for combined imaging of blood-brain barrier break down and increased blood volume in brain cancer", *Magnetic Resonance in Medicine*, vol. 74, no. 6, pp. 1556–1563, 2015.

[146] S. Goerke, M. Zaiss, P. Kunz, K. D. Klika, J. D. Windschuh, A. Mogk, B. Bukau, M. E. Ladd and P. Bachert, "Signature of protein unfolding in chemical exchange saturation transfer imaging", *NMR in Biomedicine*, vol. 28, no. 7, pp. 906–913, 2015.

[147] S. Goerke, K. S. Milde, R. Bukowiecki, P. Kunz, K. D. Klika, T. Wiglenda, A. Mogk, E. E. Wanker, B. Bukau, M. E. Ladd, P. Bachert and M. Zaiss, "Aggregation-induced changes in the chemical exchange saturation transfer (CEST) signals of proteins", *NMR in Biomedicine*, vol. 30, no. 1, e3665, 2017.

[148] E. Demetriou, M. Tachrount, M. Rega, F. Torrealdea, K. Shmueli, M. Farrow and X. Golay, "CEST Nuclear Overhauser Enhancement imaging of protein misfolding in mice at different stages of prion disease", in *Proceedings 24th Scientific Meeting, International Society for Magnetic Resonance in Medicine*, 2016, p. 2324.

[149] A. Einstein, "Investigations on the Theory of the Brownian Movement", PhD thesis, 1926.

[150] E. O. Stejskal and J. E. Tanner, "Spin Diffusion Measurements: Spin Echoes in the Presence of a TimeDependent Field Gradient", *The Journal of Chemical Physics*, vol. 42, no. 1, pp. 288–292, 1965.

[151] J. E. Tanner, "Use of the Stimulated Echo in NMR Diffusion Studies", *The Journal of Chemical Physics*, vol. 52, no. 5, pp. 2523–2526, 1970.

[152] K. D. Merboldt, W Hänicke and J Frahm, "Diffusion imaging using stimulated echoes.", *Magnetic Resonance in Medicine*, vol. 19, no. 2, pp. 233–9, 1991.

[153] D. K. Jones, T. R. Knösche and R. Turner, "White matter integrity, fiber count, and other fallacies: The do's and don'ts of diffusion MRI", *NeuroImage*, vol. 73, pp. 239–254, 2013.

[154] H. Johansen-Berg and T. E. J. Behrens, "Just pretty pictures? What diffusion tractography can add in clinical neuroscience.", *Current Opinion in Neurology*, vol. 19, no. 4, pp. 379–85, 2006.

[155] N Bharwani, M. E. Miquel, A Sahdev, P Narayanan, G Malietzis, R. H. Reznek and A. G. Rockall, "Diffusion-weighted imaging in the assessment of tumour grade in endometrial cancer.", *The British Journal of Radiology*, vol. 84, no. 1007, pp. 997–1004, 2011.

[156] L. Chen, J. Zhang, Y. Chen, W. Wang, X. Zhou, X. Yan and J. Wang, "Relationship between Apparent Diffusion Coefficient and Tumour Cellularity in Lung Cancer", *PLoS One*, vol. 9, no. 6, M. R. Emmert-Buck, Ed., e99865, 2014.

[157] M. P. Lichy, P. Aschoff, C. Plathow, A. Stemmer, W. Horger, C. Mueller-Horvat, G. Steidle, M. Horger, J. Schafer, S. M. Eschmann, B. Kiefer, C. D. Claussen, C. Pfannenberg and H.-P. Schlemmer, "Tumor Detection by Diffusion-Weighted MRI and ADC-Mapping???Initial Clinical Experiences in Comparison to PET-CT", *Investigative Radiology*, vol. 42, no. 9, pp. 605–613, 2007.

[158] P. C. Van Zijl, C. T. Moonen, P. Faustino, J. Pekar, O. Kaplan and J. S. Cohen, "Complete separation of intracellular and extracellular information in NMR spectra of perfused cells by diffusion-weighted spectroscopy.", *Proceedings of the National Academy of Sciences*, vol. 88, no. 8, pp. 3228–3232, 1991.

[159] Y Assaf and Y Cohen, "Non-mono-exponential attenuation of water and N-acetyl aspartate signals due to diffusion in brain tissue.", *Journal of Magnetic Resonance*, vol. 131, no. 1, pp. 69–85, 1998.

[160] U. Pilatus, H. Shim, D. Artemov, D. Davis, P. C. M. Van Zijl and J. D. Glickson, "Intracellular volume and apparent diffusion constants of perfused cancer cell cultures, as measured by NMR", *Magnetic Resonance in Medicine*, vol. 37, no. 6, pp. 825–832, 1997.

[161] T. Niendorf, R. M. Dijkhuizen, D. G. Norris, M. van Lookeren Campagne and K. Nicolay, "Biexponential diffusion attenuation in various states of brain tissue: Implications for diffusion-weighted imaging", *Magnetic Resonance in Medicine*, vol. 36, no. 6, pp. 847–857, 1996.

[162] A Van Harreveld, "The extracellular space in the vertebrate nervous system", in *The structure and function of nervous tissue*, G. Bourne, Ed., New York: Academic Press, 1972, pp. 447–511.

[163] I Voíšek, M Hájek, J Tintěra, K Nicolay and E. Syková, "Water ADC, extracellular space volume, and tortuosity in the rat cortex after traumatic injury", *Magnetic Resonance in Medicine*, vol. 48, no. 6, pp. 994–1003, 2002.

[164] J. V. Sehy, J. J. Ackerman and J. J. Neil, "Evidence that both fast and slow water ADC components arise from intracellular space", *Magnetic Resonance in Medicine*, vol. 48, no. 5, pp. 765–770, 2002.

[165] A. Schwarcz, P. Bogner, P. Meric, J.-L. Correze, Z. Berente, J. Pál, F. Gallyas, T. Doczi, B. Gillet and J.-C. Beloeil, "The existence of biexponential signal decay in magnetic resonance diffusion-weighted imaging appears to be independent of compartmentalization.", *Magnetic Resonance in Medicine*, vol. 51, no. 2, pp. 278–85, 2004.

[166] J. D. Quirk, G. L. Bretthorst, T. Q. Duong, A. Z. Snyder, C. S. Springer, J. J. H. Ackerman and J. J. Neil, "Equilibrium water exchange between the intra- and extracellular spaces of mammalian brain", *Magnetic Resonance in Medicine*, vol. 50, no. 3, pp. 493–499, 2003.

[167] M. D. Silva, T. Omae, K. G. Helmer, F. Li, M. Fisher and C. H. Sotak, "Separating changes in the intra- and extracellular water apparent diffusion coefficient following focal cerebral ischemia in the rat brain", *Magnetic Resonance in Medicine*, vol. 48, no. 5, pp. 826–837, 2002.

[168] H. C. Torrey, "Bloch Equations with Diffusion Terms", *Physical Review*, vol. 104, no. 15, 1956.

[169] R. Steier, M. Aradi, J. Pál, G. Perlaki, G. Orsi, P. Bogner, F. Galyas, P. Bukovics, J. Janszky, T. Dóczi and A. Schwarcz, "A biexponential DWI study in rat brain intracellular oedema.", *European Journal of Radiology*, vol. 81, no. 8, pp. 1758–65, 2012.

[170] N. Gilani, P. Malcolm and G. Johnson, "A model describing diffusion in prostate cancer", *Magnetic Resonance in Medicine*, 2016.

[171] A. R. Padhani, G. Liu, D. Mu-Koh, T. L. Chenevert, H. C. Thoeny, T. Takahara, A. Dzik-Jurasz, B. D. Ross, M. Van Cauteren, D. Collins, D. A. Hammoud, G. J. Rustin, B. Taouli and P. L. Choyke, "Diffusion-Weighted Magnetic Resonance Imaging as a Cancer Biomarker: Consensus and Recommendations", English, *Neoplasia*, vol. 11, no. 2, pp. 102–125, 2009.

[172] J.-H. Lee and C. S. Springer, "Effects of equilibrium exchange on diffusion-weighted NMR signals: The diffusigraphic ?shutter-speed?", *Magnetic Resonance in Medicine*, vol. 49, no. 3, pp. 450–458, 2003.

[173] U. Ferizi, T. Schneider, E. Panagiotaki, G. Nedjati-Gilani, H. Zhang, C. A. M. Wheeler-Kingshott and D. C. Alexander, "A ranking of diffusion MRI compartment models with in vivo human brain data.", *Magnetic Resonance in Medicine*, vol. 72, no. 6, pp. 1785–92, 2014.

[174] J. H. Jensen and J. A. Helpern, "MRI quantification of non-Gaussian water diffusion by kurtosis analysis", *NMR in Biomedicine*, vol. 23, no. 7, pp. 698–710, 2010. arXiv: NIHMS150003.

[175] D Le Bihan, E Breton, D Lallemand, M. L. Aubin, J Vignaud and M Laval-Jeantet, "Separation of diffusion and perfusion in intravoxel incoherent motion MR imaging.", *Radiology*, vol. 168, no. 2, pp. 497–505, 1988.

[176] P. W. Hales and C. A. Clark, "Combined arterial spin labeling and diffusion-weighted imaging for noninvasive estimation of capillary volume fraction and permeability-surface product in the human brain.", *Journal of Cerebral Blood Flow and Metabolism*, vol. 33, no. 1, pp. 67–75, 2013.

[177] E. Panagiotaki, S. Walker-Samuel, B. Siow, S. P. Johnson, V. Rajkumar, R. B. Pedley, M. F. Lythgoe and D. C. Alexander, "Noninvasive Quantification of Solid Tumor Microstructure Using VERDICT MRI", *Cancer Research*, vol. 74, no. 7, pp. 1902–1912, 2014.

[178] E. Panagiotaki, R. W. Chan, N. Dikaios, H. U. Ahmed, J. O'Callaghan, A. Freeman, D. Atkinson, S. Punwani, D. J. Hawkes and D. C. Alexander, "Microstructural Characterization of Normal and Malignant Human Prostate Tissue With Vascular, Extracellular, and Restricted Diffusion for Cytometry in Tumours Magnetic Resonance Imaging", *Investigative Radiology*, vol. 50, no. 4, pp. 218–227, 2015.

[179] P. Z. Sun, Y. Wang, Z. Z. Dai, G. Xiao and R. Wu, "Quantitative chemical exchange saturation transfer (qCEST) MRI RF spillover effect corrected omega plot for simultaneous determination of labile proton fraction ratio and exchange rate", en, *Contrast Media & Molecular Imaging*, vol. 9, no. 4, pp. 268–275, 2014.

[180] W. T. Dixon, J. Ren, A. J. M. Lubag, J. Ratnakar, E. Vinogradov, I. Hancu, R. E. Lenkinski and A. D. Sherry, "A Concentration-Independent Method to Measure Exchange Rates in PARACEST Agents", *Magnetic Resonance in Medicine*, vol. 63, no. 3, pp. 625–632, 2010.

[181] C. K. Jones, A. Huang, J. Xu, R. A. E. Edden, M. Schär, J. Hua, N. Oskolkov, D. Zacà, J. Zhou, M. T. McMahon, J. J. Pillai and P. C. M. van Zijl, "Nuclear Overhauser enhancement (NOE) imaging in the human brain at 7T.", *NeuroImage*, vol. 77, pp. 114–24, 2013.

[182] S. Serres, C. J. Martin, M. Sarmiento Soto, C. Bristow, E. R. O'Brien, J. J. Connell, A. A. Khrapitchev and N. R. Sibson, "Structural and functional effects of metastases in rat brain determined by multimodal MRI.", *International Journal of Cancer*, vol. 134, no. 4, pp. 885–96, 2014.

[183] Z. M. Bhujwalla, E. O. Aboagye, R. J. Gillies, V. P. Chacko, C. E. Mendola and J. M. Backer, "Nm23-transfected MDA-MB-435 human breast carcinoma cells form tumors with altered phospholipid metabolism and pH: a 31P nuclear magnetic resonance study in vivo and in vitro.", *Magnetic Resonance in Medicine*, vol. 41, no. 5, pp. 897–903, 1999.

[184] N. McVicar, A. X. Li, M. Suchý, R. H. E. Hudson, R. S. Menon and R. Bartha, "Simultaneous in vivo pH and temperature mapping using a PARACEST-MRI contrast agent.", *Magnetic Resonance in Medicine*, 2012.

[185] M. Banay-Schwartz, A. Kenessey, T. DeGuzman, A. Lajtha and M. Palkovits, "Protein content of various regions of rat brain and adult and aging human brain", *Age*, vol. 15, no. 2, pp. 51–54, 1992.

[186] F Delaglio, S Grzesiek, G. W. Vuister, G Zhu, J Pfeifer and A Bax, "NMRPipe: a multidimensional spectral processing system based on UNIX pipes.", *Journal of Biomolecular NMR*, vol. 6, no. 3, pp. 277–93, 1995.

[187] S Holm, "A simple sequentially rejective multiple test procedure", *Scandinavian Journal of Statistics*, vol. 6, pp. 65 –70, 1979.

[188] N. McVicar, A. X. Li, D. F. Gonçalves, M. Bellyou, S. O. Meakin, M. A. Prado and R. Bartha, "Quantitative tissue pH measurement during cerebral ischemia using amine and amide concentration-independent detection (AACID) with MRI.", *Journal of Cerebral Blood Flow & Metabolism*, vol. 34, no. 4, pp. 690–8, 2014.

[189] R. Damadian, K. Zaner, D. Hor and T. DiMaio, "Human Tumors Detected by Nuclear Magnetic Resonance", *Proceedings of the National Academy of Sciences*, vol. 71, no. 4, pp. 1471–1473, 1974.

[190] K. Yan, Z. Fu, C. Yang, K. Zhang, S. Jiang, D.-H. Lee, H.-Y. Heo, Y. Zhang, R. N. Cole, J. E. Van Eyk and J. Zhou, "Assessing Amide Proton Transfer (APT) MRI Contrast Origins in 9 L Gliosarcoma in the Rat Brain Using Proteomic Analysis.", *Molecular Imaging and Biology*, vol. 17, no. 4, pp. 479–87, 2015.

[191] X. Zong, P. Wang, S.-G. Kim and T. Jin, "Sensitivity and source of amine-proton exchange and amide-proton transfer magnetic resonance imaging in cerebral ischemia.", *Magnetic Resonance in Medicine*, vol. 71, no. 1, pp. 118–32, 2014.

[192] A. M. Porcelli, A. Ghelli, C. Zanna, P. Pinton, R. Rizzuto and M. Rugolo, "pH difference across the outer mitochondrial membrane measured with a green fluorescent protein mutant.", *Biochemical and Biophysical Research Communications*, vol. 326, no. 4, pp. 799–804, 2005.

[193] C. C. Overly, K. D. Lee, E Berthiaume and P. J. Hollenbeck, "Quantitative measurement of intraorganelle pH in the endosomal-lysosomal pathway in neurons by using ratiometric imaging with pyranine.", *Proceedings of the National Academy of Sciences of the United States of America*, vol. 92, no. 8, pp. 3156–60, 1995.

[194] Y. K. Tee, A. A. Khrapitchev, N. R. Sibson, S. J. Payne and M. A. Chappell, "Optimal Sampling Schedule for Chemical Exchange Saturation Transfer", *Magnetic Resonance in Medicine*, vol. 70, no. 5, pp. 1251–1262, 2013.

[195] G. J. Stanisz, A. Kecojevic, M. J. Bronskill and R. M. Henkelman, "Characterizing white matter with magnetization transfer and T2", *Magnetic Resonance in Medicine*, vol. 42, no. 6, pp. 1128–1136, 1999.

[196] A. Mcintyre, A. Hulikova, I. Ledaki, C. Snell, D. Singleton, G. Steers, P. Seden, D. Jones, E. Bridges, S. Wigfield, J.-L. Li, A. Russell, P. Swietach and A. L. Harris, "Disrupting Hypoxia-Induced Bicarbonate Transport Acidifies Tumor Cells and Suppresses Tumor Growth", *Cancer Research*, vol. 76, no. 13, OF1 –OF12, 2016.

[197] D. H. Lee, H. Y. Heo, K. Zhang, Y. Zhang, S. Jiang, X. Zhao and J. Zhou, "Quantitative assessment of the effects of water proton concentration and water T1 changes on amide proton transfer (APT) and nuclear overhauser enhancement (NOE) MRI: The origin of the APT imaging signal in brain tumor", *Magnetic Resonance in Medicine*, vol. 77, no. 2, pp. 855–863, 2017.

[198] J. Zhou, J. O. Blakeley, J. Hua, M. Kim, J. Laterra, M. G. Pomper and P. C. M. van Zijl, "Practical data acquisition method for human brain tumor amide proton transfer (APT) imaging", *Magnetic Resonance in Medicine*, vol. 60, no. 4, pp. 842–849, 2008.

[199] P. Z. Sun, J. Zhou, J. Huang and P. van Zijl, "Simplified quantitative description of amide proton transfer (APT) imaging during acute ischemia", *Magnetic Resonance in Medicine*, vol. 57, no. 2, pp. 405–410, 2007.

[200] P. Kinchesh, P. D. Allen, J. S. Beech, E. Fokas, S. Gilchrist, V. Kersemans, R. Muschel and S. C. Smart, "Dynamic Reacquisition for Respiratory Gated, Constant TR 2D multi-slice

MRI", in *Proceedings 23rd Scientific Meeting, International Society for Magnetic Resonance in Medicine*, 2015, p. 2574.

[201] M. Borenstein, L. V. Hedges, J. P. Higgins and H. R. Rothstein, "A basic introduction to fixed-effect and random-effects models for meta-analysis", *Research Synthesis Methods*, vol. 1, no. 2, pp. 97–111, 2010.

[202] D. C. Alsop, J. A. Detre, X. Golay, M. Günther, J. Hendrikse, L. Hernandez-Garcia, H. Lu, B. J. MacIntosh, L. M. Parkes, M. Smits, M. J. P. van Osch, D. J. J. Wang, E. C. Wong and G. Zaharchuk, "Recommended implementation of arterial spin-labeled perfusion MRI for clinical applications: A consensus of the ISMRM perfusion study group and the European consortium for ASL in dementia", *Magnetic Resonance in Medicine*, vol. 73, no. 1, pp. 102–116, 2015.

[203] V. L. Yarnykh, "Actual flip-angle imaging in the pulsed steady state: A method for rapid three-dimensional mapping of the transmitted radiofrequency field", *Magnetic Resonance in Medicine*, vol. 57, no. 1, pp. 192–200, 2007.

[204] B. A. Sutherland, J. C. Fordsmann, C. Martin, A. A. Neuhaus, B. M. Witgen, H. Piilgaard, M. Lønstrup, Y. Couch, N. R. Sibson, M. Lauritzen and A. M. Buchan, "Multi-modal assessment of neurovascular coupling during cerebral ischaemia and reperfusion using remote middle cerebral artery occlusion", *Journal of Cerebral Blood Flow & Metabolism*, vol. 37, no. 7, pp. 2494–2508, 2017.

[205] P. Smith, R. Krohn, G. Hermanson, A. Mallia, F. Gartner, M. Provenzano, E. Fujimoto, N. Goeke, B. Olson and D. Klenk, "Measurement of protein using bicinchoninic acid", *Analytical Biochemistry*, vol. 150, no. 1, pp. 76–85, 1985.

[206] M. M. Bradford, "A rapid and sensitive method for the quantitation of microgram quantities of protein utilizing the principle of protein-dye binding", *Analytical Biochemistry*, vol. 72, no. 1-2, pp. 248–254, 1976.

[207] J. A. Miller, P. Curella and N. R. Zahniser, "A new densitometric procedure to measure protein levels in tissue slices used in quantitative autoradiography", *Brain Research*, vol. 447, no. 1, pp. 60–66, 1988.

[208] M. J.M. J. Aminoff and R. B. Daroff, *Encyclopedia of the neurological sciences*. 2003.

[209] P. Z. Sun, C. T. Farrar and A. G. Sorensen, "Correction for artifacts induced by B(0) and B(1) field inhomogeneities in pH-sensitive chemical exchange saturation transfer (CEST) imaging.", *Magnetic Resonance in Medicine*, vol. 58, no. 6, pp. 1207–15, 2007.

[210] J Ahmadi, S Destian, M. L. Apuzzo, H. D. Segall and C. S. Zee, "Cystic fluid in craniopharyngiomas: MR imaging and quantitative analysis.", *Radiology*, vol. 182, no. 3, pp. 783–785, 1992.

[211] J Zhou, K Yan and H Zhu, "A simple model for understanding the origin of the amide proton transfer MRI signal in tissue", *Applied Magnetic Resonance*, vol. 42, no. 3, pp. 393–402, 2012.

[212] X. Zhang, Y. Lin and R. J. Gillies, "Tumor pH and its measurement.", *Journal of Nuclear Medicine*, vol. 51, no. 8, pp. 1167–70, 2010.

[213] M Chopp, S Frinak, D. R. Walton, M. B. Smith and K. M. Welch, "Intracellular acidosis during and after cerebral ischemia: in vivo nuclear magnetic resonance study of hyperglycemia in cats.", *Stroke*, vol. 18, no. 5, 1987.

[214] Y. Huang and J. O. McNamara, "Ischemic stroke: "acidotoxicity" is a perpetrator.", English, *Cell*, vol. 118, no. 6, pp. 665–6, 2004.

[215] E. K. Rofstad, B. Mathiesen, K. Kindem and K. Galappathi, "Acidic Extracellular pH Promotes Experimental Metastasis of Human Melanoma Cells in Athymic Nude Mice", *Cancer Research*, vol. 66, no. 13, pp. 6699–6707, 2006.

[216] J Pouysségur, A Franchi, G L'Allemain and S Paris, "Cytoplasmic pH, a key determinant of growth factor-induced DNA synthesis in quiescent fibroblasts.", *FEBS letters*, vol. 190, no. 1, pp. 115–9, 1985.

[217] L. Brocchieri and S. Karlin, "Protein length in eukaryotic and prokaryotic proteomes.", *Nucleic Acids Research*, vol. 33, no. 10, pp. 3390–400, 2005.

[218] F. Tekaia, E. Yeramian and B. Dujon, "Amino acid composition of genomes, lifestyles of organisms, and evolutionary trends: a global picture with correspondence analysis.", *Gene*, vol. 297, no. 1-2, pp. 51–60, 2002.

[219] M Beals, L Gross and S Harrell, *Amino Acid Frequency*, 1999.

[220] S. M. E. Truhlar, C. H. Croy, J. W. Torpey, J. R. Koeppe and E. A. Komives, "Solvent accessibility of protein surfaces by amide H/2H exchange MALDI-TOF mass spectrometry", *Journal of the American Society for Mass Spectrometry*, vol. 17, no. 11, pp. 1490–1497, 2006.

[221] G. Hernández, J. S. Anderson and D. M. LeMaster, "Experimentally assessing molecular dynamics sampling of the protein native state conformational distribution.", *Biophysical Chemistry*, vol. 163-164, pp. 21–34, 2012.

[222] M. Zaiss, P. Kunz, S. Goerke, A. Radbruch and P. Bachert, "MR imaging of protein folding in vitro employing Nuclear-Overhauser-mediated saturation transfer", *NMR in Biomedicine*, vol. 26, no. 12, pp. 1815–1822, 2013.

[223] M. Hoelscher, N. Richter, C. Melle, F. von Eggeling, A. Schaenzer and U. Nestler, "SELDI-TOF analysis of glioblastoma cyst fluid is an approach for assessing cellular protein expression.", *Neurological Research*, vol. 35, no. 10, pp. 993–1001, 2013.

[224] T. E. Shaiken and A. R. Opekun, "Dissecting the cell to nucleus, perinucleus and cytosol", *Scientific Reports*, vol. 4, no. 1, p. 4923, 2015.

[225] C. Li and M. Liu, "Protein dynamics in living cells studied by in-cell NMR spectroscopy", *FEBS Letters*, vol. 587, no. 8, pp. 1008–1011, 2013.

[226] C. A. Waudby, M. D. Mantle, L. D. Cabrita, L. F. Gladden, C. M. Dobson and J. Christodoulou, "Rapid Distinction of Intracellular and Extracellular Proteins Using NMR Diffusion Measurements", *Journal of the American Chemical Society*, vol. 134, no. 28, pp. 11 312–11 315, 2012.

[227] L. Zhao, C. D. Kroenke, J. Song, D. Piwnica-Worms, J. J. H. Ackerman and J. J. Neil, "Intracellular water-specific MR of microbead-adherent cells: the HeLa cell intracellular water exchange lifetime", *NMR in Biomedicine*, vol. 21, no. 2, pp. 159–164, 2008.

[228] D. M. Yang, J. E. Huettner, G. L. Bretthorst, J. J. Neil, J. R. Garbow and J. J. Ackerman, "Intracellular water preexchange lifetime in neurons and astrocytes", *Magnetic Resonance in Medicine*, 2017.

[229] J. D. Quirk, G. L. Bretthorst, T. Q. Duong, A. Z. Snyder, C. S. Springer, J. J. Ackerman and J. J. Neil, "Equilibrium water exchange between the intra- and extracellular spaces of mammalian brain", *Magnetic Resonance in Medicine*, vol. 50, no. 3, pp. 493–499, 2003.

[230] X. He, M. E. Raichle and D. A. Yablonskiy, "Transmembrane dynamics of water exchange in human brain", *Magnetic Resonance in Medicine*, vol. 67, no. 2, pp. 562–571, 2012.

[231] V. Pereno, D. Carugo, L. Bau, E. Sezgin, J. Bernardino de la Serna, C. Eggeling and E. Stride, "Electroformation of Giant Unilamellar Vesicles on Stainless Steel Electrodes", *ACS Omega*, vol. 2, no. 3, pp. 994–1002, 2017.

[232] C. H. Neuman, "Spin echo of spins diffusing in a bounded medium", *The Journal of Chemical Physics*, vol. 60, no. 11, pp. 4508–4511, 1974.

[233] H. Li, K. Li, X. Y. Zhang, X. Jiang, Z. Zu, M. Zaiss, D. F. Gochberg, J. C. Gore and J. Xu, "R1 correction in amide proton transfer imaging: Indication of the influence of transcytolemmal water exchange on CEST measurements", *NMR in Biomedicine*, vol. 28, no. 12, 2015.

[234] C. Soto, "Unfolding the role of protein misfolding in neurodegenerative diseases", *Nature Reviews Neuroscience*, vol. 4, no. 1, pp. 49–60, 2003.

[235] A. J. Thistlethwaite, G. A. Alexander, D. J. Moylan, D. B. Leeper, D. J. Moylan Iii and D. B. Leeper, "Modification of human tumor pH by elevation of blood glucose.", *International Journal of Radiation Oncology, Biology, Physics*, vol. 13, no. 4, pp. 603–10, 1987.

[236] T Volk, E Jähde, H. P. Fortmeyer, K. H. Glüsenkamp and M. F. Rajewsky, "pH in human tumour xenografts: effect of intravenous administration of glucose.", *British Journal of Cancer*, vol. 68, no. 3, pp. 492–500, 1993.

[237] D. B. Leeper, K. Engin, A. J. Thistlethwaite, H. D. Hitchon, J. D. Dover, D.-J. Li and L. Tupchong, "Human tumor extracellular pH as a function of blood glucose concentration", *International Journal of Radiation Oncology, Biology, Physics*, vol. 28, no. 4, pp. 935–943, 1994.

[238] M Dellian, G Helmlinger, F Yuan and R. K. Jain, "Fluorescence ratio imaging of interstitial pH in solid tumours: effect of glucose on spatial and temporal gradients.", *British Journal of Cancer*, vol. 74, no. 8, pp. 1206–15, 1996.

[239] B. Irving, A. Cifor, B. W. Papież, J. Franklin, E. M. Anderson, S. M. Brady and J. A. Schnabel, "Automated Colorectal Tumour Segmentation in DCE-MRI Using Supervoxel Neighbourhood Contrast Characteristics", in *International Conference on Medical Image Computing and Computer-Assisted Intervention (MICCAI)*, Springer, Cham, 2014, pp. 609–616.

[240] J. R. Larkin, M. A. Simard, A. A. Khrapitchev, J. A. Meakin, T. W. Okell, M. Craig, K. J. Ray, P. Jezzard, M. A. Chappell and N. R. Sibson, "Quantitative blood flow measurement in rat brain with multiphase arterial spin labelling magnetic resonance imaging", *Journal of Cerebral Blood Flow & Metabolism*, vol. In Review, 2017.

[241] Y. Li, K. W. Y. Chan, P. C. M. van Zijl, B. Vogelstein, M. T. McMahon, S. Zhou and G. Liu, "Exploring the inherent CEST MRI signal of anticancer drug gemcitabine", in *Proceedings of the International Society for Magnetic Resonance in Medicine (ISMRM)*, 2014, p. 0472.

[242] Y. Li, H. Chen, J. Xu, N. N. Yadav, K. W. Y. Chan, L. Luo, M. T. McMahon, B. Vogelstein, P. C. van Zijl, S. Zhou and G. Liu, "CEST theranostics: label-free MR imaging of anticancer drugs", *Oncotarget*, vol. 7, no. 6, pp. 6369–6378, 2016.

Detection of doxorubicin using CEST MRI

Contents

A.1 Introduction 189
A.2 Methods 190
A.3 Results 191
A.4 Discussion 193

The following appendix describes a side project completed contemporaneously with the work described in Chapter 3 — Chapter 6, but that does not form part of the main thesis itself.

A.1 Introduction

Doxorubicin is a chemotherapeutic agent, commonly used in cancer treatments. The chemical structure of doxorubicin is shown in Fig. A.1, with the labile protons highlighted. These labile protons generate a CEST effect, which may be measurable *in vivo*. Similar studies using gemcitabine, another common chemotherapeutic agent, have characterized the labile proton pool properties and detected gemcitabine *in vivo* in animal models [241, 242].

Doxorubicin has also been encapsulated within a thermally sensitive liposome, commonly known as ThermoDox® (Celsion Corporation, NJ, USA). Systemic delivery of ThermoDox® enables targeted delivery of doxorubicin by localized heating of tumour tissue using high intensity focused ultrasound (HIFU) to 42 °C. This temperature is sufficient to release the doxorubicin from the thermally sensitive liposome, but insufficient to cause ablation of tissue. This is the general premise of the Targeted Delivery of Doxorubicin (TARDOX) trial currently running within the Institute of Biomedical Engineering (IBME), University of Oxford. Fluorescence microscopy of biopsy samples is currently used to confirm delivery of doxorubicin to tumour tissue. This procedure is invasive, time-consuming, and hard to reproduce between patients.

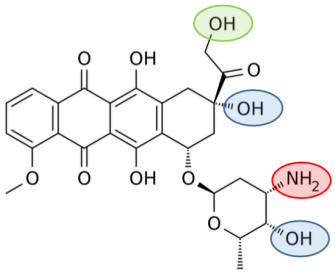

Figure A.1: Chemical structure of doxorubicin, with labile hydroxyl and amine protons highlighted.

The aims of this project, in collaboration with IBME, are to (i) investigate the CEST properties of doxorubicin and ThermoDox® *in vitro*, (ii) determine the feasibility of measuring doxorubicin concentration using CEST MRI *in vivo*, and (iii) further develop CEST MRI methods as necessary. To achieve these goals, CEST MRI studies of doxorubicin have been performed *in vitro* and optimal CEST MRI experimental parameters determined. In addition, serial dilutions of doxorubicin have been used to determine the concentration dependence of the CEST MRI signal. CEST MRI methods have been developed for the *in vivo* imaging, and initial investigations using intratumoral injection of doxorubicin into a subcutaneous tumour in post-mortem mouse have been performed.

A.2 Methods

A sample of 34 mM Doxorubicin in PBS was used for initial measurements of the CEST spectrum, determining the optimal saturation parameters, and exchange rate measurement. All MRI was performed using a horizontal bore 9.4T spectrometer (Agilent Technologies, Santa Clara, CA, USA). The exchange rate of the protons associated with the CEST effect at 3 ppm in the Doxorubicin CEST spectrum was estimated by the Omega Plot method, as described previously [180].

Briefly, this consists of plotting $\frac{M_Z}{M_0 - M_Z}$, where M_Z is the magnetization following saturation and M_0 is the unsaturated magnetization, against $1/\omega_1^2$, where $\omega_1 = \gamma B_1$ in units of rad s^{-1}. The resulting linear relationship has an x-intercept of $-1/k_{ba}^2$, where k_{ba} is the exchange rate of the labile protons.

Diluted samples of Doxorubicin at concentrations of 17 mM, 8.5 mM, 4.25 mM, 2.125 mM, 1.06 mM, 106 µM, 10.6 µM were produced to establish the concentration dependence of the CEST effect measured. The MTR_{asym} method of quantifying CEST effect was used throughout. A further sample of 3.74 mM Doxorubicin was used to generate physiological phantoms, comprising 8 % *w/v* BSA and varying concentration of Doxorubicin. The stock 3.74 mM Doxorubicin was titrated to pH ~7 before adding to the BSA solution to prevent protein precipitation. The pH of the BSA + Doxorubicin phantoms was confirmed as 7.4 immediately prior to imaging.

A postmortem BALB/c mouse with subcutaneous CT26 (mouse colorectal carcinoma) tumour was imaged using a 9.4 T horizontal bore spectrometer (Agilent). CEST MRI was performed using a 2D gradient echo multi slice pulse sequence to ensure full tumour coverage. The CEST saturation comprised a single 50 ms Gaussian pulse (flip angle 540°) followed by a single line of k-space, similar to other CEST MRI studies of subcutaneous mouse tumours. CEST MRI was performed pre- and post-intratumoral injection of 1.8 mM Doxorubicin (3×50 µl). Tumour regions of interest were segmented and the whole tumour average Z-spectrum compared to

establish the presence of Doxorubicin. The difference in $MTR_{asym}(3.5\,ppm)$ was measured, and the concentration of Doxorubicin inferred, from the calibration curve determined with Doxorubicin and BSA phantoms.

A.3 Results

CEST effects were apparent in the spectra from doxorubicin at 3 ppm, 1.2 ppm, and 0.8 ppm (Fig. A.2). The characterization of the CEST properties of doxorubicin revealed optimal CEST saturation parameters of 9.5 µT for 7.5 s (Fig. A.3), and an exchange rate for the protons associated with the CEST pool at 3 ppm of 389 Hz (Fig. A.4).

The concentration dependence of the CEST effect at 3 ppm in doxorubicin shows that, at physiologically expected concentrations of doxorubicin (10 µg ml^{-1}, 18.4 µM), the CEST effect would be undetectable above the noise level (Fig. A.5 left, linear regression slope 0.3 % M_0 mM^{-1} doxorubicin). However, measurement of the CEST MRI signal in more physiological phantoms (including BSA) with varying concentration of doxorubicin, results in an 8-fold increase in sensitivity compared to the phantoms without BSA (Fig. A.5 right, linear regression slope –2.4 % M_0 mM^{-1} doxorubicin). Interestingly, the dependence is negative (i.e. decreasing CEST MRI signal for increasing doxorubicin concentration), which suggests an indirect mechanism by which doxorubicin could be detected *in vivo*.

To determine the feasibility of detecting doxorubicin *in vivo*, a post-mortem BALB/c mouse with a CT26 (mouse colorectal carcinoma) subcutaneous tumour was imaged pre- and post-intratumoral injection of 1.9 mM doxorubicin (3×50 µl bolus). The tumour was imaged using a 2D gradient echo multi-slice CEST sequence to ensure full tumour coverage. From averaging the Z-spectra from tumour regions of interest in each slice, pre- and post-injection, and performing

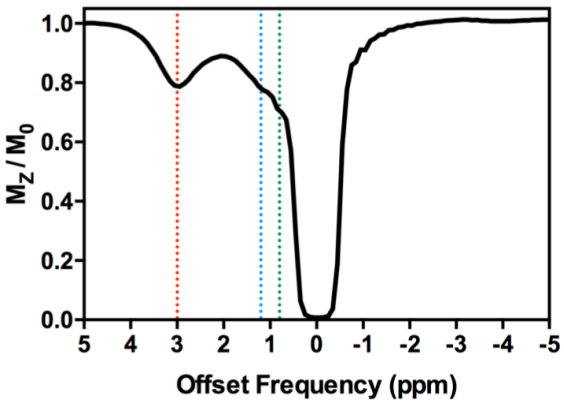

Figure A.2: Z-spectrum from a sample of 34 mM doxorubicin, showing effects at 3 ppm, 1.2 ppm, and 0.8 ppm associated with labile hydroxyl and amine groups (see Fig. A.1).

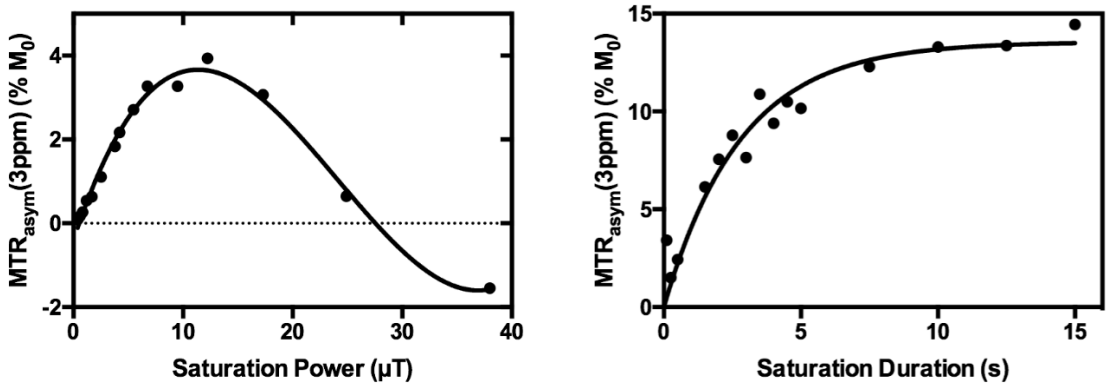

Figure A.3: Variation of CEST effect as saturation power (left) and duration (right) are varied. The optimal saturation parameters for Doxorubicin were determined as 9.5 μT for 7.5 s.

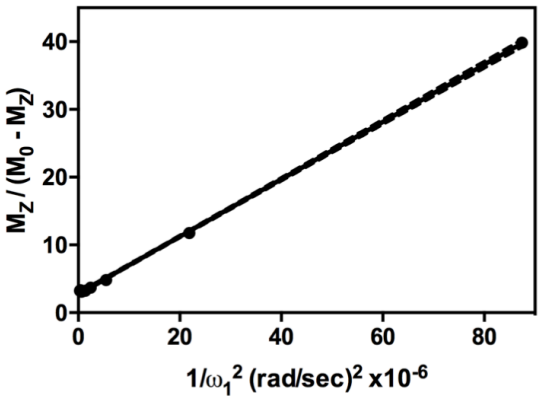

Figure A.4: Omega Plot for a sample of 34 mM doxorubicin estimates the exchange rate for the protons associated with the CEST effect at 3 ppm as 389 Hz.

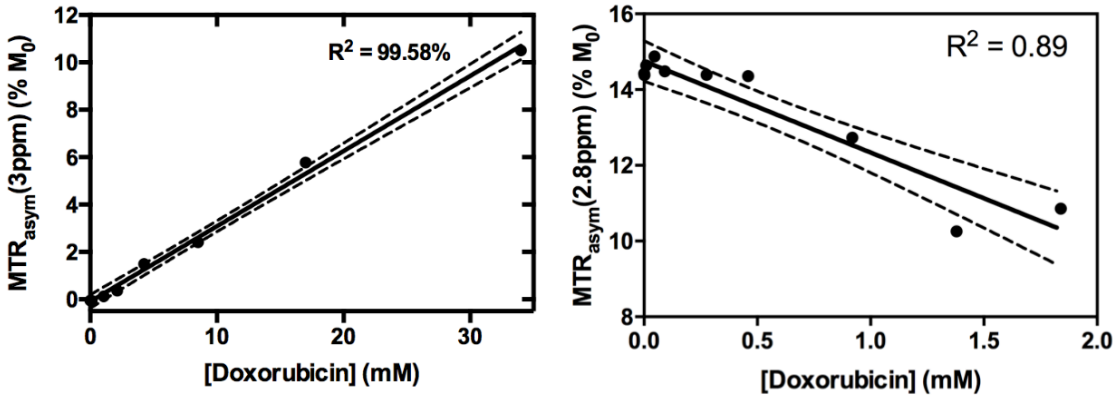

Figure A.5: Concentration dependence of CEST effect measured from samples of doxorubicin alone (left) and doxorubicin in a physiological phantom (right).

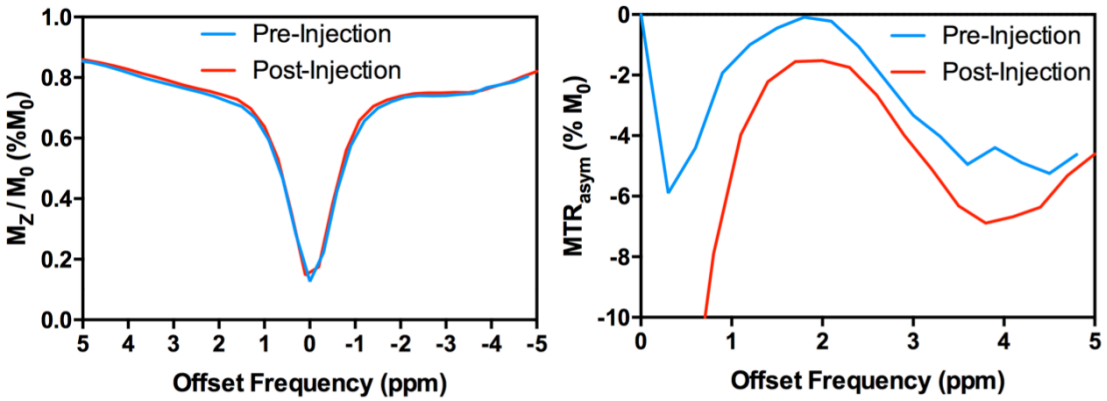

Figure A.6: Z-spectra (left) and MTR_{asym} (right) curves from subcutaneous tumour pre- and post-injection of doxorubicin ($3 \times 50\,\mu l$ bolus intratumoral). There is a small difference in signal between 2 – 4 ppm, which is more clearly shown in the MTR_{asym} spectra (right).

a conventional asymmetry analysis on these Z-spectra, a difference in signal between 2 – 4 ppm was observed, corresponding to the presence of doxorubicin (Fig. A.6). The size of the signal change at 3.5 ppm was 1.4 % M_0, which corresponded to a doxorubicin concentration of 570 µM using the *in vitro* measured calibration (Fig. A.5 right).

A.4 Discussion

This proof-of-principle study demonstrated that doxorubicin may be detected *in vivo* by virtue of its labile protons generating a CEST effect. This may be particularly useful since doxorubicin is used as a common chemotherapeutic agent already, but non-invasive measurement of delivery to tumour tissue has not previously been possible.

From the *in vitro* CEST MRI results of samples of doxorubicin, it was expected that the physiological concentration of doxorubicin would be too low to generate a substantial CEST MRI signal for its direct detection. However, CEST MRI signals detected in a physiological phantom with varying concentration of doxorubicin suggested that this may not be the case. The hypothesised mechanism by which the doxorubicin generates the change in CEST MRI signal is by virtue of its binding to intracellular protein, which decreases the availability of labile protons on the protein to chemically exchange. Initial studies in post-mortem mouse agree with this hypothesised mechanism for a change in measured CEST effect.

Treatment of Breast and Prostate Cancer by Hypofractionated Radiotherapy: Potential Risks and Benefits

Contents

B.1 Abstract . . . 196
B.2 Introduction . . . 196
B.3 Radiotherapy Treatment, Normal Tissue Effects and the Linear Quadratic Model . 196
B.4 Hypofractionated Radiotherapy . . . 198
B.5 Hypofractionated Radiotherapy in Breast and Prostate Cancer . . . 198
B.6 Benefits of Hypofractionation in Prostate and Breast Cancer . . . 199
B.7 Risks Associated with Hypofractionation in Breast and Prostate Cancer . . . 202
B.8 Discussion . . . 204
B.9 Future Directions . . . 205
B.10 Acknowledgements . . . 205
B.11 Statement of Search Strategies Used and Sources of Information . . . 205
B.12 References . . . 205

This appendix was originally published as Ray, K.J. Sibson, N.R. Kiltie, A.E. *Clinical Oncology* **27**(7) 420–6 (2015) and is reproduced here under the terms of the Creative Commons Attribution License (CC-BY).

B.1 Abstract

Breast cancer and prostate cancer are the most common cancers diagnosed in women and men, respectively, in the UK, and radiotherapy is used extensively in the treatment of both. In vitro data suggest that tumours in the breast and prostate have unique properties that make a hypofractionated radiotherapy treatment schedule advantageous in terms of therapeutic index. Many clinical trials of hypofractionated radiotherapy treatment schedules have been completed to establish the extent to which hypofractionation can improve patient outcome. Here we present a concise description of hypofractionation, the mathematical description of converting between conventional and hypofractionated schedules, and the motivation for using hypofractionation in the treatment of breast and prostate cancer. Furthermore, we summarise the results of important recent hypofractionation trials and highlight the limitations of a hypofractionated treatment regimen.

Keywords: α/β ratio, breast cancer, clinical trials, hypofractionation, prostate cancer, radiotherapy

B.2 Introduction

Breast and prostate cancer are the most common cancers, accounting for 30 and 25% of cancer diagnoses in women and men, respectively, in the UK. Efforts to improve survival in these two cancers have been highly successful; breast cancer 5 year survival in England has improved from 52% in 1971 – 1975 to 85% in 2005 – 2009, whereas the 5 year survival in prostate cancer has improved from 31 to 81.4% over the same time periods. This improved outcome is largely due to increasing awareness of these diseases, the National Health Service Breast Cancer Screening Programme and stage migration in the diagnosis of prostate cancers [1]. At the same time, radiotherapy has emerged as an important treatment modality for both breast and prostate cancer. This review discusses the risks and potential benefits of using hypofractionated radiotherapy schedules, which have been hypothesised to improve treatment outcome owing to the specific properties of each of these two cancers.

B.3 Radiotherapy Treatment, Normal Tissue Effects and the Linear Quadratic Model

Radical radiotherapy treatment regimens involve dividing the overall radiation dose into a number of fractions, as this takes advantage of the five Rs of radiotherapy: reoxygenation of hypoxic cells, repopulation of cells, repair of normal tissues, redistribution of cells through the cell cycle and differences in the intrinsic radiosensitivity of tumour cells compared with normal tissue cells

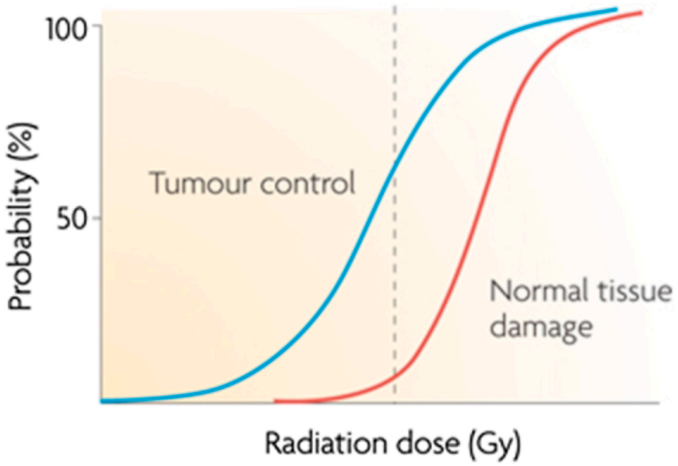

Figure B.1: Sigmoid-shaped curves for tumour control (TCP, left) and normal tissue complication/damage (NTCP, right) probability. The dashed lines indicate a 60% TCP and a 5% NTCP for a given dose. Reprinted from [4] with permission from Macmillan Publishers Ltd.

[2]. A typical conventional fractionation regimen uses 2 Gy fractions delivered daily five times a week, up to a total of 60 – 80 Gy, although this varies across treatment centres, tumour types and patients [3].

A good therapeutic outcome in radiotherapy comprises both local control of the tumour and minimal late normal tissue complications. These can be quantified using the tumour control probability (TCP) and normal tissue complication probability (NTCP) curves [4] (Figure 1). The separation between the curves gives the size of the therapeutic index, which can be altered by shifting either the TCP or the NTCP curve. As the dose per fraction increases, the probability of toxic effects in late-responding normal tissues increases disproportionately compared with early responding normal tissues, which are typically less sensitive to fractionation [4]. The cause of the rise in late-responding normal tissue toxicity is not yet well understood, but may be due to a number of factors, including cell death and the production of cytokines [5]. Late-responding normal tissue toxicity can be further subcategorised into primary effects due to apoptosis of slowly proliferating cells and consequential effects due to initially acute damage of early responding normal tissue. It is primary late-responding normal tissue toxicity that typically limits radiotherapy treatment regimens [4].

Fractionation sensitivity can be quantified using a parameter known as the α/β ratio from the linear quadratic model, which is formally defined as the dose at which the proportion of cell killing due to lethal single-hit injuries (αD) and the accumulation of sublethal injuries (βD^2) are equal. A small α/β ratio indicates tissue with a large sensitivity to changes in dose per fraction. This low α/β ratio can result from a number of intrinsic properties of the tissue, such as a greater capacity to repair DNA damage induced by radiation and a slow proliferation rate

[6]. Hence, typically, late-responding normal tissues have a smaller α/β ratio (about 2 Gy) than either tumour tissue or early responding normal tissues (about 10 Gy) [7].

B.4 Hypofractionated Radiotherapy

A hypofractionated schedule is one that delivers a dose larger than 2 Gy per fraction (with a lower overall dose). To convert between conventional and hypofractionated schedules, the biologically effective dose (BED) calculation, defined in Eq. B.1 [8], is used. In this equation, D is the total dose prescribed and d is the dose per fraction. This allows clinicians to determine a dose equivalent to the standard prescribed dose for a new schedule, resulting in the same biological effect either on the tumour or the dose-limiting normal tissues.

$$\text{BED} = \text{D}\left[1 + \frac{d}{\alpha/\beta}\right] \tag{B.1}$$

For example, if a clinician prescribes a total of 60 Gy to be delivered to a tumour with an α/β ratio of 4 Gy (typical for breast tumour) in conventional 2 Gy fractions, the BED for this regimen is 60(1 + 2/4) = 90 Gy. To deliver the same BED of 90 Gy in 3 Gy fractions, however, we need only deliver fractions up to a total dose of 90/(1 + 3/4) = 51 Gy, which in 3 Gy fractions is only 17 fractions.

An extension to the BED is the equivalent dose in 2 Gy fractions, $\text{EQD}_{2\text{Gy}}$, which is defined by Eq. B.2 [9]. The $\text{EQD}_{2\text{Gy}}$ of a 51 Gy in 3 Gy fractions hypofractionated regimen is 51(3 + 4)/(2 + 4) = 59.5Gy 60 Gy, as expected from the BED example above.

$$\text{EQD}_{2\text{Gy}} = \frac{\text{D}\,[d + \alpha/\beta]}{[2 + \alpha/\beta]} \tag{B.2}$$

B.5 Hypofractionated Radiotherapy in Breast and Prostate Cancer

Although hyperfractionation, the delivery of multiple doses smaller than 2 Gy to further spare late normal tissue effects, is of proven effectiveness in oropharyngeal cancers [10], hypofractionated schedules are potentially attractive in the treatment of breast and prostate cancer. The α/β ratios of these tumours are thought to be the same or less than the surrounding late-reacting normal tissues. Prostate tumours are estimated to have an α/β ratio of about 1 – 3 Gy [11] and breast tumours an α/β ratio of about 4 Gy [12]; this compares with oropharyngeal cancers and other head and neck squamous cell carcinomas, with α/β ratios of over 8 Gy [11]. These low α/β ratios are thought to reflect the characteristically slower proliferation rates of breast and prostate tumours compared with other tumour types. As a consequence of this slower proliferation,

these tumours respond in a similar manner to late-responding normal tissue rather than early responding normal tissue [13 – 15], thereby removing the rationale for hyperfractionated schedules. Radiotherapy is usually used in breast cancer in the adjuvant setting, delivering whole breast irradiation by external beam radiotherapy after breast-conserving surgery to a lower dose than radical doses given at other tumour sites. The purpose of treatment is to eliminate any cancer cells not removed during surgery. In contrast, irradiation of the prostate is given to a higher radical dose either by external beam radiotherapy or brachytherapy [6,12].

B.6 Benefits of Hypofractionation in Prostate and Breast Cancer

The primary benefit of treating breast and prostate cancer with a hypofractionated regimen is the improved therapeutic index that can be obtained. Hypofractionation can achieve this in one of two ways when compared with the conventional fractionated scheme [6]: (i) dose escalation to increase tumour control while maintaining the same normal tissue complication probability (i.e. shift the TCP curve to the left in Figure 1) or (ii) maintaining dose equivalence in terms of tumour cure probability while decreasing the normal tissue dose (i.e. shifting the NTCP curve to the right in Figure 1). Physical methods, such as intensity-modulated radiotherapy, three-dimensional conformal radiotherapy and charged particle therapy, have been used in conventionally fractionated radiotherapy to decrease the normal tissue dose [6] and their use minimises the toxicity of hypofractionated radiotherapy.

As well as the therapeutic gain of hypofractionation, a number of other advantages are conferred in terms of logistical, patient convenience and resource allocation considerations [16]. Reduced numbers of fractions will reduce radiotherapy costs in terms of work-hours and fewer fractions also results in fewer visits for a patient to the radiotherapy clinic, which is more convenient and less costly [17]. However, these advantages should be considered as 'added bonuses' to a hypofractionated schedule: its primary purpose should be for therapeutic gain. To this end, numerous clinical trials in breast and prostate cancer have been conducted. Although the aim of many of these trials was to show a therapeutic gain from using a hypofractionated schedule, others sought only to show that normal tissue toxicity is comparable for the conventional and hypofractionated treatment regimens. Therefore, as long as a hypofractionated schedule is no more toxic than the conventional schedule, it can be argued that the logistical advantages are sufficient to warrant clinical implementation.

Hypofractionation in breast cancer radiotherapy entered clinical trials in the UK in 1986 with the Standardisation of Breast Radiotherapy pilot trial (START-pilot; n = 1410) and in Canada in 1993 with the Ontario trial (n = 1234) [18]. These were followed in 1999 with the START-A and START-B trials [19]. These trials challenged conventional wisdom, which justified the rationale

End Point	α/β ratio (Gy)	95% confidence interval
Locoregional relapse *	4.0	0.0 — 8.9
Locoregional relapse †	3.5	1.2 — 5.7
Breast shrinkage	3.5	0.7 — 6.4
Breast induration	4.0	2.3 — 5.6
Telangiectasia	3.8	1.8 — 5.7
Breast oedema	4.7	2.4 — 7.0

Table B.1: α/β ratios estimated from START-A trial [19]. * Locoregional relapse α/β START-A results. † Locoregional relapse α/β from START-A combined with START-pilot results.

for 50 Gy in 25 fractions, namely that cancers in the breast are less sensitive to changes in dose per fraction than the dose-limiting surrounding normal tissues. They then tested the hypothesis that breast tumour tissue and surrounding late-reacting normal tissue are similarly sensitive to fraction size. The then-conventional 50 Gy in 25 fractions over 5 weeks was compared with 41.6 Gy or 39 Gy in 13 fractions over 5 weeks in START-A (n = 2236) and with 40 Gy in 15 fractions over 3 weeks in START-B (n = 2215), the latter being a dose-fractionation already commonly used in the UK. Primary end points were locoregional relapse and late normal tissue effects. The START-pilot and START-A trial were designed to allow estimation of the α/β ratios of breast tumour and late-responding normal tissue, and similar α/β ratios were found for breast tumour using locoregional relapse as the end point and surrounding normal tissue in the range 3.5 – 4.7 Gy [19] (Table B.1). Ten year follow-up data are now available [19] and these found that breast shrinkage, telangiectasia and breast oedema were significantly less frequent with 40 Gy than 50 Gy in START-B, with no evidence that 40 Gy in 15 fractions was less efficient in achieving locoregional control. These trials resulted in the standard breast cancer radiotherapy treatment protocol in the UK changing to 40 Gy in 15 fractions [19].

The randomised UK FAST trial (2004 – 2007, n = 915) went further with its hypofractionation regimen, testing 50 Gy in 25 fractions over 5 weeks against either 30 or 28.5 Gy in five fractions over 5 weeks [20]. Acute tissue toxicity effects as well as late tissue effects were measured, with the primary end point being adverse effects in the breast. Where the START trials showed that the principle of hypofractionation in breast cancer treatment was effective, the FAST trial investigated how much the dose per fraction could be increased before adverse acute normal tissue reactions became intolerably high. After a 3 year median follow-up, the 28.5 Gy fractionation scheme was comparable with the 50 Gy scheme in terms of adverse reactions, and lower than the 30 Gy scheme because the total dose to the tissue was lower [20]. This trial has

Trial name	Dates	No. patients	Trial arm	Control arm	α/β estimate
START pilot	1986 – 1998	1410	39 Gy or 42.9 Gy, 13 fractions, 5 weeks	50 Gy, 25 fractions, 5 weeks	3.5 – 4.7 Gy *
Ontario	1993 – 1996	1234	42.5 Gy, 16 fractions, 3 weeks	50 Gy, 25 fractions, 5 weeks	N/A
START-A	1999 – 2002	2236	39 Gy or 41.6 Gy, 13 fractions, 5 weeks	50 Gy, 25 fractions, 5 weeks	3.5 – 4.7 Gy *
START-B	1999 – 2002	2215	40 Gy, 15 fractions, 3 weeks	50 Gy, 25 fractions, 5 weeks	N/A
FAST	2004 – 2007	915	28.5 Gy or 30 Gy, 5 fractions, 5 weeks	50 Gy, 25 fractions, 5 weeks	2.3 – 2.6 Gy *
RAPID	2006 – 2011	2135	38.5 Gy, 10 fractions, 5 days (partial breast)	42.5 Gy, 16 fractions or 50 Gy, 25 fractions daily (whole breast)	N/A
FAST Forward	2011 – present	4000	26 Gy or 27 Gy, 5 fractions, 5 days	40 Gy, 15 fractions, 3 weeks	Follow-up

Table B.2: Summary of the breast cancer hypofractionation trials mentioned in this review. * Range of α/β values calculated depending on end point used, see Table B.1.

been followed by the FAST Forward trial, which closed 2 years earlier than expected after very rapidly recruiting 4000 patients. FAST Forward is testing 40 Gy in 15 fractions over 3 weeks against two accelerated hypofractionation schemes of 26 or 27 Gy in five fractions over 5 days. The decreased overall treatment time may improve tumour cure probability by decreasing the effect of tumour repopulation over the treatment time, but may also increase early responding normal tissue complications, although this could be mitigated by the decreased overall dose. The five-fractions-in-5-days schedule is hugely convenient to patients, and frees up large amounts of machine capacity in an era where, with increasing patient numbers, this is at a premium. Further hypofractionation may be possible, where a single fraction delivered to part of the breast is sufficient for tumour control [21]. The clinical trials referred to in this review are summarised in Table 2.

The breadth and success of clinical trials of hypofractionation in breast cancer is encouraging; for prostate cancer the situation is less clear-cut. A recent review of 16 prospective randomised clinical trials comprising a total of 1828 patients concluded that hypofractionation for prostate cancer should still only be used in a clinical trial setting, owing to the uncertainties associated with the measurement of the α/β ratio for prostate tumour tissue [3]. Nevertheless, studies have continued, with one phase III randomised trial in Australia (n = 217) reporting a long-term therapeutic advantage in terms of biochemical relapse-free survival and also genitourinary side-effects at 4 years. Here the authors compared hypofractionated radiotherapy, using 55 Gy in 20 fractions over 4 weeks, to conventional radiotherapy, comprising 64 Gy in 32 fractions over 6.5 weeks, at a median follow-up of 7.5 years [22]. A recent meta-analysis of seven trials of 5969 patients, from a radiobiological perspective, gave an estimate of the α/β ratio for biochemical relapse-free survival of 1.4 (95% confidence interval 0.9 – 2.2) Gy [23], supporting the strategy of hypofractionation in prostate cancer.

The Conventional versus Hypofractionated High-dose intensity-modulated radiotherapy for Prostate cancer (CHHiP) study (n = 3216) between 2002 and 2006 in the UK compared the standard 74 Gy in 37 fractions over 7.5 weeks against two hypofractionated schedules: 60 or 57 Gy in 20 or 19 fractions, respectively [24]. Although still in active follow-up, preliminary analysis of 457 patients

Trial name	Dates	No. patients	Trial arm	Control arm	α/β estimate
"Australian trial"	1996 – 2003	217	55 Gy, 20 fractions, 4 weeks	64 Gy, 32 fractions, 6.5 weeks	N/A
CHHiP	2002 – 2006	3216	60 Gy, 20 fractions or 57 Gy, 19 fractions	74 Gy, 37 fractions, 7.5 weeks	Follow-up
PROFIT	2005 – 2012	1204	60 Gy, 20 fractions, 4 weeks	78 Gy, 39 fractions, 8 weeks	N/A
HYPRO	2006 – 2011	800	64.6 Gy, 19 fractions, 7 weeks	78 Gy, 39 fractions, 8 weeks	N/A
HYPO-RT-PC	2005 – present	592	42.7 Gy, 7 fractions, 3 weeks	78 Gy, 39 fractions, 8 weeks	N/A
PACE	2012 – present	1700	36.25 Gy, 5 fractions or 38 Gy, 4 fractions with CyberKnife	78 Gy, 39 fractions, 8 weeks	Recruitment

Table B.3: Summary of the prostate cancer hypofractionation trials mentioned in this review

using grade 2 toxicity in the bowel or bladder on the Radiation Therapy Oncology Group (RTOG) scale as an end point seems to suggest that the hypofractionated schedules are safe and cause no more early/late normal tissue complications than the conventional regime 2 years after treatment [24]. The study design is also such that an estimate of the α/β ratio should be possible, and with 3216 patients in the trial it is thought the result will have a narrower 95% confidence interval than previous estimates. Further clinical trials either ongoing or in follow-up in Canada ('PROFIT', ISRCTN 43853433), the Netherlands ('HYPRO', ISRCTN 85138529), Scandinavia ('HYPO-RT-PC', ISRCTN 45905321) and the UK ('PACE', NCT01584258) will also contribute to a further enhancement in the precision of α/β estimates. These trials are summarised in Table B.3.

B.7 Risks Associated with Hypofractionation in Breast and Prostate Cancer

To some extent the hypofractionation approach is less toxic to normal tissue in breast cancer than in prostate cancer, as for the former lower relative doses are used in the adjuvant rather than radical setting. The improved therapeutic ratio when using a hypofractionated schedule is based on the assumption that the α/β ratio in breast and prostate cancer is lower than that of the surrounding normal tissue. Although measurements of α/β have been carried out using clinical data, these represent population averages and suffer from very large 95% confidence intervals reflecting large inter-patient variability [11,19]. The START-A breast cancer hypofractionation trial recruited 2236 women, but still yielded notably large 95% confidence intervals (Table 1) [19]. One prostate hypofractionation trial [11], which used a combination of external beam radiotherapy with high dose rate brachytherapy delivered in two or three implants, measured an estimated α/β of 1.2. However, because only 192 patients were recruited to their trial, the 95% confidence interval on this value was 0.03 – 4.1 Gy. The inter-patient variability of α/β values suggests that not all patients will benefit from the same hypofractionated schedule.

Assuming that breast tumour α/β ratio estimates are correct, there may be a limit to the extent of hypofractionation that can be used safely. For example, patients in the RAPID trial that underwent hypofractionated treatment with multiple fractions per day (38.5 Gy in 10 fractions over a week) suffered from greater normal tissue toxicity than those in the control arm (42.5 Gy in 16 fractions) [25]. The increased toxicity could be a result of many factors, including

insufficient time for normal tissue to repair between fractions and the prescribed dose being delivered to too large a volume [25]. The FAST Forward trial may help to elucidate the lower limit of hypofractionation for breast cancer treatments.

Early prostate hypofractionation trials yielded low α/β ratios on comparing tumour control rates obtained with external beam radiotherapy and low dose rate brachytherapy [26,27]. However, these trials are limited in their power by the fact that they compare two therapy modalities as opposed to two different schedules of the same therapy modality, as well as the poorer dose conformity available at the time [6,27]. In fact, the findings of some recent trials using modern radiotherapy techniques are actually rejecting the hypothesis that hypofractionation is beneficial [3]. The lack of sufficient follow-up time has hindered many modern prostate cancer hypofractionation trials as they cannot adequately report on late-responding normal tissue complications, freedom from biochemical failure or morbidity. One multicentre international study, in 2003 – 2007, reported equivalent late toxicity effects between the hypofractionated and conventional treatment arms and significantly higher freedom from biochemical failure for the hypofractionated arm (88% versus 76%, P = 0.014), but only after a 3 year follow-up [28]. Such equivalence also limits the precision of any estimations of the α/β ratio, which in turn may also be dependent on the stage of the prostate tumour [6].

If the α/β ratios are not accurately estimated and doses selected appropriately, a hypofractionated schedule, as with all radiotherapy treatments, may increase normal tissue complications unnecessarily and potentially induce secondary cancers. One study comparing the late-responding normal tissue complications in prostate cancer radiotherapy found that, for patients with initial urinary problems, there was an increased frequency of complications following a hypofractionated radiotherapy schedule when compared with a conventional schedule [29]. An assumption is also being made that the linear quadratic model is valid at the sizes of dose per fraction used in clinical hypofractionated treatments. Although not a major issue in trials involving doses per fraction up to 3 Gy, the FAST Forward trial for breast cancer hypofractionation used a dose per fraction of over 5 Gy. The validity of the linear quadratic model at a high dose per fraction is yet to be confirmed [6,30 – 32].

Another factor that has not been considered in many clinical studies is the heterogeneous nature of tumour tissue [33]. Most tumours have both poorly and well-differentiated cells [34]; this heterogeneity leads to a heterogeneous α/β ratio across the tumour site (poorly differentiated cells have a higher α/β than well-differentiated cells). Consequently, a hypofractionated treatment could be sparing poorly differentiated sections of the tumour relative to the nearby organs at risk. Simulation of this effect showed that treatment efficacy decreases for a hypofractionated schedule even if 5 – 10% of the cells in the tumour are poorly differentiated [33]. The

variation in genetic mutations across the tumour volume also contributes to its heterogeneity; it has previously been shown that there is as much inter-patient variability as there is intra-patient variability when considering the genetic mutations in biopsies of many tumour types [35]. These genetic mutations affect the ability of DNA repair pathways to function after radiation damage, hence affecting the α/β ratio.

Tumour heterogeneity also has implications on the use of biochemical relapse-free rate as an end point for measuring successful treatment of prostate cancer, as poorly differentiated cells produce less prostate-specific antigen than well-differentiated tumour cells [36]. Prostate cancer-specific survival or local tumour control and a long follow-up time period (10 – 20 years) are more robust end points. Heterogeneity of cell oxygenation within a tumour is also an issue; hypofractionation can result in reduced cell killing in hypoxic regions of tumour tissue [37]. Arguably, the importance of heterogeneity of the α/β ratio in tumour tissue is a factor that has been underestimated when determining the efficacy of hypofractionation treatment schedules.

B.8 Discussion

Hypofractionated therapy schemes have obvious logistical and patient convenience advantages for individuals with breast or prostate cancer. However, although the breast cancer trial results are encouraging, the therapeutic gain in prostate cancer is less clear. This difference is mainly due to the measurement uncertainty of the α/β ratio for prostate tumour tissue. Although in vitro work with cell lines has supported a lower tumour α/β than the surrounding normal tissue for both cases [38,39], these results have not been conclusively replicated in human studies of prostate cancer. This variability may reflect insufficient follow-up time or patient numbers to report a precise result, suboptimal choice of end points or the radiotherapy modality used.

Hypofractionation in breast cancer treatment is now the standard protocol in the UK. The results of further trials investigating the limits of hypofractionation, such as the five-fractions-over-5-days regimen of the FAST Forward study, are eagerly awaited. Judging by the success of breast cancer hypofractionation, if we could get to a point where the α/β ratio for prostate cancer can be measured in vivo in a reliable manner and shown to be lower than surrounding organs at risk, hypofractionated therapy will probably have a beneficial impact for prostate cancer patients.

In order to address the issue of heterogeneity of tumour tissue, intensity-modulated radiotherapy could be used to increase the dose delivered to poorly differentiated areas of the tumour, but this would require in vivo imaging of cell differentiation. Adaptive radiotherapy, where the dose distribution is altered during the treatment schedule to account for changes in patient anatomy, tumour volume or areas of tumour that respond later in the course of treatment, may be used to provide more personalised and, ultimately, more efficacious treatment for each individual

patient [40]. Alternatively, novel agents might be developed to alter the protein expression of selected parts of the tumour, thereby rendering it homogeneous in terms of radiotherapy response. If areas of tumour with a high α/β could be targeted based on genetic mutations that impair DNA repair capability, and this capability manipulated to decrease the α/β ratio, the tumour may respond more effectively to hypofractionated schedules. Moreover, calculations of therapeutic gain when using a hypofractionated schedule should be carried out using a model that accounts for the presence of hypoxia in tumours so as not to overestimate the cell killing, as can occur when using the linear quadratic model.

B.9 Future Directions

Future steps in the clinical implementation of hypofractionated schedules will involve the development of biomarkers to measure individual α/β ratios for each patient and personalise treatment schedules to provide the optimum outcome. Estimates of α/β are currently based on population studies and variation between patients may have a significant effect on treatment efficacy for individuals. An ideal situation would be to measure the α/β ratio in each patient, while factoring in tumour heterogeneity, to enable prediction of the response to a particular treatment regimen, ultimately personalising the radiotherapy schedule to maximise the therapeutic index for each patient. This is a complex, and active, area of research.

B.10 Acknowledgements

KJR is funded by a Medical Research Council studentship; NRS and AEK are funded by Cancer Research UK Core Grant C5255/A15935. This is a modified version of Kevin Ray's Radiobiology MSc essay which was based on the topic of Dr. Navita Somaiah's lecture. The authors thank Dr. Somaiah for very helpful comments on the essay and discussion.

B.11 Statement of Search Strategies Used and Sources of Information

The review is based on a search of peer-reviewed publications found using Web of Science, PubMed and Google Scholar. The reference lists from some articles were also used to obtain other pertinent articles. Information on relevant clinical trials was obtained from the International Clinical Trials Registry Platform.

B.12 References

1. Noldus J, Graefen M, Haese A, Henke RP, Hammerer P, Huland H. Stage migration in clinically localized prostate cancer. European urology. 2000;38(1):74-8.
2. Withers HR. Biological basis of radiation therapy for cancer. Lancet. 1992;339(8786):156-9.

3. Zaorsky NG, Ohri N, Showalter TN, Dicker AP, Den RB. Systematic review of hypofractionated radiation therapy for prostate cancer. Cancer treatment reviews. 2013;39(7):728-36.

4. Barnett GC, West CM, Dunning AM, Elliott RM, Coles CE, Pharoah PD, et al. Normal tissue reactions to radiotherapy: towards tailoring treatment dose by genotype. Nature reviews Cancer. 2009;9(2):134-42.

5. Stone HB, Coleman CN, Anscher MS, McBride WH. Effects of radiation on normal tissue: consequences and mechanisms. The lancet oncology. 2003;4(9):529-36.

6. Ritter M. Rationale, conduct, and outcome using hypofractionated radiotherapy in prostate cancer. Seminars in radiation oncology. 2008;18(4):249-56.

7. Williams MV, Denekamp J, Fowler JF. A review of alpha/beta ratios for experimental tumors: implications for clinical studies of altered fractionation. International journal of radiation oncology, biology, physics. 1985;11(1):87-96.

8. Barendsen GW. Dose fractionation, dose rate and iso-effect relationships for normal tissue responses. International journal of radiation oncology, biology, physics. 1982;8(11):1981-97.

9. Barton M. Tables of equivalent dose in 2 Gy fractions: a simple application of the linear quadratic formula. International journal of radiation oncology, biology, physics. 1995;31(2):371-8.

10. Horiot JC, Le Fur R, N'Guyen T, Chenal C, Schraub S, Alfonsi S, et al. Hyperfractionation versus conventional fractionation in oropharyngeal carcinoma: final analysis of a randomized trial of the EORTC cooperative group of radiotherapy. Radiotherapy and oncology : journal of the European Society for Therapeutic Radiology and Oncology. 1992;25(4):231-41.

11. Brenner DJ, Martinez AA, Edmundson GK, Mitchell C, Thames HD, Armour EP. Direct evidence that prostate tumors show high sensitivity to fractionation (low alpha/beta ratio), similar to late-responding normal tissue. International journal of radiation oncology, biology, physics. 2002;52(1):6-13.

12. Whelan TJ, Kim DH, Sussman J. Clinical experience using hypofractionated radiation schedules in breast cancer. Seminars in radiation oncology. 2008;18(4):257-64.

13. Haustermans KM, Hofland I, Van Poppel H, Oyen R, Van de Voorde W, Begg AC, et al. Cell kinetic measurements in prostate cancer. International journal of radiation oncology, biology, physics. 1997;37(5):1067-70.

14. Pollack A, Zagars GK, Kavadi VS. Prostate specific antigen doubling time and disease relapse after radiotherapy for prostate cancer. Cancer. 1994;74(2):670-8.

15. Rew DA, Wilson GD. Cell production rates in human tissues and tumours and their significance. Part II: clinical data. European journal of surgical oncology : the journal of the European Society of Surgical Oncology and the British Association of Surgical Oncology. 2000;26(4):405-17.

16. Parthan A, Pruttivarasin N, Davies D, Taylor DC, Pawar V, Bijlani A, et al. Comparative cost-effectiveness of stereotactic body radiation therapy versus intensity-modulated and proton radiation therapy for localized prostate cancer. Frontiers in oncology. 2012;2:81.

17. Sethukavalan P, Cheung P, Tang CI, Quon H, Morton G, Nam R, et al. Patient costs associated with external beam radiotherapy treatment for localized prostate cancer: the benefits of hypofractionated over conventionally fractionated radiotherapy. The Canadian journal of urology. 2012;19(2):6165-9.

18. Whelan TJ, Pignol JP, Levine MN, Julian JA, MacKenzie R, Parpia S, et al. Long-term results of hypofractionated radiation therapy for breast cancer. The New England journal of medicine. 2010;362(6):513-20.

19. Haviland JS, Owen JR, Dewar JA, Agrawal RK, Barrett J, Barrett-Lee PJ, et al. The UK Standardisation of Breast Radiotherapy (START) trials of radiotherapy hypofractionation for treatment of early breast cancer: 10-year follow-up results of two randomised controlled trials. The lancet oncology. 2013;14(11):1086-94.

20. Agrawal RK, Alhasso A, Barrett-Lee PJ, Bliss JM, Bliss P, Bloomfield D, et al. First results of the randomised UK FAST Trial of radiotherapy hypofractionation for treatment of early breast cancer (CRUKE/04/015). Radiotherapy and oncology : journal of the European Society for Therapeutic Radiology and Oncology. 2011;100(1):93-100.

21. Coles CE, Brunt AM, Wheatley D, Mukesh MB, Yarnold JR. Breast radiotherapy: less is more? Clinical oncology. 2013;25(2):127-34.

22. Yeoh EE, Botten RJ, Butters J, Di Matteo AC, Holloway RH, Fowler J. Hypofractionated versus conventionally fractionated radiotherapy for prostate carcinoma: final results of phase III randomized trial. International journal of radiation oncology, biology, physics. 2011;81(5):1271-8.

23. Miralbell R, Roberts SA, Zubizarreta E, Hendry JH. Dose-fractionation sensitivity of prostate cancer deduced from radiotherapy outcomes of 5,969 patients in seven international institutional datasets: alpha/beta = 1.4 (0.9-2.2) Gy. International journal of radiation oncology, biology, physics. 2012;82(1):e17-24.

24. Dearnaley D, Syndikus I, Sumo G, Bidmead M, Bloomfield D, Clark C, et al. Conventional versus hypofractionated high-dose intensity-modulated radiotherapy for prostate cancer: preliminary safety results from the CHHiP randomised controlled trial. The lancet oncology. 2012;13(1):43-54.

25. Olivotto IA, Whelan TJ, Parpia S, Kim DH, Berrang T, Truong PT, et al. Interim cosmetic and toxicity results from RAPID: a randomized trial of accelerated partial breast irradiation using three-dimensional conformal external beam radiation therapy. Journal of clinical oncology : official journal of the American Society of Clinical Oncology. 2013;31(32):4038-45.

26. Fowler J, Chappell R, Ritter M. Is alpha/beta for prostate tumors really low? International journal of radiation oncology, biology, physics. 2001;50(4):1021-31.

27. Fowler JF, Nahum AE, Orton CG. Point/Counterpoint. The best radiotherapy for the treatment of prostate cancer involves hypofractionation. Medical physics. 2006;33(9):3081-4.

28. Arcangeli G, Saracino B, Gomellini S, Petrongari MG, Arcangeli S, Sentinelli S, et al. A prospective phase III randomized trial of hypofractionation versus conventional fractionation in patients with high-risk prostate cancer. International journal of radiation oncology, biology, physics. 2010;78(1):11-8.

29. Pollack A, Walker G, Horwitz EM, Price R, Feigenberg S, Konski AA, et al. Randomized trial of hypofractionated external-beam radiotherapy for prostate cancer. Journal of clinical oncology : official journal of the American Society of Clinical Oncology. 2013;31(31):3860-8.

30. Kirkpatrick JP, Meyer JJ, Marks LB. The linear-quadratic model is inappropriate to model high dose per fraction effects in radiosurgery. Seminars in radiation oncology. 2008;18(4):240-3.

31. Courdi A. High doses per fraction and the linear-quadratic model. Radiotherapy and oncology : journal of the European Society for Therapeutic Radiology and Oncology. 2010;94(1):121-2; author reply 2-3.

32. Otsuka S, Shibamoto Y, Iwata H, Murata R, Sugie C, Ito M, et al. Compatibility of the linear-quadratic formalism and biologically effective dose concept to high-dose-per-fraction irradiation in a murine tumor. International journal of radiation oncology, biology, physics. 2011;81(5):1538-43.

33. Lennernas B, Nilsson S, Levitt S. Hypofractionation for radiotherapy of prostate cancer using a low alfa/beta ratio–possible reasons for concerns? An example of five dimensional radiotherapy. Acta Oncol. 2011;50 Suppl 1:111-5.

34. Bloom HJ, Richardson WW. Histological grading and prognosis in breast cancer; a study of 1409 cases of which 359 have been followed for 15 years. British journal of cancer. 1957;11(3):359-77.

35. Burrell RA, McGranahan N, Bartek J, Swanton C. The causes and consequences of genetic heterogeneity in cancer evolution. Nature. 2013;501(7467):338-45.

36. Aihara M, Lebovitz RM, Wheeler TM, Kinner BM, Ohori M, Scardino PT. Prostate specific antigen and gleason grade: an immunohistochemical study of prostate cancer. The Journal of urology. 1994;151(6):1558-64.

37. Carlson DJ, Keall PJ, Loo BW, Jr., Chen ZJ, Brown JM. Hypofractionation results in reduced tumor cell kill compared to conventional fractionation for tumors with regions of hypoxia. International journal of radiation oncology, biology, physics. 2011;79(4):1188-95.

38. Kal HB, Van Gellekom MP. How low is the alpha/beta ratio for prostate cancer? International journal of radiation oncology, biology, physics. 2003;57(4):1116-21.

39. Oliveira SM, Teixeira NJ, Fernandes L. What do we know about the alpha/beta for prostate cancer? Medical physics. 2012;39(6):3189-201.

40. Ghilezan M, Yan D, Martinez A. Adaptive radiation therapy for prostate cancer. Seminars in radiation oncology. 2010;20(2):130-7.